

THE COSMOLOGICAL DEPENDENCE OF THE
FORMATION AND EVOLUTION OF DARK
MATTER HALOES

Shaun T. Brown

A thesis submitted in partial fulfilment of the requirements of
Liverpool John Moores University
for the degree of
Doctor of Philosophy.
July 2022

Declaration

The work presented in this thesis was carried out at the Astrophysics Research Institute, Liverpool John Moores University. Unless otherwise stated, it is the original work of the author.

While registered as a candidate for the degree of Doctor of Philosophy, for which submission is now made, the author has not been registered as a candidate for any other award. This thesis has not been submitted in whole, or in part, for any other degree.

Shaun T. Brown
Astrophysics Research Institute
Liverpool John Moores University
IC2, Liverpool Science Park
146 Brownlow Hill
Liverpool
L3 5RF
UK

AUGUST 25, 2022

Abstract

Over the past few decades numerical simulations with collisionless dynamics have reached a consensus about the form of the internal structure of dark matter (DM) haloes. However, the theoretical origin of these is still poorly understood. In this thesis I focus on studying the link between the initial primordial power density fluctuations and the internal structure of collapsed DM haloes today. This is the main focus of this thesis, and is split into three main parts; in the first chapter I study the dependence of the internal properties of DM haloes, primarily the mass density and pseudo phase space density (PPSD) profiles, on initial density fluctuation by systematically varying both the amplitude and slope of the linear power spectrum. It is observed that a number of previously assumed universal results break down when the initial power spectrum deviates from the CMB normalised case with the density profile deviating strongly from an NFW form, with steeper slopes than -3 , and the PPSD power law slope now exhibiting a clear cosmological dependence. In the second part of this thesis the simulations introduced in the first section are used to develop a model to predict the density profiles of DM haloes for a general mass, redshift and cosmology. To fully describe the density profiles observed in simulations two parameters are required: concentration, c , and an additional ‘shape’ parameter, α . I demonstrate that these two parameters can be expressed as a single, universal function of peak height using an appropriately chosen window function, allowing for a simple model to be developed. In the final section of this thesis I explore the joint effects of warm dark matter (WDM) and baryonic effects on the satellite populations of Milky Way mass systems. Here it is found that there is a strong degeneracy between the feedback (subgrid) parameters and the assumed WDM strength that should be taken into account when placing constraints on WDM

and similar cosmological extensions.

Publications

In the course of completing the work presented in this thesis, the following papers have been submitted for publication in a refereed journal:

First author papers:

Brown Shaun T., McCarthy Ian G., Diemer Benedikt, Font Andreea S., Stafford Sam G., Pfeifer Simon. Connecting the structure of dark matter haloes to the primordial power spectrum // MNRAS. VI 2020. 495, 4. 4994–5013

Brown Shaun T., McCarthy Ian G., Stafford Sam G., Font Andreea S. Towards a universal model for the density profiles of dark matter haloes // MNRAS. II 2022. 509, 4. 5685–5701

Coauthor papers:

Hill Alexander D., Crain Robert A., McCarthy Ian G., Brown Shaun T. Intrinsic alignments of the extended radio continuum emission of galaxies in the EAGLE simulations // MNRAS. IV 2022. 511, 3. 3844–3862

Font Andreea S., McCarthy Ian G., Belokurov Vasily, Brown Shaun T., Stafford Sam G. Quenching of satellite galaxies of Milky Way analogues: reconciling theory and observations // MNRAS. III 2022. 511, 1. 1544–1556

Stafford Sam G., McCarthy Ian G., Kwan Juliana, Brown Shaun T., Font Andreea S., Robertson Andrew. Testing extensions to Λ CDM on small scales with forthcoming cosmic shear surveys // MNRAS. XII 2021. 508, 2. 2537–2555

Poole-McKenzie Robert, Font Andreea S., Boxer Billy, McCarthy Ian G., Burdin Sergey, Stafford Sam G., Brown Shaun T. Informing dark matter direct detection limits with the ARTEMIS simulations // *JCAP*. XI 2020. 2020, 11. 016

Font Andreea S., McCarthy Ian G., Poole-Mckenzie Robert, Stafford Sam G., Brown Shaun T., Schaye Joop, Crain Robert A., Theuns Tom, Schaller Matthieu. The ARTEMIS simulations: stellar haloes of Milky Way-mass galaxies // *MNRAS*. X 2020. 498, 2. 1765–1785

Pfeifer Simon, McCarthy Ian G., Stafford Sam G., Brown Shaun T., Font Andreea S., Kwan Juliana, Salcido Jaime, Schaye Joop. The BAHAMAS project: effects of dynamical dark energy on large-scale structure // *MNRAS*. X 2020. 498, 2. 1576–1592

Stafford Sam G., Brown Shaun T., McCarthy Ian G., Font Andreea S., Robertson Andrew, Poole-Mckenzie Robert. Exploring extensions to the standard cosmological model and the impact of baryons on small scales. 2020a

Acknowledgements

As a young PhD student you are routinely warned that at some point you will come to hate your PhD, and no longer enjoy the research that you are doing. Whether this contempt will arise in the second, third or even final year is never made clear, only that it will happen at some point. However, this was never the case for me and I have fortunately enjoyed every moment of my time at Liverpool. I attribute this in no small part to the fantastic culture that has been developed at the ARI, where everyone is made to feel welcome and part of the institute, no matter their seniority.

There are many people I wish to thank from my time at Liverpool. I am generally indebted to everyone at the ARI, and would specifically like to thank my supervisors Ian and Andreea, who have always been there to offer guidance and support, and most importantly taught me how to be a researcher. I would additionally like to thank my amazing PhD cohort Conor, Fiona, Allister, Danny, Egidijus, Jon, Alex, Alberto, Rob and most importantly Sam and Simon who I have probably learnt the most from over the past four years. I would finally like to thank my partner Charlotte and my parents who have always supported me through my education and made it possible to complete this Thesis.

Contents

Declaration	ii
Abstract	iii
Publications	v
Acknowledgements	vii
Contents	viii
List of Tables	xiii
List of Figures	xv
1 Cosmology Introduction	1
1.1 Cosmological overview	2
1.2 An expanding universe	4
1.2.1 Comoving coordinates and Friedmann equations	4
1.3 The Λ CDM model	7
1.3.1 Extensions to Λ CDM	9
1.4 Analytic models for structure collapse	11

1.4.1	Overdensities & Gaussian random fields	11
1.4.2	Linear evolution	13
1.4.3	Spherical Collapse Model	15
1.4.4	Secondary infall models	18
1.4.5	Press-Schechter and peak height	23
2	Simulation Techniques	28
2.1	Key equations and general simulation principles	29
2.2	Gravity solver	30
2.3	Time Integration	33
2.4	Initial Conditions	34
2.5	Halo finder	36
2.6	Key results from numerical simulations	39
2.6.1	Density profiles of dark matter haloes	40
2.6.2	Small scale challenges of Λ CDM	42
3	Connecting the structure of dark matter haloes to the primordial power spectrum	45
3.1	Introduction	46
3.2	Simulations and halo property estimates	50
3.2.1	Halo mass and radius definitions	50
3.2.2	General simulation setup	50
3.2.3	Primordial power spectra	51
3.2.4	Halo selection criteria	53

3.2.5	Density and velocity dispersion profiles	55
3.2.6	Halo entropy vs. PPSD	57
3.3	Stacked profiles	58
3.3.1	Stacked density profiles	59
3.3.2	Stacked entropy profiles	64
3.3.3	Stacked velocity dispersion profiles	66
3.4	Mass and peak height dependence	69
3.4.1	Mass dependence	70
3.4.2	Peak height dependence	74
3.4.3	Interpreting A_s as a change of redshift	76
3.5	Accretion histories and (semi-)analytic models	77
3.5.1	Mass accretion and collapsed mass histories	78
3.5.2	Comparison to analytic models	80
3.6	Summary	83
4	Towards a universal model for the density profiles of dark matter haloes	86
4.1	Introduction	87
4.2	Simulation and analysis details	90
4.2.1	Cosmologies	90
4.2.2	Simulation details	92
4.2.3	Fitting density profiles	93
4.3	Peak height definition	99
4.4	Peak height relations	102

4.5	Optimal window functions	104
4.5.1	Smooth k -space window function	107
4.5.2	Quantitatively determining universality	110
4.5.3	An optimal window function	111
4.5.4	Predicting the density profile of DM haloes	117
4.6	Testing the model	122
4.7	Summary and conclusions	124
5	ARTEMIS Dark	129
5.1	Introduction	130
5.2	Simulation details	131
5.2.1	Initial conditions	131
5.2.2	Baryonic and subgrid physics	133
5.3	The Emulator	133
5.3.1	Parameter choices	134
5.3.2	Building the emulator	139
5.4	Analysis	140
5.4.1	Host stellar mass, fixed WDM mass	142
5.4.2	Host stellar mass and satellite GSMF, fixed WDM mass . . .	144
5.4.3	Variable WDM	147
5.5	Conclusions and future work	149
6	Summary & Conclusions	151

6.1	Connecting the structure of dark matter haloes to the primordial power spectrum	151
6.2	Towards a universal model for the density profiles of dark matter haloes	152
6.3	ARTEMIS Dark	153
A		154
A.1	Density and velocity dispersion calculation methods	154
A.1.1	Choosing appropriate parameters	157
A.2	Resolution test and box size tests	162
B		165
B.1	Resolution and box size study	165
	Bibliography	168

List of Tables

- 1.1 List of the best fit parameters, with errors, from the Planck 2018 results. The top section are the fitted, independent, parameters while the bottom section represents the derived parameters for a Λ CDM cosmology. 9
- 3.1 Summary of the various cosmological parameters for all simulations presented in this work. The main two parameters varied are n_s and A_s . Along with k_{pivot} , they completely specify the initial power spectrum. Note that for the ‘Matched amplitude’ suite, the shape is fixed ($n_s = 0.96$) while the amplitude at a scale of $1 h \text{ Mpc}^{-1}$ is adjusted to match the various runs in the ‘WMAP9 pivot’ suite. All cosmologies have the same background expansion: $h = 0.7$, $\Omega_m = 0.2793$, $\Omega_b = 0.0463$ and $\Omega_\Lambda = 0.7207$ 54
- 4.1 Optimal χ_r^2 values for different choices of window functions, with the associated optimal parameters. The value of χ_r^2 is calculated by fitting a second order polynomial. For the smooth k -space filter there is no unique choice of μ and β that gives a minimum value of χ_r^2 , the parameters provided here are just one such possible combination. I have also provided the χ_r^2 values for the prediction of c for two models from the literature for comparison. 120

5.1 Table of the 6 parameters that are jointly varied for the simulations. This includes the WDM mass, m_{DM} , the reionisation redshift, z_{re} , and four parameters associated with stellar feedback, f_{min} , f_{max} , $n_{\text{H},0}$ and α , see Eqn. (5.4). The fiducial values used in the ARTEMIS simulations are shown in the middle column. The final column shows the emulation range for these parameters. 136

List of Figures

1.1	Results from the secondary infall model. Here is shown the resulting particle trajectories, as expressed in the dimensionless quantities λ and ϵ . This result can either be interpreted as the trajectory of an individual particle, or as a snapshot of particle positions.	20
1.2	Results from the secondary infall model. Here is shown the contained mass within the dimensionless radius λ . From this plot the density profile $\rho \propto r^{-2.25}$ can be inferred.	21
1.3	Results from the secondary infall model. Here is shown the (analogous) density D as a function of the dimensionless radius λ . Here the features imprinted on the density profile by the specific scale of the turn around radius can be seen.	22
1.4	Schematic one-dimensional depiction of how individual regions can be identified in the linear Gaussian field that will collapse into individual haloes. Here is shown an arbitrarily normalised one-dimensional Gaussian random field and corresponding critical density. In this example we would expect 4 haloes would be expected to form from the corresponding regions where $\delta_{\text{lin}} > \delta_c$	24
2.1	Depiction of the PM and octree approaches applied to an example two-dimensional particle distribution. Here the dynamic nature of the octree can be seen, where the internal structures of the individual haloes are more finely resolved than using the static PM approach.	32

2.2	Example distribution of particles taken from a WMAP-9 cosmology initialised at $z = 127$. This is a sub-sample of a thin layer of particles taken from a full three-dimensional set of initial particle coordinates. The initial homogeneous grid positions are shown as dashed lines.	36
2.3	Example of the FOF algorithm applies to the same two-dimensional particle distribution as shown in Fig. 2.1. Here, FOF groups with less than 40 particles have been discounted. Different colours denote particles as belonging to a given FOF groups, with black used for those not identified into FOF groups with less than 40 particles.	37
3.1	Linear power spectra used to create the initial conditions of the various simulations at $z = 127$, generated using CAMB (Lewis et al., 2000). All cosmologies have the same background cosmology (best fit WMAP 9-yr results), but with variable A_s , n_s and k_{pivot} . Left panel shows the fiducial suite with adopting a WMAP pivot point ($k = 2.85 \times 10^{-3} h\text{Mpc}^{-1}$) with systematically varying n_s . The middle-left panel is the initial power spectra for the suite of simulations that have a fixed n_s but a varied A_s such that at $k = 1 h\text{Mpc}^{-1}$ they have the same power as the corresponding WMAP pivot simulations (left panel). The middle-right panel shows the same but for a <i>Planck</i> pivot point ($k = 7.14 \times 10^{-2} h\text{Mpc}^{-1}$). The suite using a $k_{\text{pivot}} = 1 h\text{Mpc}^{-1}$ with systematically varied n_s is shown in the right most panel. The value of n_s , or equivalently matched A_s is shown in the colour bar above each plot. The vertical dashed lines represent the Nyquist frequency and the fundamental mode for the box size, i.e. the resolved range of the simulations.	52

- 3.2 Surface density maps of the six WMAP pivot cosmologies with variable n_s at $z=0$. From top left to bottom right we have increasing values of n_s from 0.5–1.75, see label in bottom left of each panel. These plots are meant to show the qualitative behaviour of the different density fields so no colour bar is given. Each colour map is normalised the same and represents the logarithmic projected surface density. These images have been made using the publicly available code `SPH-Viewer` (Benitez-Llambay, 2015). 58
- 3.3 Top panels show the stacked median density profiles of haloes in the mass range $M_{200c} = 10^{13} - 10^{13.5} h^{-1} M_{\odot}$ while the bottom panels the logarithmic slope of the above plot, defined as $\gamma_{\rho} = d(\ln \rho)/d(\ln r)$ at $z = 0$. Densities are normalised to the critical density today while the radii are normalised to each haloes R_{200c} . The left column shows the WMAP pivot cosmology with variable n_s , the middle-left panels the equivalently matched A_s with fixed n_s , the middle-right panels the *Planck* pivot point with variable n_s and the far right panels the $k_{\text{pivot}} = 1 h \text{ Mpc}^{-1}$ suite. The colours represent the different suites of simulations while the shade represents the value of n_s or matched A_s , see colour bar above each plot. Each curve is plotted transparent where the criteria for convergence is not met. A comparison of the different panels indicates that the dominant factor in setting the density profile of a halo is the *amplitude* of the linear power spectra at an associated k -mode. 59

- 3.4 Top panels show the density profiles of the WMAP pivot cosmology with variable n_s , see legend. This is identical to the top left panel of Fig. 3.3, apart from multiplying by $(r/R_{200c})^2$ to reduce the dynamic range. I have then fit each profile with either a NFW (left) or Einasto curve (right), allowing both the scale radius and shape parameter to vary when fitting the Einasto profile. The fitting routine minimises the figure of merit, ψ^2 , and is only fit over the range where $r/R_{200c} < 0.7$, to avoid fitting to the splashback radius, and above the convergence radius. On the bottom panels I show the fractional residuals, $(\rho_{\text{fit}} - \rho)/\rho$, from this fit. The NFW form breaks down for runs with large n_s (corresponding to large amplitudes at $k = 1h \text{ Mpc}^{-1}$). 62
- 3.5 Entropy profiles of haloes in the mass range $M_{200c} = 10^{13}\text{--}10^{13.5}h^{-1} M_{\odot}$. In the top panels is plotted the entropy, defined as $S(r) = (\rho/\sigma^3)^{-2/3}$, normalised by a ‘virial’ entropy, $S_{200c} = (200\rho_{\text{crit}}/v_{\text{circ},200c}^3)^{-2/3}$. The bottom panel shows the logarithmic slope of those profiles, $\gamma_S(r) = d(\ln(S))/d(\ln(r))$. See Fig. 3.3 for a description of the general structure of the figure. In general it is observed that the slope of the entropy profiles are not constant and in general depend on the underlying cosmology. Similar to the density profiles, the dominant factor in determining the entropy profiles is the amplitude of the linear power spectra at an associated k -mode. 64
- 3.6 Stacked velocity dispersion and velocity anisotropy profiles of haloes in the mass range $M_{200c} = 10^{13}\text{--}10^{13.5}h^{-1} M_{\odot}$. In the top panels is plotted the total velocity dispersion while the bottom panel shows the velocity anisotropy, $\beta = 1 - \sigma_T^2/\sigma_r^2$. See Fig. 3.3 for a description of the general structure of the figure. 67

- 3.7 Fitted parameters as a function of mass. Haloes with greater than 2000 particles are stacked in mass bins of 0.3 dex, only bins with more than 15 haloes are plotted. The resulting stacked density and entropy profiles are then fit by minimising ψ^2 , see Eqn. (A.7). There are two fitted parameters shown, halo concentrations, c , and entropy power law exponent χ . Each row shows one of these parameters as a function of halo mass, M_{200c} , while each column represents the four suites of simulations; WMAP pivot variable n_s (left), matched A_s (middle-left), *Planck* pivot point with variable n_s (middle-right) and $k_{\text{pivot}} = 1h^{-1} M_{\odot}$ variable n_s (right). The different shades represent the particular value of n_s , or A_s , see colourbar. 71
- 3.8 Entropy normalisation, Δ_S , as a function of power law exponent, χ , see Eqn. 3.11 for definition, for all cosmologies sampled. Each data point represents a mass bin with the colour denoting the particular cosmology, as originally specified in Fig. 3.1. The black dashed line represents the best fit power law relation of $\Delta_S = 0.94\chi^{3.92}$. There is no discernible dependence on the initial power spectra and the relation appears to be universal. 72
- 3.9 Fitted parameters, halo concentration, c , and entropy power law exponent, χ , as a function of peak height, ν . See Eqn.(3.13) for the definition of ν . The plot, and associated analysis, is identical to Fig. 3.7 but with the mass converted to peak height for each different cosmology. In general amplitude changes to the primordial power spectra are well described by peak height, however there are secondary ‘shape’ changes to the linear power spectra that are not accounted for by a change in peak height. 76

- 3.10 The normalised MAH and CMH plotted as a function of critical density, for stacked haloes in the mass range $M_{200c} = 10^{13} - 10^{13.5} h^{-1} M_{\odot}$. See 3.5.1 for the definition of MAH and CMH. The different panels and colours represent the different suite of simulations, see label in bottom left of each panel. The shades of each colour represent the value of n_s , or matched A_s , used for the simulations, see colourbar. The different line-styles represent either the MAH or CMH, see legend. The changes to the MAH and CMH of haloes is in qualitative agreement with what is expected from the change in their concentration. Haloes with higher (lower) concentrations are those that formed earlier (later) with subsequent slower (faster) accretion today. 79
- 3.11 Comparisons between the predictions of Correa et al. (2015), Ludlow et al. (2016) and Diemer, Joyce (2019) to this work for the $c-\nu$ relation. Predictions from the various works are shown as dashed lines while the simulation results are shown in solid lines. Each column represents the different simulations suites with the shaded colour the value of n_s (or A_s). Each row is is the predictions from the different models, see bottom left of left most panel. Unlike Fig. 3.9 I have used variable dynamic ranges to more easily highlight the differences. 81
- 4.1 *Top:* The $z = 0$ linear power spectra for the various cosmologies studied in this work. *Bottom:* The rms density fluctuations in spheres of radius R . The left and right panels represent the two different suites (introduced in Brown et al. 2020), which use different pivot points for the linear power spectrum (see label in bottom left). For each suite (or pivot point), the primordial spectral index, n_s is systematically varied from 0.5 to 1.75 with $n_s = 0.96$ being the best-fit WMAP 9-yr value. The different shades represent different values of n_s , see colour bar. . . 91

4.2 Stacked density profiles for a range of masses (see legend) at $z = 0$ for a WMAP 9-yr cosmology. The $\log M_{200c} = 13.25, 13.75$ and 14.25 mass bins constitute stacks of 5, 713, 1, 318 and 211 haloes, respectively. The profiles are only plotted up to their convergence radius (Eqn. (4.4)) which varies strongly with halo mass. For each density profile, r_{-2} and ρ_{-2} are estimated non-parametrically from the logarithmic slope. The density profiles are normalised by their respective scale radii, r_{-2} , and plotted as ρr^2 to reduce the dynamic range. Normalising the radial coordinate in this way removes the dependence on concentration. As can be seen, there is a clear halo mass dependence to the normalised density profiles, demonstrating that the density profiles are not self-similar and that an additional ‘shape’ parameter is required to fully describe them. Plotted as dashed lines are Einasto profiles that approximately follow the simulated density profiles. In these units, the Einasto profile has only one free parameter, α (see legend). 97

4.3 Stacked density profiles for a range of masses (see legend) at $z = 0$ for a WMAP 9-yr cosmology. The $\log M_{200c} = 13.25, 13.75$ and 14.25 mass bins constitute stacks of 5, 713, 1, 318 and 211 haloes, respectively. The profiles are only plotted up to their convergence radius (Eqn. (4.4)) which varies strongly with halo mass. For each density profile, r_{-2} and ρ_{-2} are estimated non-parametrically from the logarithmic slope. The density profiles are normalised by their respective scale radii, r_{-2} , and plotted as ρr^2 to reduce the dynamic range. Normalising the radial coordinate in this way removes the dependence on concentration. As can be seen, there is a clear halo mass dependence to the normalised density profiles, demonstrating that the density profiles are not self-similar and that an additional ‘shape’ parameter is required to fully describe them. Plotted as dashed lines are Einasto profiles that approximately follow the simulated density profiles. In these units, the Einasto profile has only one free parameter, α (see legend). 103

4.4 *Top:* The smooth k -space window function (Eqn. (4.13)) for a few combinations of μ and β (see legend). Qualitatively, μ changes the scale at which the transition occurs, with smaller values of μ resulting in the transition occurring at higher values of kR (corresponding to smaller physical scales), while β controls how quickly the transition from $W = 1$ to $W = 0$ occurs. Plotted for reference is the standard STH window function (shown in black). Additionally plotted in the inset panel is $(kR)^2W^2(kR)$ for the same window functions in the main plot, with each curve has been normalised by its global maximum. No units have been plotted for the inset, as the purpose of the figure is to demonstrate that $(kR)^2W^2(kR)$, for all window functions studied here, exhibits a clear peak, with the location of that peak depending on both μ and β . *Bottom:* The resulting relation between peak height and mass, normalised at $M = 10^{13.5}h^{-1}M_{\odot}$ for the WMAP-9 yr cosmology. The STH (black lines) and smooth k -space window function with $\mu = 1$ and $\beta = 1$ (blue lines) follow a very similar $\nu(M)$ relation. . . . 108

4.5 Parameter space demonstrating how χ_r^2 varies with the free parameters of the smooth k -space window function, μ and β , for the two density parameters c (*top*) and α (*bottom*). χ_r^2 is used to quantitatively determine how close to universal the resulting peak height relations are, with smaller values of χ_r^2 corresponding to more universal relations. To first order the value of peak height is set by the amplitude of the linear power spectrum at an associated k -scale, with that scale depending on the given window function. The key property is where $(kR)^2W^2(kR)$ is a maximum, as described through the parameter κ , see Eqn.(4.17). Plotted as dashed black lines are contours of constant κ (see Eqn. (4.18)), with $\kappa = 9$ and $\kappa = 2$ for c and α , respectively. These contours follow very closely the observed degeneracies between μ and β 112

- 4.6 Variation of χ_r^2 as a function of μ_g for the generalised spherical top-hat window function (see Eqn. (4.19)) for the two density parameters c (solid line) and α (dashed line). χ_r^2 is used to quantitatively determine how close to universal the resulting peak height relations are, with smaller values of χ_r^2 corresponding to more universal relations. These distributions exhibit clear minima at $\log \mu_g = -0.67$ and $\log \mu_g = -0.01$ for c and α , respectively. Note that $\log \mu_g = 0$ ($\mu_g = 1$) corresponds to the standard spherical top-hat window function. 115
- 4.7 Resulting $c-\nu_c$, top panel, and $\alpha-\nu_\alpha$, bottom panel, relations for the optimal choice of window function. The data points presented are all those used to constrain the window function. The colour indicates the given cosmology, matching those in Fig. ??, while the marker style corresponds to the redshift (see legend). The black dashed lines represent the empirical relations used for the model to predict c and α for a general cosmology. The fractional difference from the data and the empirical fits are shown in the bottom panels, for both c and α 118
- 4.8 Resulting $c-M_{200c}$ (*top*) and $\alpha-M_{200c}$ (*bottom*) relations for the WMAP 9-yr cosmology (*left*), $\Omega_m = 0.2$ (*middle*) and $\Omega_m = 0.2$ (*right*) cosmologies. For each cosmology the relations are shown at $z = 0$ and 1 (see legend). The solid lines with errors represent the data from the simulations while the dashed lines the predictions from the model. In general both c and α are accurately predicted by the model with any differences being within 5% (or approximately one sigma), demonstrating that the model generalises to cosmologies with different background expansions as well as changes to the linear power spectrum. . 123

5.1	<p>Example plot for the relation between the feedback efficiency and stellar birth density. This is the relation used in the EAGLE model to control the total effectiveness of stellar feedback in the simulations, see Eqn. (5.4). Here there are 4 free parameters. f_{\min} and f_{\max} control the minimum and maximum efficiencies, respectively, with $n_{\text{H},0}$ controlling the density at which the transition from low to high efficiencies occurs. α, not shown in the plot, controls how quickly the transition occurs with higher values of α corresponding to relation more closely following a step function.</p>	135
5.2	<p>Corner plot showing the combination of the 6 parameters for the 25 simulations used to build the emulator. Here the sampling is done using an orthogonal Latin hypercube. This results in an even sampling of the space, as can be seen by all 2-dimensional projections shown. .</p>	138
5.3	<p>Resulting training data from the Latin hypercube sampling (see Fig 5.2). The left panel shows the cumulative satellite GSMF with different coloured lines corresponding to the different simulations, with the dashed black line showing the fiducial ΛCDM simulation for reference. The right panel shows the distribution of host stellar masses, quoted with respect to the fiducial ΛCDM simulation.</p>	140
5.4	<p>Accuracy of the emulator, tested against a range of simulations not in the training set. The left panel shows the difference in cumulative satellite GSMF from the emulator prediction to the simulation, with different coloured lines corresponding to different simulations. The right panel shows the distribution of differences in host stellar masses from the emulator prediction and the simulation results. The standard deviations from these plots are then treated as the error on the emulator. .</p>	141

5.5	Posterior distribution from the MCMC analysis for the baryonic parameters, presented as a corner plot with the 2-dimensional projections showing the 1-sigma contours. Here the posterior is constrained by only the host stellar mass, see Section 5.4 for details. In the analysis the WDM mass is held fixed for a range of values, see legend. The top right panel shows the data being fit to (solid black Gaussian distribution), i.e. the host stellar mass, with the resulting median values from the MCMC chains shown as coloured lines.	143
5.6	Same as Fig. 5.5, but fitting to both the host stellar mass and cumulative satellite GSMF. The top tight panel shows the data, with errors, being fit to (black lines) with the median relation from a random subsample of the MCMC chains (coloured lines).	145
5.7	Same analysis as Fig. 5.6, fitting to both the host stellar mass and the GSMF. However, here the WDM mass was not held fixed but rather allowed to vary to test how well m_{DM} can be constrained. Here the corner plot now shows the 1 and 2-sigma contours. Note that the m_{DM} axis is scaled according to Eqn. (5.5), with a linear sampling for $m_{\text{DM}} < 5$ and a reciprocal scaling for $m_{\text{DM}} > 5$. As such, $m_{\text{DM}} = 0$ corresponds to the far left of the plotted axis.	148

Chapter 1

Cosmology Introduction

Over the past few decades numerical simulations of collisionless universes have arrived at a number of key results that appear to be universal. Particularly interesting and important is the form of the density profiles of the dark matter haloes, that are well fit by a simple empirical form, the NFW profile. Similarly, the pseudo phase space density, defined as the ratio of the density to velocity dispersion cubed, is observed to take on a simple power law behaviour with a constant slope. It is somewhat surprising that such simple forms for the internal structure of DM haloes arise from the complexities of structure collapse and virialisation. As such, the theoretical origin of these empirical results is poorly understood. Trying to understand the link between these results and the underlying cosmology is the focus of much of this thesis.

With this general topic in mind the thesis is organised as follows. In this chapter I review some of the basic concepts within modern cosmology and cover some of the key analytic theories for the formation and evolution of collapsed objects, particularly how to link them to the initial density fluctuations of our Universe. In Chapter 2 I cover the key techniques involved in numerical simulations of structure formation, which are used extensively throughout this thesis. In Chapter 3 I look to study the link between the primordial power spectrum and the internal properties of DM haloes. This is done by systematically varying the slope and amplitude of the initial power spectrum to test if the ‘universal’ results discussed above generalise to cosmologies with significantly

different initial conditions than our own Universe. Based on results from this chapter a model to link the density profiles of DM haloes, described through the concentration and shape parameters, to the linear power spectrum is developed in Chapter 4. This link is quantitatively described through a generalisation of the peak height definition. Finally, in Chapter 5 I present ongoing work studying the interplay between baryonic feedback and the effects of WDM. This is studied in the context of Milky Way mass systems and their satellite populations.

1.1 Cosmological overview

It is currently believed that our Universe is made of three key components: dark energy, dark matter (DM) and ‘normal’ baryonic matter, which, respectively, make up approximately 70%, 25% and 5% of the present day energy budget. Currently there is no agreed upon theory for the origin of both dark energy and DM, with no direct observations of either component. We are therefore in an uneasy position where we believe that our Universe is dominated by components that we do not yet understand.

Although the theoretical origin and nature of these dark components is currently unknown we do have strong evidence for their existence.

Some of the strongest evidence for dark matter comes from measuring the total mass of objects and comparing this to the observed mass in stars and gas. Here it is ubiquitously observed that the total amount of matter is significantly larger than the baryonic component, across systems of vastly different scales, from galaxy clusters to dwarf galaxies. The total mass of systems can be inferred by applying the virial theorem to the observed velocity dispersion (e.g. Zwicky, 1933; Faber, Jackson, 1976), measuring the stellar rotation curves of spiral galaxies (e.g. Schmidt, 1957; Corbelli, Salucci, 2000), and from the strong or weak lensing of background galaxies (e.g. Taylor et al., 1998; Natarajan et al., 2017). Another compelling piece of evidence for DM is the bullet cluster (Clowe et al., 2006), which is a system of two merging clusters. Here it is observed that the visible gaseous component is distinctly offset from the

gravitational potential. A result that is naturally explained if both clusters contained a significant amount of matter that only interacts by gravity (i.e. DM).

There are three key pieces of evidence for the existence of dark energy. The first piece of evidence is the current most direct detection. Using type 1a supernovae as standard candles it is observed that the expansion of our universe is accelerating (Riess et al., 1998). This acceleration is then directly associated with dark energy. The second important piece of evidence is from combining measurement of CMB, to constrain the total amount of matter, with local measurements of the Hubble constant. Here, if no dark energy is assumed then the prediction for the Hubble constant from fitting the CMB is in significant tension with what is measured (e.g. Smoot et al., 1992). Introducing some form of late time acceleration, typically described as a cosmological constant, resolves this tension and allows the amount of dark energy to be inferred. The final piece of evidence is more subtle; a universe without some form of accelerated expansion today, but with the same current expansion rate observed in our Universe, does not form as much structure as we observe (e.g. White et al., 1993). Similar to the second piece of evidence this discrepancy can be resolved by introducing a cosmological constant that causes this late time expansion. This results in the ‘standard’ concordance cosmological model of Λ CDM (see Section 1.3).

An additional very powerful probe of cosmology is studying structure formation. While geometric probes (such as CMB anisotropies and the local expansion rate) can put tight constraints on the abundance of DM and dark energy they cannot differentiate between physical models of DM and dark energy, or theories of modified gravity. By combining both geometric probes, that sample the expansion of the universe, with structure formation, that probes the effect of gravity on, comparably, small scales, these degeneracies can be broken and strong constraints can be placed on various models for the nature of DM and dark energy.

In this chapter I will review some of the most fundamental concepts and equations for the origin and growth of structures within our Universe. In section 1.2 I review how to formulate and describe the evolution of expansion of our Universe, as described by the Friedmann equations. In section 1.4.1 I will describe the form of the

initial density fluctuations in the early universe and how these initially, before finally discussing the link between the initially small density fluctuations and the collapsed structure known as DM haloes that we expect to host galaxies in our own Universe in section 1.4.

1.2 An expanding universe

The field of cosmology arguably began with the seminal work of Hubble (1929) who demonstrated that galaxies outside our own Milky Way (originally referred to as extragalactic Nebulae) are observed to be predominantly redshifted, and hence moving away from us. Furthermore, it was observed that the recession velocity of a given galaxy was proportional to the distance of the object, with further away galaxies receding at higher velocities. This relation is characterised as ‘Hubble’s Law’,

$$v = H_0 D. \quad (1.1)$$

Where v is the recession velocity, D is the distance to the galaxy and H_0 is Hubble’s constant.

This result leads to the rather profound conclusion that we live in a dynamic universe, implying a start, and potential, end to our Universe. Hubble’s constant therefore quantifies the current rate of expansion of our Universe. A natural question to ask is then what is the previous and future expansion rate of the universe? Will it expand forever, or is there some maximum size it will reach before contracting under the force of gravity? In this section I will present how general relativity, and the Friedmann equations, quantitatively describe this evolution.

1.2.1 Comoving coordinates and Friedmann equations

When considering a universe that is constantly expanding it is useful to work in so-called ‘comoving coordinates’. In this coordinate system the distance between points

is independent of time. The comoving position, \vec{x} , is related to the proper physical position, \vec{r} , via

$$\vec{r}(t) = a(t)\vec{x}(t). \quad (1.2)$$

Where we have introduced the scale factor, a that quantifies the ‘size’ of the Universe at a given time. Typically, a is normalised to unity today.

Taking the derivative of the above equation with respect to time,

$$\dot{\vec{r}} = \frac{\dot{a}}{a} \vec{r} + a\dot{\vec{x}}. \quad (1.3)$$

Comparing this expression to Eqn. 1.1 we see that this is the same form as Hubble’s law, with an additional peculiar velocity component. This naturally leads to the following definition of the Hubble parameter,

$$H = \frac{\dot{a}}{a}. \quad (1.4)$$

This definition of H can then be applied to any cosmology with an arbitrary evolution of scale factor. The current value of H observed today in our own Universe is known as the Hubble constant, H_0 .

The evolution of the Hubble parameter and scale factor can be predicted from general relativity. For a universe that is isotropic and homogeneous the evolution is described by the Friedmann–Lemaître–Robertson–Walker (FLRW) metric. In this case the solution to Einstein’s field equations are the Friedmann equations,

$$H^2(a) \equiv \left(\frac{\dot{a}}{a}\right)^2 = \frac{8\pi G}{3}\rho(a) - \left(\frac{c}{a}\right)^2 k + \frac{\Lambda c^2}{3} \quad (1.5)$$

and

$$\frac{\ddot{a}}{a} = -\frac{4\pi G}{3}\left(\rho(a) + \frac{3p(a)}{c^2}\right) + \frac{\Lambda c^2}{3}. \quad (1.6)$$

Here ρ is the average density of the universe and p the pressure of the fluid. k and Λ are constants and represent the spatial curvature and cosmological constant respectively,

¹Here $\dot{r} \equiv \frac{dr}{dt}$.

while G is the gravitational constant.

In the above I have described the evolution using the scale factor. However, that is not what is observed. Typically, what is observed is the redshift of galaxies due to this expansion. For a FLRW universe the scale factor and redshift are related by

$$a = \frac{1}{1+z}. \quad (1.7)$$

As such I will use the scale factor, a , and redshift, z , interchangeably to describe the universe at a given time.

Eqn. 1.5 and 1.6 therefore relate the rate of expansion, as described by the scale factor, to the density and pressure of the constituent matter in the universe as well as the intrinsic curvature of our Universe. For a cosmology without a cosmological constant the first Friedmann equation indicated that in an expanding universe the dominant contribution will always be the curvature term at late times. We would therefore expect that a universe with positive curvature to eventually stop expanding and eventually collapse, while a universe with negative curvature will continue to expand indefinitely, hence we refer to these two scenarios as closed and open universes respectively. Alternatively a universe could have no contribution due to the curvature and expand only due to its constituent parts, from the first Friedmann equation we can see that such a universe would have to have a very specific density, referred to as the critical density, $\rho_c = \frac{3H^2}{8\pi G}$. Notably, for a cosmology with a cosmological constant this term will be dominant at late times and cause an accelerated expansion.

There are a number of interesting limiting solutions to these equations. Assuming a single perfect fluid with equation of state $p = w\rho c^2$ dominates (i.e. $k = \Lambda = 0$) we have the following solutions,

$$a(t) = \begin{cases} a_0 t^{2/3}, & \text{matter dominated, } w = 0 \\ a_0 t^{1/2}, & \text{radiation dominated, } w = 1/3. \end{cases} \quad (1.8)$$

Due to these different dependences on the age of the Universe, as well as $\rho \propto a^{-3}$ and

$\rho \propto a^{-4}$ for matter and radiation domination, respectively, we can infer that the very early universe must have been dominated by radiation before subsequently cooling and going through a transition to matter domination.

For a universe that is made up of non interacting perfect fluids the solutions to the Friedmann equations can be expressed as a linear combination of its various components. It is therefore common to write the first Friedmann equation as such a linear combination with the relative contributions normalised to today's values,

$$H(z)^2 = \Omega_{r,0}a^{-4} + \Omega_{m,0}a^{-3} + \Omega_{k,0}a^{-2} + \Omega_{\Lambda}. \quad (1.9)$$

Here $\Omega = \rho/\rho_c$. It is these values, $\Omega_{r/m/k/\Lambda,0}$ that are then constrained by cosmological observations (this is discussed in more detail in Section 1.3).

1.3 The Λ CDM model

So far we have discussed the evolution of a universe in a relatively general context with minimal assumptions. However, for certain cosmological models we can reduce the number of free parameters needed to describe our Universe by making key assumptions. One such model, currently treated as the standard cosmological model, is that of Λ CDM.

In the Λ CDM model the Universe is assumed to be made of three key elements: dark matter (Ω_c), baryons (Ω_b) and a cosmological constant (Ω_{Λ}). The universe is also assumed to be flat (i.e. $\Omega_k = 0$), as such the current amount of matter and dark energy is given by

$$\Omega_{m,0} + \Omega_{\Lambda,0} = 1. \quad (1.10)$$

Where $\Omega_{m,0}$ is the total matter, $\Omega_{m,0} = \Omega_{c,0} + \Omega_{b,0}$.²

There are also a number of assumptions about the nature of DM: (i) It is non-

²Strictly, these relations should include terms for the radiation component and neutrinos, which act like radiation at early times and matter at late times. However, these components do not dominate the energy budget

baryonic, meaning that it consists of some form of currently unidentified matter not in the standard model of particle physics. (ii) It is cold and non-relativistic at the time of recombination. (iii) It is dissipationless, it cannot cool by radiating photons. (iv) It is collisionless, it interacts with itself and other forms of matter only through gravity. These assumptions are the simplest model that is consistent with the data and account for there yet to be a direct detection of a DM candidate. As such, any form of DM must not interact strongly (other than through gravity) with other forms of matter, or strongly emit observable radiation.

It is also assumed that dark energy takes the form of a cosmological constant, that is temporally and spatially uniform.

The final key assumption is about the nature of the density perturbations immediately after the period of inflation. It is assumed that the power spectrum³ takes the form of a perfect power,

$$P(k) = A_s \left(\frac{k}{k_{\text{pivot}}} \right)^{n_s}. \quad (1.11)$$

Here n_s is known as the scalar spectral index, corresponding to the slope of the power law, and A_s represents the amplitude of these fluctuations. Note that A_s is defined to be the amplitude at k_{pivot} . Although there are three parameters defined above there are only two free parameters. Typically, k_{pivot} is held fixed and chosen to be a scaled well sampled by the given observation, A_s and n_s are then varied and constrained.

Due to these key assumptions the temperature fluctuations in the cosmic microwave background (CMB) can be well fit using only 6 free parameters: $\Omega_c h^2$, $\Omega_b h^2$, n_s , A_s , the angular size of the baryon acoustic oscillations, θ_{MC} , and the Thompson optical depth at reionisation. In general the Λ CDM model fits all observations data extremely well (though a number of tensions do exist as we will discuss later), suggesting that with only these 6 parameters we can describe the complete evolution of our Universe. These represent all of the independent parameters in the Λ CDM model, however there are a number of other useful cosmological parameters that can be derived, most notably the Hubble constant. A list of the free parameters and important derived pa-

³The power spectrum is a way of characterising the initial density fluctuations. This is defined and discussed in detail in section 1.4.1

Table 1.1: List of the best fit parameters, with errors, from the Planck 2018 results. The top section are the fitted, independent, parameters while the bottom section represents the derived parameters for a Λ CDM cosmology.

Parameter	Planck best fit value
$\Omega_b h^2$	0.02233 ± 0.00015
$\Omega_c h^2$	0.1198 ± 0.0012
$100\theta_{\text{MC}}$	1.04089 ± 0.0031
τ	0.0540 ± 0.0074
$\ln(10^{10} A_s)$	3.043 ± 0.014
n_s	0.9652 ± 0.0042
Ω_m	0.3147 ± 0.0011
t_{age} [Gyr]	13.801 ± 0.024
H_0 [$\text{km s}^{-1} \text{Mpc}^{-1}$]	67.37 ± 0.54
σ_8	0.8101 ± 0.061

rameters with the best fit parameters from Planck 2018 results (Planck Collaboration et al., 2020), is given in Table 1.1.

It is primarily from these observations of the CMB that we get the key results for the age and contents of our Universe. Primarily, the results that we live in a universe currently dominated by dark energy with $\Omega_\Lambda \sim 0.7$, the abundance of matter is dominated by dark matter with normal baryonic matter making up around $\sim 15\%$ and that our Universe is roughly 13.8 Gyr old.

1.3.1 Extensions to Λ CDM

Although Λ CDM is our current standard cosmological model it makes a number of key assumptions, as well as not providing an explanation for the physical origin of its two main components, dark matter and dark energy. As such there is significant interest in possible deviations from Λ CDM, requiring extensions to the model.

Typically, extensions to Λ CDM challenge one of the key assumptions previously mentioned and fall into two broad categories; those that affect the expansion of the Universe, and those that change the nature or form of dark matter.

For instance, one can no longer force the universe to be flat and instead allow a non-negligible amount of curvature, $\Omega_{k,0}$. The equation of state for dark energy can no

longer be fixed to $w = -1$ but rather be some other constant, and therefore no longer represent a cosmological constant, or it is possible to go further and let the equation of state be redshift dependent, known as dynamical dark energy (e.g. Ratra, Peebles, 1988; Linder, 2003; Pfeifer et al., 2020).

A number of notable extensions that do not affect the background expansion but instead change the initial density fluctuations or the equations of motion of DM and effect only the small scales are warm dark matter (WDM), self-interacting dark matter (SIDM) and a running of the scalar spectral index. WDM posits that DM has a non-negligible thermal velocity during the period of recombination and results in the suppression of density fluctuations on small scales. A running of the scalar spectral index also changes the form of the initial linear power spectrum, by no longer assuming the primordial power spectrum is a perfect power law but instead has a more complex form, i.e. a running. SIDM on the other hand makes no changes to the initial linear power spectrum but instead allows for self interactions between dark matter particles, and hence changes the equations of motion for DM.

The above list is by no means exhaustive and highlights just a few notable extensions to Λ CDM. Although there exists many possible extensions it is worth noting that we currently have no compelling evidence for the existence of deviations from the standard Λ CDM model. Though, there are a number of recent, and ongoing, tensions that hint at some problems with the model.

On large scales there currently exist a few tensions between late and early time measurements, the most famous being the H_0 tensions. The prediction for H_0 using the Λ CDM fitted to measurements of the CMB infer $H_0 = 67.37 \pm 0.54$ (Planck Collaboration et al., 2020), while the most recent value using more direct measurements of type 1a supernovae infer $H_0 = 73.04 \pm 1.04$ (Riess et al., 2021). Where these observations have recently reached a statistical significance $> 5\sigma$. It is still unclear if this tension is due to missing physics or unaccounted for systematics in either CMB measurements or in the calibration of type 1a using the distance ladder.

Another tension currently exists in the observed amount of structure from large

scale structure (LSS) measurements such as weak lensing and galaxy clustering (e.g. Heymans et al., 2021; Abbott et al., 2022). The amount of structure is typically described through the σ_8 , or related $S_8 \equiv \sigma_8 \sqrt{\Omega_m/0.3}$, parameter. Here it is found that the amount of observed structure is lower than that inferred from the CMB, with the majority of LSS measurements being lower than the Planck value. The current tension is not as significant as the H_0 value and is currently $\sim 3\sigma$.

As well as the tensions on large scales, there are also a number of small scale tensions that potentially hint at the nature of DM being different than that assumed in Λ CDM. We discuss these in more detail in section 2.6.2.

1.4 Analytic models for structure collapse

So far we have only discussed the behaviour of a universe that is perfectly homogeneous and isotropic. Although this is observed to be true on the largest scales, i.e. the cosmological principle, there are small but clear fluctuations in the CMB. These small fluctuations in the CMB background correspond to small fluctuations in the initial density field of our universe. It is these initial density perturbations that then give rise to the observed structures on the Universe today. The force of Gravity causes the collapse and clustering of objects from the smallest of dwarf galaxies to giant galaxy clusters and massive voids.

In this section I overview some of the key analytic models that describe the evolution of these perturbations. Particularly focusing on how the form of these initial perturbations links to the origin and evolution of collapsed objects, such as galaxies and DM haloes.

1.4.1 Overdensities & Gaussian random fields

Rather than describing the evolution of the density field, $\rho(\vec{x})$, directly it is useful to remove the dependence on the background expansion and instead describe the over-

density,

$$\delta(\vec{x}, t) = \frac{\rho(\vec{x}, t) - \rho_m(t)}{\rho_m(t)}. \quad (1.12)$$

$\delta(\vec{x})$ therefore describes the perturbations from the mean density. $\delta(\vec{x}) = 0$ therefore corresponds to a cosmology with no fluctuations or structure and would evolve exactly as described by the Friedmann equations, as discussed in the previous section.

For density fluctuations generated by quantum fluctuations it is expected that the initial density fluctuations take the form of a Gaussian random field. This is also what is observed in the CMB, with the temperature anisotropies matching those expected from a Gaussian random field. It is often useful to work with the Fourier transform of the overdensity field, $\tilde{\delta}(\vec{k})$. From this we can define the power spectrum,

$$\langle \tilde{\delta}^2(\vec{k}) \rangle = (2\pi)^3 P(k). \quad (1.13)$$

Here the triangular brackets represent averaging over all k-modes with the same magnitude ($k \equiv |\vec{k}|$). For a random Gaussian field, where the phases are uniformly distributed and uncorrelated, the power spectrum, $P(k)$, (or its real space analogue, the autocorrelation function) fully and completely describe the density distribution. This means that we can work exclusively with the power spectrum, allowing us to reduce a three dimensional scalar field to a single one dimensional function, $P(k)$. The initial density field, i.e. post recombination, is measured to be close to, and in the Λ CDM model assumed to be exactly, a Gaussian random field. As such, the initial conditions for structure collapse can be treated this way, however structure collapse itself causes the field to become non-Gaussian over time, as discussed later in this chapter.

$P(k)$ has the units of $length^{-3}$. Therefore, it is common to instead discuss the dimensionless power spectrum, defined as

$$\Delta^2(k) = \frac{k^3 P(k)}{2\pi^2}. \quad (1.14)$$

1.4.2 Linear evolution

Having just discussed how one can describe the initial, small density perturbations. The natural next question to ask is then how do these perturbations evolve with time? For simplicity we will consider the evolution of a universe dominated by a collisionless fluid (i.e. DM), a good approximation of our own universe today.

In such a universe the evolution of matter can be modelled as a perfect Newtonian fluid.⁴ The density perturbations evolve according to the following set of coupled differential equations.

$$\frac{\partial \delta}{\partial t} + \frac{1 + \delta}{a} \vec{\nabla} \cdot \vec{v} = 0, \quad (1.15)$$

$$\frac{\partial \vec{v}}{\partial t} + \frac{1}{a} (\vec{v} \cdot \nabla) \vec{v} + \frac{\dot{a}}{a} \vec{v} = -\frac{1}{a} \vec{\nabla} \phi, \quad (1.16)$$

$$\nabla^2 \phi = 4\pi G a^2 \rho_{m,0} \delta. \quad (1.17)$$

The above equations represent the continuity, Euler and Poissons equations, respectively, in a comoving reference frame. Here we have also introduced the velocity component of the fluid, \vec{v} , and the gravitational potential, ϕ . In general δ and \vec{v} will depend on both time and spatial position. The above equations describe how the density and velocity perturbation couple both to each other as well as the background expansion of the Universe, as described through the scale factor.

Due to the non-linear nature of the above equations there is, in general, no analytic solutions. However, a useful limit is when we consider the density and velocity perturbations to be small. In this case higher order terms of δ and \vec{v} can be dropped. From the above equations we can then derive a single equation for the time evolution of δ in the small perturbation limit,

$$\frac{\partial^2 \delta}{\partial t^2} + 2\frac{\dot{a}}{a} \frac{\partial \delta}{\partial t} = \frac{3}{2} \Omega_{m,0} H_0^2 a^{-3} \delta. \quad (1.18)$$

One of the key things to note in the above equation is that we have simplified the previous nonlinear system of coupled differential equations to a single, linear partial

⁴A good approximation as long as the matter is non-relativistic, as is assumed in the Λ model.

differential equation. This then implies that the perturbations can be expressed as a separable equation where we can write⁵

$$\delta(\vec{x}, t) = D(t)\delta(\vec{x}, t = t_0). \quad (1.19)$$

$D(t)$ is known as the growth factor. In the above expression we have used the standard convention $D(t_0) = 1$. Therefore, when the perturbations are small (commonly referred to as the linear regime) they grow independently of one another and their spatial configuration is fixed. The only evolution is an increase in the amplitude that is governed by the background expansion and expressed through the growth factor.

$D(t)$ obeys the following second order linear differential equation,

$$\frac{d^2 D}{dt^2} + 2\frac{\dot{a}}{a}\frac{dD}{dt} = \frac{3}{2}\Omega_{m,0}H_0^2 a^{-3}D. \quad (1.20)$$

It is common to express the growth factor as a function of redshift, or scale factor, rather than time. Using the Friedmann equations (see Section 1.2.1) the solution for the growth factor can be written as

$$D(z) = \frac{5\Omega_{m,0}H_0^2}{2}H(z)\int_z^\infty \frac{1+z'}{H^3(z')}dz'. \quad (1.21)$$

In general this integral cannot be expressed analytically for a cosmology dominated by matter and a cosmological constant, however it is easily numerically evaluated (alternatively there exist multiple analytic fitting functions).

As discussed previously it is often useful to work with the power spectrum, $P(k)$, as opposed to δ . As the evolution of density perturbations in this regime does not change the spatial configuration this separable solution also applies to the power spectrum, where

$$P(k, z) = D^2(z)P(k, z = 0). \quad (1.22)$$

⁵The general solution will be a sum of two growth functions, i.e. $\delta = D_1(t)\delta_1(\vec{x}) + D_2(t)\delta_2(\vec{x})$. Typically, one solution is a growing mode and the other a decaying one, as such the growing mode will always dominate and we can safely ignore the decaying solution.

Here the growth factor is squared as the amplitude of $P(k) \propto \delta^2$. The above equation then describes what is known as the linear power spectrum, a fundamental quantity used in modern cosmology. Although it is only accurate in regimes where $\delta \ll 1$ it is still useful for a number of reasons. (i) One can always find large scales where the linear approximation holds, and as such accurately describes the density fluctuations on the largest scales (in our own Universe $\gtrsim 100$ Mpc), a fact that is particularly useful for clustering of galaxies and clusters. (ii) The fluctuations in the CMB are observed to be in this regime at all scales, as such the initial evolution of the power spectrum after recombination will evolve linearly. The linear power spectrum can therefore be viewed as the initial conditions for the later collapse of individual objects, such as galaxies and clusters. For this reason $P(k)$ is used extensively throughout this thesis.

1.4.3 Spherical Collapse Model

I have yet to describe how individual objects collapse and for the galaxies we observe in our own galaxy. It is clear that linear theory is insufficient to describe these processes on its own, primarily as it is limited to the regime $\delta \ll 1$. As mentioned previously, general analytic solutions for $\delta(\vec{x}, t)$ do not exist. However, some useful insight can be discerned by considering simplified systems. One particularly useful scenario is the spherical collapse model, and is described in this section.

For transparency the results derived here will assume an Einstein de Sitter cosmology ($\Omega_\Lambda = 0$) and consider the evolution of collisionless matter, though many of the key results and concepts will apply to any universe. Where appropriate I will also provide the corrections, or differences, for a Λ CDM universe.

The spherical collapse model begins by considering an initial top hat perturbation in an otherwise homogeneous expanding universe, with a initial density $\bar{\rho}_i = \rho_{m,i}(1 + \delta)$. Here, the subscript i is used to denote some initial time and configuration. Hence, the mass enclosed within a shell of radius r , that is within the overdensity, will take the form,

$$M(< r) = \frac{4}{3}\pi r_i^3 \rho_{m,i}(1 + \delta_i). \quad (1.23)$$

By spherical symmetry the mass enclosed within that spherical shell will be conserved during the initial collapse, though this assumption breaks down once shell crossing occurs.

The evolution of each shell then follows Newton's equation and we can express the conservation of energy as

$$\frac{1}{2} \left(\frac{dr}{dt} \right)^2 - \frac{GM}{r} = E, \quad (1.24)$$

where E is the specific energy of each shell. As we are interested in the cases where the system eventually collapses, and is therefore gravitationally bound, we want $E < 0$. In this case the solution to the above equation can then be written in parametric form as

$$r = \frac{GM}{2|E|} (1 - \cos \theta), \quad (1.25)$$

$$t = \frac{GM}{(2|E|)^{3/2}} (\theta - \sin \theta), \quad (1.26)$$

where θ is between 0 and 2π . From the first equation we see that the radius of each shell initially grows before reaching a maximum at $\theta = \pi$ and subsequently collapsing to $r = 0$ at $\theta = 2\pi$. The maximum radius reached is known as the turn around radius and is the point at which the overdensity begins to collapse. It is found that $r_{\text{ta}} = \frac{GM}{2|E|}$ and $t_{\text{ta}} = \frac{GM(\pi-1)}{(2|E|)^{3/2}}$.

It is useful to express the evolution of the overdensity of the perturbation rather than just the evolution of the radius. From the above equations, and using the evolution of the background density for a EdS cosmology, we find

$$\delta + 1 = \frac{9(\theta - \sin \theta)^2}{2(1 - \cos \theta)^3}. \quad (1.27)$$

The overdensity at the turn around radius is therefore $\delta = \frac{9\pi^2}{16} \approx 5.55$.

It is useful to compare the spherical collapse model to the predictions from linear theory. Clearly, the predictions from linear theory will not be accurate in this regime as $\delta > 1$. However, by comparing the linear prediction to the spherical collapse model,

objects, or scales, that should have already collapsed can be identified from the linear extrapolation. From Eqn. (1.25) & (1.25) we can derive the linear (corresponding to $\theta \ll 1$) evolution to be

$$\delta_{\text{lin}} = \frac{3}{20}(6\pi)^{2/3} \left(\frac{t}{t_{\text{ta}}} \right)^{2/3}. \quad (1.28)$$

Here we can see that $\delta_{\text{lin}}(t = t_{\text{ta}}) = \frac{3}{20}(6\pi)^{2/3} \approx 1.062$ and at the time of collapse $\delta_{\text{lin}}(t = t_{\text{collapse}}) = \frac{3}{5} \left(\frac{3\pi}{2} \right)^{2/3} \approx 1.686$. Where the spherical collapse model would predict $\delta \approx 5.55$ and $\delta = \infty$, respectively. Therefore, the prediction of the spherical collapse model is that any overdensities that reach $\delta = 1.686$ should have already collapsed. This is a useful quantity used extensively in the Press-Schechter formalism (see later in Section 1.4.5). This is then referred to as the critical density, denoted δ_c .

The final key prediction of the spherical collapse model discussed here is the overdensity of the final object that forms after collapse. Directly using the above relation predicts an infinite final overdensity. However, during this final stage of collapse shell crossing will occur and the assumptions in the spherical collapse model break down. To find the final overdensity one can assume that the matter will undergo some period of violent relaxation, ending in a virialised system. Enforcing the virial theorem ($2K + P = 0$) and using energy conservation we find that the radius at which the system virialises is $r_{\text{vir}} = r_{\text{ta}}/2$. The density enclosed by the shell is therefore 8 times larger than at the turn around radius. By approximating the time of virialisation to be the collapse time ($t_{\text{coll}} = 2t_{\text{ta}}$) we can derive the final overdensity to be

$$\Delta_{\text{vir}} \equiv \delta_{\text{vir}} = 18\pi^2 \approx 178. \quad (1.29)$$

Therefore, any objects in our own Universe that are observed to have an overdensity greater than or equal to 178 should be in virial equilibrium.

As mentioned previously, the above discussion and derivations correspond to an EdS universe and therefore not one with a cosmological constant such as Λ CDM. However, a correction for Λ CDM can be derived. Two of the key quantities that come out of the spherical collapse model are the critical density, δ_c , and the virial overdensity, Δ_{vir} . In a cosmology with a cosmological constant $\delta_c = 1.686\Omega_m^{0.055}(t_{\text{coll}})$. There is

therefore only a very mild cosmological dependence, and to a good approximation δ_c is simply a constant equal to the value predicted for an EdS cosmology. Similarly, there is also a cosmological dependence introduced to Δ_{vir} for a universe with a cosmological constant. Δ_{vir} is well approximated as

$$\Delta_{\text{vir}} = (18\pi^2 + 82(1 + \Omega_m) - 39(1 + \Omega_m)^2)/\Omega_m, \quad (1.30)$$

where Ω_m is the matter density at the time of virialisation (Bryan, Norman, 1998). Here we can see that the cosmological effect on Δ_{vir} is much stronger. For example, consider a universe close to our own with $\Omega_{m,0} = 0.3$, in such a universe the prediction is that $\Delta_{\text{vir}} \approx 218$. Typically, the changes to Δ_{vir} are $\sim 20\%$, as opposed to the $\sim 1\%$ expected for δ_c .

Δ_{vir} is a key quantity used extensively throughout this thesis. It is common to elevate the virial radius corresponding to given overdensity from a prediction to a *definition* of the size and mass of galaxies and DM haloes, both in numerical simulations and observations. Typically, the mass is defined so that the spherically averaged density is Δ^6 times larger than some reference density, typically using either the mean or critical density. The prediction from the spherical collapse model, for a Λ CDM cosmology, would be the previous relation where Δ is redshift dependent. However, there is not a consensus on the ‘correct’ mass definition. Common choices include the Bryan, Norman (1998) relation given above, $\Delta = 200$ or 500 with respect to either the mean and critical density. Throughout this work we primarily use the mass definition of $\Delta = 200$ with respect to the critical density, the corresponding mass and radius are then denoted M_{200c} and R_{200c} , respectively.

1.4.4 Secondary infall models

The spherical collapse model described above gives key insights into the initial collapse and formation of DM haloes from the linear regime, as well as motivating many

⁶It is common to drop the subscript when using Δ as a mass definition and simply quote the value used

of the mass definitions currently used. However, the theory cannot describe the evolution of objects after shell crossing. As such a key property not predicted in the spherical collapse model is the expected density profile of the resulting virialised object. In this section we describe so-called secondary infall models, that aim to model the evolution after shell crossing and make predictions for the resulting density profile. We will focus on how results from this theory continue to inform our current understanding of the formation and evolution of collapsed structure. We specifically focus on the results of Fillmore, Goldreich (1984) and Bertschinger (1985).

The key difficulty in modelling the evolution after shell crossing is that the mass contained within a given shell is no longer conserved. The mass, and therefore potential, for a given shell is time dependent, and therefore the energy of individual shells is no longer a conserved quantity.

As discussed in Bertschinger (1985) it is useful to work in dimensionless quantities. Here we define

$$\lambda \equiv \frac{r}{r_{\text{ta}}(t)} \quad (1.31)$$

and

$$\xi \equiv \ln \left(\frac{t}{t_{\text{ta}}} \right). \quad (1.32)$$

Where r_{ta} is the radius of the current shell undergoing its first turn around and not the turn around radius of the particular shell being considered. In these units the equation of motion for the shell becomes

$$\frac{d^2 \lambda}{d\xi^2} + \frac{7}{9} \frac{d\lambda}{d\xi} - \frac{8}{81} \lambda = -\frac{2}{9} \frac{M(\lambda)}{\lambda^2}, \quad (1.33)$$

subject to the boundary condition

$$\lambda = 1, \quad \frac{d\lambda}{d\xi} = -\frac{8}{9} \quad \text{at} \quad \xi = 0. \quad (1.34)$$

From the above equation we can see that, in these units, the potential only depends on one variable, $M(\lambda)$, reducing the problem to a linear second order differential equation. We can see that the general form of the equation is to describe a damped system subject

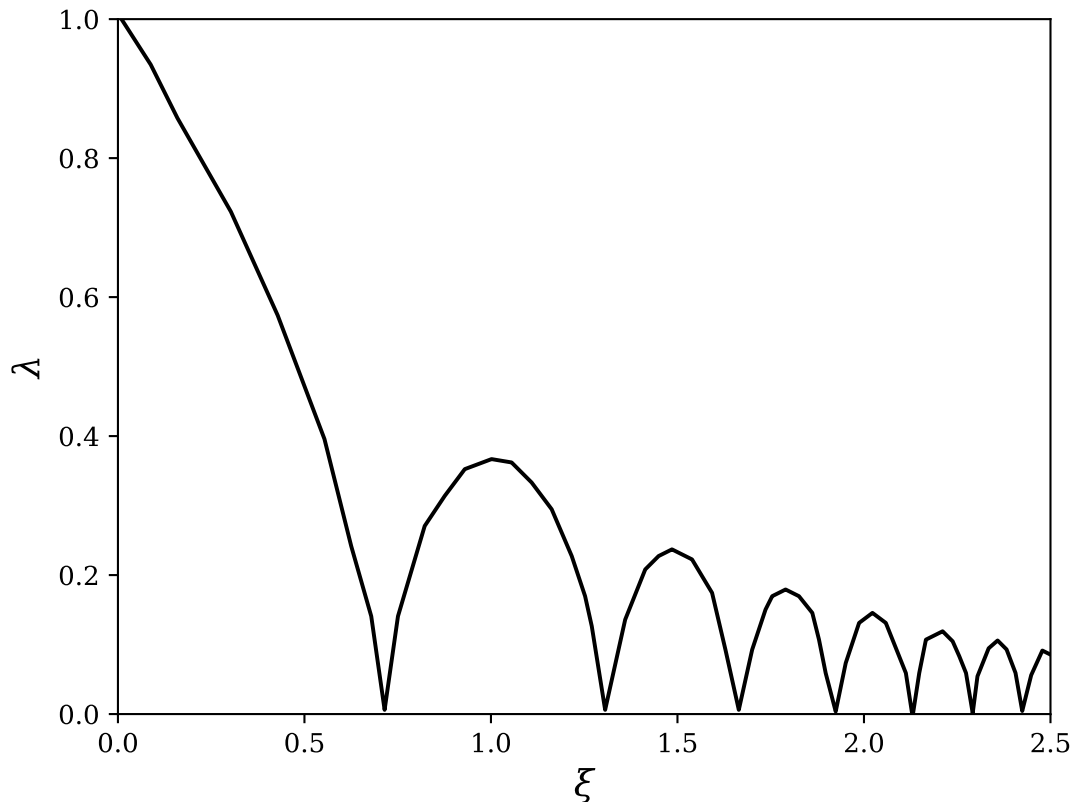


Figure 1.1: Results from the secondary infall model. Here is shown the resulting particle trajectories, as expressed in the dimensionless quantities λ and ϵ . This result can either be interpreted as the trajectory of an individual particle, or as a snapshot of particle positions.

to a modified potential. Unfortunately, Eqn. 1.33 cannot be solved analytically, but an accurate solution can be obtained numerically.

Fig. 1.1 shows the numerical solution for λ as a function of ξ .⁷ $\lambda(\xi)$ can be viewed as either the trajectory of a given shell, or alternatively the radius of different shells at a given snapshot. Initially, the shell falls into the halo from r_{ta} ($\lambda = 1$, $\xi = 0$) before passing through the centre and subsequently turning around again and continuing to oscillate about the centre. Over time the maxima, or apocentre of the orbit, decreases due to energy being dissipated, leading the shell to sink further and further into the centre of the halo.

The mass contained within the radius λ is shown in Fig. 1.2. The non dimen-

⁷The data for Fig. 1.1, 1.3 and 1.2 are all taken directly from Bertschinger (1985)

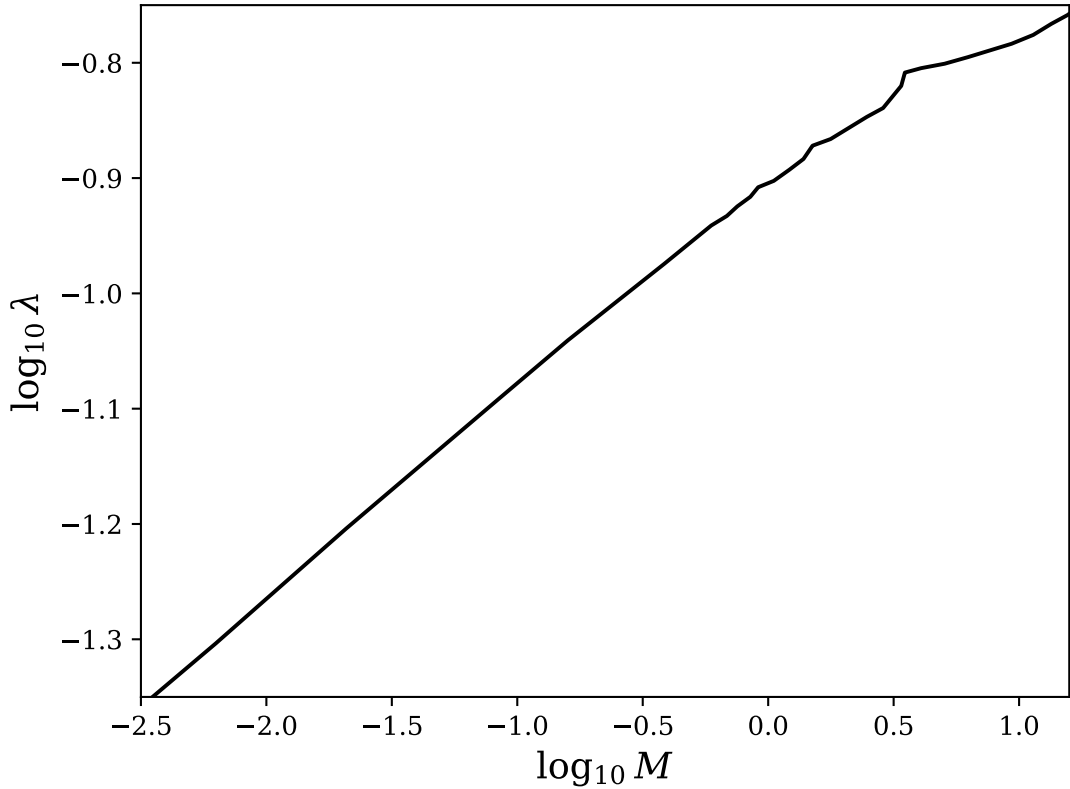


Figure 1.2: Results from the secondary infall model. Here is shown the contained mass within the dimensionless radius λ . From this plot the density profile $\rho \propto r^{-2.25}$ can be inferred.

sional density, analogues to the mass density, can be defined as

$$D(\lambda) \propto \frac{1}{\lambda^2} \frac{dM}{d\lambda}, \quad (1.35)$$

and is shown in Fig. 1.3. Here it is seen that the secondary and higher turn around radii have noticeable imprints on density profile, where there are sharp discontinuities corresponding to the apocenter of the orbiting shells that occur at fixed fractions of the first turn around radius. These features are also visible in the mass profiles, though are not as dramatic as the density profiles. From the mass profiles we arrive at the prediction that $\rho \propto r^{-2.25}$, though with the additional prediction of multiple caustics imprinted in the density profile, due to the specific scale imposed by the turn around radius.

There are a number of key limitations of the secondary infall model discussed above. A key assumption in the above derivation is that the initial overdensity is spher-

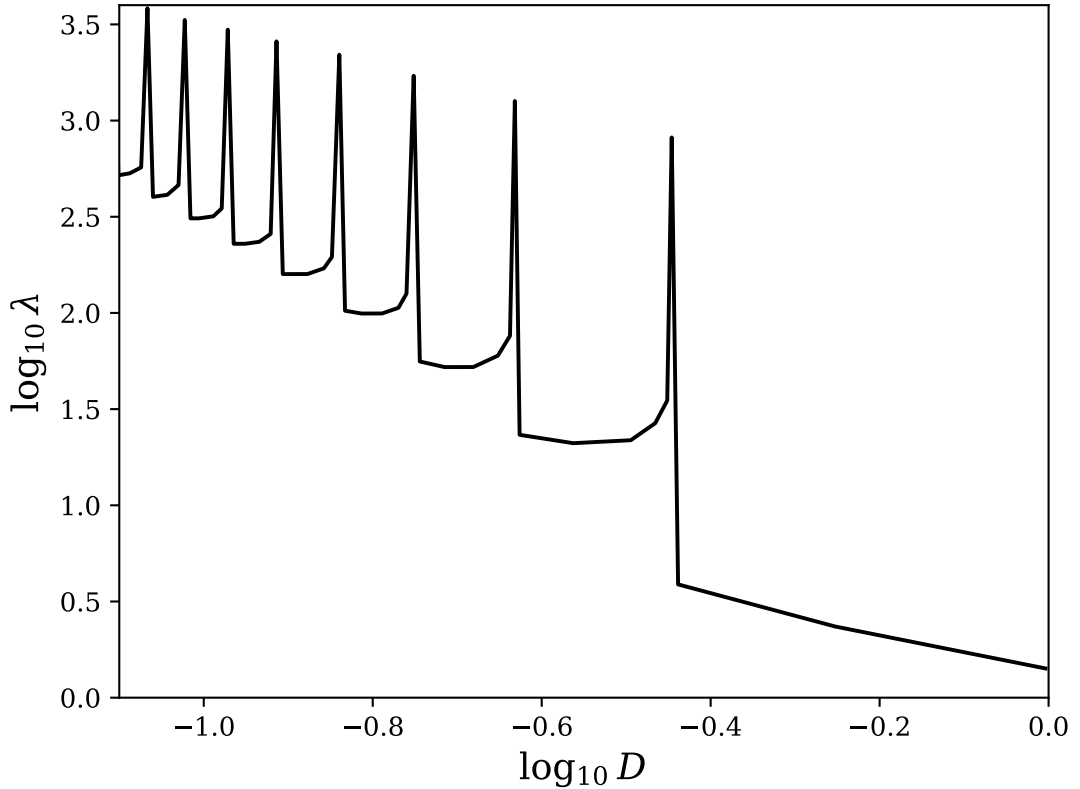


Figure 1.3: Results from the secondary infall model. Here is shown the (analogous) density D as a function of the dimensionless radius λ . Here the features imprinted on the density profile by the specific scale of the turn around radius can be seen.

ically symmetric and there are initially no peculiar velocities (i.e. everything starts in the Hubble flow). As such, the solution is also spherically symmetric with particles only having a radial velocity. Whereas, it is expected that the initial overdensity from the Gaussian field to not be spherically symmetric and for gravity to enhance any initial deviations from spherical symmetry (e.g. Zel'dovich, 1970). As it is expected for the initial collapse to be ellipsoidal and the subsequent dynamics to be close to isothermal, as opposed to purely radial orbits. Additionally, the assumption of spherical symmetry leads to purely 'smooth' accretion and does not model the evolution of hierarchical growth through many mergers that is at the heart of our current cosmological paradigm.

Even though the predictions of secondary infall models break down in detail there are two qualitative predictions that are of use and appear in more realistic numerical simulations. The first is the idea that the growth of haloes, and similarly galaxies, is an inside out process with matter at the very centre corresponding to that which

was accreted much earlier, and vice versa. The second is the features in the density profile associated with the apocentre of the orbits. Although the majority of these are smoothed out due to phase mixing the second turn around radius is observed in the density profiles of numerical simulations (e.g. Diemer, Kravtsov, 2014a; More et al., 2015). This feature is often referred to as the splashback radius and can be used to demarcate material that is being accreted for the first time from that that has already passed through the halo.

1.4.5 Press-Schechter and peak height

When discussing the formation and evolution of collapsed objects we have, notably, yet to consider the role of the linear (or nonlinear) power spectrum. As the linear power spectrum represents the form of the initial density field, and can be viewed as the initial conditions, we expect it to play a key role in the form and evolution of collapsed objects.

From the spherical collapse model we know that any overdensities in the linear power spectrum with $\delta_{\text{lin}}(\vec{x}, t_0) > \delta_c/D(t)$ will have already collapsed today. A schematic of this is shown in Fig. 1.4. Here is shown a one-dimensional Gaussian random field with an arbitrary normalised critical density. The evolution of this is for the perturbation to grow with time, or alternately to fix the perturbation but evolve the critical density with time, resulting in the collapse of more and more structure.

From inspecting Fig. 1.4 we can see that for this particular configuration there are four distinct regions above the critical density, resulting in the formation of four DM haloes. This then naturally leads to the question of how do we identify given regions as belonging to an individual halo and how do we assign a given mass to that halo. One approach, as proposed by Bardeen et al. (1986), is to consider filtering the density field with a given window function to produce a smoothed density field,

$$\delta_{\text{sm}}(\vec{x}; R) \equiv \int \delta(\vec{x}') W(\vec{x} - \vec{x}'; R) d^3 \vec{x}'. \quad (1.36)$$

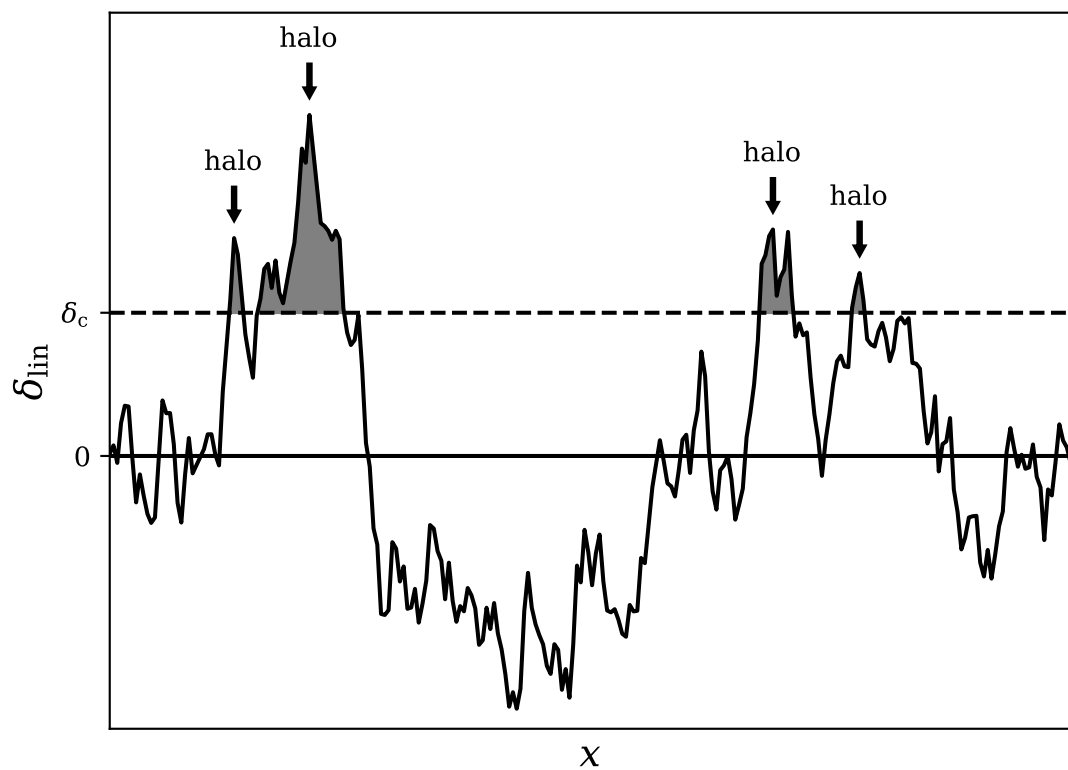


Figure 1.4: Schematic one-dimensional depiction of how individual regions can be identified in the linear Gaussian field that will collapse into individual haloes. Here is shown an arbitrarily normalised one-dimensional Gaussian random field and corresponding critical density. In this example we would expect 4 haloes would be expected to form from the corresponding regions where $\delta_{\text{lin}} > \delta_c$.

Where $W(\vec{x}; R)$ is the window function, with a few common choices, though here we will only consider the window function to represent a spherical top hat function in real space. Specifically

$$W(\vec{x}; R) = \begin{cases} \frac{3}{4\pi R^3} & r \leq R \\ 0 & r > R, \end{cases} \quad (1.37)$$

with the corresponding Fourier transform,

$$\tilde{W}(kR) = \frac{3}{(kR)^3} (\sin(kR) - (kR) \cos(kR)). \quad (1.38)$$

The average mass contained within a sphere of radius R will be

$$M = \frac{4\pi}{3} R^3 \rho_{m,0}. \quad (1.39)$$

This then allows us to associate a given smoothing of the overdensity field to a given halo mass.

$\delta_{\text{sm}}(\vec{x}; R)$ is itself a Gaussian random field with a mean of 0, the same as the unsmoothed field. However, it will have a different variance that depends on both the window function and the power spectra of the unsmoothed density field. The variance of the smoothed field can be written as

$$\sigma^2(R) = \frac{1}{2\pi^2} \int k^2 P(k) \tilde{W}^2(kR) dk. \quad (1.40)$$

This is where the cosmological parameter σ_8 comes from, it is defined to be $\sigma_8 \equiv \sigma(R = 8h^{-1} \text{ Mpc}, z = 0)$. Where it then follows that σ_8 corresponds to a measure of the amount of structure present for the given cosmology at roughly cluster scales.⁸

We can now think of each peak above δ_c in the smoothed density field, $\delta_{\text{sm}}(\vec{x}; R)$, as belonging to a halo of corresponding mass or larger. Under such an assumption the number of peaks greater than δ_c will equal the number of haloes above that associated mass, and can therefore predict the number density of dark matter haloes as a function

⁸For example, a Λ CDM cosmology with $\Omega_{m,0} = 0.3$ and $h = 0.7$ σ_8 corresponds to a mass scale of $M \sim 10^{13} M_{\odot}$.

of mass, $n(M, z)$.

Directly counting the number of peaks quickly runs into the cloud-in-cloud problem, making it unclear how to associate a given peak with a given halo. Press, Schechter (1974) avoids this problem by making a different, though similar, assumption that each peak corresponds to a given halo. Instead, the key ansatz in Press-Schechter (PS) theory is that the probability of the smoothed overdensity field being larger than δ_c is equal to the mass fraction contained within haloes greater than the associated mass. For a Gaussian random field the corresponding probability is

$$\mathcal{P}(\delta_M > \delta_c) = \frac{1}{2} \operatorname{erfc} \left(\frac{\sigma_c}{2\delta_M} \right), \quad (1.41)$$

where $\operatorname{erfc}(x)$ is the complementary error function. While the fraction of mass in haloes above mass M , $F(> M)$ is

$$F(> M) = \frac{1}{\rho_{m,0}} \int_M^\infty M' n(M', z) dM'. \quad (1.42)$$

From these relation we can then arrive at the prediction for the abundance of haloes

$$n(M, z) = \sqrt{\frac{2}{\pi}} \frac{\rho_{m,0}}{M^2} \frac{\delta_c}{\sigma(M)} \exp \left(-\frac{\delta_c^2}{2\sigma^2(M)} \right) \frac{d \ln \sigma(M)}{d \ln M}. \quad (1.43)$$

This relation therefore gives a link between the linear density field to the number of collapsed structures expected for such a universe. From this a characteristic mass, M_* , can be defined where $\sigma(M_*) = \delta_c$. From this we can see the behaviour that for $M \ll M_*$ $n(M) \propto M^{-2}$ while for $M \gg M_*$ $n(M)$ decays exponentially, effectively due to sampling the very tail of the Gaussian distribution.⁹ As this transition from power law to exponential depends strongly on $\sigma(M)$, and hence the linear power spectrum, it means that the abundance of high mass haloes is very sensitive to the underlying cosmology. As such the observed mass function should be, in principle, a powerful tool for constraining cosmology.

Bond et al. (1991) introduced an alternative derivation of the PS mass function

⁹The behaviour at low masses assumes a Λ CDM cosmology with $n_s \approx 1$.

based on an excursion set formalism. Here the evolution of the smoothed overdensities as a function of mass can be modelled as a Markovian random walk (if using a sharp k -space filter). The formalism is generally referred to as extended Press-Schechter (ePS) theory. This formalism has a number of advantages over the ‘standard’ PS formalism. One particularly notable example is that it allows the construction of the accretion history for a population of haloes as a function of mass. This merger history can then be coupled to (semi-)analytic models of the evolution of the gas and star formation to create a (semi-)analytic model of galaxy formation and evolution.

The predictions of the PS (and ePS) model broadly agree with what is observed in numerical simulations, particularly replicating the power law behaviour at low masses and the exponential suppression at larger scales. However, it is not quantitatively accurate, with errors $\gtrsim 20\%$, when compared to numerical simulations. As such, there exist many empirical extensions to the functional form of Eqn. 1.43 motivated by the results of numerical simulations (e.g Tinker et al., 2008).

From the above discussion there is a key quantity that is natural to define. The peak height

$$\nu(M, z) \equiv \frac{\delta_c}{\sigma(M, z)} = \frac{\delta_c}{D(z)\sigma(M, z=0)}. \quad (1.44)$$

We make extensive use of peak height throughout this thesis and regularly describe properties of DM haloes as a function of ν as opposed to mass. Fundamentally, ν is a more useful quantity as it embeds information about the given cosmology and initial conditions (i.e. $P(k)$), whereas the mass alone contains no such information.

Chapter 2

Simulation Techniques

In the previous chapter I have discussed many of the basic ideas and theories underpinning our current understanding of the formation and evolution of structures in our universe. For a few specific systems, such as an isolated spherical top hat perturbation, there exist analytic solutions. However, generally analytic solutions cannot be found due to the non-linear and coupled nature of the equations of motion. It is therefore often necessary to resort to numerical methods to directly integrate the equations of motion. A particular numerical scheme's results are often referred to as a simulation. Numerical simulations are the main tool used throughout this thesis and their results are studied extensively throughout.

In this chapter I will outline the main aspects of the simulations used and the underlying equations that are being solved. In Section 2.1 I will outline the key equations of motion to be solved. In Section 2.2 I will review how the gravitational potential, and associated gravitational force, is estimated. In section 2.3 I will outline how the equations of motion are directly integrated to propagate their time evolution. In Section 2.4 I will outline how the initial conditions are generated. In Section 2.5 I will describe how structures are identified from the output of a given simulation to identify individual haloes. Finally, in section 2.6 I will review some of the key results from numerical simulations of the growth of structure.

2.1 Key equations and general simulation principles

The majority of the work in this thesis utilises so-called ‘DM only’ simulations where all matter is treated as a collisionless fluid. This means that the only force needed to model is gravity.

The key equations to be solved are presented below. For brevity and clarity they are presented in physical coordinates and the focus is on the numerical techniques employed, however the actual simulations will use comoving coordinates, resulting in slightly modified equations of motion (see Section 1.4.2). Additionally, the equations are presented in the form that is most relevant to the numerical techniques used.

Throughout this work the collisionless fluid, i.e. DM, is modelled using an N-body approach. Here the fluid is split up into individual particles that sample the underlying fluid distribution, and as such represent a Lagrangian simulation method. Each particle has 3 key properties, its position, \vec{r} , velocity, \vec{v} and mass. The acceleration of a given particle obeys Newtonian gravity,

$$\frac{d^2\vec{r}}{dt^2} = -\vec{\nabla}\phi(\vec{r}, t). \quad (2.1)$$

Where ϕ is the gravitational potential, given by Poisson’s equation. Written in integral form this is

$$\phi(\vec{x}) = \int \frac{G\rho(\vec{r}')}{|\vec{r} - \vec{r}'|} d^3r', \quad (2.2)$$

where the integral is over all mass elements.

As an N-body approach is used it is possible to reach arbitrarily large accelerations when particles undergo close encounters. However, such close encounters are purely numerical and therefore unphysical. To avoid this it is common to adopt a gravitational softening where the gravitational potential is modified to reduce the gravitational forces at small scales. The easiest way to do this is to add a small constant to the distance, resulting in a minimum separation, where the gravitational potential

between two mass elements would then be

$$\phi = -\frac{Gm_1m_2}{r + \epsilon}. \quad (2.3)$$

Here ϵ is the gravitational softening length and chosen to be small compared to the mean interparticle separation. One limitation of the above form is that the potential never reduces exactly to the correct Newtonian form. Instead, a spline can be used to smooth the potential. Here

$$\phi = -\frac{Gm_1m_2}{r + W(r, h)} \quad (2.4)$$

where

$$W(r, h) = \frac{8}{\pi h^3} \begin{cases} 1 - 6\left(\frac{r}{h}\right)^2 + 6\left(\frac{r}{h}\right)^3, & 0 \leq \frac{r}{h} \leq \frac{1}{2} \\ 2\left(1 - \frac{r}{h}\right)^3, & \frac{1}{2} < \frac{r}{h} \leq 1 \\ 0, & \frac{r}{h} > 1. \end{cases} \quad (2.5)$$

Here h is again the softening length and it is clear that for $r > h$ the potential reduces exactly to the correct Newtonian calculation.

Broadly speaking, the goal of a given simulation is to accurately evolve all particles' velocity and position with time. From the above equations we can see that there are two components necessary to achieve this. First the gravitational potential needs to be estimated, which will be referred to as the gravity solver, and secondly the particle position and velocity must be directly integrated for a given acceleration.

2.2 Gravity solver

In this section I describe a few different approaches to estimate the gravitational potential for a distribution of particles. The most obvious, and accurate, approach would be to use direct summation where the acceleration of particle j is equal to the sum of

forces from all N other particles,

$$\frac{d^2\vec{r}_j}{dt^2} = \sum_{i \neq j}^N \frac{Gm_i}{|\vec{r}_i - \vec{r}_j|^3} (\vec{r}_i - \vec{r}_j). \quad (2.6)$$

The limitation of this approach is the computational cost, with scaling $\mathcal{O}(N^2)$. Additionally, the direct summation method is unnecessarily accurate in certain regimes. For example the acceleration on a particle within a given halo is not sensitive to the internal structure of a halo many megaparsecs away but only on the total mass of that object.

One common approach is to use a particle mesh (PM) to estimate the gravitational potential. Here particles are binned using an equally spaced grid (similar to a 3-dimensional histogram). From this grid the density field $\rho(\vec{r})$ can be estimated at each grid point, either by using the nearest neighbour or a cloud-in-cell approach where the mass of each particle is interpolated between all neighbouring grid points. The gravitational potential, which is a convolution of $\rho(\vec{r})$, can then be efficiently calculated using a discrete Fourier transform. This results in a very quick and efficient method, $\mathcal{O}(N \log N)$, to estimate the gravitational potential. An example of the method is shown in the left hand panels of Fig. 2.1, where the top panel shows an example distribution of particle in two dimensions with the PM overlaid with the bottom panel showing the resulting estimation of $\rho(\vec{r})$.

One key limitation of using a static PM is the fixed spatial resolution. Initially, when the density field is approximately homogeneous this is not an issue. However, as structures begin to collapse below the resolution of the mesh the static spatial resolution results in the internal structure of haloes not being resolved. Due to this issue PM codes are typically only used for large volume, low spatial resolution simulations.

An alternative approach is to use an octree algorithm. Here the box volume is initially split into eight equal sub-volumes, each of these are subsequently split into eight smaller cells, with this refinement ongoing till a certain condition is met. Typically, this is either a maximum number of particles contained within a grid or a minimum spatial

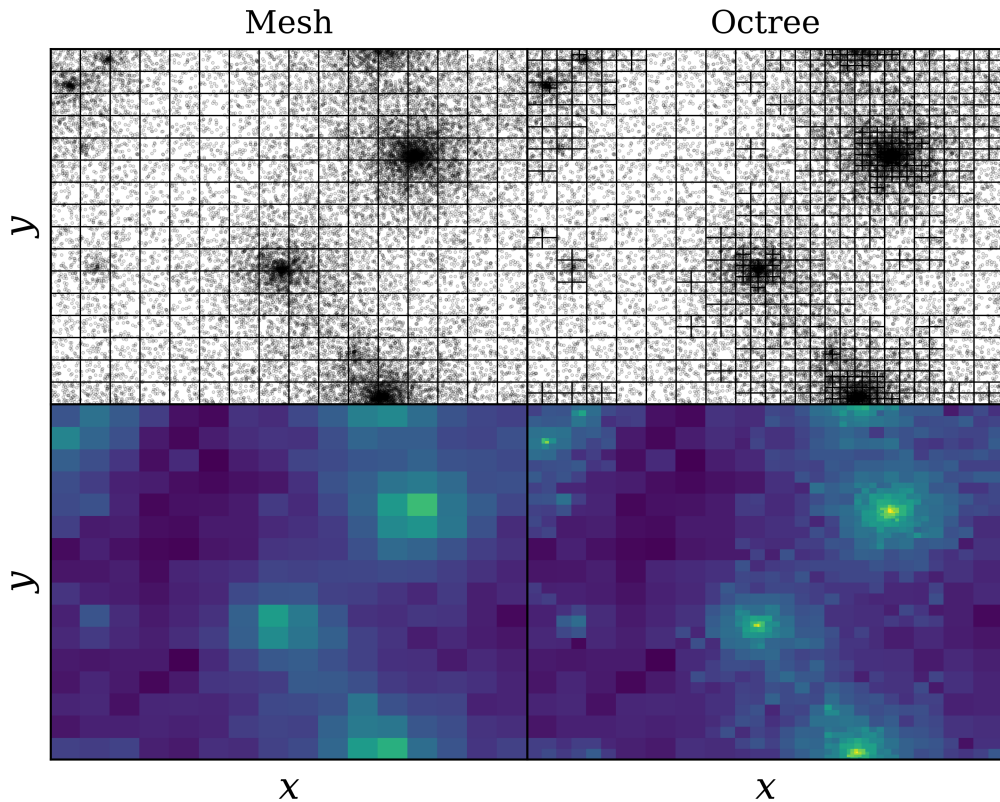


Figure 2.1: Depiction of the PM and octree approaches applied to an example two-dimensional particle distribution. Here the dynamic nature of the octree can be seen, where the internal structures of the individual haloes are more finely resolved than using the static PM approach.

resolution of the grid. This dynamic approach then naturally leads to high density regions being more spatially resolved, and vice versa. A 2-dimensional example of this is shown in the right hand panels of Fig. 2.1.¹ Again, the top panel shows the example particle distribution with corresponding cells and the bottom panel the corresponding estimation of $\rho(\vec{r})$. It is immediately clear the dynamic nature of this approach, with individual haloes being much more finely resolved than the underdense background. Notably, this results in much larger resolved densities at the centres of the haloes that gets smoothed out when using the static PM approach.

In practice a hybrid approach between the octree and PM methods is used (tree-PM), where gravitational forces on large scales are calculated using the PM while local forces are calculated from the octree. This is the approach used in the Gadget-2 code.

¹In 2-dimensions this kind of structure is a quad-tree.

2.3 Time Integration

With the acceleration calculated for each particle it is then necessary to propagate the current position and velocity to some later time (step), Δt . There are a few commonly used methods when numerically integrating differential equations, such as Runge–Kutta and the Euler method. In Gadget-2 a leap frog, with a kick-drift-kick scheme, is used. The leap frog method much better conserves energy than similar methods while being relatively computationally inexpensive, making it reliable at modelling periodic systems, such as the orbits of particles.

The leap frog scheme is as follows,

$$\vec{v}_{i+1/2} = \vec{v}_i + \vec{a}_i \frac{\Delta t}{2}, \quad (2.7)$$

$$\vec{x}_{i+1} = \vec{x}_i + \vec{v}_{i+1/2} \Delta t, \quad (2.8)$$

$$\vec{v}_{i+1} = \vec{v}_{i+1/2} + \vec{a}_{i+1} \frac{\Delta t}{2}. \quad (2.9)$$

Here \vec{x}_i , \vec{v}_i and \vec{a}_i represents the initial position, velocity and acceleration while \vec{x}_{i+1} , \vec{v}_{i+1} and \vec{a}_{i+1} the position, velocity and acceleration at a time Δt later.

In general the error in the integration scheme will be $\propto |\vec{a}|^{1/2} \Delta t$, which implies that to minimise the errors in a given simulation the time steps should be chosen so that $\Delta t \propto \frac{1}{|\vec{a}|^{1/2}}$ and will therefore be dynamic and depend on the particle's evolution. An interesting problem in cosmological simulations is the very large dynamic range of the gravitational forces; particles in voids will feel almost no gravitational force, while particles at the centres of haloes will feel orders of magnitude larger accelerations. Due to this large dynamic range, it would not be computationally efficient to use the same time step for all particles. Dynamic time steps are therefore used so that each particle's individual time step evolves with time and independently of other particles. In practice, a discretised set of time steps are used to allow particles to stay synchronised, otherwise all particles would be at different times.

2.4 Initial Conditions

As discussed in detail in Section 1.4.1 the initial overdensity field of the universe is described by a Gaussian random field with a specified initial power spectrum. For the types of simulations used in this work the fluid is modelled as individual particles, with a given position and velocity. It is therefore necessary to translate a given overdensity field, $\delta(\vec{x})$, to a given distribution of particle positions and velocities.

The first important thing to note is the initial time of the simulations. As the non-linear evolution of the growth of structure is to be modelled then it is necessary to start the simulations in the linear regime, but still late enough that effects such as free streaming and changes due to the cosmological horizon at early times are no longer present. Generally, this forces into the regime after recombination, i.e. $z \lesssim 1000$, and before transitioning into the non-linear regime, $z \gtrsim 10$. For the simulations presented in this work an initial redshift of $z = 127$ is used.

The general method is outlined below. Initially the particles are arranged homogeneously, corresponding to a distribution with no overdensities. This can be either a glass distribution or, as used in this work, arranged on a uniform grid. The initial position and velocities of the particles for the given overdensity realisation are calculated using the Zeldovich approximation. The Zeldovich approximation, for the displacement of particles, can be written as

$$\vec{x}(t) = \vec{x}_i - \frac{D(a)}{4\pi G \rho_{m,i}} \vec{\nabla} \phi_i. \quad (2.10)$$

Where the subscript i corresponds to some initial configuration. Therefore for a given initial overdensity distribution δ , and corresponding potential ϕ_i , the position of that particle at a later time can be calculated. This is how the initial positions of the particles are calculated for the simulations.² The same approach is used for the initial particle velocities, using the equivalent Zeldovich approximation for particle velocities.

²Strictly, the simulations presented in this work use a second order Lagrangian perturbation approximation, while the Zeldovich approximation is a first order approximation. However, the general approach is the same as described here.

Due to the finite volume and resolution of a given simulation there will be an associated minimum and maximum scale that the power spectrum can be sampled for. The largest physical scale, smallest k-scale, is the fundamental mode

$$k_0 = \frac{2\pi}{L}, \quad (2.11)$$

and the smallest scale is the Nyquist frequency

$$k_{\text{Nyq}} = \pi \frac{N^{1/3}}{L}. \quad (2.12)$$

Where N is the number of particles used and L is the box length. Below and above these scales the simulation will not be able to reliably describe the evolution of structure.

The left panel of Fig. 2.2 shows a typical power spectrum for the initial conditions. In this case a modified version of N-GENIC is used to generate the initial particle distribution.³ The linear power spectrum provided is shown as the dashed line, while the measured power spectrum for the distribution of particles is shown in the solid dashed line. The fundamental and Nyquist frequencies are shown as vertical dotted lines. In general it can be seen that the measured power spectrum closely follows the input linear power spectrum, up to the Nyquist frequency where it quickly deviates, as expected. There is often significant scatter between the measured and supplied power spectra, particularly at low k values. This is due to the finite sampling resulting in only a small number of large k-modes within the simulation volume. This randomness results in cosmic variance, where the largest scales and most massive haloes in the simulation will be subject to the random fluctuations of the given realisation.

An example of the resulting particle distribution is given in the right hand panel of Fig. 2.2. This is a thin slice from the full three dimensional distribution. Overplotted is the initial grid positions of the particles. As can be seen the distribution of the particles is relatively homogeneous, corresponding to the small overdensities at this

³The publicly available version of this code can be found at <https://github.com/sbird/S-GenIC>.

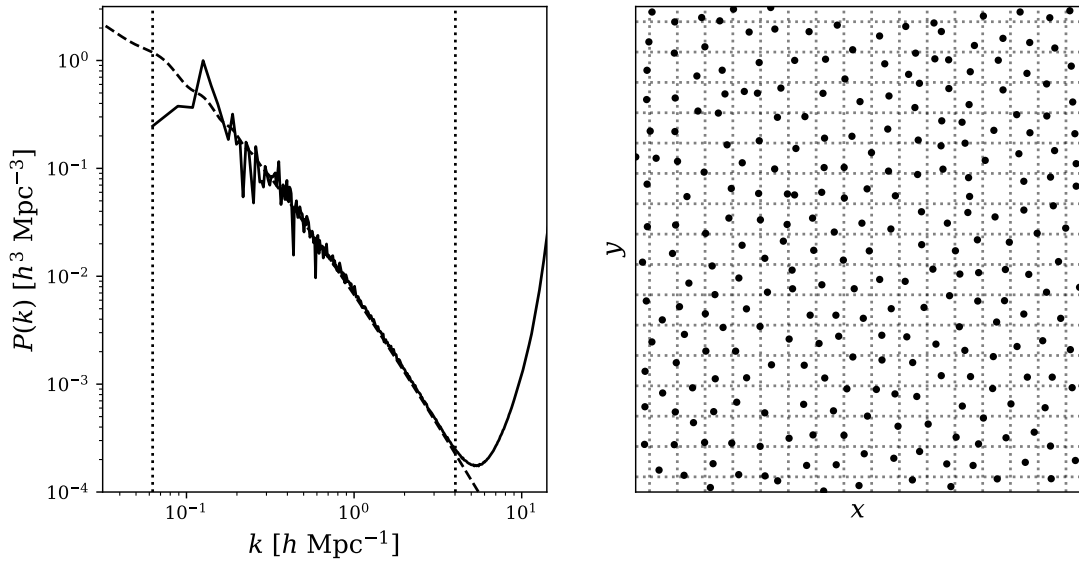


Figure 2.2: Example distribution of particles taken from a WMAP-9 cosmology initialised at $z = 127$. This is a sub-sample of a thin layer of particles taken from a full three-dimensional set of initial particle coordinates. The initial homogeneous grid positions are shown as dashed lines.

early redshift ($z = 127$). However, the particles have clearly moved from their initial configuration, as discussed above.

2.5 Halo finder

The above discussions provide all of the necessary details to perform an N-body simulation of structure formation. However, there is still one key aspect that is important for studying DM haloes. Primarily, how to define and assign particles to individual haloes. Take, for example, the two dimensional distribution of particles in Fig. 2.1. Here, it is easy to visually identify different structures that we would consider to be DM haloes, however it is unclear where to put the ‘edge’ of these structures.

One common approach is the friends-of-friends (FOF) algorithm (Davis et al., 1985). In the FOF algorithm all neighbouring particles within a given distance, known as the linking length, are identified as that particle’s immediate ‘friends’. From this initial identification any particles with mutual friends, regardless of how long the chain is, are then grouped together into a single FOF group. This simple algorithm allows for

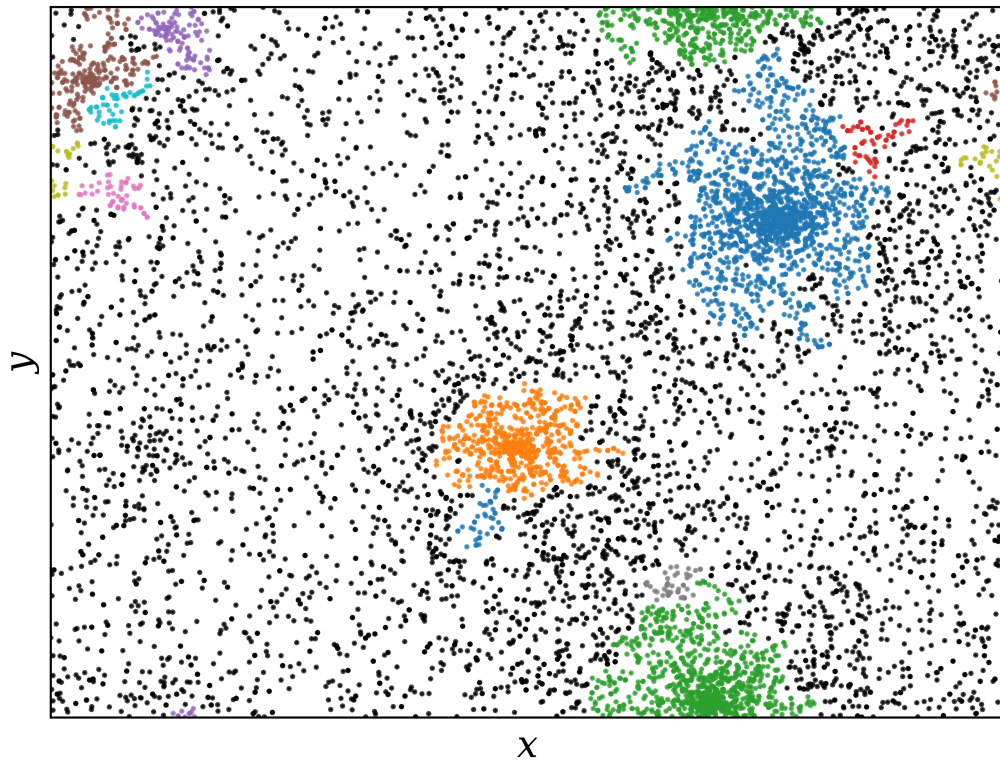


Figure 2.3: Example of the FOF algorithm applies to the same two-dimensional particle distribution as shown in Fig. 2.1. Here, FOF groups with less than 40 particles have been discounted. Different colours denote particles as belonging to a given FOF groups, with black used for those not identified into FOF groups with less than 40 particles.

particles to be quickly identified into individual, discrete objects, where every particle is then uniquely assigned to a FOF halo, or identified as being in the field (i.e. not assigned to any FOF group).

The results of applying the FOF algorithm to the previous two dimensional example is shown in Fig. 2.3. Here each particle's colour demarcates it as belonging to a given FOF group, where black is used for particles not assigned to any FOF group or to one containing fewer than 40 particles. All of the major haloes that would be identified visually are also identified using the FOF algorithm.

One key aspect of the FOF algorithm that needs to be chosen carefully is the linking length. It is clear that the number of identified objects, as well as their size, depends sensitively on the choice of the linking length. To remove the dependence on the resolution and volume of the simulation the linking length is often quoted in terms

of the mean interparticle separation, $l = (N/V)^{1/3}$. It is common to choose the linking length so that the FOF group contains the radius used for the spherical overdensity mass definition, typically using M_{200m} and corresponding radius R_{200m} . The linking length, chosen to meet this criteria, used in this work is $0.2l$.

There are a few characteristic features of the structures identified using the FOF algorithm. Firstly, the FOF groups are rarely spherically bounded, often with long tendril-like features. For example, the probability density functions used to generate the DM halo analogues in Fig. 2.3 are perfectly spherical, but none of the FOF groups are bounded by spherical regions. Another feature is the identification of spurious structures that do not represent collapsed bound haloes but rather a chance configuration of particles. This can be overcome by applying a cut to the minimum number of particles in a FOF group to be considered, as well as being an issue that will improve with increased resolution. Another aspect of FOF groups is their tendency to build ‘bridges’ between two objects only connected by a handful of particles that could potentially be identified as separate objects. An example of this would be if a somewhat larger linking length was used in Fig. 2.3 where the two largest structures (in green and blue) would be linked together. Due to these ambiguities the FOF algorithm, with a given linking length, is typically used as the definition for individual groups of DM halos, both in simulations and observations.

The final limitation of the FOF algorithm is that it does not identify individually bound structures within a FOF group itself. These structures within the FOF group are generally referred to as subhaloes and in this work are identified with the `subfind` algorithm (Springel et al., 2001). There are two general steps to the `subfind` algorithm. Initially, minima in the potential field are identified, with each identified minima corresponding to a subhalo. The gravitational potential of the surrounding particles is then calculated,⁴ with all particles that are gravitationally bound to the given potential minima being assigned to that subhalo. Here it is worth noting that the initial identification of the subhaloes uses only spatial information, while the assignment of particles to a given subhalo uses 6 dimensional phase space information. As such, there can

⁴This is done with the octree approach described in Section 2.2.

be particles that are spatially contained within a subhalo but are not assigned to it due to their larger velocities meaning they are identified as being unbound. Typically the properties of subhaloes, such as their mass, are calculated using only the bound particles.

The most massive identified subhalo is then defined to be the host (or sometimes referred to as the central), regardless of its spatial position within the FOF group. Each FOF group will have only one host halo, but an unspecified number of satellites. Additionally, the centre of the FOF group is commonly chosen to be the centre of potential of the central subhalo, as is done in this work. All radial distances, including calculating overdensity mass definitions, are then calculated with respect to the host halo's centre of potential.

In summary, particles are first identified into groups using the FOF algorithm. These particles are then further divided into bound subhaloes with the `subfind` algorithm. Particles are always uniquely assigned to a given FOF group or subhalo. Particles therefore fall into three categories: those that are not identified into any FOF group, those that are within a FOF group but not assigned to any subhalo and those that are part of a FOF group and subhalo (that is either considered the host or a satellite).

2.6 Key results from numerical simulations

In the previous chapter I have discussed in detail some of the key analytic models of the growth of structures in a cosmological context. However, these analytic models often have key limitations not present in numerical simulations. Therefore there are many important results from N-body simulations. Broadly these can be split into two categories: the large-scale distribution of DM, such as the clustering of galaxies and the DM halo mass function, and the internal structure of individual DM haloes. It is this second category that is the main focus of this thesis.

2.6.1 Density profiles of dark matter haloes

One key prediction from N-body simulations is the spherically averaged density profiles of DM haloes, which can be inferred observationally from stellar rotation curves.

Early analytic models typically predict a power law density profile,

$$\rho(r) = \rho_0 r^{-\gamma}. \quad (2.13)$$

For example the model of violent relaxation predicts $\gamma = 2$ (Lynden-Bell, 1967), while secondary infall models predict $\gamma = 2.25$ (Fillmore, Goldreich, 1984; Bertschinger, 1985), with analytic models typically predicting slopes in the range $\gamma = 2-3$.

Early, low resolution numerical simulations typically agreed with this result of the density profile being power law in nature. However, later simulations demonstrated that the predicted density profiles take on a more complex form with the slope of the profile exhibiting a clear radial dependence. This led to a family of empirical density profiles that took on a self-similar form. Typically these would be of the form of a broken power law. One of the key properties of these early density profiles is that they imply that the density profiles are self-similar, meaning that they can be rescaled perfectly to one another by a given radius. In general these kind of profiles can be written in the form

$$\rho(r) = \frac{\rho_0}{\left(\frac{r}{r_s}\right)^\alpha \left(1 + \frac{r}{r_s}\right)^\beta}. \quad (2.14)$$

Such a parameterisation represents a smoothed broken power law, where the inner slope as $r \rightarrow 0$ is $-\alpha$ and the outer slope as $r \rightarrow \infty$ is $-(\alpha + \beta)$. The scale radius, r_s , represents the point which transitions between the two regimes, and corresponds to a slope of $-(\alpha + 0.5\beta)$. Typically a given profile will use a fixed value for α and β . For example the Hernquist profile uses $\alpha = 1$, $\beta = 3$ (Hernquist, 1990).

One of the most important empirical forms for the focus of this work is the NFW profile (Navarro et al., 1996b; Navarro et al., 1997), that is used extensively throughout the field to model the density profile of DM haloes and is often referred to

as the ‘universal density profile’. The NFW profile uses $\alpha = 1$ and $\beta = 2$, predicting that the inner and outer slopes of the DM density profile to be -1 and -3 , respectively. The scale radius represents where the slope is -2 .

One key aspect of the NFW, and similar, formalisms is that the density profile of a DM halo only depend on its mass and scale radius, often quoted as a halo concentration

$$c \equiv \frac{R_{\Delta c/m}}{r_s}. \quad (2.15)$$

It is well established that c depends strongly on both mass and redshift for a given cosmology, albeit with significant scatter. As such, predicting the mass, redshift and cosmology dependence of c has been the focus of much research (e.g. Bullock et al., 2001a; Eke et al., 2001b; Prada et al., 2012; Diemer, Kravtsov, 2015; Correa et al., 2015a). In general it is found that for a Λ CDM cosmology the concentration increases for lower mass haloes, while at a fixed mass, concentration increases at lower redshifts. This general dependence is naturally explained by positing that the concentration of haloes is driven by a halo’s formation time, where haloes that form earlier have larger concentrations. As lower mass haloes form earlier than their larger counterparts this naturally explains the general mass and redshift evolution of halo concentration. Formation time has therefore been used to develop many (semi-)analytic models for predicting halo concentration (e.g. Navarro et al., 1996b; Wechsler et al., 2006; Ludlow et al., 2014).

It was later demonstrated, with even higher resolution simulations, that the density profiles are not perfectly self similar and are better fit by an Einasto profile (Gao et al., 2008a; Navarro et al., 2010b),

$$\ln(\rho(r)/\rho_{-2}) = -\frac{2}{\alpha} \left[\left(\frac{r}{r_{-2}} \right)^\alpha - 1 \right]. \quad (2.16)$$

The Einasto profile is defined such that the logarithmic slope is a power law, $d \log \rho / d \log r \propto r^\alpha$. Here α is known as the shape parameter and in the above form r_{-2} represents where the logarithmic slope is -2 , equivalent to the scale radius for an NFW profile. There are a few key differences between the Einasto and NFW pro-

files. Firstly, is the prediction for the inner and outer slopes, while the NFW profile predicts clear asymptotic slopes of -1 and -3 the Einasto profile has no such limits and instead reaches arbitrarily steep profiles at large radii and a flat profile at the centre. Secondly, the Einasto profile predicts that haloes are not self similar, requiring an additional ‘shape’ parameter, α , beyond concentration to describe their profiles. The NFW profile does not have any equivalent parameter. This is additionally important as α , like halo concentration, has been shown to vary systematically with halo mass, redshift and cosmology (e.g. Gao et al., 2008a).

There are still a number of outstanding questions regarding the internal structure of dark matter haloes. Firstly, the theoretical origin of the form of the density profile (NFW or Einasto) is poorly understood. Additionally, although there exist many models to predict the concentration of DM haloes there is yet to be developed a model to predict the mass, redshift and cosmology dependence of both halo concentration and the shape parameter. The density profiles of DM haloes and their dependence on changes to the underlying cosmology is the focus of much of this thesis and discussed in more detail within both Chapter 3 and 4.

2.6.2 Small scale challenges of Λ CDM

In general, the agreement of numerical simulations match very closely the large scale structure of our observed universe, such as the clustering of galaxies, cosmic shear and the observed Lyman- α forest. In these fields the use of numerical N-body simulations has become invaluable in interpreting observations and being able to use these observables to constrain cosmological models and parameters.

Despite the success of the Λ CDM model on large scales there have been a number of tensions identified on small scales:

Missing satellites problem (e.g. Moore et al., 1999; Klypin et al., 1999). The prediction of collisionless simulations of Λ CDM cosmologies is that all haloes should be surrounded by a plethora of satellite haloes. However when comparing observations of

the local group it became clear that the abundance of systems at small masses, typically in the dwarf regime, are significantly lower than predicted by simulations.

Core-cusp problem (e.g. Flores, Primack, 1994; Moore, 1994). Early predictions from collisionless simulations suggested that the density profile of DM haloes are ‘cuspy’, with the NFW prediction being an inner slope of -1 . However, observations of the stellar rotation profiles in low mass galaxies suggested that the profile of the DM haloes are not cuspy but much closer to a cored profile with roughly a constant density in the inner regions.

Too big to fail problem (e.g. Boylan-Kolchin et al., 2011). This is a similar issue to the missing satellites problem and regards the distribution of satellites around Milky way like systems. However, the too big to fail problem regards the largest satellite galaxies. It is observed that the largest satellite systems in simulations have significantly different $V_{\max} - R_{\max}$ relations, with the simulations predicting lower R_{\max} values at a fixed V_{\max} than observed for the satellites of the Milky way.

There are a number of proposed solutions to these small scale problems with Λ CDM. One way is to evoke an extension to the Λ CDM model. For instance, warm DM models, with a truncated linear power spectrum, suppress the formation of haloes below an associated mass scale as well as affecting their concentration, and can therefore offer a potential solution to the missing satellite and too big to fail problem. While self-interacting dark matter, which allows for scatter between DM particles, produces cores in the centre of DM, offering a solution to the core-cusp problem.

Although extensions to Λ CDM can offer solutions to these tensions there is, potentially, a more obvious solution; baryonic physics. A key part of how these tensions were originally formulated relied on comparing observations to collisionless simulations. Indeed, it has been shown that these tensions can all, potentially, be resolved with the inclusion of baryonic processes. The missing satellites problem can be explained by a significant number of dwarf mass DM haloes being ‘dark’ and not hosting a stellar component (i.e. a galaxy). These dark subhaloes are due to a combination the effects of reionisation, stellar and AGN feedback and environmental process. Sim-

ilarly, baryonic processes, particularly stellar feedback, can reduce the concentration of DM haloes leading to a resolution of the too big to fail problem. Finally, it has also been shown that if stellar feedback is sufficiently ‘bursty’ it can lead to the formation of a core in the central DM halo.

Although baryonic processes have been shown to resolve these tensions, it does not rule out the possibility of deviations from Λ CDM. Particularly as there are significant uncertainties in how to accurately and reliably model the baryonic processes. A key aspect of modern computational models for galaxy evolution is the need for calibration. Due to the finite resolution of numerical simulations many of the processes have to be modelled as so-called ‘sub grid’ routines, with associated free parameters. As such these models must be tuned to match certain observations. Typically, these models are calibrated on a Λ CDM. Therefore, to truly test if Λ CDM offers a unique solution, and put reliable constraints on extension Λ CDM, a joint exploration of the baryonic models and a given extension is needed. This is the motivation and focus for Chapter 5.

Chapter 3

Connecting the structure of dark matter haloes to the primordial power spectrum

This chapter appeared in Brown et al. (2020). The appendices for this work are in Appendix A.

A large body of work based on collisionless cosmological N-body simulations going back over two decades has advanced the idea that collapsed dark matter haloes have simple and approximately universal forms for their mass density and pseudo-phase space density (PPSD) distributions. However, a general consensus on the physical origin of these results has not yet been reached. In the present study, I explore to what extent the apparent universality of these forms holds when the initial conditions (i.e., the primordial power spectrum of density fluctuations) are varied away from the standard CMB-normalised case, but still within the context of Λ CDM with a fixed expansion history. Using simulations that vary the initial amplitude and shape, I show that the structure of dark matter haloes retains a clear memory of the initial conditions. Specifically, increasing (lowering) the amplitude of fluctuations increases (decreases) the concentration of haloes and, if pushed far enough, the density profiles deviate strongly from the NFW form that is a good approximation for the CMB-

normalised case. Although, an Einasto form works well. Rather than being universal, the slope of the PPSD (or pseudo-entropy) profile steepens (flattens) with increasing (decreasing) power spectrum amplitude and can exhibit a strong halo mass dependence. Our results therefore indicate that the previously identified universality of the structure of dark matter haloes is mostly a consequence of adopting a narrow range of (CMB-normalised) initial conditions for the simulations. Our new suite provides a useful test-bench against which physical models for the origin of halo structure can be validated.

3.1 Introduction

The study of how structure forms in a Λ -Cold Dark Matter (Λ CDM) universe has been an active area of research since its general acceptance as the leading cosmological paradigm (Smoot et al., 1992; Riess et al., 1998; Spergel et al., 2003; Planck Collaboration et al., 2014). Of particular interest within the large-scale structure of our Universe are collapsed, gravitationally-bound, virialised objects that are commonly referred to as dark matter (DM) ‘haloes’.

Due to their non-linear evolution, DM haloes are most widely studied in the context of cosmological N-body simulations where the equations of motion are solved explicitly. From numerous such numerical studies there has emerged a few key results that appear to exhibit a degree of *universality*. First, the density profiles of relaxed haloes are well described by a Navarro-Frenk-White (NFW) profile (Navarro et al., 1996a, 1997), defined as

$$\rho(r) = \frac{\rho_0}{r/r_s(1+r/r_s)^2}. \quad (3.1)$$

where ρ_0 is a simple normalisation term,¹ while r_s is a scale radius. The NFW profile has asymptotic inner and outer slopes of $\rho \propto r^{-1}$ and r^{-3} , respectively, with r_s being the radius at which the logarithmic slope is -2 . The scale radius, r_s , is often quoted

¹In fact, the normalisation does not need to be a free parameter, but can be specified by requiring that the integral of the profile matches the total mass of the halo (e.g., within some spherical overdensity radius).

as a concentration parameter, $c \equiv R_\Delta/r_s$, where R_Δ is the radius containing a mean density of Δ times the critical (or mean) density of the universe. It has been shown that DM haloes are approximately self similar, as the NFW profile would suggest, however in general DM densities are more accurately described with an additional ‘shape’ parameter (Navarro et al., 2010a). For this an Einasto profile is often used (see Eqn. 3.10) (Einasto, 1965).

The second result is that the radial dependence of the pseudo-phase space density (PPSD) profile, $Q(r)$, appears to be well described by a simple power law over radii sampled by simulations (e.g., Taylor, Navarro 2001). The PPSD is defined as

$$Q(r) \equiv \frac{\rho(r)}{\sigma(r)^3}, \quad (3.2)$$

with $\sigma(r)$ being the total velocity dispersion at a given radii. The exponent of the power law is seemingly a constant for all haloes, with $Q(r) \propto r^{-1.875}$. This suggests that the PPSD profiles are identical for all haloes, potentially indicating that the PPSD is a more fundamental property of DM haloes than the mass density.

Both of these results are well established within the literature, however their physical origins are relatively poorly understood. It has been argued that an inner and outer slopes of the density profile -1 and -3 , respectively, are expected from hierarchical structure formation. Halo assembly can be split into two regimes, an early rapid accretion phase followed by slower accretion. The inner slope of -1 is formed during this initial phase and the outer slope of -3 during the second phase of slow accretion, with the scale radius being linked to the time a halo transitions between these stages (e.g. Syer, White, 1998; Lu et al., 2006). The power law nature of the PPSD, as well as the specific exponent of $Q(r) \propto r^{-1.875}$, is predicted by secondary infall models (Bertschinger, 1985). However, these models are built on the strong assumption that the initial perturbation and subsequent accretion is spherically symmetric and smooth, i.e. there is no hierarchical growth of structure. Why such a model should correctly match the PPSD profiles of haloes in a ‘real’ universe that grow through the continual anisotropic accretion of clumps of matter is still an open question within the field.

Moreover, there is significant scatter on a halo to halo basis as well as some debate over the exact exponent (e.g. Dehnen, McLaughlin, 2005; Faltenbacher et al., 2007). It has also been claimed that the PPSD profiles are slowly rolling power laws that only appear to be a perfect power law over the radial ranges sampled by N-body simulations (e.g. Nadler et al., 2017), which is typically above 1% of a halo's virial radius.

The above discussion applies specifically to a collisionless simulation with no hydrodynamics or non-gravitational physics (e.g., cooling, feedback processes) that are employed in many of the modern galaxy formation and cosmological simulations (e.g., Vogelsberger et al., 2014a; Le Brun et al., 2014; Schaye et al., 2015; Sawala et al., 2016; McCarthy et al., 2017; Hopkins et al., 2018; Nelson et al., 2019). Additionally, the structure of haloes can be significantly affected by extensions to the Λ CDM model. This can be done through direct changes to the equations of motion, such as self-interacting dark matter (e.g. Vogelsberger et al., 2014b; Robertson et al., 2019a), or changes to the linear power spectra in the early Universe, such as warm dark matter (e.g. Lovell et al., 2017; Hellwing et al., 2016) and a running of the spectral index (e.g. Garrison-Kimmel et al., 2014; Stafford et al., 2020b) to name but a few possible extensions (see Stafford et al. 2020a for a recent comparison of the effects of these extensions along with baryonic processes). There are many open questions associated with these more complex simulations, and as such are the focus of much research. However, there is still strong motivation to further study the structure in comparably simple collisionless simulations. If we cannot understand the formation and evolution of haloes in these simulations, it is difficult to see how a rigorous physical picture can be established when the problem is made considerably more complex with additional processes.

The evolution of structure in a cold dark matter universe is driven by three things: i) the initial conditions, i.e. the primordial power spectra; ii) the nature of the gravitational force law; and iii) the cosmological parameters that, with the gravitational force law, determine the expansion history of the universe. In the present study, I leave the force law and expansion history unchanged from the accepted Λ CDM model and focus solely on the effects of varying the primordial power spectrum on the properties of

late-time collapsed haloes. This is achieved by systematically varying the primordial spectral index, n_s , and amplitude, A_s , to study both the effects of shape and amplitude changes in the initial power spectra. I note that it has previously been shown that the NFW form and power law PPSD generally continue to be accurate descriptions of the structure of DM haloes for a wide range of changes to the shape of the linear power spectra and to the cosmological parameters that control the expansion history (e.g., Navarro et al. 1997; Moore et al. 1999; Reed et al. 2005; Wang, White 2009) and even for some setups that avoid hierarchical clustering altogether (e.g., Huss et al. 1999). It is interesting to note, however, that previous studies did not explore a wide range of primordial power spectrum amplitudes, which I find to be key.

Using cosmological simulations, I show that many of the results discussed above are only valid in universes close to our own, specifically for universes with a similar amplitude of initial density fluctuations. Varying away from the standard initial conditions, I find that the slope of the PPSD is in general not a constant and instead exhibits a clear mass dependence. Furthermore, the NFW form becomes an increasingly poor description of the mass structure of haloes as the amplitude of the primordial power spectrum is increased.

The chapter is organised as follows. In Section 3.2 I discuss the technical details of the simulations and provide motivation for the choice of parameters. In Section 3.3 I present stacked density, entropy and velocity profiles of haloes in the various simulations. In Section 3.4 I study how fitted density and entropy parameters vary with mass and peak height. In Section 3.5 I present how the accretion histories of haloes vary in the cosmologies studies here as well as comparing these results for the concentration–mass (or similarly concentration–peak height) relation to the predictions of a number of (semi-)analytic models. Finally, in Section 3.6 I summarise the findings.

3.2 Simulations and halo property estimates

In this section I describe the general simulation setup and the generation of initial conditions. I also describe the halo selection criteria and how halo properties are estimated.

3.2.1 Halo mass and radius definitions

Throughout this chapter the size and mass of haloes are described using definition as a spherical overdensity, Δ , with respect to the critical density of the universe. The labels M_{200c} and R_{200c} , as used in this work, therefore correspond to the mass and size, respectively, of haloes defined such that the average density within R_{200c} is equal to 200 times the critical density.

3.2.2 General simulation setup

All simulations used in this work share the same technical details. Specifically, the linear power spectra that are used to generate the initial conditions (see Section 3.2.3) are computed using the Boltzmann code CAMB (Lewis et al., 2000), at a starting redshift of $z = 127$. The initial particle positions and velocities are then generated using a modified version of N-GENIC² (Springel, 2005), including second-order Lagrangian perturbation theory (2LPT) corrections and adopting identical phases for all simulations. The simulations use a comoving $200 h^{-1}$ Mpc on a side box with 512^3 particles. For the background cosmology the best fit WMAP 9-yr results are used (Hinshaw et al., 2013), with $h = 0.7$, $\Omega_m = 0.2793$, $\Omega_b = 0.0463$ and $\Omega_\Lambda = 0.7207$. As such the particle masses of all these simulations is $4.62 \times 10^9 h^{-1} M_\odot$. The simulations are run with a modified version of the GADGET-3 code (Springel, 2005; McCarthy et al., 2017). The gravitational softening is fixed to $4 h^{-1}$ kpc (in physical coordinates for $z \leq 3$ and in co-moving at higher redshifts). In Appendix A.2 I present a resolution and box size study for a range of the cosmologies studied here to make sure these numerical

²The publicly available version of this code can be found at <https://github.com/sbird/S-GenIC>.

parameters do not effect the results presented in this chapter.

All haloes are identified with the `SUBFIND` algorithm (Springel et al., 2001). In this work I will only present results of host haloes, which are defined as the largest halo in the friend-of-friends (FOF) group. The halo finder here is only used to initially find the FOF group, provide the location of the centre of potential and bulk properties such as M_{200c} and R_{200c} .

3.2.3 Primordial power spectra

I study the effect of the initial density field by varying two free parameters in the Λ CDM model that directly affect the primordial density perturbations, A_s and n_s . Here, n_s is referred to as the primordial scalar spectral index and it is the slope of the primordial power spectrum, assumed to be a power law. n_s is a free parameter in the Λ CDM model that is well-constrained by the CMB to have a value of $n_s \approx 0.96$ – 0.97 (Spergel et al., 2003; Planck Collaboration et al., 2016). A_s is the amplitude of the initial power spectrum, which is specified at a chosen pivot point, k_{pivot} . Systematically varying these two parameters, as well as the pivot point, allows us to isolate shape and amplitude changes to the initial power spectrum, but without changing the background expansion or the nature and abundance of dark matter. Thus, the simulations are still run in the context of Λ CDM.

To study the dependence of n_s and A_s on the properties of DM haloes I initially take a WMAP 9-yr cosmology and systematically vary n_s between 0.5 to 1.75. While all of the runs considered (apart from the fiducial $n_s = 0.96$ case) are ruled out by observations. The goal here is to see whether and to what extent the properties of collapsed haloes ‘remember’ the initial conditions.

The initial linear power spectra at $z = 127$ for this suite of simulations are shown in the left panel of Fig. 3.1. The change in n_s can clearly be seen in the slope of the power spectra at small k-modes ($k \sim 10^{-2} h \text{ Mpc}^{-1}$), with larger n_s values giving steeper profiles and vice versa. Another notable feature is the pivot point, in this case

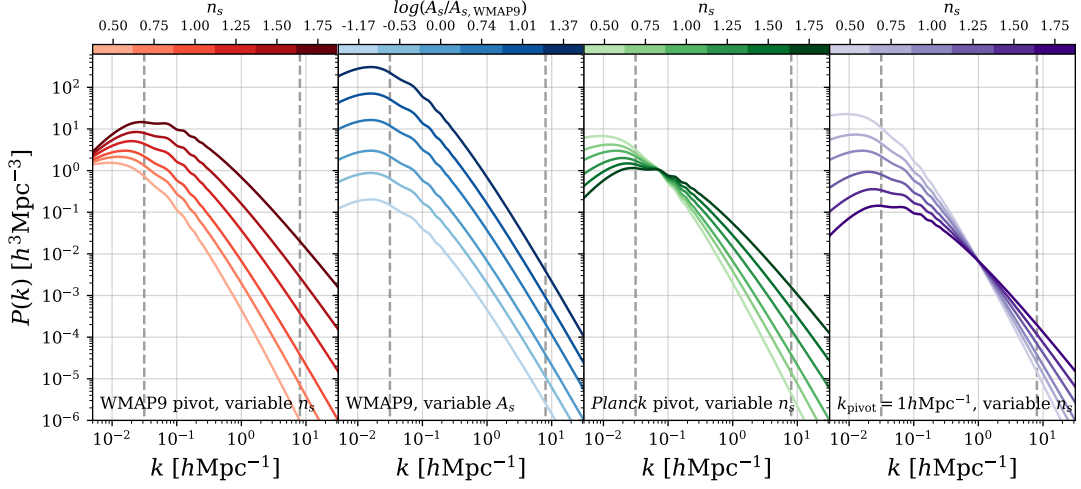


Figure 3.1: Linear power spectra used to create the initial conditions of the various simulations at $z = 127$, generated using CAMB (Lewis et al., 2000). All cosmologies have the same background cosmology (best fit WMAP 9-yr results), but with variable A_s , n_s and k_{pivot} . Left panel shows the fiducial suite with adopting a WMAP pivot point ($k = 2.85 \times 10^{-3} h \text{Mpc}^{-1}$) with systematically varying n_s . The middle-left panel is the initial power spectra for the suite of simulations that have a fixed n_s but a varied A_s such that at $k = 1 h \text{Mpc}^{-1}$ they have the same power as the corresponding WMAP pivot simulations (left panel). The middle-right panel shows the same but for a *Planck* pivot point ($k = 7.14 \times 10^{-2} h \text{Mpc}^{-1}$). The suite using a $k_{\text{pivot}} = 1 h \text{Mpc}^{-1}$ with systematically varied n_s is shown in the right most panel. The value of n_s , or equivalently matched A_s is shown in the colour bar above each plot. The vertical dashed lines represent the Nyquist frequency and the fundamental mode for the box size, i.e. the resolved range of the simulations.

$k_{\text{pivot}} = 2.86 \times 10^{-3} h \text{Mpc}^{-1}$ (or $2 \times 10^{-3} \text{Mpc}^{-1}$), where the power spectra are normalised. When looking at the region sampled by the simulations (delineated by the vertical dashed lines), it becomes clear that the power spectra will depend on both n_s and A_s , as well as the choice of k_{pivot} . n_s can be interpreted as a shape change but the change in amplitude at a given k scale is a combination of n_s , A_s and k_{pivot} . Due to this complexity, I isolate the amplitude and shape changes by running three complementary sets of simulations: (i) a set of simulations where n_s is fixed to 0.96 but the amplitude A_s is varied, such that the power at $k = 1 h \text{Mpc}^{-1}$ is equivalent to the WMAP 9-yr simulations with varied n_s (see middle-left panel of Fig. 3.1); (ii) a set of simulations using the same pivot point as the *Planck* team, $k_{\text{pivot}} = 7.14 \times 10^{-2} h \text{Mpc}^{-1}$, and again systematically vary n_s (see middle-right panel of Fig. 3.1); and (iii) a set of simulations where $k_{\text{pivot}} = 1 h \text{Mpc}^{-1}$ is used and again systematically vary n_s (see right panel of Fig. 3.1). In this way there are two suites of simulations with a combination of shape

and amplitude changes, but to varying degrees, and additionally two sets of simulations where I have tried to isolate the changes in amplitude and shape. For two suites I have specifically emphasised $k = 1h \text{ Mpc}^{-1}$, either by using it as the pivot point or specifically matching the amplitude at that k -scale. This particular k -mode is chosen as it is well sampled in the box, well away from the Nyquist frequency and far from cosmic variance at larger k -modes, as well as being a k scale associated with haloes of $M_{200c} \sim 10^{13-14} h^{-1} M_{\odot}$ (van Daalen, Schaye, 2015), which is the mass of a typical halo in the simulations.

While different power spectra are often normalised by σ_8 (e.g. Knollmann et al., 2008), in this work I choose to normalise at a particular k -scale, k_{pivot} . Using a pivot scale allows us to isolate the effects of amplitude and shape changes to the initial power spectrum by varying k_{pivot} . The use of a pivot point also allows a more intuitive link between a halo of a certain mass and the initial linear power spectrum. Systematically varying the pivot point is similar, though not identical, to choosing to normalise by differing values of $\sigma(R)$ rather than $\sigma(R = 8h^{-1}\text{Mpc})$ specifically.

A list of the various cosmologies and simulations parameters is given in Table. 3.1. The format used in Fig 3.1 to represent the different simulations (such as the colour, panel position, etc.) is the same throughout the chapter. Throughout the chapter I will use n_s as a reference to a particular simulation regardless of whether n_s is the direct cause of observed effects. When describing the effect of changing the slope of the power spectrum, which is a change of n_s , we will specifically describe it as a slope or general shape change, n_s is simply a reference to the particular simulation being discussed.

3.2.4 Halo selection criteria

To ensure the robustness of these results, I will focus on well-resolved, relaxed haloes. The first cut made to the halo sample is to remove haloes that are too poorly sampled to generate reliable density and velocity dispersion profiles. This cut is such that the number of particles within R_{200c} , N_{200} , is greater than 2×10^3 . This choice results

Table 3.1: Summary of the various cosmological parameters for all simulations presented in this work. The main two parameters varied are n_s and A_s . Along with k_{pivot} , they completely specify the initial power spectrum. Note that for the ‘Matched amplitude’ suite, the shape is fixed ($n_s = 0.96$) while the amplitude at a scale of $1 h \text{ Mpc}^{-1}$ is adjusted to match the various runs in the ‘WMAP9 pivot’ suite. All cosmologies have the same background expansion: $h = 0.7$, $\Omega_m = 0.2793$, $\Omega_b = 0.0463$ and $\Omega_\Lambda = 0.7207$.

Simulation suite	n_s	$A_s [10^{-9}]$	$k_{\text{pivot}} [h \text{ Mpc}^{-1}]$	σ_8
WMAP9 pivot	0.96	2.392	2.86×10^{-3}	0.801
WMAP9 pivot	0.5	2.392	2.86×10^{-3}	0.328
WMAP9 pivot	0.75	2.392	2.86×10^{-3}	0.530
WMAP9 pivot	1.25	2.392	2.86×10^{-3}	1.442
WMAP9 pivot	1.5	2.392	2.86×10^{-3}	2.422
WMAP9 pivot	1.75	2.392	2.86×10^{-3}	4.114
Matched amplitude	0.96	0.1617	2.86×10^{-3}	0.208
Matched amplitude	0.96	0.6992	2.86×10^{-3}	0.433
Matched amplitude	0.96	13.08	2.86×10^{-3}	1.874
Matched amplitude	0.96	24.45	2.86×10^{-3}	3.897
Matched amplitude	0.96	56.55	2.86×10^{-3}	8.103
<i>Planck</i> pivot	0.5	2.103	7.14×10^{-2}	0.687
<i>Planck</i> pivot	0.75	2.103	7.14×10^{-2}	0.743
<i>Planck</i> pivot	1.25	2.103	7.14×10^{-2}	0.904
<i>Planck</i> pivot	1.5	2.103	7.14×10^{-2}	1.016
<i>Planck</i> pivot	1.75	2.103	7.14×10^{-2}	1.154
$k_{\text{pivot}} = 1 h \text{ Mpc}^{-1}$	0.5	1.892	1.00	1.261
$k_{\text{pivot}} = 1 h \text{ Mpc}^{-1}$	0.75	1.892	1.00	0.980
$k_{\text{pivot}} = 1 h \text{ Mpc}^{-1}$	1.25	1.892	1.00	0.616
$k_{\text{pivot}} = 1 h \text{ Mpc}^{-1}$	1.5	1.892	1.00	0.498
$k_{\text{pivot}} = 1 h \text{ Mpc}^{-1}$	1.75	1.892	1.00	0.407

in converged density and velocity dispersion profiles and also avoids some systematic issues observed when fitting poorly sampled haloes (see Appendix A.1 for further details). The second cut is to remove unrelaxed haloes from the sample. For this I use one of the criteria advocated in the work of Neto et al. (2007). Specifically, that the normalised offset of the centre of mass (CoM) to centre of potential (CoP) is $s = (r_{\text{CoP}} - r_{\text{CoM}})/R_{200c} < 0.07$. Neto et al. (2007) applied additional cuts to the relative mass in substructure and virial ratio, however Duffy et al. (2008) found that a simple cut on CoM and CoP offsets is sufficient to remove the majority of unrelaxed haloes. The fraction of haloes removed from the sample due to this relaxation criteria varies from simulation to simulation but is typically in the range 5–10% for most of the simulations, with the exception of the two simulations with the smallest amplitudes (the lightest red and blue lines in Fig. 3.1 corresponding to the cosmologies with $\sigma_8 = 0.328$ and 0.208, see Table 3.1) where around 30% of haloes are discounted. I have included the relaxation cut to be consistent with other work in the literature, however, it is found that there is little to no effect if I include the relaxation cuts or not. I attribute this to us exclusively studying median stacked profiles throughout this work as opposed to individual haloes (see Section 3.4).

3.2.5 Density and velocity dispersion profiles

I introduce a new method to measure smoothed density and velocity dispersion profiles that have reduced noise and fewer systematic errors compared to the standard method of radial binning. In this section I will outline the general method. An in depth discussion can be found in Appendix A.1.

The general procedure is to use a weight function to calculate the spherically-averaged density and velocity dispersion of a DM halo. The density is calculated as

$$\rho(r) = \sum_i^{N_{\text{kern}}} W(r_i; h, r) m_i. \quad (3.3)$$

r_i is used to denote particle position whereas r is the radius at which the density is

being estimated. Here I have written it in a generalised form with variable mass, m_i , but for the simulations this is a constant. $W(r_i)$ is a general weight function, which is defined shortly. Bulk velocities, in the three spherical directions, are calculated as

$$\mathbf{v}_{\text{bulk}}(r) = \frac{\sum_i^{N_{\text{kern}}} W(r_i; h, r) \mathbf{v}_i}{\sum_i^{N_{\text{kern}}} W(r_i; h, r)} \quad (3.4)$$

and from this the velocity dispersion is calculated as

$$\sigma^2(r) = \frac{\sum_i^{N_{\text{kern}}} W(r_i; h, r) (\mathbf{v}_i - \mathbf{v}_{\text{bulk}})^2}{\sum_i^{N_{\text{kern}}} W(r_i; h, r)}. \quad (3.5)$$

In this manner I calculate the velocity dispersion in all three orthogonal directions. Throughout this work I present results for the total velocity dispersion, $\sigma^2 = (\sigma_r^2 + \sigma_\theta^2 + \sigma_\phi^2)/3$, and the velocity anisotropy averaged over both angular directions, $\beta = 1 - 0.5\sigma_\theta^2/\sigma_r^2 - 0.5\sigma_\phi^2/\sigma_r^2$.

The weight function adopted is the cubic spline implemented in many smoothed particle hydrodynamics methods (Monaghan, Lattanzio, 1985):

$$W(r_i; h, r) = \frac{1}{\pi h(0.25h^2 + 3r^2)} \begin{cases} 1 - 6x^2 + 6x^3 & \text{if } x < 0.5 \\ 2(1 - x)^3 & \text{if } 0.5 < x < 1, \\ 0 & \text{otherwise} \end{cases} \quad (3.6)$$

where I have let $x = \frac{|r_i - r|}{h}$. The normalisation factor is only relevant for calculating the density and is the effective volume of the kernel (equivalent to the factor of $\frac{4}{3}\pi[(r+h)^3 - (r-h)^3]$ for a square or top hat kernel).³

As can be seen in Eqn. (3.6) this method has one free parameter h , the width (or ‘smoothing length’) of the kernel. h is varied as a function of radius to be equivalent to using logarithmically spaced bins, meaning that $h(r) = Ar$. I then let A be a function of N_{200c} , the number of particles within R_{200c} . This is done in such a way that the two types of error associated with this method, random Poisson errors from having a finite

³The normalisation term is different from the usual factor of $8/(\pi h^3)$ as this equation is designed to calculate the mass per unit volume from radial coordinate.

number of data points and systematic errors from having a kernel with a finite width, scale the same with resolution. The relation used is then

$$h(r) = (N_{200c}/500)^{-1/3}r. \quad (3.7)$$

where $N_{200c}^{-1/3}$ is derived analytically and the factor of 500 found empirically. In general particles are not required to be uniquely associated with a particular ‘bin’ and kernels can overlap. This allows the kernel width and sampling positions to be independent, which is of particular importance when taking derivatives of the density profiles as I do in this work.

3.2.6 Halo entropy vs. PPSD

Before proceeding further let us discuss PPSD a little more, particularly why it is referred to as *pseudo phase-space density*. The quantity defined in Eqn. (3.2) is referred to as PPSD as a simple analogy to true phase-space density as both quantities have the same dimensionality. I believe, however, that there is a better analogous property to be compared to, that of entropy. Taking the definition of entropy in an astrophysical context⁴ (e.g., as often employed in studies of the X-ray emission of galaxy clusters), $S \equiv k_B T n_e^{-2/3}$, and making the substitution $T \rightarrow \sigma^2$ and $n_e \rightarrow \rho$, the ‘entropy’ can be written as

$$S = \left(\frac{\rho}{\sigma^3} \right)^{-2/3} = Q^{-2/3}. \quad (3.8)$$

If the PPSD profiles are power laws with an exponent -1.875 then the implied entropy profiles will be power laws with an exponent of ≈ 1.25 . The entropy profiles of both real and simulated clusters (this being true entropy of the hot intracluster gas) can be well fit by a power law at large radii, with observed exponents of $\sim 1.1 - 1.3$ (e.g., Voit et al. 2005; McCarthy et al. 2008; Cavagnolo et al. 2009), suggesting this analogy is not completely unwarranted. Strictly speaking, the quantity in Eqn. (3.8) should be referred to as *pseudo-entropy*; as I will not be presenting any results from

⁴Boltzmann entropy and ‘astrophysical’ entropy are related by the following, $S_{\text{Boltz}} = \ln(S_{\text{Astro}}^{3/2}) + \text{const.}$

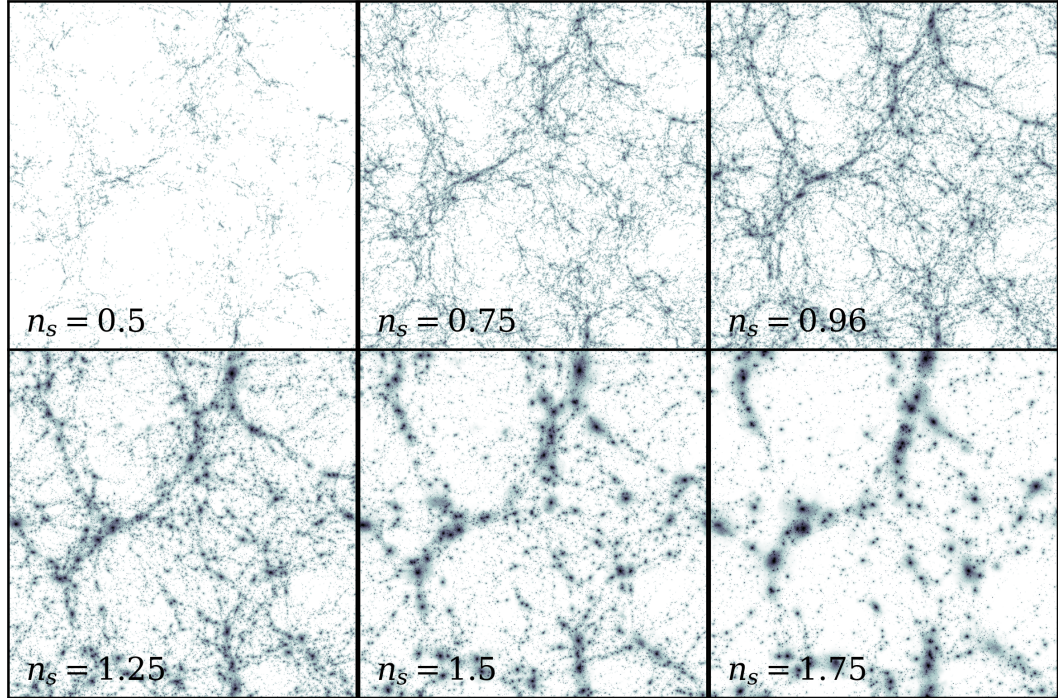


Figure 3.2: Surface density maps of the six WMAP pivot cosmologies with variable n_s at $z=0$. From top left to bottom right we have increasing values of n_s from 0.5–1.75, see label in bottom left of each panel. These plots are meant to show the qualitative behaviour of the different density fields so no colour bar is given. Each colour map is normalised the same and represents the logarithmic projected surface density. These images have been made using the publicly available code `SPH-Viewer` (Benitez-Llambay, 2015).

hydrodynamic simulations I simply refer to it as entropy without the risk of confusion. Throughout the rest of this chapter I refer solely to entropy and not the PPSD, noting that the former can be trivially converted to the latter as described above.

3.3 Stacked profiles

In this section I present the stacked density, entropy and velocity profiles of haloes within a narrow mass range at $z = 0$ for the various simulations. An alternative to studying haloes at fixed mass and redshift would be to instead look at haloes as a function of ‘peak height’, as discussed in Section 3.4.2. The discussion in this section will mainly be limited to describing the recovered features and trends, leaving interpretation of the results until Sections 3.4 & 3.5.

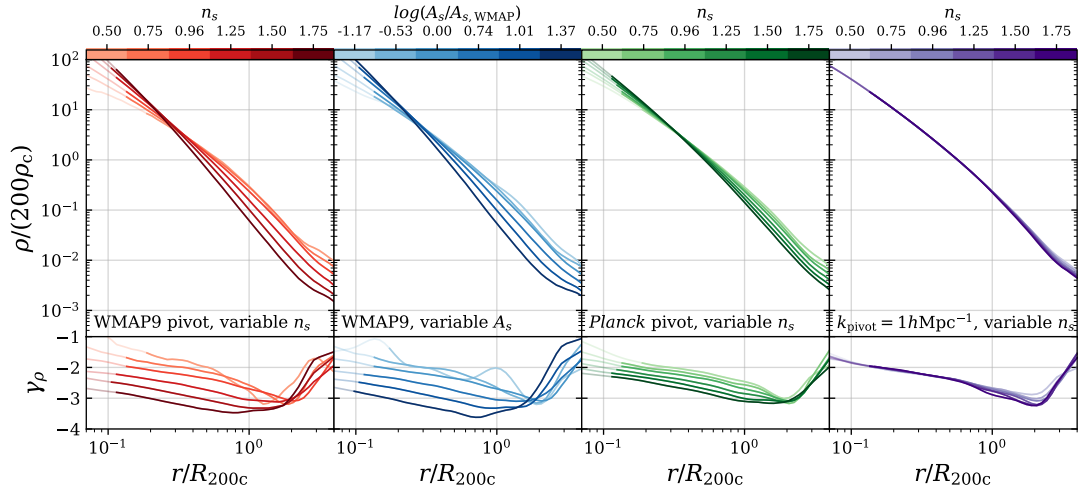


Figure 3.3: Top panels show the stacked median density profiles of haloes in the mass range $M_{200c} = 10^{13} - 10^{13.5} h^{-1} M_{\odot}$ while the bottom panels the logarithmic slope of the above plot, defined as $\gamma_{\rho} = d(\ln \rho) / d(\ln r)$ at $z = 0$. Densities are normalised to the critical density today while the radii are normalised to each haloes R_{200c} . The left column shows the WMAP pivot cosmology with variable n_s , the middle-left panels the equivalently matched A_s with fixed n_s , the middle-right panels the *Planck* pivot point with variable n_s and the far right panels the $k_{\text{pivot}} = 1 h \text{ Mpc}^{-1}$ suite. The colours represent the different suites of simulations while the shade represents the value of n_s or matched A_s , see colour bar above each plot. Each curve is plotted transparent where the criteria for convergence is not met. A comparison of the different panels indicates that the dominant factor in setting the density profile of a halo is the *amplitude* of the linear power spectra at an associated k -mode.

In Fig. 3.2 I show the projected density maps for the WMAP 9-yr with variable n_s suite of simulations. I present this plot to highlight in a qualitative way the effect that varying this parameter has on the overall present-day density field. It is readily apparent that the size and mass of haloes in the various simulations are extremely different, with $n_s = 0.5$ (top left) having a largest halo of only $M_{200c} \sim 10^{13} h^{-1} M_{\odot}$ while $n_s = 1.75$ has haloes that exceed $10^{16} h^{-1} M_{\odot}$.

3.3.1 Stacked density profiles

In Fig. 3.3 I present the stacked density profiles of haloes in the mass range $M_{200c} = 10^{13} - 10^{13.5} h^{-1} M_{\odot}$ at $z = 0$. Haloes are stacked by taking the median densities of individual haloes in units of r/R_{200c} . The top panels show the density as a function of radius, with density normalised by $200\rho_c(z = 0)$ and radii scaled by R_{200c} of each halo (i.e., stacked in bins of normalised radius). All profiles are plotted out to $4R_{200c}$.

In the bottom panels I plot the corresponding logarithmic slopes, defined as $\gamma_\rho = d(\ln \rho)/d(\ln r)$. The different columns represent the different sets of simulations: left (in red) is the WMAP pivot point with variable n_s ; middle-left (in blue) is the WMAP pivot with fixed n_s but variable A_s to match the amplitude of the equivalent n_s run at $k = 1 h \text{ Mpc}^{-1}$; middle-right (in green) is the *Planck* pivot with variable n_s ; and right (in purple) is the case with variable n_s and a pivot scale of $k_{\text{pivot}} = 1 h \text{ Mpc}^{-1}$. The shade of the colour represents the value of n_s used (or amplitude matched to) with darker colours corresponding to higher values of n_s (or higher matched A_s), see colour bars above each column. The colour schemes are equivalent to Fig. 3.1 so can be directly compared. I recommend the reader refer back to Fig. 3.1 for intuition of what part of the initial power spectra has changed.

Let us first focus our attention on the left column of Fig. 3.3, which is used as the fiducial suite of simulations. The first thing to notice is the strong dependence that the steepness of the density profiles at a fixed r/R_{200c} has on n_s , simulations with larger values of n_s result in more negative logarithmic slopes. It appears that the main difference between these density profiles is a change in concentration or similarly scale radius. Looking at the logarithmic slope of these profiles (bottom panel), the profiles all behave roughly log-linearly before a sharp decrease at $\sim R_{200c}$. This feature in the density profile corresponds to the splashback radius, the radii at which particles reach the apocenter of their first orbit. The splashback radius roughly delineates a region that is actively accreting onto the halo from the background universe. The behaviour and shape of $\gamma_\rho(r)$ in this region is in qualitative agreement with other work (e.g. Diemer, Kravtsov, 2014b; Adhikari et al., 2014; More et al., 2015).

At all radii within the splashback radius, we see that larger values of n_s lead to steeper density slopes. Recall that these plots are at fixed mass and redshift, we are therefore not studying haloes of the same age or equivalent accretion histories. The results are therefore not necessarily directly due to the change in the slope of the initial power spectra, as discussed shortly.

It appears that the differences in logarithmic slope for different values of n_s are primarily just an amplitude offset, suggesting that the density profiles remain approxi-

mately self similar but with different concentrations. Further out, near and beyond the splashback radius, there is a much more complicated dependence on n_s . For example, the radius at which the splashback feature occurs (i.e. the minima of γ_ρ) seems to be a non-monotonic function of n_s . Similarly, the logarithmic slope beyond the splashback radius has a complicated dependence on n_s with no easily discernible trend, although there are weak hints that the logarithmic slope past the splashback radius grows more slowly for larger n_s .

If we now look at the other columns (blue, green and purple), we see the same key features described above, but to variable degrees. The inner density profile of the middle left panel (matched initial amplitude) is almost identical with the equivalently matched simulations in the left panel. Similarly, the splashback radii occur at roughly the same location but the effect is stronger in this case, with steeper minimum slopes. Looking at the middle right panel, which corresponds to variable n_s but with a *Planck* pivot that effectively decreases the variation in the initial amplitude of the power spectra at modes sampled in the box, we see that the qualitative dependence on n_s is the same (more cuspy inner profiles with increased n_s , the splashback radius having a non-monotonic dependence on n_s , etc) but to a milder degree than seen in the left panel. The right panel, which corresponds to the $k_{pivot} = 1h \text{ Mpc}^{-1}$ suite all with similar initial amplitudes, shows that the density profiles are almost identical with indistinguishable inner slopes and only slight differences at larger radii. The general trend at high radii for this suite (purple) is for the higher n_s values to have steeper slopes out to the splashback radius.

With the middle left panel being broadly indistinguishable from the fiducial suite, the middle right panel exhibiting the same dependence on n_s but to a more subdued level and the right panel being broadly independent of n_s , it can be concluded that the dominant effect is due to the change in amplitude of the initial power spectra at modes sampled within the box, as opposed to changes in the slope of the initial power spectra. This is not to say that changes in the shape have no effect whatsoever, as shown in other works (e.g. Dalal et al., 2010; Diemer, Kravtsov, 2015; Ludlow, Angulo, 2016) and as I will discuss later in Section 3.4.

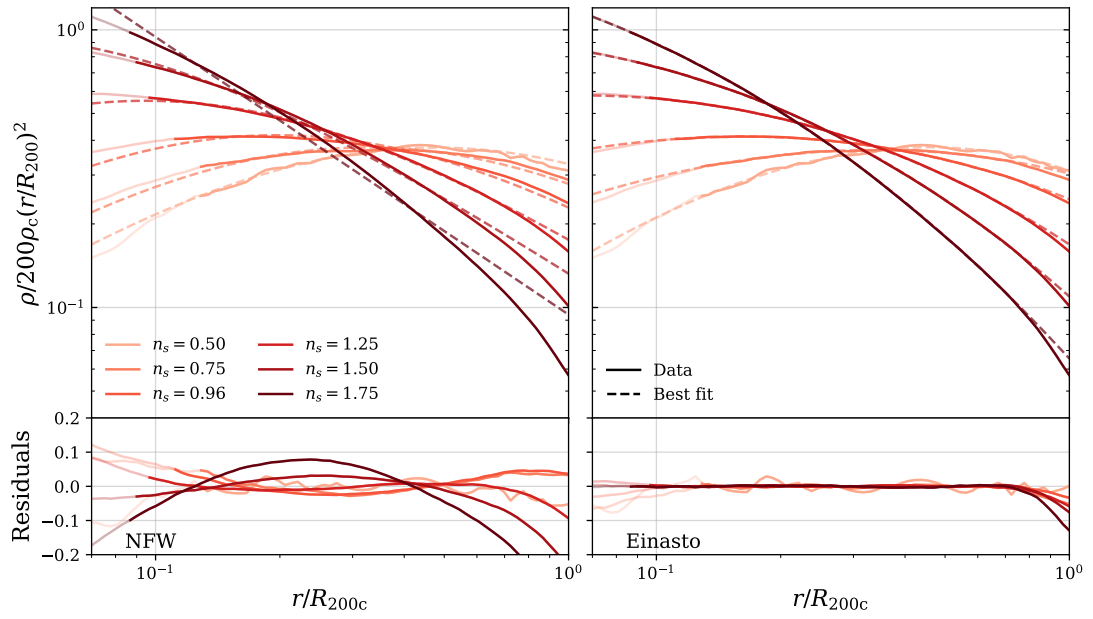


Figure 3.4: Top panels show the density profiles of the WMAP pivot cosmology with variable n_s , see legend. This is identical to the top left panel of Fig. 3.3, apart from multiplying by $(r/R_{200c})^2$ to reduce the dynamic range. I have then fit each profile with either a NFW (left) or Einasto curve (right), allowing both the scale radius and shape parameter to vary when fitting the Einasto profile. The fitting routine minimises the figure of merit, ψ^2 , and is only fit over the range where $r/R_{200c} < 0.7$, to avoid fitting to the splashback radius, and above the convergence radius. On the bottom panels I show the fractional residuals, $(\rho_{\text{fit}} - \rho)/\rho$, from this fit. The NFW form breaks down for runs with large n_s (corresponding to large amplitudes at $k = 1h \text{ Mpc}^{-1}$).

One particularly interesting result seen here is the exact values of the logarithmic slope. At the outer radii, but within the splashback radius, we see in some cases the slope reaches particular steep values, with slopes of $\gamma_\rho(r) \approx -3.5$ in the most extreme cosmologies. By definition, the asymptotic outer slope of an NFW profile is $\gamma_\rho = -3$. This, therefore, indicates that these density profiles will not be well fit by an NFW profile. Indeed this is the case, as I show in Fig. 3.4.⁵ It is worth highlighting that this is in the radial regime that for ‘normal’ cosmologies an NFW profile would be a good fit for stacked relaxed halos. Although these profiles cannot be fit with an NFW profile they can be well fit by an Einasto profile, see Fig. 3.4. Note that it is not surprising that an Einasto profile fits the profiles better, as it has an additional free parameter and, unlike the NFW profile, there is no finite limit on the inner or outer slope.

It is interesting to note that, if one *assumes* an Einasto profile instead of an NFW form, then such steep logarithmic outer slopes are expected within r_{200} for haloes that are sufficiently concentrated. The logarithmic slope of an Einasto profile can be written as $\gamma_\rho(r) = -2(cr/R_{200c})^\alpha$. Hence, for a profile with $\alpha = 0.16$ it would be expected that the slope of density profile to be steeper than -3 within R_{200c} if $c > 12.6$. Additionally, for $\gamma_\rho(r = 0.6R_{200c}) = -3.5$ (the most extreme case in the simulations), one requires $c \approx 50$, which is consistent with the concentrations measured (see Section 3.4).

It has been shown in other work that an Einasto profile is a better fit to the density profiles of DM haloes than and NFW, even with a fixed shaped parameter (Navarro et al., 2004; Merritt et al., 2006; Navarro et al., 2010a; Wang et al., 2019). The key result here is not that the Einasto provides a better fit, but that the outer asymptotic slopes have $\gamma_\rho < -3$, which is incompatible with the NFW form. The strong deviations from the NFW form appears to be at odds with some literature that state it is independent of changes to the initial power spectrum (e.g. Moore et al., 1999; Reed et al., 2005; Wang, White, 2009). This statement is usually based upon work that has studied cosmologies with differently shaped power spectra to Λ CDM; such as a strict power law or that

⁵See Section 3.4 for details of how the best fit parameters are obtained, as well as the figure of merit used.

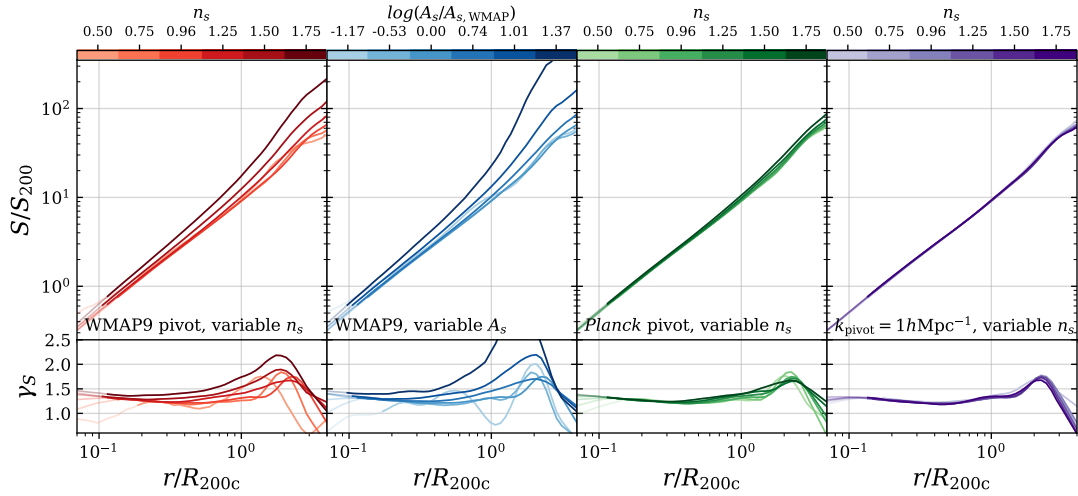


Figure 3.5: Entropy profiles of haloes in the mass range $M_{200c} = 10^{13} - 10^{13.5} h^{-1} M_{\odot}$. In the top panels is plotted the entropy, defined as $S(r) = (\rho/\sigma^3)^{-2/3}$, normalised by a ‘virial’ entropy, $S_{200c} = (200\rho_{\text{crit}}/v_{\text{circ},200c}^3)^{-2/3}$. The bottom panel shows the logarithmic slope of those profiles, $\gamma_S(r) = d(\ln(S))/d(\ln(r))$. See Fig. 3.3 for a description of the general structure of the figure. In general it is observed that the slope of the entropy profiles are not constant and in general depend on the underlying cosmology. Similar to the density profiles, the dominant factor in determining the entropy profiles is the amplitude of the linear power spectra at an associated k -mode.

associated with hot and warm dark matter. The main differences between these works and my own appears to be the amplitudes of the initial power spectra. In this work the most extreme cases are seen in the simulations with the largest initial amplitudes, while other works have predominantly fixed the amplitude (usually through σ_8).

3.3.2 Stacked entropy profiles

In Fig. 3.5 I show the stacked entropy profiles of the various suites of simulations. Haloes are stacked by taking the median entropy of individual haloes in units of r/R_{200c} . The colour scheme and ordering of the panels in the plot are identical to that of Fig. 3.3.

It is apparent that the entropy profiles in Fig. 3.5 are much more similar to one another than the density profiles and that these profiles are much closer to being scale independent. Let us focus initially on the fiducial suite (left panels). As noted previously in the literature the entropy profiles appear to have a simple power law form

at smaller radii. It is clear that the inner logarithmic slope is dependent on n_s , highlighting that the slope of the power law does not appear to be a constant in this suite. As discussed later, in general the slope of the entropy profiles exhibit a clear mass dependence and are *not* a universal constant. It also appears that for the individual simulations the inner logarithmic slopes are not exactly constant with slight radial dependences, as such the entropy profiles are not a perfect power law.

At small radii the slopes are approximately constant but a sharp spike is observed at larger radii, this feature corresponds to the splashback radius. The splashback radius is therefore not only a feature in the density of a halo but also in its entropy (or, equivalently, its phase-space density). The entropy profiles of DM therefore exhibit very similar behaviour as the true entropy of gas in galaxy clusters: approximately power law behaviour within R_{200c} and a sharp increase at high radii. In clusters this feature in the gaseous entropy corresponds to the outer shock radius and not directly to the splashback radius (as the DM entropy does), however, the two are strongly linked as discussed in Lau et al. (2015). Studying the density and velocity dispersion profiles individually the increase in entropy gradient at the splashback radius is predominantly due to the change in the gradient of the density profile, as opposed a change in the gradient of the velocity dispersion profile.

Interestingly, it can be seen in the logarithmic slope that the simple power law nature of the entropy profiles changes somewhat before the splashback radius, as γ_S increases noticeably before the spike corresponding to the splashback radius. This behaviour has been noted before in the literature (see for instance Ludlow et al. 2011) and is actually predicted by secondary infall models (Bertschinger, 1985). In these models this break in the power law at higher radii is caused by outer mass shells that have yet to be fully virialised and reach stable orbits.

When looking at the other sets of simulations (blue, green and purple lines) we see the same qualitative behaviour as for the density profiles. The variable n_s with WMAP pivot (left) and matched A_s (middle-left) behave almost identically, the *Planck* pivot (middle-right) has the same qualitative behaviour as the other two but to a milder degree, and the $k_{\text{pivot}} = 1h \text{ Mpc}^{-1}$ (right) are almost all identical with

indistinguishable inner behaviour but with slightly different outer profiles.

It appears that the inner slope of the entropy profiles are, in general, dependent on changes to the initial power spectra. The inner slopes vary in the range $\gamma_S \approx 1.2$ – 1.4 with most simulations exhibiting a slight increase in logarithmic slope to lower radii. These values are within the range quoted in the literature (e.g. Taylor, Navarro, 2001; Dehnen, McLaughlin, 2005; Faltenbacher et al., 2007). These results therefore suggest that the entropy profiles are, in general, not precisely simple power laws within the splashback radius. Instead the logarithmic slopes have a slight radial dependence. This appears to be consistent with claims from previous work (e.g., Nadler et al. 2017) that the PPSD profiles have slopes that vary mildly with radius over the range sampled by simulations.

Although a simple power law does not provide a perfect description of the shape of the entropy profiles, it does provide a reasonably good approximation over the ranges that sampled. As such, I fit the entropy profiles with simple power laws to look at the dependence on mass and other factors, in Section 3.4.

3.3.3 Stacked velocity dispersion profiles

In Fig. 3.6 I present the stacked total velocity dispersion, σ and velocity anisotropy profiles, β , as a function of radius, see Section. 3.2.5 for definitions. The structure of the plot and which colours correspond to which simulation are identical to that of Fig. 3.3.

We will again focus our attention on the fiducial suite of simulations first (left panels in red). Looking at the total velocity dispersions (top panel) we can see that larger values of n_s result in velocity dispersion profiles that have larger inner velocity dispersions and smaller values at large radii (and vice-versa for smaller n_s). This is in qualitative agreement with what would be expected from equilibrium arguments such as Jeans theory, in order to support the changes in the mass structure discussed in Section 3.3.1. Interestingly, there does not appear to be any obvious feature in the velocity

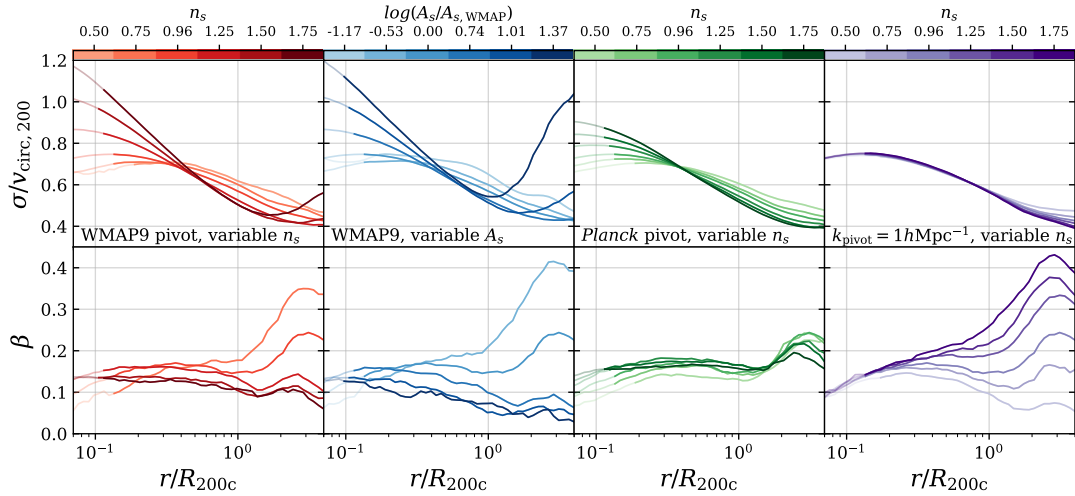


Figure 3.6: Stacked velocity dispersion and velocity anisotropy profiles of haloes in the mass range $M_{200c} = 10^{13} - 10^{13.5} h^{-1} M_{\odot}$. In the top panels is plotted the total velocity dispersion while the bottom panel shows the velocity anisotropy, $\beta = 1 - \sigma_T^2/\sigma_r^2$. See Fig. 3.3 for a description of the general structure of the figure.

dispersion profiles corresponding to the splashback radius. Although not shown here, such a feature can be seen when looking at the logarithmic slope of the *radial* velocity dispersion. That this feature is most obvious in the logarithmic slope of the profile agrees with the observed behaviour of the density distribution. The feature only being dominant in the radial velocity dispersion and not the total velocity dispersion is similarly expected; the splashback radius represents the first apocenter when the particles turn around we would expect little change to the angular velocities but a significant effect on the radial component.

The velocity dispersion profiles for the rest of the simulations (middle-left, middle-right and right) exhibit the same general trends seen in the density profiles (see Fig. 3.3). The fiducial and matched amplitude suites behave almost the same while the suite that uses a *Planck* pivot point exhibit the same trends to a milder degree and the $k_{\text{pivot}} = 1 h \text{Mpc}^{-1}$ suite are almost indistinguishable in the inner radii with only slight differences beyond R_{200c} .

Looking at the velocity anisotropy profiles (bottom) the differences between the simulations is not as clearly pronounced as the velocity dispersion. The approximate inner values, $\beta \sim 0.1 - 0.2$, are consistent with that found in previous work (e.g. Ludlow

et al., 2011). The inner behaviour of β is approximately constant with larger values of n_s leading to more isotropic particle orbits, except for $n_s = 0.75$ that reverses this trend. At large radii, the velocity anisotropy increases strongly as we transition into a regime where matter is being actively accreted onto the halo. The small inner differences in β suggest that haloes in the different simulations are roughly in the same dynamical state but with different density profiles. However, the more significant differences at large radii strongly suggest that they are accreting matter in different ways. It is also clear from the results of the $k_{\text{pivot}} = 1h \text{ Mpc}^{-1}$ suite shown in Fig. 3.3 and Fig. 3.6 that the anisotropy-density slope relation is not universal as claimed by some works (e.g. Hansen, Moore, 2006).

The velocity anisotropy profiles between the fiducial model and matched amplitude behave very similarly to the rest studied previously; broadly agreeing with the same amplitude differences but slightly different radial dependencies. The two suites with smaller amplitudes (green and purple) have much clearer radial profiles with a weakly parabolic-shaped curve as opposed to the roughly constant profiles seen for the two other suites. Interestingly, the suite of simulations with the most similar β profiles is that which adopts a *Planck* pivot instead of the $k_{\text{pivot}} = 1h \text{ Mpc}^{-1}$ suite, the opposite trend of what was seen for the density, entropy and velocity dispersions profiles. It seems as though the inner behaviour of the $k_{\text{pivot}} = 1h \text{ Mpc}^{-1}$ simulations is very similar but the outer dependence, but within the virial radius, on n_s is drastically different, with the main change arising from the radius where β begins to quickly increase.

This highlights that, even though the density and velocity dispersion profiles are almost identical between the different values of n_s , the haloes are in different dynamical states and growing in distinctly different ways. The suite that adopts a *Planck* pivot (middle-right panel), on the other hand, has clearly different inner β values but a very similar outer behaviour.

There are two interesting features in all β profiles occurring. The first feature occurs at roughly R_{200c} , which is most clearly seen in the *Planck* pivot and $k_{\text{pivot}} = 1h \text{ Mpc}^{-1}$ suites (right two panels). The feature correspond to where β suddenly increases. This feature likely demarcates an inner region of the halo that is in equilib-

rium from the region where matter is still being actively accreted. It is interesting that this radius roughly corresponds to R_{200c} but not precisely, with the $k_{\text{pivot}} = 1h \text{ Mpc}^{-1}$ pivot case (right) having profiles that under- and over-shoot R_{200} . This suggests that R_{200} gives a reasonable approximation to where the halo is in equilibrium, but it is not a perfect prediction. The second feature occurs at approximately $2R_{200c}$ where the β exhibit a local maxima, it is unclear what exactly this feature corresponds to but is likely related to the splashback feature observed in the density profiles.

3.4 Mass and peak height dependence

I have demonstrated that varying the initial power spectrum can have a significant effect on the density and entropy profiles of collapsed structures. Here I study how these profiles vary with halo mass and peak height.

The following figure of merit is minimised to obtain the best fit parameters for a given fitting routine and data set,

$$\psi^2 = \sum_i [\log(y_i) - \log(y_{\text{fit}})]^2. \quad (3.9)$$

Where y_i is the set of data (either density or entropy in this work) and y_{fit} the prediction from the specific profile used to fit.

Halo density profiles are fit with an Einasto curve (Einasto, 1965),

$$\rho_E(r) = \rho_{-2} \exp\left(-\frac{2}{\alpha} \left[\left(\frac{r}{r_{-2}}\right)^\alpha - 1\right]\right). \quad (3.10)$$

where r_{-2} is the radius where the logarithmic density slope is -2 , α is a shape parameter that quantifies how quickly the density varies as a function of radius. The normalisation, ρ_{-2} , is equal to the density at r_{-2} . Although I use the above equation to fit the profiles, I do not quote r_{-2} values but instead concentration, defined as $c = R_{200c}/r_{-2}$. A fixed $\alpha = 0.16$ is used when fitting these profiles as I find that when left to vary it clusters around this value but with significant scatter, it is also consistent

with values quoted in the literature (e.g. Gao et al., 2008b). Additionally, it is found that r_{-2} and α are strongly correlated, fixing α allows us to significantly reduce the noise while providing approximately the same values for r_{-2} . It is possible to leave α free when fitting (as is done in Chapter 4), this generally results in no difference in c at low masses and a slight decrease at higher masses. The scale radius, r_{-2} is not always resolved in these simulations, as can be seen in Fig. 3.3. Note that the inferred values of r_{-2} , and similarly c , presented in this work represent the best-fit values over the resolved radial range, whether r_{-2} is directly sampled or not.

To fit entropy profiles I use a power law,

$$S(r)/S_{200c} = \Delta_S (r/R_{200c})^\chi. \quad (3.11)$$

where Δ_S is a normalisation parameter, equal to the virial normalised entropy (S/S_{200c}) at R_{200c} , and χ is the exponent of the power law.

3.4.1 Mass dependence

In Fig. 3.7 I present the dependence of c and χ on halo mass, M_{200c} . I present here the normalisation of the entropy but not the density, ρ_{-2} , as it can be found through the overdensity definition of M_{200c} and R_{200c} , however Δ_S cannot. Each row shows a different parameter's dependence on mass, while each column represents the different set of simulations with colours consistent with the rest of the chapter. Note the left and middle-left panels do not have data plotted for the $n_s = 0.5$ case as there are too few haloes above the mass cut to examine the mass dependencies.

As before I will focus first on the fiducial suite, shown in the left column of Fig. 3.7. Looking at the concentration, I see the same bulk trends as found for the stacked density profiles (see Fig. 3.3); larger values of n_s , corresponding to larger amplitudes in this suite, results in haloes that are more concentrated, with values as high as $c \approx 70$. For all values of n_s , the concentration monotonically decreases with mass and in general the concentration–mass relations for the different cosmologies

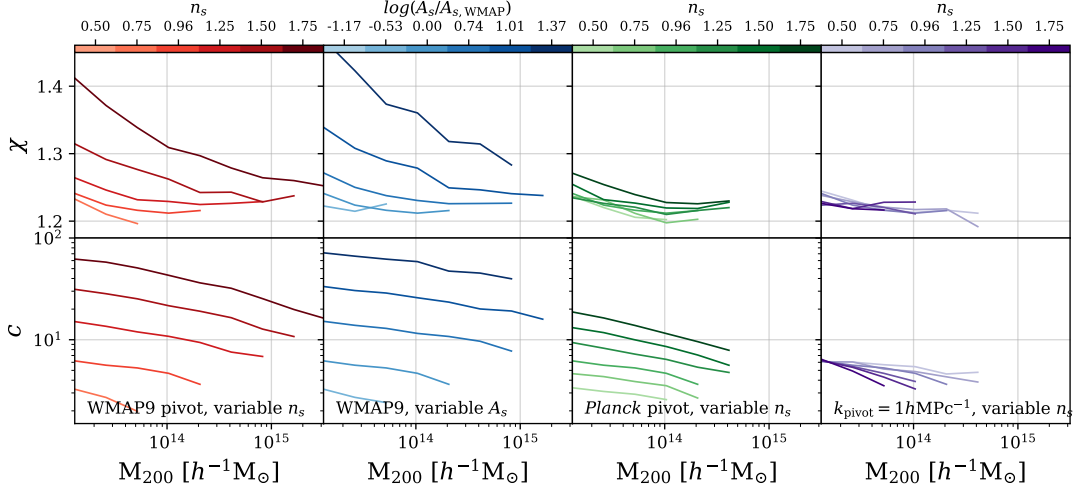


Figure 3.7: Fitted parameters as a function of mass. Haloes with greater than 2000 particles are stacked in mass bins of 0.3 dex, only bins with more than 15 haloes are plotted. The resulting stacked density and entropy profiles are then fit by minimising ψ^2 , see Eqn. (A.7). There are two fitted parameters shown, halo concentrations, c , and entropy power law exponent χ . Each row shows one of these parameters as a function of halo mass, M_{200c} , while each column represents the four suites of simulations; WMAP pivot variable n_s (left), matched A_s (middle-left), *Planck* pivot point with variable n_s (middle-right) and $k_{\text{pivot}} = 1 h^{-1} \text{Mpc}^{-1}$ variable n_s (right). The different shades represent the particular value of n_s , or A_s , see colourbar.

have similar slopes but distinctly different amplitudes.

I now focus on the mass dependence of the entropy profiles in the various simulations. Firstly we notice that, in general, the slope, χ , does depend on halo mass. However, for the standard $n_s = 0.96$ case, the dependence on mass is quite mild with an almost constant value of $\chi \approx 1.21$, in agreement with previous studies on the PPSD profile (see the Introduction). For all simulations studied χ monotonically decreases with mass, with larger n_s resulting in a stronger mass dependence and values of χ at the low mass end distinctly larger than 1.25 in the more extreme cosmologies. The fact that the slope and its dependence on halo mass varies with n_s in these suites demonstrates that there is nothing particularly special about the $\chi \approx 1.25$ result from the standard cosmology (i.e., with $n_s = 0.96$), calling into question the perceived fundamental nature of the, previously, apparent universality of the PPSD.

As mentioned previously Δ_S , the amplitude of the normalised entropy profiles, is not specified by the overdensity definition of halo mass and radius, i.e. R_{200c} and M_{200c} , unlike the density normalisation. As such I have additionally studied how Δ_S

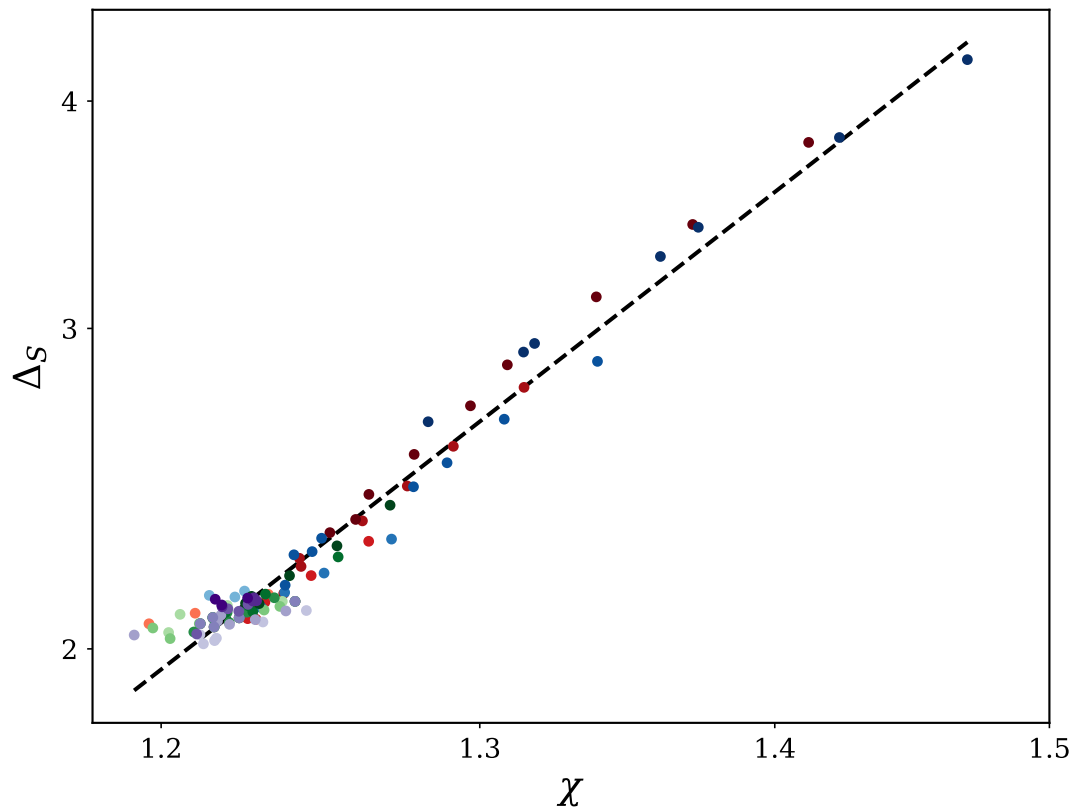


Figure 3.8: Entropy normalisation, Δ_S , as a function of power law exponent, χ , see Eqn. 3.11 for definition, for all cosmologies sampled. Each data point represents a mass bin with the colour denoting the particular cosmology, as originally specified in Fig. 3.1. The black dashed line represents the best fit power law relation of $\Delta_S = 0.94\chi^{3.92}$. There is no discernible dependence on the initial power spectra and the relation appears to be universal.

varies in these cosmologies. Recall that Δ_S is defined such that it is the amplitude of the virial normalised entropy at R_{200c} , see Eqn. 3.11. From Fig. 3.5 it is clear that for haloes with a larger slope, χ , correspond to larger values of Δ_S . Indeed, this is a general feature of all of the cosmologies studies here with there appearing to be a universal relation between the entropy slope and normalisation that is independent of primordial amplitude or spectral index, as shown in Fig. 3.8. The relation between χ and Δ_S is well fit by

$$\Delta_S = 0.94\chi^{3.92}. \quad (3.12)$$

Looking at all sets of simulation we can see that the dominant behaviour of c and χ is due to the amplitude change of the primordial power spectra on scales sampled in the box, as opposed to the shape (n_s) change of the initial power spectra. The fiducial model (left most panel) and matched amplitude (middle-left) have the closest c and χ values for equivalent masses, while the *Planck* pivot suite (middle-right) show the same general trends but to a milder degree. The $k_{\text{pivot}} = 1h \text{ Mpc}^{-1}$ suite (right most panel) has the most similar dependence on mass between different values of n_s , with roughly the same amplitude but distinctly different detailed dependencies. Although the bulk of the changes in the trends appear to be due to the amplitude change in the primordial power spectrum, the fiducial and matched A_s suites do have different mass dependencies. In general it seems that larger initial amplitudes lead to larger values of c and χ ; for $n_s > 0.96$ the matched amplitude simulations have more power for smaller k corresponding to larger massed objects, and vice-versa for $n_s < 0.96$. The results here are then consistent with the bulk offsets, at high masses the matched A_s simulations have comparably larger c and χ values than the fiducial suite.

The concentrations in the $k_{\text{pivot}} = 1h \text{ Mpc}^{-1}$ suite exhibit a particularly notable feature that they all converge at $M_{200c} \approx 10^{13}h^{-1}M_{\odot}$, see bottom right panel of Fig. 3.7. This is, in part, by construction. The pivot point was specifically chosen to correspond to haloes of approximately this mass. The interpretation is therefore that the dominant factor in setting the concentration of a halo is the amplitude of the as-

sociated k-mode. It is plausible that the deviations above $M_{200c} \approx 10^{13} h^{-1} M_{\odot}$ and different dependences on mass are predominately due to the amplitude of the power spectra being different in $k > 1 h \text{ Mpc}^{-1}$ (see Fig. 3.1) as opposed to differences in the slope directly.

3.4.2 Peak height dependence

I now focus on the dependence as a function of peak height, which is defined as

$$\nu = \frac{\delta_c}{\sigma(M, z)}. \quad (3.13)$$

where δ_c is the condition for collapse⁶ in the spherical collapse model (Gunn, Gott, 1972a) and σ is the RMS of density fluctuations. $\sigma(M, z)$ itself is calculated from the linear power spectra, $P(k)$, by

$$\sigma^2(R) = \frac{1}{2\pi^2} \int_0^{\infty} k^2 P(k) |\tilde{W}(kR)|^2 dk. \quad (3.14)$$

$\tilde{W}(kR)$ is the Fourier transform of a spherical top hat function. Halo mass is converted to a radius by projecting onto a sphere with the same average density as the universe, i.e. $R^3 = M/(4/3\pi\rho_m)$, and then peak height calculated using Eqn. (3.13). The intuitive interpretation of peak height is to quantify, on average, how old and how rare a halo is, with larger values of ν corresponding to rarer, younger objects.

It is well established that for a given cosmology the c - M relation varies with redshift and when comparing different cosmologies this behaviour is even more complex. However, previous work has shown that the c - M - z relation can approximately be reduced to a peak height-concentration relation, effectively removing the redshift dependence (e.g. Prada et al., 2012; Ludlow et al., 2014). Although it is clear that peak height is the dominant factor in setting the halo concentration there are complex secondary terms required to accurately predict the concentration at all redshifts for a given cosmology. Halo concentration is expected to scale much more closely with

⁶I take $\delta_c = 1.686$ and ignore the mild redshift and cosmology dependence.

peak height than mass for two main reasons; (i) in calculating peak height any change to the cosmology is implicitly accounted for by integrating over $P(k)$ (see Eqn. (3.14)); and (ii) the formation time and age of a halo, which is intimately linked to the concentration (e.g. Bullock et al., 2001b; Wechsler et al., 2002; Zhao et al., 2003), is expected to scale with peak height and not, in general, with mass. Although the dominant factor in setting the density profiles of a halo is indeed the peak height, there is a residual dependence on the shape of the power spectrum as shown in Diemer, Kravtsov (2015), leading us to study the dependence on n_s directly.

In Fig. 3.9 I present how the fitted density and entropy parameters, c and χ , vary with peak height, ν , at $z = 0$. The structure of the plot is identical to that of Fig. 3.7. Let us first focus on how these parameters vary for the two suites that are dominated by amplitude changes to the initial power spectrum (left and left-middle panels). We see that for these suites all of the fitted parameters are close to a single function of ν , with the large amplitude offsets seen when plotted as a function of mass removed. The c - ν relation appears to be closest to a single function in the suite with fixed n_s and matched A_s , however all simulations exhibit slight but clearly different dependences on ν .

It is clear in all suites that peak height is the dominant term in setting χ and c , however, there is a secondary dependence observed for both changes to A_s and n_s . Focusing on the parameters in the suites dominated by a shape change to the power spectra (right-middle and right panels) we see that they are very clearly not described by a single function of ν , with the $k_{\text{pivot}} = 1 \text{ h Mpc}^{-1}$ suite becoming even more stratified than when plotted as a function of mass. This stratification and strong dependence on n_s , as well as ν , is most clearly seen in the concentrations. I therefore conclude that, in general, the concentration–peak height relation is a function of A_s and n_s , but is more sensitive to changes in the shape, or slope, of the power spectra than amplitude differences. The result here that the $c - \nu$ relation depends strongly on the shape of the power spectra is in qualitative agreement with the works of Diemer, Kravtsov (2015) who showed that for scale free cosmologies concentration has a different dependence on peak height for different slopes of the linear power spectra.

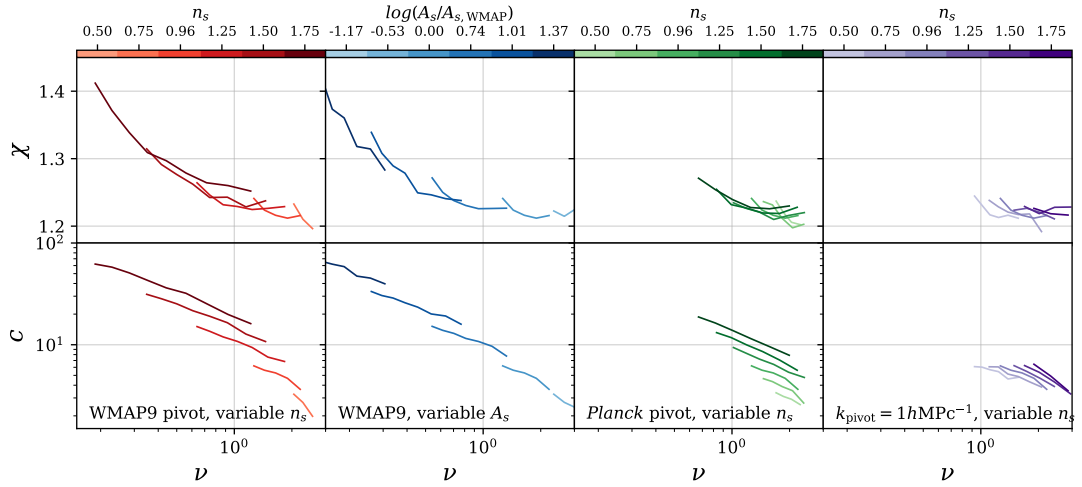


Figure 3.9: Fitted parameters, halo concentration, c , and entropy power law exponent, χ , as a function of peak height, ν . See Eqn.(3.13) for the definition of ν . The plot, and associated analysis, is identical to Fig. 3.7 but with the mass converted to peak height for each different cosmology. In general amplitude changes to the primordial power spectra are well described by peak height, however there are secondary ‘shape’ changes to the linear power spectra that are not accounted for by a change in peak height.

Although I have not studied how α , the shape parameter in the Einasto profile, varies with mass or redshift in these cosmologies same general behaviour would be expected that is observed for concentration. Ludlow, Angulo (2017) showed that, again, for a scale free universe the α - ν relation is redshift independent for a given cosmology but does depend on the slope of the linear power spectrum.

3.4.3 Interpreting A_s as a change of redshift

The results observed in the suite with only an amplitude change to the primordial power spectra are qualitatively similar to what is seen for a single cosmology at multiple redshifts. This is not surprising as the difference in the linear power spectra between different redshifts is purely an amplitude one. This is often expressed through the linear growth factor, $D(z)$,

$$P(k, z) = D^2(z)P(k, z = 0). \quad (3.15)$$

Therefore cosmologies with different values of A_s will have identical linear power spectra at different redshifts. This suggests that the effects of changes to the amplitude seen in Fig 3.7 & 3.9 can be expressed as a change in redshift. Quantitatively remapping changes in A_s to a change in redshift would involve the detailed modelling of the secondary effects on concentration mentioned previously, which is beyond the scope of this work. However, I can still discuss the qualitative expectations. In general it is expected that universes with $A_s < A_{s,\text{WMAP}}$ at $z = 0$ to look very similar to our own Universe at higher redshift. Similarly, cosmologies with $A_s > A_{s,\text{WMAP}}$ at $z = 0$ would be expected to be like our own Universe in the future. Even though this is in general true it is found that the cosmologies with $A_s > A_{s,\text{WMAP}}$ sampled in this work are actually more extreme than our own universe will ever be. This is due to the accelerated expansion, caused by the cosmological constant, suppressing the growth of structure to such a degree that our own Universe will never reach as large amplitudes as sampled by some of the cosmologies in this work (i.e. $D_{\text{max}}^2 < A_s/A_{s,\text{WMAP}}$).

3.5 Accretion histories and (semi-)analytic models

It is generally thought that concentration is predominantly determined by the formation time of a halo (e.g., Eke et al., 2001a; Bullock et al., 2001b; Wechsler et al., 2002). Halo formation is sometimes described as an inside out process, (e.g. Reed et al., 2005; Zhao et al., 2003; Hoffman et al., 2007; Ludlow et al., 2013), with a collapsed bound core forming early on in the universe with later accretion not penetrating this inner core and instead relaxing to larger radii. Under this interpretation, haloes that form earlier will be more concentrated. As, on average, low-mass haloes form earlier than high-mass haloes, this mechanism naturally accounts for the qualitative trend of the c - M relation in a standard cosmology.

In this section I will check whether this interpretation of the c - M relation agrees with these results for more extreme variations of the initial conditions by directly comparing the accretion histories and formation times of haloes in these simulations. I also compare the predictions of halo concentration from a range of recent models (Correa

et al., 2015; Ludlow et al., 2016; Diemer, Joyce, 2019) to the results seen in this work.

3.5.1 Mass accretion and collapsed mass histories

I study here if the link between halo concentration and mass accretion history (MAH), and similarly the collapsed mass history (CMH) (both quantities are defined below), still holds in these extreme cosmologies.

The MAH and the CMH are two separate but complementary statistics that reduce the full merger history of haloes into more tangible quantities. The MAH is defined by following the most massive progenitor at each snapshot; how the mass, M_{200c} , of these progenitors varies with redshift is then the MAH. The MAH is a useful statistic for the growth of a halo, highlighting how its most massive branch of its merger tree grows with redshift. It does not, however, encapsulate the full spectrum of accreted collapsed structure, particularly ignoring smaller haloes that contributed to the final halo. The CMH, on the other hand, better encompasses the full plethora of accreted structure. The CMH is defined as all progenitors that have collapsed by redshift, z , above a certain fraction, f , of the final mass. In this work I use $f = 0.02$, but this is in principle a free parameter in defining the CMH (see Ludlow et al. (2016) for a discussion of how the CMH changes with f). To calculate the stacked MAH I take the median from all haloes in the quoted mass range, while for the CMH I take the mean. All merger trees are generated using the algorithm presented in Jiang, Bosch van den (2014), using the $M_{200,c}$ of the central halo to keep the mass definition consistent.

In Fig. 3.10 I present the MAH and CMH histories for the various suites of simulations as a function of critical density, the mass range sampled is the same as that of Fig. 3.3–3.6 so is directly comparable to them. The colours are the same as previous figures, with the line style denoting either the MAH or CMH (see legend). Initially focusing on the fiducial suite, left panel (red), the results are what is expected from the current understanding; the most cuspy haloes correspond to those that formed earliest. The general trend is for larger values of n_s to lead to haloes that collapsed earlier, these haloes then accrete most rapidly in the earlier universe before growing more slowly

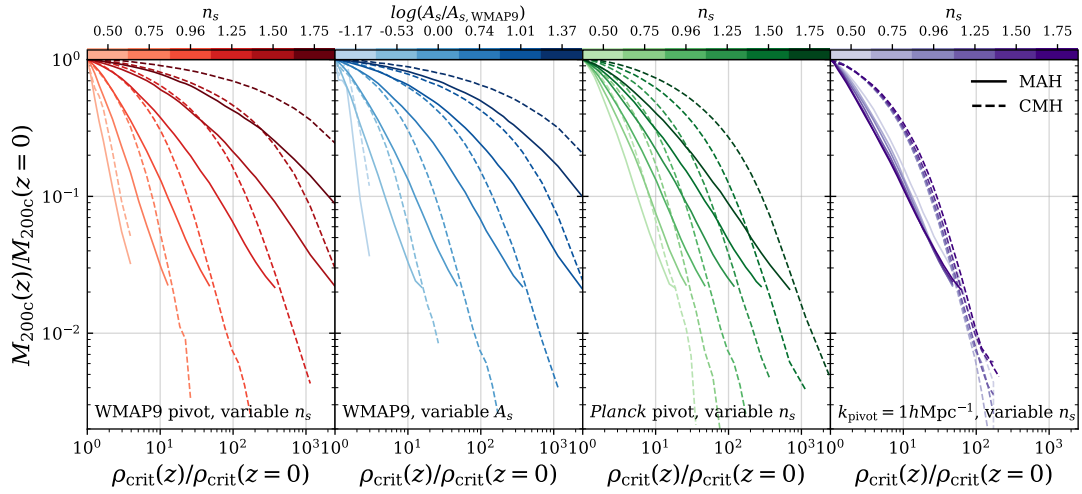


Figure 3.10: The normalised MAH and CMH plotted as a function of critical density, for stacked haloes in the mass range $M_{200c} = 10^{13} - 10^{13.5} h^{-1} M_{\odot}$. See 3.5.1 for the definition of MAH and CMH. The different panels and colours represent the different suite of simulations, see label in bottom left of each panel. The shades of each colour represent the value of n_s , or matched A_s , used for the simulations, see colourbar. The different line-styles represent either the MAH or CMH, see legend. The changes to the MAH and CMH of haloes is in qualitative agreement with what is expected from the change in their concentration. Haloes with higher (lower) concentrations are those that formed earlier (later) with subsequent slower (faster) accretion today.

today, and vice versa. This difference in growth is clearly dominated by the amplitude change to the initial power spectra as opposed to the shape change of this suite. The fact that the largest values of n_s are accreting the slowest today implies they are more relaxed haloes, highlighting that haloes with density profiles most different from NFW and with the steepest outer slopes are actually those which are most relaxed. Looking at the other suites we again see changes in qualitative agreement with the differences in the density profiles: the matched amplitude simulations, middle left (blue), exhibit very similar changes to the MAH and CMH compared to the fiducial suite with the same bulk offset but slight different redshift dependences, the suite with *Planck* pivot point, middle right (green) exhibits the same general trends with n_s but to varying degree, while the $k_{\text{pivot}} = 1 h \text{ Mpc}^{-1}$ suite exhibit almost the same MAH and CMH. These results of this work appear to be consistent with the picture proposed in Dalal et al. (2010). While the dominant term appears to be the amplitude of initial power spectra, i.e. peak height, the initial collapse and subsequent halo concentration is sensitive to the shape of the power spectra, hence the c - ν relation not being universal.

It seems that the observed trends in the density profiles discussed in Section 3.3.1 are consistent with the current consensus as to their origin, with haloes more concentrated forming earlier when the universe was much denser. The key qualitative changes between the MAH/CMH match well those of the density profile, however it is unclear if this is in quantitative agreement of current models. I discuss this next.

3.5.2 Comparison to analytic models

In this section I compare the results of this work to three notable works that aim to predict halo concentrations for a general cosmology. Specifically the works of Correa et al. (2015), Ludlow et al. (2016) and Diemer, Joyce (2019). The predictions from Ludlow et al. (2016) and Diemer, Joyce (2019) are generated using the publicly available python package `COLOSSUS` (Diemer, 2018), while the predictions Correa et al. (2015) are generated uses the publicly available `COMMAH` package. In Fig.3.11 I compare the predictions of the aforementioned models to those observed in these simulations. Below I discuss each model in turn.

Comparison to the model of Correa et al.

The model of Correa et al. predicts halo concentration given a mass and redshift for any general Λ CDM cosmology. There are two key parts to the model; the prediction of the MAH in a general cosmology using extended Press-Schechter theory and an empirical relation mapping a given MAH to a halo concentration found from simulations by Ludlow et al. (2014). This empirical relation was found studying the Millennium simulations (Springel et al., 2005b; Boylan-Kolchin et al., 2009; Angulo et al., 2012), which are at a fixed cosmology but variable resolution. I refer the reader to Correa et al. (2015b,c); Correa et al. (2015); Ludlow et al. (2014) for details.

In the top panels of Fig. 3.11 I present the predicted $c-\nu$ relation (dashed lines) for the model of Correa et al. compared to the simulation results (solid lines). For the $n_s = 0.96$ cosmology, the analytic model accurately predicts the $c-\nu$, as is expected

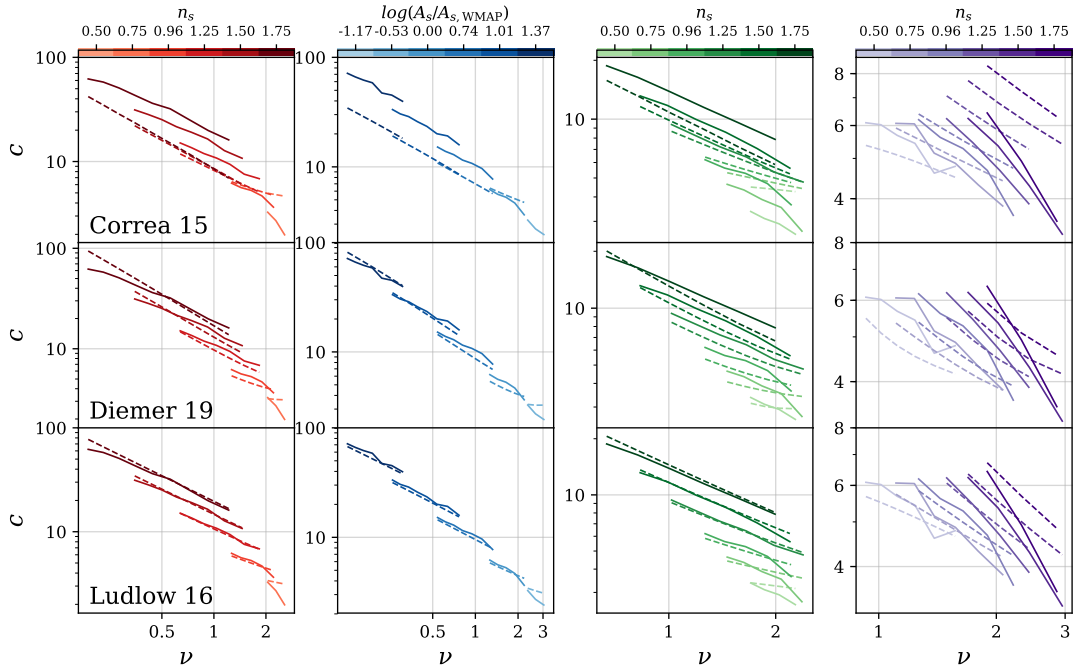


Figure 3.11: Comparisons between the predictions of Correa et al. (2015), Ludlow et al. (2016) and Diemer, Joyce (2019) to this work for the c - ν relation. Predictions from the various works are shown as dashed lines while the simulation results are shown in solid lines. Each column represents the different simulation suites with the shaded colour the value of n_s (or A_s). Each row is the predictions from the different models, see bottom left of left most panel. Unlike Fig. 3.9 I have used variable dynamic ranges to more easily highlight the differences.

from their work being tested and somewhat calibrated on a very similar cosmology. However, for cosmologies distinctly different from our own the predictions consistently disagree from the simulation results. In general it appears that for simulations with increased primordial amplitudes (darker red and blue lines) the concentration is under predicted while the opposite is true for the simulations with reduced primordial amplitudes. Studying the MAHs for the different cosmologies it appears that the prediction of Correa et al. don't agree with the results of this work (i.e. Fig. 3.10). In general it is found that for cosmologies with larger initial amplitudes the Correa et al. model predicts haloes to form later than is observed, vice versa for smaller initial amplitudes. The discrepancy in halo formation time is therefore in qualitative agreement with the differences in concentration observed in Fig. 3.11. I re-emphasise that all cosmologies other than $n_s = 0.96$ are well outside of observational constraints; as long as the predictions of these models are accurate for universes close to our own, which they appear to be, they can still be reliably applied/compared to observations.

Comparison to the model of Diemer & Joyce

The work of Diemer, Kravtsov (2015) studied scale free cosmologies, that being a universe with a power law linear power spectra, with differing slopes, n . They observed that at fixed n the $c-\nu$ relation is universal, but does in general depend on the slope of the power spectrum. These results are therefore in general agreement to the key features observed in Fig. 3.9; although n and n_s are not the same quantities they both represent a general ‘shape’ change to the power spectra. The interpretation of this result was that the concentration of a halo depends on its peak-height as well as the effective slope of the linear power spectrum at an associated k -scale. From these observations a semi-analytic model was created and calibrated against simulations with a range of cosmologies to predict the $c-M$ in a general cosmology at any redshift or mass. The cosmologies used for calibration include WMAP 7-yr, Planck15 and scale free cosmologies. Here I compare to Diemer, Joyce (2019) which is an updated version of the original Diemer, Kravtsov (2015) model, I refer the readers to the papers for detailed differences between the models.

In the bottom panel of Fig. 3.11 I show the predictions of Diemer, Joyce (2019) compared to the simulation results at $z = 0$. I have shown here the $c-\nu$ relation instead of $c-M$ as the model fundamentally works with peak-height as opposed to mass. For the two suites dominated by amplitude changes (left and middle-left panels) the predictions of the model are in very good agreement with the simulation results. There does appear to be a systematic amplitude offset from the predictions and the simulation results. The method used to estimate concentration in these simulations is different to the one they used when calibrating their model. The observed amplitude offset is qualitatively consistent with the expectation from different methods of determining halo concentration as well as choosing whether to include a relaxation cut or not (e.g. Child et al., 2018). However, when focusing on the suite dominated by a shape change to the initial power spectra, we see that the predictions of Diemer et al. do not reproduce the simulations particularly well. Specifically, their model does appear to match the amplitude but predicts a much flatter dependence on ν than seen in the simulations.

Comparison to the model of Ludlow et al.

In the work of Ludlow et al. (2016) they demonstrated that the concentration of a halo, in both a cold and warm dark matter (WDM) universe, can be directly linked to its CMH. This was shown to work in a range of cosmologies, both with CDM and WDM cosmologies with differently assumed particles masses using the COCO (Hellwing et al., 2016), Millenium (Springel et al., 2005b; Boylan-Kolchin et al., 2009; Angulo et al., 2012) as well as some additional Λ CDM cosmologies. From this observation a semi-analytic model was created to predict halo concentration for a general cosmology.

In the middle panel of Fig. 3.11 I show the predictions of Ludlow et al. (2016) compared to the simulation results. Very similar results are seen to the model of Diemer & Joyce; for cosmologies with higher concentrations, effectively higher initial amplitudes, the predictions match well the simulation results. For cosmologies with lower concentrations, particularly the $k_{\text{pivot}} = 1h \text{ Mpc}^{-1}$ suite, the predictions match the approximate magnitude but do not agree with the exact ν dependence. The model of Ludlow et al. does not include a turn up in concentration, unlike the Diemer & Joyce model, so the discrepancy at low concentration and large peak height appears to be independent of relaxation cuts. It is interesting that all models studied here essentially fail for this suite, it is not clear why this is the case and something I leave for future work.

3.6 Summary

In this work I have examined how changes in the primordial power spectrum of density fluctuations affect the internal structure of haloes in a collisionless universe. I have done this by varying the amplitude of fluctuations, A_s , the primordial spectral index, n_s , and the normalisation k scale (or pivot point), k_{pivot} , within the context of a Λ CDM model with a fixed expansion history. By varying these parameters systematically (see Fig. 3.1), I am able to isolate the impacts of amplitude and shape variations in the

initial power spectra on the properties of collapsed haloes. I find that when studying universes that deviate strongly from our own, some key results on the structure of dark matter haloes that have been assumed to be universal no longer hold true.

The main results of this study are as follows:

(i) The mass structure of collapsed haloes retains a memory of the primordial power spectrum (see Fig. 3.3). It is found that the NFW form which works well for haloes in simulations with CMB-normalised fluctuations, breaks down when the amplitude of initial density fluctuations is increased (see Fig. 3.4), these simulations correspond to haloes with small peak heights and early formation times. The NFW profile no longer offers a good description of halo density profiles in this regime due to their outer logarithmic slopes being steeper than $\gamma = -3$. An Einasto form works relatively well for all of the simulations investigated here.

(ii) The pseudo-entropy (or pseudo-phase space density) profiles can be described relatively well by a simple power law in all cosmologies studied here (see Fig. 3.5), however, the exponent is not a constant. A clear mass dependence is seen in many of the simulations (see Fig. 3.7). For the case of CMB-normalised power spectra, there is only a very mild mass dependence of the range sampled by the simulations, with roughly a constant value of $\chi \approx 1.22$, in agreement with previous studies.

(iii) The general physical picture identified in many previous studies that the concentration of dark matter haloes is tied to halo formation time continues to hold in all the simulations examined here (see Fig. 3.5). I find that the prediction for halo concentration of the models from Ludlow et al. (2016) and Diemer, Joyce (2019) in general match well the simulation results, particularly for cosmologies with much larger initial amplitudes to our own. However, in cosmologies with reduced primordial amplitudes, resulting in lower concentrations today, these models do not appear to accurately match the simulation results predicting much shallower dependence on peak height, ν , than observed (see Fig. 3.11).

(iv) It is found that the dominant effect on the density profiles of haloes, expressed through the concentration parameter, is due to changes to the amplitude of

the initial power spectra as oppose to the ‘shape’ (see Fig. 3.3 & 3.7). The effect of that changing the amplitude of the primordial power spectra has on halo concentration is broadly encapsulated by peak height, ν , but there are clear secondary effects (see Fig. 3.9). However, it is found that changes to the shape of the initial power spectra (studied here through the primordial spectral index, n_s) are not accounted for by peak height alone. The secondary effects observed for only an amplitude change are exacerbated when the shape also changes, resulting in peak height correlating poorly with halo concentration for the suites dominated by a shape change to the linear power spectra (see right most panel of Fig. 3.9).

Summarising the above, this work has demonstrated that the internal properties (mass structure and dynamics) of collapsed haloes retain a clear memory of the initial conditions of the universe. I again point out that the simulations presented here are fully in the context of Λ CDM, in terms of expansion history and the nature of dark matter (cold and collisionless). Thus, these results indicate that the apparent universality of previously reported results for Λ CDM (e.g., NFW or similar forms for the mass structure, a power law of specific form for the phase-space density/pseudo-entropy profiles) is mostly a consequence of starting from a narrow range of normalisations for the initial power spectra. This work provides important new results that link the initial conditions to the present-day structure of collapsed dark matter haloes and can provide an important test-bench for physical models of structure formation.

Chapter 4

Towards a universal model for the density profiles of dark matter haloes

This chapter appeared in Brown et al. (2022). The appendices for this work are in Appendix B.

It is well established from cosmological simulations that dark matter haloes are not precisely self-similar and an additional parameter, beyond their concentration, is required to accurately describe their spherically-averaged mass density profiles. I present, for the first time, a model to consistently predict both halo concentration, c , and this additional ‘shape’ parameter, α , for a halo of given mass and redshift for a specified cosmology. Following recent studies, I recast the dependency on mass, redshift, and cosmology to a dependence on ‘peak height’. I show that, when adopting the standard definition of peak height, which employs the so-called spherical top hat (STH) window function, the concentration–peak height relation has a strong residual dependence on cosmology (i.e., it is not uniquely determined by peak height), whereas the α –peak height relation is approximately universal when employing the STH window function. Given the freedom in the choice of window function, I explore a simple modification of the STH function, constraining its form so that it produces universal relations for concentration and α as a function of peak height using a large suite of cosmological simulations. It is found that universal relations for the two density pro-

file parameters can indeed be derived and that these parameters are set by the linear power spectrum, $P(k)$, filtered on different scales. I show that the results of this work generalise to any (reasonable) combination of $P(k)$ and background expansion history, $H(z)$, resulting in accurate predictions of the density profiles of dark matter haloes for a wide range of cosmologies.

4.1 Introduction

The mass density profile of dark matter (DM) haloes is a key prediction of the current concordance Λ CDM cosmology. The density distribution has been shown to depend both on the mass of a halo and redshift, with the precise dependencies being set by the cosmological parameter values that specify the initial conditions and expansion rate of the Universe (e.g. Frenk et al., 1988).

It has been shown in many previous studies that the density profiles of DM haloes can be reasonably well approximated by an NFW profile (Navarro et al., 1996b; Navarro et al., 1997):

$$\rho(r) = \frac{\rho_0}{(r/r_s)(1 + r/r_s)^2} \quad , \quad (4.1)$$

where r_s is the scale radius, often quoted as a concentration $c = R/r_s$ (where R is the halo radius, usually defined using a spherical overdensity definition), and ρ_0 is the normalisation, which can be constrained by the total mass of the halo. A key prediction of this formalism is that the structure of DM haloes, as a function of mass, requires a single free parameter, the scale radius or concentration. Consequently, many empirical and analytic models have been developed to try to accurately predict the concentration of haloes as a function of mass, redshift, and cosmological parameters (e.g. Bullock et al., 2001a; Eke et al., 2001b; Prada et al., 2012; Ludlow et al., 2014; Diemer, Kravtsov, 2015; Correa et al., 2015a).

Although it is common to describe the density profiles of DM haloes through a scale radius (i.e. a single parameter), it has been demonstrated that DM haloes are not perfectly self-similar and that a second parameter (other than concentration) is required

to accurately describe the density profiles. This is true for both individual and stacked density profiles (e.g. Gao et al., 2008a; Navarro et al., 2010b). The Einasto profile (Einasto, 1965) has been shown to better reproduce the density profiles observed in high-resolution simulations:

$$\ln(\rho(r)/\rho_{-2}) = -\frac{2}{\alpha} \left[\left(\frac{r}{r_{-2}} \right)^\alpha - 1 \right]. \quad (4.2)$$

Here r_{-2} is again a scale radius, defined to be the radius where the logarithmic slope $d \ln \rho / d \ln r$, is equal to -2 , and is therefore equivalent to r_s used in the NFW parameterisation. The parameter α is commonly referred to as the ‘shape’ parameter and describes how quickly the slope of the density profile varies as a function of radius. For $\alpha \approx 0.18$, the Einasto profile closely resembles an NFW form over radii typically sampled in cosmological simulations.

As shown in Gao et al. (2008a), the parameter α exhibits a clear dependence on both halo mass and redshift, and also has a dependence on the underlying cosmology as later demonstrated by Ludlow, Angulo (2017). Therefore, both c and α depend on mass, redshift, and cosmology, motivating a model that can consistently predict both parameters for a general cosmology. Compared to the halo concentration, the shape parameter has received relatively little attention in the literature and as such there does not yet exist a model aimed at predicting α for a general cosmology, only empirical models that predict the α - M relation for a specific cosmology (e.g. Duffy et al., 2008; Ludlow et al., 2013; Dutton, Macciò, 2014). Note that a significant number of models infer the concentration of haloes from simulations adopting a fixed shape parameter when fitting to the density profiles, which can lead to biased estimates of concentration (as the two parameters are not independent).¹ Clearly α and c should be modelled in a consistent way to be able to reliably predict the density profiles of DM haloes.

In this chapter I aim to link changes to both the initial density fluctuations, i.e., the linear power spectrum $P(k)$, and the background expansion, $H(z)$, to the result-

¹In principle the radius where the logarithmic slope is -2 can be directly estimated independent of α , and the concentration can be defined with this radius. However, in practice this is very rarely done and when fitting the measured density profile over a wide radial range c and α are not independent.

ing density profiles of DM haloes and to quantify the dependence on halo mass and redshift. Ideally, predictions for both c and α should fit into a consistent and physically-motivated theoretical framework. Following recent work, I recast the dependencies on halo mass and redshift into a single dependence on ‘peak height’, a quantity which characterises the amplitude of density fluctuations with respect to some critical threshold for collapse (see Section 4.3 for a general definition). The use of peak height is well motivated by the spherical collapse model (Gunn, Gott, 1972b) and plays an important role in the successful (extended) Press-Schechter formalism (Press, Schechter, 1974). Previous simulation work has shown that peak height correlates very strongly, though not perfectly, with both c and α (e.g. Prada et al., 2012; Gao et al., 2008a). In this work I re-examine the definition of peak height and explore the freedom therein in order to derive accurate universal relations (i.e., applicable for wide ranges of cosmological parameters) for c and α . Specifically, I exploit the freedom in the form of the window function that is used to filter the linear power spectrum when computing the peak height. I will show that the standard window function, the so-called spherical top hat function, is not the optimal choice for predicting the density profile parameters and that a relatively simple modification thereof results in a substantially improved model.

The chapter is organised as follows. In Section 4.2 I discuss the technical details of the simulations and how they are processed, particularly focusing on how the density profiles are stacked and fitted to obtain values and errors for c and α . In Section 4.3 I discuss the definition and key properties of peak height and how it is calculated for a given cosmology. In Section 4.4 I present how the two density parameters, c and α , vary with peak height for the cosmologies using the standard definition. In Section 4.5 I motivate the use of an alternative window function when defining peak height and quantitatively determine an optimal choice so that both c and α are universally described by this new definition of peak height. I additionally develop and present the model to predict halo concentration and shape parameter for a general cosmology. In Section 4.6 I test the model using additional cosmologies with very different background expansion rates to those used to calibrate the model. Finally, in Section 4.7 I conclude and summarise the results.

4.2 Simulation and analysis details

In this section I present the various cosmologies studied as well as the technical details of the simulations used in this work. I also describe how the density profiles are calculated and fitted to determine values for halo concentration, c , and shape parameter, α .

4.2.1 Cosmologies

In this work I primarily study a subset of the cosmologies first presented in Brown et al. (2020), particularly examining the two suites closest to our own universe. I discuss here briefly these different cosmologies. For a more in depth description of how these cosmologies were chosen see Chapter 3.

The cosmologies presented in Brown et al. (2020) were chosen to systematically study the effects of changes to both the amplitude and shape (i.e. slope) of the linear power spectrum at different k -scales on the internal properties of dark matter haloes, such as the density and velocity dispersion profiles. The amplitude and shape were changed by using a combination of free parameters in the Λ CDM model: the primordial amplitude, A_s , the primordial spectral index, n_s , which directly affects the slope of the linear power spectrum and k_{pivot} , which is the k -scale used for normalising the linear power spectra. The cosmologies used in the present work are split into two suites, the ‘Planck pivot’ and ‘ $k_{\text{pivot}} = 1h \text{ Mpc}^{-1}$ ’ suites. For each suite the primordial spectral index, n_s , is systematically varied from 0.5 to 1.75 with a fixed A_s and k_{pivot} . The $n_s = 0.96$ case represents the best-fit WMAP 9-yr results and is therefore a close match to what we believe is our own Universe. The values of A_s , n_s , k_{pivot} and σ_8 for these different cosmologies can be found in the previous chapter (see Table. 3.1). These cosmologies share the same best-fit WMAP 9-yr background expansion (Friedmann) parameters: $h = 0.7$, $\Omega_m = 0.2793$, $\Omega_b = 0.0463$ and $\Omega_\Lambda = 0.7207$ (Hinshaw et al., 2013).

In Fig. 4.1 I present the $z = 0$ linear power spectra (top panels) for the $k_{\text{pivot}} =$

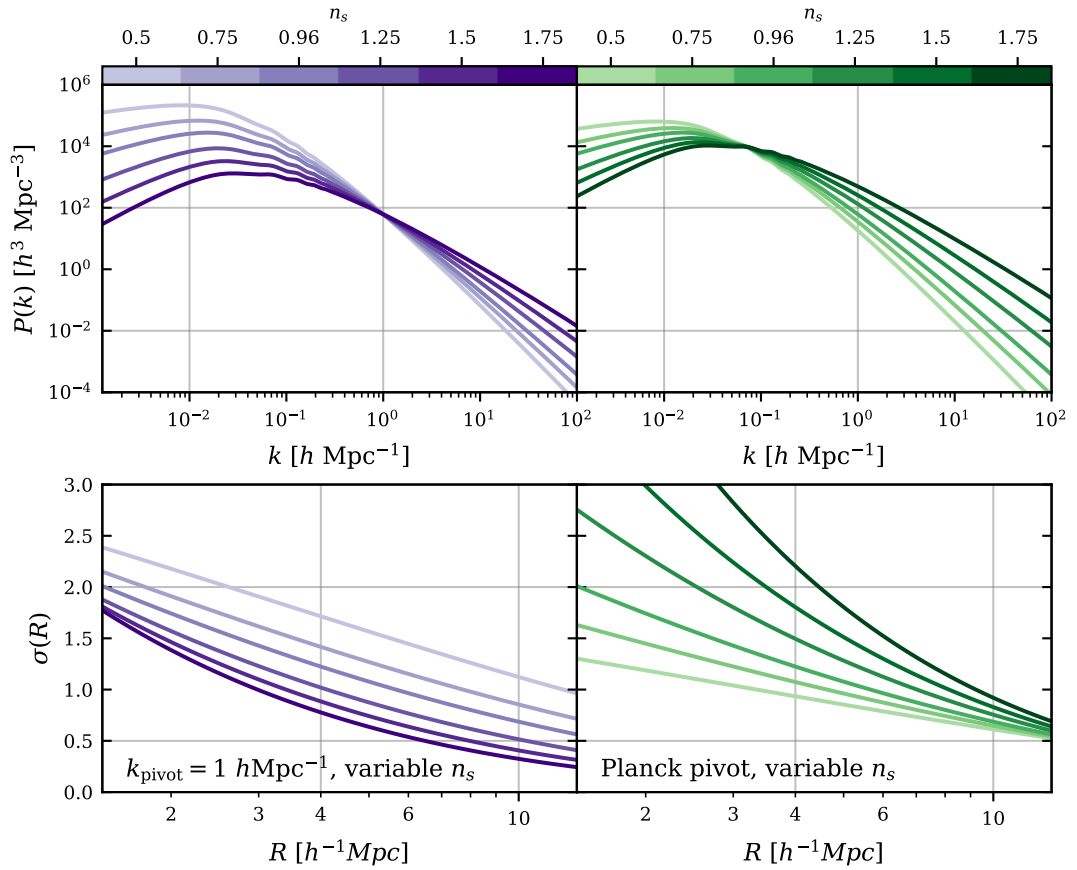


Figure 4.1: *Top*: The $z = 0$ linear power spectra for the various cosmologies studied in this work. *Bottom*: The rms density fluctuations in spheres of radius R . The left and right panels represent the two different suites (introduced in Brown et al. 2020), which use different pivot points for the linear power spectrum (see label in bottom left). For each suite (or pivot point), the primordial spectral index, n_s is systematically varied from 0.5 to 1.75 with $n_s = 0.96$ being the best-fit WMAP 9-yr value. The different shades represent different values of n_s , see colour bar.

$1h \text{ Mpc}^{-1}$ (left panels, purple lines) and Planck pivot (right panels, green lines) suites. The different shades represent the different values of n_s , as shown by the colour bars above each column. The two different pivot points can clearly be seen at $k_{\text{pivot}} = 1h \text{ Mpc}^{-1}$ and $k_{\text{pivot}} = 0.05 \text{ Mpc}^{-1}$ (Planck pivot point), allowing for the power spectra to be normalised at different physical scales. Additionally plotted in the bottom panels is the root mean square (rms) density fluctuations as a function of Lagrangian radius. Note that $\sigma(R)$, which is formally defined in Eqn. (4.6) below, correlates strongly with the expected amount of structure and abundance of haloes at different scales and masses, with larger mass haloes corresponding to larger Lagrangian radii, and vice-versa. I discuss these quantities further in Section 4.3.

As can be seen in Fig. 4.1, the cosmologies studied in this work represent a wide range of different shapes and amplitudes to the linear power spectrum, which in turn results in a diverse amount of expected structure, as described through $\sigma(R)$. This results in a sample of haloes with widely different evolutions and formation histories, offering a broad context in which to study the cosmological dependence of the density profiles of DM haloes.

4.2.2 Simulation details

The simulations studied in this work are virtually identical to those presented in Brown et al. (2020); the only difference being that all cosmologies from the original work have been re-run with a box twice the size (but with the same mass resolution), resulting in a factor of 8 increase in volume. This was done to increase the number of haloes in each simulation, allowing larger mass haloes to be studied as well as improve the statistics at all masses. Other than the box size, the technical details are the same as for the simulations presented in Brown et al. (2020), which I describe below.

The linear power spectra are generated using the Boltzmann code CAMB (Lewis et al., 2000). Initial particle positions and velocities are calculated using a modified version of N-GenIC² (Springel, 2005) at a starting redshift of $z = 127$. The initial

²The publicly available version of this code can be found at <https://github.com/sbird/>

conditions include second-order Lagrangian perturbation theory corrections and identical phases are adopted for all simulations. The collisionless, or ‘DM-only’, N-body simulations have been run with a modified version of the `Gadget-3` code (Springel, 2005; McCarthy et al., 2017). The simulations have been run with a comoving periodic volume of size $400 h^{-1}\text{Mpc}$ on a side with 1024^3 particles. For a WMAP 9-yr background cosmology (Hinshaw et al., 2013), as used for the majority of cosmologies in this work, this corresponds to a particle mass of $4.62 \times 10^9 h^{-1} M_{\odot}$. The gravitational softening is fixed to $4h^{-1}\text{kpc}$ (in physical coordinates for $z \leq 3$ and in co-moving at higher redshifts).

All haloes are identified with the `SUBFIND` algorithm (Springel et al., 2001). In this work I present the spherically averaged density profiles of DM haloes, using the most bound particle of the central halo as the halo centre. The central halo is defined as the largest (sub)halo in the friend-of-friends (FOF) group. Density profiles are calculated using all particles within the given spherical shell, whether they are identified as belonging to a subhalo or not. In principle the density of the smooth component with substructure removed can also be calculated (e.g. Fielder et al., 2020). In general, the halo finder is primarily used to initially identify the FOF group, provide the location of the centre of potential and calculate bulk properties such as halo mass and radius (for a given definition).

4.2.3 Fitting density profiles

As already stated, the goal of this work is to accurately study and model both c and α for a wide range of cosmologies. It is therefore essential that the simulation data are processed in an appropriate way to obtain reliable and robust measures of c and α with their associated errors.

Throughout this work ‘stacked’ density profiles are used exclusively, as described as follows. The spherically-averaged density profile of individual haloes are calculated using 32 logarithmically spaced bins over the radial range $10^{-2.5} <$

$r/R_{200c} < 0.7$, where R_{200c} is a measure of the halo size (see Section 4.3 for definition). The stacked profile is then calculated as the median density in each radial bin from all the haloes in the stack of a given halo mass bin. The values of c and α are then calculated by fitting the stacked density profiles with an Einasto profile (see Eqn. (4.2)) such that the following figure of merit, ψ , is minimised:

$$\psi^2 = \sum_i [\log \rho_i(r) - \log \rho_{\text{Einasto}}(r)]^2, \quad (4.3)$$

here $\rho_i(r)$ is the density profile from the simulation and $\rho_{\text{Einasto}}(r)$ is the Einasto profile for a given set of parameters. To estimate the errors on c and α bootstrap resampling is used. Specifically, 1,000 different realisations of the stacked profile are generated by randomly sampling (with repetition) haloes within the mass bin (or stack) using the same number of haloes. Hence, the number of haloes in the stacked profile depends strongly on mass, redshift and the cosmology. The values of c and α are then estimated as the median of the resulting distribution with the lower and upper errors calculated as the 16th and 84th percentiles respectively, equivalent to a 1σ uncertainty for a Gaussian distribution.

Although the stacked density profiles are calculated over a relatively large radial range only a subset of these radial bins are actually used when fitting to obtain values for c and α . In this work I fit over the radial range $r_{\text{conv}} < r < 0.7R_{200c}$, where r_{conv} is the convergence radius and dictates the minimum radius before numerical uncertainties affect the density profiles, which is discussed below.

The maximum radius of $0.7R_{200c}$ was chosen to avoid the very outer parts of a halo that are potentially not in equilibrium and do not follow the NFW or Einasto forms particularly well (e.g. Ludlow et al., 2010). The minimum radius adopted is the so-called convergence radius, r_{conv} , that specifies the radius at which the density profile is subject to numerical effects. Specifically, at small radii two-body interactions lead to a resolution dependent density core. The convergence radius can therefore be

expressed as a ratio of the timescale of two-body interactions and the Hubble time via:

$$\frac{r_{\text{conv}}}{R_{200c}} = 4 \left(\frac{\kappa_{\text{P03}} \ln N_c}{\sqrt{N_{200c} N_c}} \right)^{2/3}, \quad (4.4)$$

where N_c is the number of particles below the convergence radius and κ_{P03} is the ratio of the collisional relaxation time and the age of the universe (Power et al., 2003; Ludlow et al., 2019a). Larger values of κ_{P03} represent a more conservative convergence criterion. Power et al. (2003) propose that a value of $\kappa_{\text{P03}} = 0.6$ leads to convergence for individual haloes, while Ludlow et al. (2019a) find a similar, though smaller, value of $\kappa = 0.18$ for the convergence of stacked density profiles. However, in this work I find a larger value is needed to provide unbiased estimates for c and α . It is found that $\kappa_{\text{P03}} = 7^3$ provides reliable results and this value has also been suggested for improved convergence by Navarro et al. (2010b). It is found that, as well as a clear numerical core forming at the centre of haloes as documented in these works, there also occurs a slight enhancement in the density at larger radii of $r \approx r_{\text{conv}}$ (for $\kappa_{\text{P03}} = 0.6$), as is expected in order to conserve halo mass. Using $\kappa_{\text{P03}} = 0.6$ does avoid fitting to the density profile where there is a significant suppression in the density but typically does not avoid fitting to the region exhibiting an enhancement in density. Although this enhancement in density is relatively small, typically at most $\approx 5\%$, the difference can propagate through to $\approx 20\%$ systemic differences when determining the best-fit values of c and α . This appears to only be a significant issue when fitting the density profiles with a free shape parameter, due to the increased versatility of the fit. If a fixed shape parameter is used, either by explicitly fixing α or using a fitting formula without an equivalent ‘shape’ term, such as an NFW profile, then the determination of c is only mildly affected by the systematic differences in the inner density profile. It is likely that $\kappa_{\text{P03}} = 7$ is somewhat overly conservative, but it does ensure that there are no systematic errors associated with either the numerical core or the aforementioned enhancement in density. In this work Eqn. (4.4) is explicitly solved, with $\kappa_{\text{P03}} = 7$, for all individual haloes within a stack and use the median r_{conv} when fitting the stacked

³Using $\kappa_{\text{P03}} = 7$ means that for the cosmologies with the highest halo contractions, specifically the $n_s = 1.75$ cosmology in the Planck pivot suite, have $r_{\text{conv}} \sim r_{-2}$. Though the scale radii are well resolved for the majority of haloes.

density profiles. For a more detailed discussion of the convergence radius, including derivations and alternative forms to Eqn. (4.4), we refer the reader to Power et al. (2003) and Ludlow et al. (2019a).

As discussed above, I focus on studying stacked density profiles to derive both the c and α mass relations. For most of the cosmologies studied I use logarithmically-spaced mass bins of width 0.3 dex for haloes with at least 5,000 particles. For these simulations this results in a minimum mass of $M_{200c} = 2.31 \times 10^{13} h^{-1} M_{\odot}$. The only exception to this is the most extreme cosmology considered in this work, using a primordial spectral index of $n_s = 1.75$ with a Planck pivot point, where a cut of 10,000 particles is used (see Appendix B.1 for details). I, additionally, only consider mass bins with at least 100 haloes. The maximum halo mass considered therefore depends strongly on the halo mass function and varies as a function of cosmology and redshift.

As well as imposing a cut on both the number of particles within a halo as well as the number of haloes within a stack, I also apply a relaxation cut to discount haloes that have been significantly affected by ongoing or recent major mergers. Specifically, I only consider haloes with a normalised offset of the centre of mass (CoM) to centre of potential (CoP) of $|\mathbf{x}_{\text{CoP}} - \mathbf{x}_{\text{CoM}}|/R_{200c} < 0.07$. This relaxation criterion is similar to that presented in Neto et al. (2007), who applied the same cut to the CoP and CoM offset but with additional criteria based on the relative mass of substructure and the virial ratio. I find that simple cut on the CoM to CoP offset is sufficient to remove severely unrelaxed haloes and gives unbiased estimates for c and α . Additionally, applying the extra criteria proposed in Neto et al. (2007) does not significantly change the inferred c and α values, a similar conclusion to that found in Duffy et al. (2008).

In Fig. 4.3 I present examples of the density profiles that are fit in this work. Here I have plotted the profiles for a range of masses at $z = 0$ for a WMAP 9-yr cosmology, normalised by r_{-2} and ρ_{-2} . The radius r_{-2} and is taken to be where the logarithmic slope equals -2 and is found by directly interpolating the logarithmic slope of the stacked density profiles.⁴ This allows for r_{-2} and ρ_{-2} to be determined empirically

⁴To reliably estimate the slope of the profiles a Savitzky–Golay filter is used, with a window length

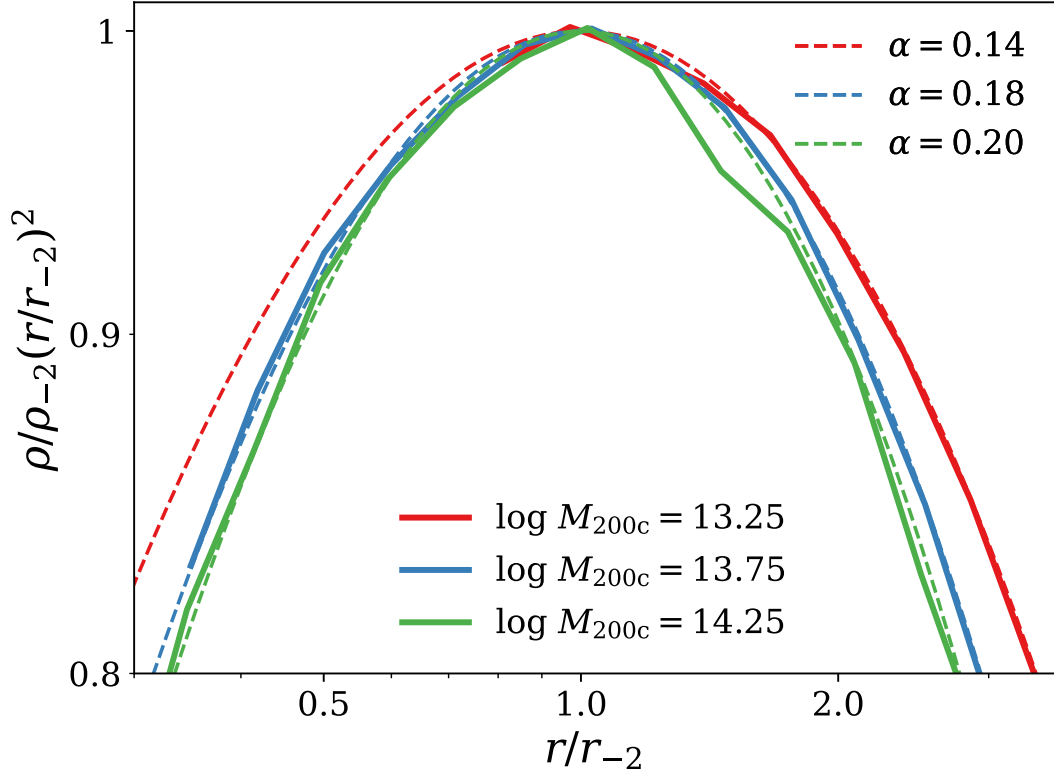


Figure 4.2: Stacked density profiles for a range of masses (see legend) at $z = 0$ for a WMAP 9-yr cosmology. The $\log M_{200c} = 13.25, 13.75$ and 14.25 mass bins constitute stacks of 5, 713, 1,318 and 211 haloes, respectively. The profiles are only plotted up to their convergence radius (Eqn. (4.4)) which varies strongly with halo mass. For each density profile, r_{-2} and ρ_{-2} are estimated non-parametrically from the logarithmic slope. The density profiles are normalised by their respective scale radii, r_{-2} , and plotted as ρr^2 to reduce the dynamic range. Normalising the radial coordinate in this way removes the dependence on concentration. As can be seen, there is a clear halo mass dependence to the normalised density profiles, demonstrating that the density profiles are not self-similar and that an additional ‘shape’ parameter is required to fully describe them. Plotted as dashed lines are Einasto profiles that approximately follow the simulated density profiles. In these units, the Einasto profile has only one free parameter, α (see legend).

from the density profiles directly, without any assumptions about the parametric form the overall density profile may take. Plotting in these units, i.e. r/r_{-2} and ρ/ρ_{-2} , removes the dependence on halo concentration. If the density profiles were perfectly self-similar they should be indistinguishable when plotted in this manner. However, as shown in Fig. 4.3 the density profiles (solid lines) do not follow the same radial dependence as each other, with higher (lower) masses resulting in profiles where the ρr^2 profile varies more quickly (slowly) with radius. This difference demonstrates the need for an additional parameter other than concentration; i.e., the shape parameter. When plotted in these units, i.e. r_{-2} and ρ_{-2} , the Einasto profile has only one free parameter, α (see Eqn. (4.2)). Additionally plotted as dashed line in Fig. 4.3 is a number of Einasto profiles with values for α chosen by eye to approximately follow to observed density profiles. It can be seen that the role of α is to control how quickly ρr^2 varies with radius.

If one uses the definition that the scale radius is where the logarithmic slope is -2 then the concentration of haloes can, in principle, be determined separately from the shape parameter and any assumptions about the density profile, as done above. However, practically it is often more reliable to determine c and α by fitting directly to the density profiles, as is done in this work (see Section 4.2) and many others. When determining c and α in this way they are no longer independent, and there will be a certain amount of degeneracy between the two parameters. Additionally the value of c inferred by fitting to the density profile will depend on the assumed density profile, including, for an Einasto profile, if α is allowed to be free or not.

Fig. 4.3 also demonstrates the main sources of errors when fitting to stacked profiles at different mass scales. Specifically the number of haloes within the stack and the limited radial range fit over. For higher mass bins (green line) the main limiting factor is the relatively small number of haloes within the mass range, resulting in a somewhat noisy density profile with relatively large fluctuations. For lower masses (red line) there are many more systems resulting in a much smoother density profile, however, there is a significantly reduced radial range over which the profiles can be

of 3 and a second order polynomial.

reliably measured due to the low number of particles in each halo and hence a larger convergence radius.

In Appendix B.1 I present a resolution study to check the convergence of both the simulations and analysis and I motivate further some of the selection choices, such as only considering haloes with at least 5,000 particles.

4.3 Peak height definition

Throughout this work I discuss how the density profiles of haloes vary as a function of peak height for a range of cosmologies. Here I discuss the definition of peak height and highlight some of the free aspects of the formalism where certain choices, or assumptions, have to be made; primarily the halo mass definition and window function used.

Peak height, ν , is traditionally defined as,

$$\nu(M, z) = \frac{\delta_c}{\sigma(M, z)} \quad , \quad (4.5)$$

where δ_c is the critical density for collapse, as predicted by the spherical collapse model,⁵ and σ is the rms overdensity associated with the halo, and is calculated from the linear power spectrum via:

$$\sigma^2(R, z) = \frac{1}{2\pi^2} \int_0^\infty k^2 P(k, z) |W(kR)|^2 dk \quad . \quad (4.6)$$

In the above, $P(k, z)$ is the linear power spectrum and $W(kR)$ is the window function (sometimes referred to as the filter function). R is the so-called Lagrangian radius defined as

$$R^3 = \frac{M}{4/3\pi\rho_{m,0}} \quad , \quad (4.7)$$

⁵I take $\delta_c = 1.68$ and ignore the mild cosmology dependence. I also do not consider any additional dependence on mass present in ellipsoidal collapse models.

where M is the halo mass (e.g., the virial mass or that corresponding to some other spherical overdensity) and $\rho_{m,0}$ is the mean background density of the universe today.

The redshift evolution of the linear power spectrum can be written as

$$P(k, z) = D^2(z)P(k, z = 0) \quad , \quad (4.8)$$

where $D(z)$ is the linear growth factor, which can be calculated from the background expansion, i.e. $H(z)$, and is normalised to unity at the current epoch. The redshift evolution of peak height can therefore also be expressed in terms of the growth function, where

$$\nu(M, z) = \nu(M, z = 0)/D(z) \quad . \quad (4.9)$$

Hence for a given cosmology, with $P(k)$ and $H(z)$ specified, the peak height of a halo can be straightforwardly calculated from the above equations.

There are a few key aspects in the above equations that are open to interpretation and therefore certain choices must be made. The first of these is how the mass of a halo is defined. It is common to define the mass as an overdensity with respect to either the critical or mean density of the universe at a given redshift. The mass, and in turn radius, of the halo is defined to obey the following,

$$\Delta\rho_{c/m} = M_{\Delta c/m}/(4/3\pi R_{\Delta c/m}^3) \quad , \quad (4.10)$$

where Δ is the adopted overdensity. I will use the notation specified in this equation to identify the given mass definition, identifying both the overdensity parameter (from the number in the subscript) and reference density (with either denoting c or m for using the critical or mean density, respectively). Common choices are $M_{200c/m}$ and $M_{500c/m}$. The definition with respect to the higher overdensity and smaller radius, $M_{500c/m}$, is typically used for galaxy clusters (since X-ray observations typically probe the hot gas within this radius), while $M_{200c/m}$ is often used when examining the properties of dark matter haloes, of all sizes, in cosmological simulations. It has been shown that large scale properties of DM halos, such as the abundance at a given mass or

the position of the splashback radius, correlate more strongly with a M_{200m} definition (e.g. Tinker et al., 2008; Diemer, Kravtsov, 2014; Diemer, 2020). On the other hand, internal properties, such as halo concentration, tend to correlate more strongly with an M_{200c} mass definition (e.g. Diemer, Kravtsov, 2015). Why different properties of dark matter haloes seem to prefer a mass definition with respect to either the critical or mean density is unclear and is an open question in the field. In this work I am focused on studying and developing a model for the density profiles of DM haloes and a mass definition of M_{200c} is used. I leave the exploration of alternative mass definitions for future work, though I do briefly discuss this possibility in the context of these results in Section 4.5.3.

The second aspect of peak height formalism for which there is freedom is in the choice of the window function, $W(kR)$, which is the main focus of this paper. It has become common place in the literature that $W(kR)$ is chosen so that it represents a spherical top hat (STH) function in configuration (real) space. With this choice, the window function takes the following form:

$$W_{\text{STH}}(kR) = \frac{3}{(kR)^3} [\sin(kR) - kR \cos(kR)] \quad . \quad (4.11)$$

This choice of window function provides a very obvious and clear interpretation of Eqn. (4.6); it represents the rms overdensity averaged over a sphere of radius R for the given linear power spectrum. This choice also makes it clear how to compare to and use the spherical collapse model, which considers the evolution of a top hat perturbation in an otherwise homogeneous expanding universe. However, the spherical collapse model does not offer a complete picture of how real haloes assemble, particularly ignoring the hierarchical growth that is at the heart of the current cosmological paradigm. It is therefore not clear that this is the correct choice of window function for such a cosmology and potentially a different choice of window function would better represent (or correlate with) the growth and structure of haloes in a cold DM dominated universe.

Throughout this chapter I will use a subscript to identify the window function

used to calculate peak height. For instance ν_{STH} refers to peak height values calculated using the standard spherical top hat window function. I reserve the use of ν *without* a subscript when discussing peak height in a general sense with, in principle, any choice of window function, as above.

4.4 Peak height relations

Before proceeding to study if c and α can be better modelled by an alternative window function, it is worth studying how these density parameters vary as a function of peak height using the standard STH definition.

In Fig. ?? I present how c and α vary as a function of ν_{STH} for the main cosmologies studied in this work (see Section 4.2.1), at $z = 0$ and $z = 1$. Individual errors are not plotted (though the mean error is plotted in black at the top left of each panel) to improve the readability of the plot, but note that not all values here are equally reliable with some data points having significantly larger fractional errors than others. In general, larger values of ν_{STH} correspond to fewer haloes within the mass bin and therefore larger uncertainties. The relation between α and ν_{STH} proposed by Gao et al. (2008a) is shown as the dotted black line, specifically $\alpha = 0.0095\nu_{\text{STH}}^2 + 0.155$.

Focusing initially on the concentration of the haloes at $z = 0$ (top panels, solid lines), we see that there is a clear cosmological dependence to the c - ν_{STH} relation. This is particularly clear for the Planck pivot suite where the different cosmologies are significantly stratified. Additionally, for a given cosmology, ν_{STH} does not appear to completely describe the redshift evolution. This is most easily seen for the $k_{\text{pivot}} = 1 \text{ hMpc}^{-1}$ suite where haloes at $z = 1$ (dashed lines) have significantly lower concentrations at a fixed ν_{STH} than at $z = 0$ (solid lines).

The dependence of α on ν_{STH} (bottom panels) is much closer to universal than for c . In general both the cosmological and redshift dependences appear to be well described by ν_{STH} with no obvious trend of a certain cosmology or redshift lying distinct from the main distribution, as is observed for c . The α - ν_{STH} relation matches

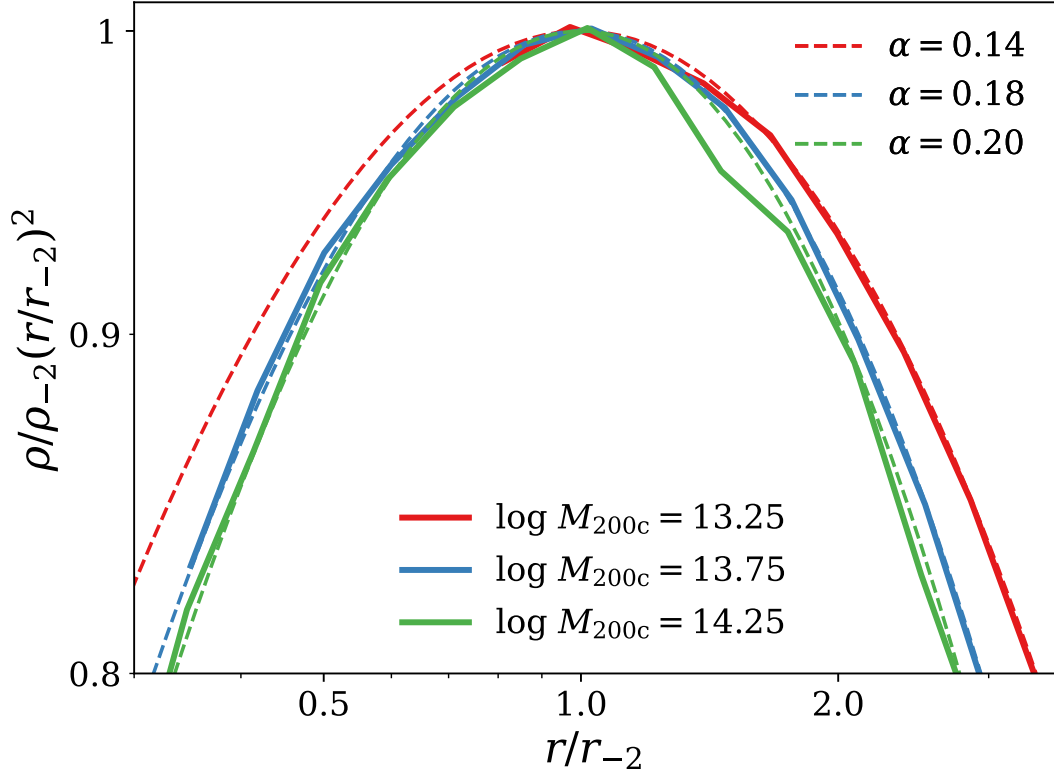


Figure 4.3: Stacked density profiles for a range of masses (see legend) at $z = 0$ for a WMAP 9-yr cosmology. The $\log M_{200c} = 13.25, 13.75$ and 14.25 mass bins constitute stacks of 5, 713, 1, 318 and 211 haloes, respectively. The profiles are only plotted up to their convergence radius (Eqn. (4.4)) which varies strongly with halo mass. For each density profile, r_{-2} and ρ_{-2} are estimated non-parametrically from the logarithmic slope. The density profiles are normalised by their respective scale radii, r_{-2} , and plotted as ρr^2 to reduce the dynamic range. Normalising the radial coordinate in this way removes the dependence on concentration. As can be seen, there is a clear halo mass dependence to the normalised density profiles, demonstrating that the density profiles are not self-similar and that an additional ‘shape’ parameter is required to fully describe them. Plotted as dashed lines are Einasto profiles that approximately follow the simulated density profiles. In these units, the Einasto profile has only one free parameter, α (see legend).

reasonably well that previously proposed by Gao et al. (2008a).

From these results there is clearly room for improving the universality of the relation between c and peak height, which may potentially be achieved by altering the window function (away from the standard STH case) in the peak height definition. On the other hand, the standard definition of peak height already correlates very well with α in a way that is apparently independent of cosmology and redshift. This suggests that the STH window function is already close to optimal for α . Taken together, these results suggest that c and α favour separate and distinct window functions. Indeed, this is what is found in the next section.

4.5 Optimal window functions

In a Λ CDM universe, where the initial density fluctuations are assumed to be small and Gaussian in nature, the initial density field can be, statistically, described by the power spectrum alone. The subsequent gravitational evolution depends only on these initial conditions and the background expansion history, given a theory for gravity. Hence, the averaged internal structure of haloes as a function of mass depends only on the linear power spectrum, $P(k)$, and Hubble expansion, $H(z)$, which together form a given cosmology.

The aim of the present study is to determine how the averaged structure of haloes depends on $P(k)$ and $H(z)$ in a quantitative fashion. A promising theoretical framework to use is the Press-Schechter formalism (Press, Schechter, 1974). In the Press-Schechter formalism the abundance of haloes is predicted to be a universal function of peak height. This has motivated previous studies to also correlate halo properties with peak height, as it is expected that peak height will account for a significant part of the cosmological dependence. However, the abundance of haloes is only approximately universal and numerical simulations have shown that there is a clear redshift and cosmology dependence when using the standard Press-Schechter formalism, i.e. a STH window function (e.g. Tinker et al., 2008). There have been a number of suggestions

for how to improve this model, with a notable extension being the use of an alternative window function. For instance, Leo et al. (2018) found that using a smooth k -space filter can accurately model the abundance of haloes in cosmologies with truncated power spectra (e.g., due to non-standard inflation scenarios). By allowing the window function to vary, I am able to study what aspects of $P(k)$ are most important for setting the density parameters, where it is found that both density parameters are approximately set by the amplitude of $P(k)$ at an associated k -scale (see Section 4.5.3).

As demonstrated in the previous section, the density parameters, particularly c , are clearly not universal as a function of peak height when using a STH window function. Similar to how Leo et al. (2018) found the abundance of haloes can be closer to universal with an alternative window function, it is possible that a different window function will result in $c-\nu$ and $\alpha-\nu$ relations that are universal; i.e., do not depend on redshift or cosmology.

It is worth considering if the use of an alternative window function is consistent with some of the key results from the literature as well as the features already observed in Section 4.4.

The first result considered is from Diemer, Kravtsov (2015), who study the concentration of haloes in scale free cosmologies, that being a cosmology with a power law linear power spectrum and an Einstein de Sitter background expansion (i.e., $\Omega_\Lambda = 0$ and $\Omega_m = 1$). They find that for a single cosmology the redshift evolution closely follows a single function of ν_{STH} . However, the particular relation between c and ν_{STH} exhibits a clear dependence on the choice of the slope of the linear power spectrum (see Fig. 3 of Diemer, Kravtsov 2015). Their interpretation was that it is the effective slope of the linear power spectrum at an associated k -scale that affects the $c-\nu$ relation and led Diemer, Kravtsov (2015) to develop a model that incorporates an effective slope in addition to peak height in order to better predict halo concentration. However, this is not the only interpretation of their results, it is also consistent with the possibility of using a different window function. For a power law linear power

spectrum, $P(k) = Ak^n$, calculating σ (see Eqn. (4.6)) is somewhat simplified:

$$\sigma^2(R, z) = \frac{A}{2\pi^2} D^2(z) R^{-(n+3)} \int_0^\infty x^{n+2} |W(x)|^2 dx. \quad (4.12)$$

Therefore, $\sigma(R, z) \propto D^2(z) R^{-3-n}$. It is clear that for these cosmologies the window function only plays a role in the normalisation of the peak height. Therefore, for a given cosmology, any choice of window function would preserve ν - c being redshift independent. However, when comparing different cosmologies, i.e. different values of n , the window function and its effect on the normalisation will play a role, as can be seen by the x^{n+2} term within the integrand. It is therefore likely that the window function could be chosen appropriately so that the normalisation between different values of n would result in a single c - ν_{STH} relation independent of n , or the normalisation of the power spectrum.

Another key result that should be accounted for, or preserved, is the redshift evolution of c and α in a standard Λ CDM cosmology. It is well established that the redshift evolution of c is not perfectly described by ν_{STH} , while ν_{STH} offers a good description of the redshift evolution of α . Therefore developing a model to predict c and α must predict this general behaviour. For a Λ CDM cosmology the linear power spectrum is no longer a power law, meaning that the window function contributes in a more complex way to the peak height of different mass haloes than simply by a different normalisation. Therefore, changing the window function from the standard STH case can potentially change the relationship between peak height and mass in such a way as to resolve the discrepancy in the redshift evolution of c ; meanwhile if the window function remains relatively close to the STH case then the redshift evolution of α can be preserved.

One potential limitation of any model that links the density profiles of DM haloes to only $P(k)$ and $H(z)$, as is the goal of this work, is that the density profiles of individual haloes cannot be predicted. Due to the statistically-averaged nature of the power spectrum, the model predicts averaged quantities for c and α . As such, in this chapter I focus exclusively on modelling the averaged density parameters as a function of mass

and redshift. However, it seems inevitable that the density profiles of individual haloes depends, in detail, on the initial overdensity in the linear power spectrum with which they are associated. Therefore, differences in these overdensities would correspond to differences in individual halo density profiles. It is therefore likely that the theoretical framework presented in this chapter could be extended to describe the expected scatter in c and α for a fixed mass, however, this is beyond the scope of this paper.

An alternative approach to that presented in this work is to identify an appropriate mediator that correlates strongly with the density profiles of haloes. For example, it is common to attribute halo concentration with the formation history of the halo (e.g. Navarro et al., 1997; Wechsler et al., 2006; Ludlow et al., 2014). This therefore offers a natural explanation for the general mass dependence, with smaller haloes forming earlier and resulting in higher concentrations, as well as the observed scatter in c at fixed mass corresponding to an equivalent scatter in formation time. However, formation history is not a fundamental property and depends on the given cosmology. Hence, to make a prediction for a given cosmology (i.e. $P(k)$ and $H(z)$), some theoretical framework is required to predict the formation history as a function of mass, redshift and cosmology. Extended Press-Schechter theory (e.g. Lacey, Cole, 1993) is one such theoretical framework that aims to predict the distribution of formation histories. A prescription for the link between formation history and halo concentration can therefore be used alongside such a theoretical framework to predict the distribution of expected halo concentrations (e.g. Benson et al., 2019).

4.5.1 Smooth k -space window function

Assuming a correct choice of window function exists there is no obvious way to derive, from first principles, the form that it should take. As such a more heuristic approach is used by utilising a versatile parameterisation for the window function that maintains key properties that are expected to be present for a realistic window function.

I use the *smooth k -space* window function originally proposed in Leo et al. (2018) to study how the c - ν relation changes for various choices of window function.

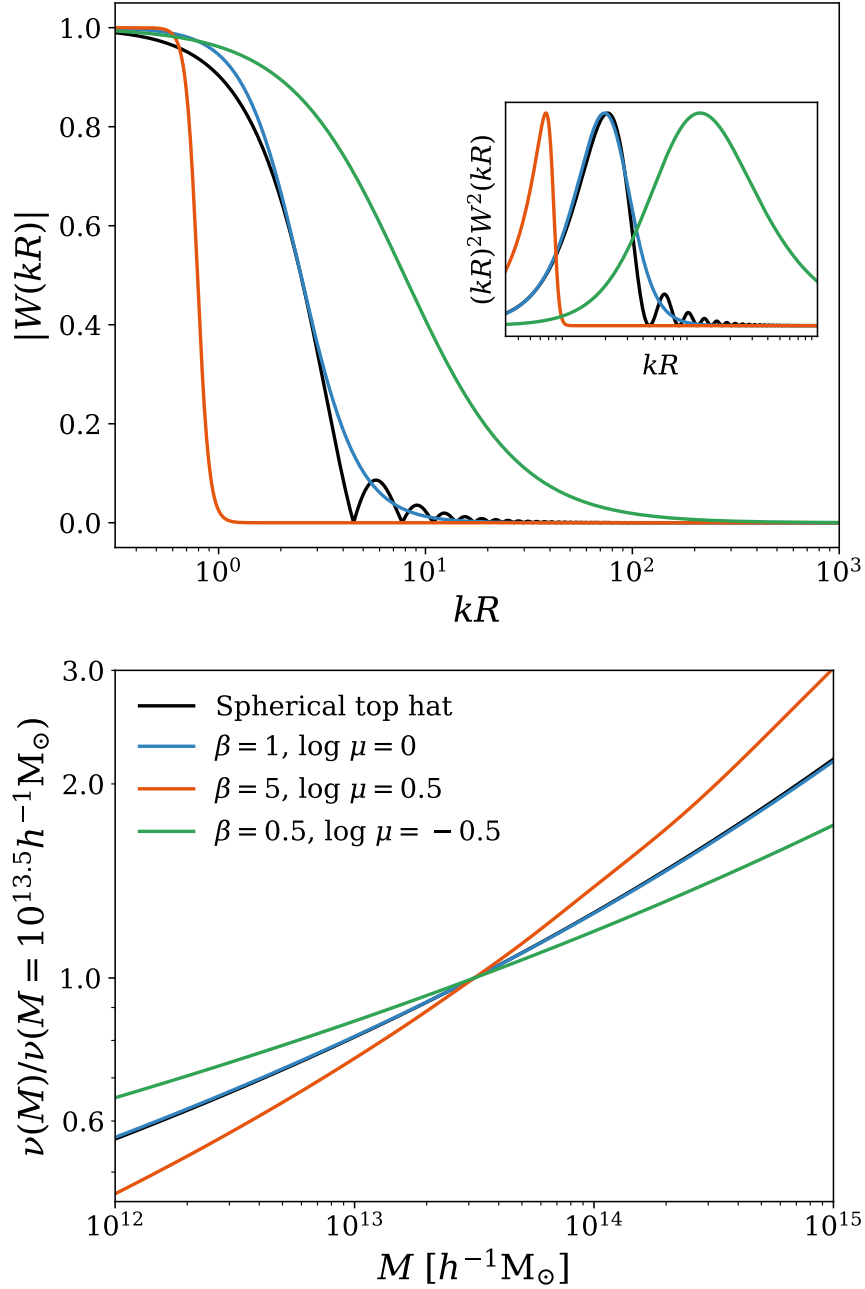


Figure 4.4: *Top*: The smooth k -space window function (Eqn. (4.13)) for a few combinations of μ and β (see legend). Qualitatively, μ changes the scale at which the transition occurs, with smaller values of μ resulting in the transition occurring at higher values of kR (corresponding to smaller physical scales), while β controls how quickly the transition from $W = 1$ to $W = 0$ occurs. Plotted for reference is the standard STH window function (shown in black). Additionally plotted in the inset panel is $(kR)^2 W^2(kR)$ for the same window functions in the main plot, with each curve has been normalised by its global maximum. No units have been plotted for the inset, as the purpose of the figure is to demonstrate that $(kR)^2 W^2(kR)$, for all window functions studied here, exhibits a clear peak, with the location of that peak depending on both μ and β . *Bottom*: The resulting relation between peak height and mass, normalised at $M = 10^{13.5} h^{-1} M_\odot$ for the WMAP-9 yr cosmology. The STH (black lines) and smooth k -space window function with $\mu = 1$ and $\beta = 1$ (blue lines) follow a very similar $\nu(M)$ relation.

The smooth k -space window function is defined as the following,

$$W_{\text{smooth}}(kR) = \frac{1}{1 + (\mu kR/2.50)^{3.12\beta}} \quad . \quad (4.13)$$

The smooth k -space window function behaves very similarly to a step function (in fourier-space), with β determining how quickly the transition from 0 to 1 occurs⁶ and μ the scale at which the transition happens. When defining Eqn. (4.13) I have normalised the free parameters to resemble closely the standard STH window function when μ and β are unity. This is done so that for $\mu = 1$, $\beta = 1$ the scale where $W(kR) = 0.5$ and the first derivative at that scale match the standard STH window function. This results in the factors of 2.50 and 3.12. In practice, this means that the results for a choice of $\mu = 1$ and $\beta = 1$ when using the smooth k -space window function will resemble closely the spherical top hat case, allowing for an easier interpretation of these parameters compared to the standard definition for peak height. In the top panel of Fig. 4.4 I show the smooth k -space function for a few combinations of μ and β , and discuss the inset panel later in Section 4.5.3. The standard STH function (see Eqn. (4.11)) is plotted for comparison. As can be seen in Fig. 4.4, the smooth k -space window function can closely resemble the standard STH filter (by construction at $\mu = 1$, $\beta = 1$). One feature that cannot be replicated is the series of ‘wiggles’ at high values of kR , however these do not contribute significantly to the peak height calculation.

In the bottom panel of Fig. 4.4 I show the resulting peak height values as a function of mass for the standard WMAP 9-yr cosmology at $z = 0$, normalised by the peak height at $M = 10^{13.5} h^{-1} M_{\odot}$. This demonstrates that the relation between mass and peak height depends intimately on the choice of window function. When the window function is changed significantly so does the relationship between mass and peak height, which therefore propagates through to changes in the c and α peak height relations. Note that $\nu(M)$ is almost indistinguishable when using the STH window function or the smooth k -space filter with $\mu = 1$ and $\beta = 1$.

⁶As $\beta \rightarrow \infty$ the function reduces exactly to a step function.

4.5.2 Quantitatively determining universality

As mentioned previously, the aim of this chapter is to determine if, with an appropriate window function, the density profiles are universal with peak height. Practically this means that both c and α follow a single function of peak height, ν , for any $P(k)$ at any redshift. The cosmologies studied previously in Brown et al. (2020) (see Section 4.2.1) offer a wide range of different linear power spectra that is ideal to constrain the optimal window function(s).

To determine the optimal window function and constrain the associated parameters an appropriate figure of merit that quantitatively describes how close to a single function, and hence how universal, the resulting c and α -peak height relations are is required. We choose to fit a second order polynomial, in log space, that minimises the χ^2 error. The fitting formula is specifically

$$\log(y) = a_2 \log(\nu)^2 + a_1 \log(\nu) + a_0 \quad . \quad (4.14)$$

Here y represents the parameter being constrained, either concentration, c , or the shape parameter, α . The χ^2 value for a given choice of $a_{0,1,2}$ and window function is calculated as,

$$\chi^2 = \sum_i \frac{(y - y_i)^2}{\sigma_i^2} \quad , \quad (4.15)$$

with the sum over all data points. y is the given prediction for a choice of $a_{0,1,2}$, y_i and σ_i represent the value and error of the given data point. $a_{0,1,2}$ are then chosen to minimise Eqn. (4.15) for the given window function. Throughout the chapter I will quote the reduced χ^2 error, $\chi_r^2 = \chi^2/DoF$, with the number of degrees of freedom (DoF) remaining constant.

In this work I want to study whether an appropriate choice of window function can lead to a universal relation between the two density parameters, c and α , and peak height, ν . Therefore, the exact form that the c - ν or α - ν relations take is of secondary importance compared to it obeying a single function for all cosmologies and redshifts studied. As such, we do not consider $a_{0,1,2}$ free parameters of the model, as they are

only used to quantitatively determine ‘universality’.

Using a second order polynomial in log space offers a fitting function that is versatile enough to describe the data without introducing higher order terms that could lead to overfitting. Ideally, a non-parametric method that does not impose a functional form on the $c-\nu$ and $\alpha-\nu$ relations would be used. One such method would be to minimise the Spearman rank correlation coefficient, which makes no assumptions about the functional form of the underlying data (other than the relation being monotonic). However, it is important to incorporate the associated errors for the density parameters, and it is unclear how to reliably include these in such a ranked statistic.

4.5.3 An optimal window function

In Fig. 4.5 I show how χ_r^2 changes as a function of μ and β when using a smooth k -space window function (Eqn. (4.13)). The optimal window function is constrained separately for c and α (top and bottom panels, respectively). Firstly, it is clear that there does indeed appear to be a choice of window function that results in a universal $c-\nu$ and $\alpha-\nu$ relation with minimum values of $\chi_r^2 \approx 2$ for both c and α . This is more clearly shown in Fig. 4.7, which presents the resulting $c-\nu$ and $\alpha-\nu$ relations for an optimal choice of window function parameters (I discuss this in detail in the next subsection).

Although the minimal values of χ_r^2 are comparable for c and α , there are significant differences in the range of χ_r^2 values. This does not appear to be a reflection of the smooth k -space filter better describing one parameter over the other, but rather features that are intrinsic to the data, independent of the choice of window function. The primary reason for this difference is that c varies over a much larger dynamic range than α , meaning that relatively small changes in peak heights result in large differences to how universal the $c-\nu$ relation is, while α is much less sensitive to these changes.

Focusing initially on the parameter space for the smooth k -space window function constrained by halo concentration (top panel of Fig. 4.5), it is clear that there are strong degeneracies in determining the optimal values of μ and β . However, a choice

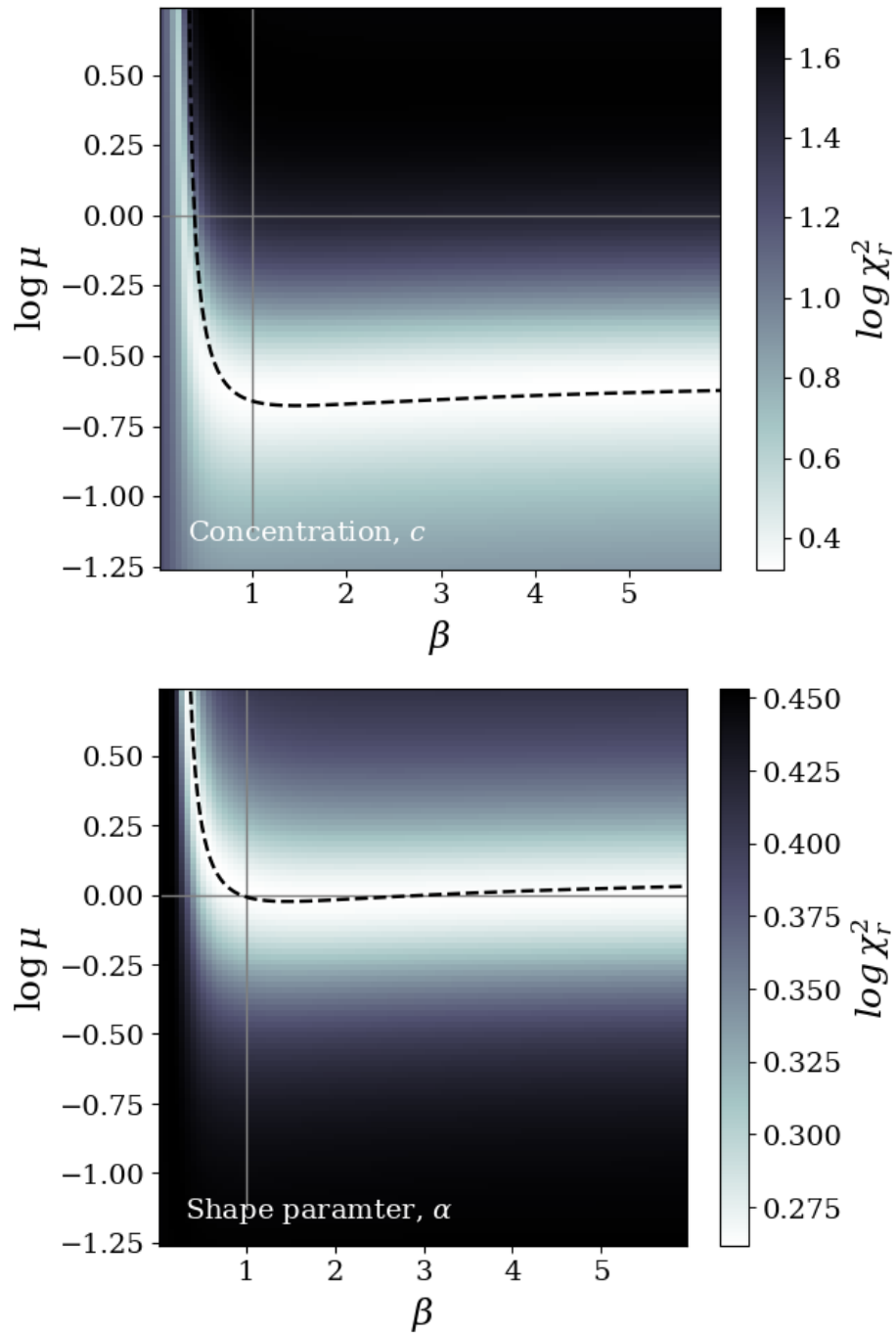


Figure 4.5: Parameter space demonstrating how χ_r^2 varies with the free parameters of the smooth k -space window function, μ and β , for the two density parameters c (top) and α (bottom). χ_r^2 is used to quantitatively determine how close to universal the resulting peak height relations are, with smaller values of χ_r^2 corresponding to more universal relations. To first order the value of peak height is set by the amplitude of the linear power spectrum at an associated k -scale, with that scale depending on the given window function. The key property is where $(kR)^2 W^2(kR)$ is a maximum, as described through the parameter κ , see Eqn.(4.17). Plotted as dashed black lines are contours of constant κ (see Eqn. (4.18)), with $\kappa = 9$ and $\kappa = 2$ for c and α , respectively. These contours follow very closely the observed degeneracies between μ and β .

of parameters close to the standard spherical top hat case ($\mu = 1, \beta = 1$) is clearly disfavoured, as expected from the earlier discussion (see Section 4.4). For $\beta \gtrsim 1$, the value of μ is relatively well determined and the optimal values appear to be independent of β , favouring a value of $\log \mu \approx -0.7$. However, in this region there is little constraint on β with all values sampled performing similarly well. It is clear that a key factor in determining the concentration is the k -scale of the transition of the window function, how ‘quickly’ this transition occurs is of secondary importance. There also exist degeneracies in the region $\beta \lesssim 1$. Here the form of the degeneracy is much more complicated than for $\beta \gtrsim 1$, exhibiting a nontrivial dependence on μ and β . I discuss the origin and form of this degeneracy shortly.

Examining the constraints on μ and β when optimising for the shape parameter α (top panel of Fig. 4.5), we see the same general behaviour as for concentration. The overall shape of the degeneracy in the parameter space is almost identical, except with it being translated to larger values of μ from what is found for c . Interestingly, the (approximate) STH window function ($\mu = 1, \beta = 1$) lies almost perfectly on the observed degeneracy and is therefore close to an optimal choice of parameters. Again we observe for $\beta \gtrsim 1$ that there is no constraint on β , but μ is relatively well constrained. The optimal value in this region is $\mu \approx 1$ as opposed to $\log \mu \approx -0.7$, as was observed for halo concentration. The optimal window function appears to be somewhat at odds with the results of Ludlow, Angulo (2017) who found that the α – ν_{STH} relation was not universal. There is no obvious explanation for this, but may be linked to the very different cosmologies studied in their work, specifically scale free cosmologies with EdS background expansions.

To further understand the observed degeneracies between μ and β we must consider what are the most important features when calculating peak height. From Eqn. (4.6) it can be seen that peak height is effectively a convolution between $P(k)$ and $k^2 W^2(kR)$. For both a smooth k -space and a STH window function $k^2 W^2(kR)$ exhibits a clear maximum at a specific scale,⁷ where the associated scale is at $(kR)_{\text{max}} \equiv \kappa$. This can clearly be seen in the inset panel of Fig. 4.4, where I have plotted

⁷For the smooth k -space window function this is only strictly true for $\beta > 1/3.12$.

$(kR)^2W^2(kR)$ for a few different choices of window functions and parameters. Hence, to first order peak height is set by the amplitude of the linear power spectrum at the associated k -scale:

$$\nu^2 \propto R^3/P(k_0) \quad . \quad (4.16)$$

where

$$k_0 = \frac{\kappa}{R} \quad . \quad (4.17)$$

Here R is the Lagrangian radius (see Eqn. (4.7)) and κ corresponds to where $(kR)^2W^2(kR)$ is a maximum. κ is a dimensionless quantity and depends on the choice of window function and associated parameters. For a STH window function, $\kappa = 2.08$. For the smooth k -space window function, κ depends on both μ and β and is found to be

$$\kappa = \frac{2.50}{\mu} \left(\frac{1}{3.12\beta - 1} \right)^{1/3.12\beta} \quad . \quad (4.18)$$

If we consider contours of constant κ , we see this equation provides a relationship between μ and β that has the general behaviour of the observed degeneracy, a roughly $\mu = 1/\beta$ behaviour. Indeed, it is found that this relationship follows almost perfectly the observed degeneracy for an appropriate choice of κ . This is shown in Fig. 4.5 where I have plotted lines of constant κ . The values of κ have been chosen by eye to approximately follow the optimal μ - β relation and correspond to $\kappa = 9$ and 2 for constraining c (top panel) and α (bottom panel), respectively. In detail, it appears that the degeneracy at $\beta \approx 0.5$ is not completely characterised by this relation. In this region of the parameter space the peak in $(kR)^2W^2(kR)$ is not as clearly defined and therefore higher-order terms will play a more significant role, implying that the simple approximation of $\nu \propto R^3/P(k_0)$ will not be as accurate.

The above results suggest a rather simple interpretation of what sets the average density profiles of DM haloes. It is, to a good approximation, the amplitude of the linear power spectrum at an associated k -scale, given by Eqn. (4.17), with the one complication that c and α appear to be set by fluctuations on *different* scales. The concentration of DM haloes is set by smaller scale fluctuations than the shape parameter, by roughly a factor of 4.5, with the shape parameter matching closely the same value of

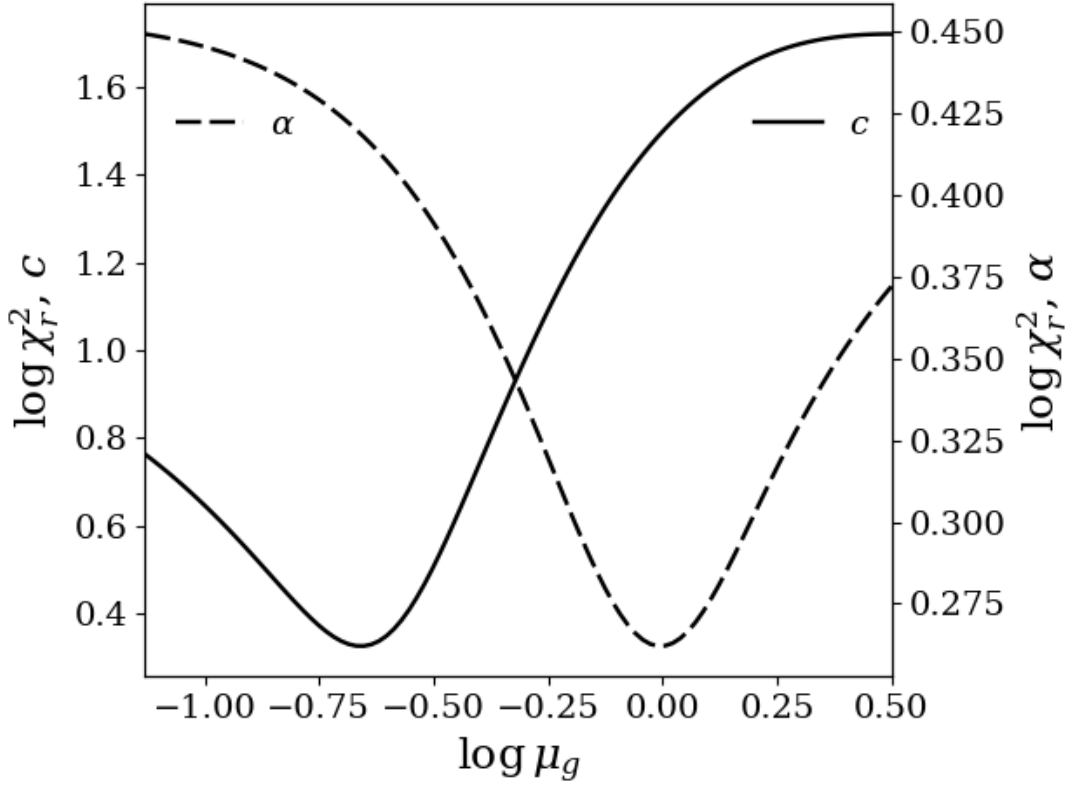


Figure 4.6: Variation of χ_r^2 as a function of μ_g for the generalised spherical top-hat window function (see Eqn. (4.19)) for the two density parameters c (solid line) and α (dashed line). χ_r^2 is used to quantitatively determine how close to universal the resulting peak height relations are, with smaller values of χ_r^2 corresponding to more universal relations. These distributions exhibit clear minima at $\log \mu_g = -0.67$ and $\log \mu_g = -0.01$ for c and α , respectively. Note that $\log \mu_g = 0$ ($\mu_g = 1$) corresponds to the standard spherical top-hat window function.

κ for the standard spherical top hat window function. However, it is not clear why this should be the case, and the physical origin of these two preferences requires further study.

The result that at $\beta \approx 1$ there are optimal choices for the smooth k -space window function where $\mu \neq 1$ (for halo concentration at least), as well as the dominant factor not being μ or β directly but rather the resulting value of κ , implies that a STH-like window function can also lead to universal behaviour if an equivalent parameter to μ is introduced. Let us generalise the STH window function as follows

$$W_{\text{STH,general}}(kR) = \frac{3}{(\mu_g kR)^3} [\sin(\mu_g kR) - \mu_g kR \cos(\mu_g kR)] \quad . \quad (4.19)$$

Here the window function is identical to the standard definition (see Eqn. (4.11)) but with an additional free parameter, μ_g , that behaves the same as the parameter μ for the smooth k -space window function. In Fig. 4.6 μ_g is allowed to vary, as was done for the smooth k -space window function. Unlike the smooth k -space window function, the generalised STH does not exhibit any degeneracies and there are clearly defined optimal values for μ_g . It is found that for the concentration the optimal value is $\log \mu_g = -0.67$ with $\chi_r^2 = 2.12$, while for the shape parameter $\log \mu_g = -0.01$ with $\chi_r^2 = 1.83$. The optimal values for χ_r^2 are comparable to those found for the smooth k -space filter. The associated values of κ are $\kappa = 9.73$ and 2.13 for the concentration and shape parameters, which are again comparable to the values of κ that match the observed degeneracy between μ and β for the smooth k -space window function.

In the above discussion, and throughout the paper, I have adopted a single halo mass definition (M_{200c}) and argued that the two density parameters are effectively set by fluctuations at different physical scales, as described by the optimal window function. However, there is an alternative interpretation that is consistent with the results and formalism presented. As mentioned in Section 4.3 the parameter μ , or μ_g , is equivalent to changing the mass associated with the halo. Therefore, an alternative interpretation from the above discussion is to assign a different masses, with a fixed STH window function, for the two density parameters. The shape parameter would therefore use the standard M_{200c} definition, while halo concentration would favour a mass definition of $\mu_{g,c}^3 = (10^{-0.67})^3 \approx 0.01 M_{200c}$, i.e., treating the halo as two orders of magnitude smaller mass. A rough calculation, assuming an Einasto profile with $c = 5$ and $\alpha = 0.18$, suggests that this would require an overdensity definition of $\Delta \sim 10^5$, which is significantly larger than most standard mass definitions commonly used. Additionally, this mass definition would represent only a fraction of the amount of accreted matter in virial equilibrium within the halo, and therefore would not represent a physically meaningful quantity. For both these I prefer the interpretation that a single mass definition is used, specifically M_{200c} , with α and c being set by fluctuations at different associated scales.

4.5.4 Predicting the density profile of DM haloes

To develop a model that is able to predict halo concentration and shape parameter for a general cosmology a choice for the best window function must be made. As there are strong degeneracies between μ and β there is no unique choice. I therefore choose to instead use the generalised spherical top hat window function, which I have demonstrated provides equally as universal c - ν and α - ν relations. Using this window function also has the advantage that it reduces the number of free parameters in the model as well as allowing for a more intuitive interpretation of its results, i.e., it corresponds to the density rms averaged over a sphere. For this, I use the optimal parameters found in the previous section, specifically $\log \mu_g = -0.67$ and -0.01 for c and α . I denote the peak height values calculated with these two choices of window function as ν_c and ν_α , respectively.

In Fig. 4.7 I present the resulting c - ν_c and α - ν_α relations in top and bottom panels, respectively. In the top row of each plot I show c and α as a function of their respective peak height for all eleven cosmologies studied at $z = 0, 0.5, 1, 1.5$ & 2 . Each data point represents a mass bin from its associated cosmology. The choice of cosmology is specified by the colour, matching that from Figs. 4.1 & ???. The redshift is then specified by the style of the data point (see legend). In general, both c and α are very close to a single function, as expected from the small χ_r^2 values for these choices of window function; $\chi_r^2 = 1.83$ and 2.12 for c and α , respectively.

In general most data points lie within 10% of the prediction (black dashed line) and the data points that lie significantly further away than this tend to be those with particularly large error bars, but still within a few standard deviations. It is clear from Fig. 4.7 that using these window functions leads to significantly more universal c and α peak height relations compared with using the standard spherical top hat function in Fig. ???.

Plotted with black dashed lines in each panel of Fig. 4.7 are the best-fit relations

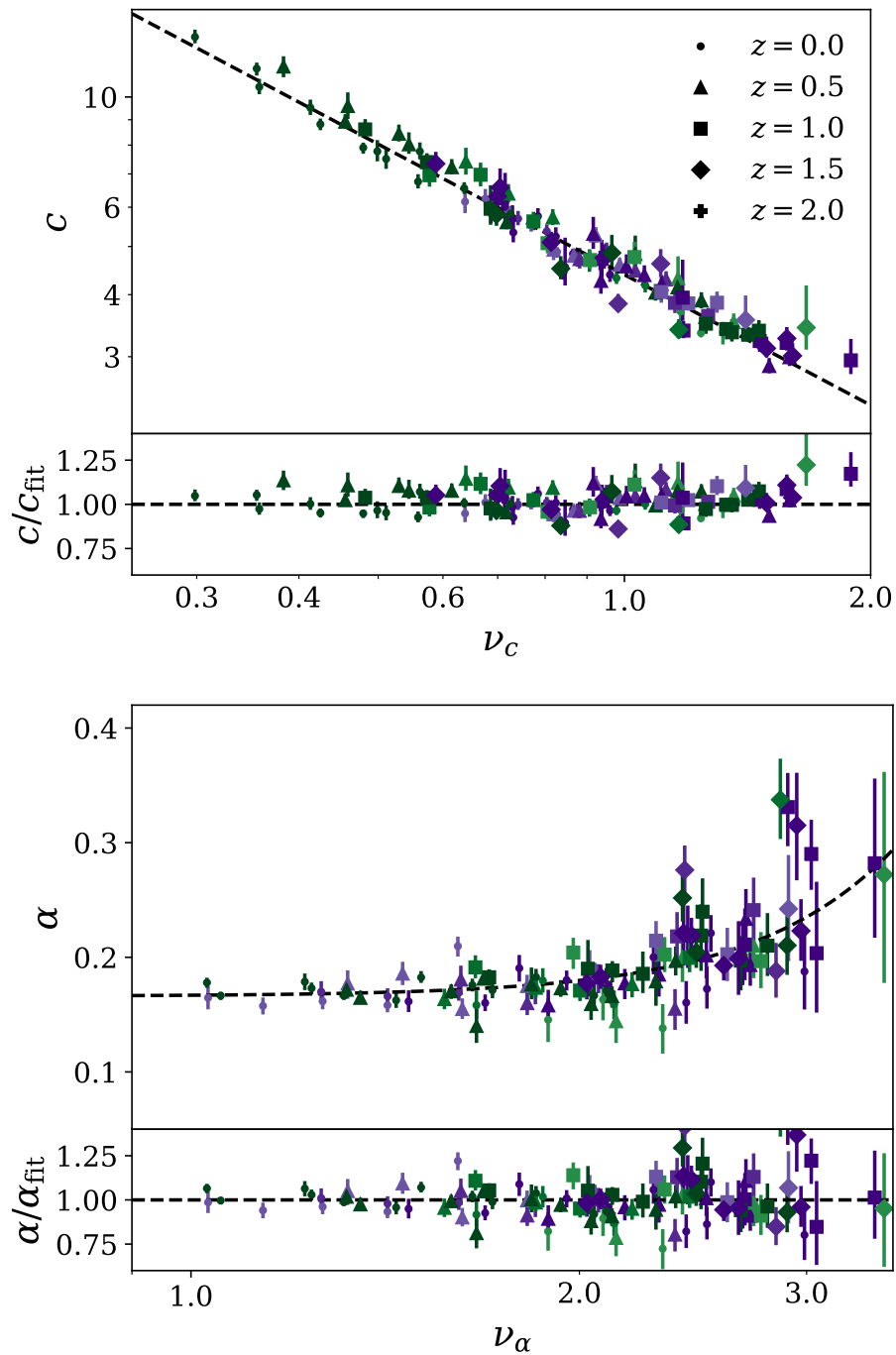


Figure 4.7: Resulting c - ν_c , top panel, and α - ν_α , bottom panel, relations for the optimal choice of window function. The data points presented are all those used to constrain the window function. The colour indicates the given cosmology, matching those in Fig. ??, while the marker style corresponds to the redshift (see legend). The black dashed lines represent the empirical relations used for the model to predict c and α for a general cosmology. The fractional difference from the data and the empirical fits are shown in the bottom panels, for both c and α .

that are used in the model to predict c and α . Specifically I use,

$$c = 4.39\nu_c^{-0.87} \quad , \quad (4.20)$$

and

$$\alpha = 8.52 \times 10^{-4} \nu_\alpha^4 + 0.166 \quad . \quad (4.21)$$

Here ν_c and ν_α are calculated using Eqns. (4.5–4.7) and a generalised spherical top hat window function (Eqn. (4.19)). ν_c uses the parameters $\log \mu_g = -0.67$, while ν_α uses $\log \mu_g = -0.01$.

Note that, although a general second order polynomial was used to calculate χ_r^2 values when determining the optimal window function, I re-parameterise these here to better represent the observed trends as well as to have empirical relations that will more reliably extrapolate beyond the values of ν_c and ν_α sampled in this work. For instance, the c – ν_c relation appears to follow very closely a simple power law, allowing the relation to be expressed with only two free parameters. Additionally, using a second order polynomial in log space (see Eqn. (4.14)) for the α – ν_α relation would predict an increase in the value of α as $\nu_\alpha \rightarrow 0$. There is no indication from this or other work (e.g. Gao et al., 2008a; Ludlow, Angulo, 2017) that such an increase would occur, and it seems more likely that α approaches a constant as ν_α approaches zero. Such a behaviour is better represented in the chosen parameterisation in Eqn. (4.21). Using these alternative parameterisations to predict c and α gives consistent χ_r^2 values as found in the previous section using a more complex second order polynomial.

There is much debate in the literature around the form of the c – M relation at high masses ($M_{200c} \gtrsim 10^{14}$ at $z = 0$ for a cosmology close to our own Universe), with some works reporting an upturn in halo concentration at high values of ν_{STH} (e.g. Prada et al., 2012; Diemer, Kravtsov, 2015) while others see no evidence for an upturn but, in some cases, do report a minimum concentration (e.g. Zhao et al., 2009; Ludlow et al., 2014; Correa et al., 2015a). The nature of the high-mass end of the c – M relation depends on how the data is processed; if an unbiased sample of haloes is used then there is expected to be an upturn, while if a relaxation cut is applied

Table 4.1: Optimal χ_r^2 values for different choices of window functions, with the associated optimal parameters. The value of χ_r^2 is calculated by fitting a second order polynomial. For the smooth k -space filter there is no unique choice of μ and β that gives a minimum value of χ_r^2 , the parameters provided here are just one such possible combination. I have also provided the χ_r^2 values for the prediction of c for two models from the literature for comparison.

Model or window function	χ_r^2 for c	χ_r^2 for α	Parameters for c	Parameters for α
Smooth k -space (Eqn. (4.13))	2.10	1.83	$\log \mu = -0.64, \beta = 2$	$\log \mu = -0.02, \beta = 2$
Standard spherical top hat (Eqn. (4.11))	31.4	1.83	–	–
Generalised spherical top hat (Eqn. (4.19))	2.12	1.83	$\log \mu_g = -0.67$	$\log \mu_g = -0.01$
Diemer, Joyce (2019)	23.8	–	–	–
Ludlow et al. (2016)	8.30	–	–	–

(as adopted in this work) the preference for an upturn disappears (see Ludlow et al. 2012 for more details). In the present study no clear evidence of either an upturn or a minimum concentration is observed.⁸ A potential explanation for this is that the inferred values of c depend on whether a free or fixed shape parameter is used, hence the largest discrepancy between this work and those using a fixed shape parameter is expected at high values of ν_{STH} where α exhibits the strongest mass dependence. But I note that it is also possible that such features may be present at sufficiently large values of peak height not sampled in this work.

In Table 4.1 I present the χ_r^2 values calculated from the halo concentration for few choices of the window function as well as comparing to some models in the literature. Specifically, the models of Ludlow et al. (2016) and Diemer, Joyce (2019). The publicly available code `COLOSSUS` (Diemer, 2018) has been used to generate the quantitative predictions of these two models. I compare to these models as they are designed to predict halo concentration for a general cosmology and were found in Brown et al. (2020) to reproduce the general behaviour observed in those simulations. It is clear by the χ_r^2 values shown in Table 4.1 that our new model matches more closely the concentrations observed in these simulations.

There are a few key differences between how the concentration of haloes are inferred in our analysis and in these previous studies. Firstly, both these models infer the concentration–mass relation averaged over fits to individual haloes, whereas I have used stacked density profiles. Secondly, they have adopted a fixed shape parameter, α , when developing and calibrating their models, as was also done for the concentrations presented in Brown et al. (2020). This was achieved either by explicitly fixing α in the Einasto profile or by using a fitting formula without a comparable shape parameter (i.e., an NFW profile). Allowing both the concentration and shape parameter to be free in the present study, this has arguably led to more accurate measurements of both parameters, which in turn has led to a more accurate model for these quantities.

⁸I have quantitatively verified this by fitting a power law plus a constant (to represent a minimum concentration) and a double power law (to represent an upturn in concentration) to the $c-\nu_c$ relations observed in Fig. 4.7. In both cases a single power law is preferred.

4.6 Testing the model

In this section I study the predictions of our empirical model for c and α and check that they generalise to cosmologies not already studied here. One key aspect that remained fixed in the cosmologies used to develop and calibrate the model was the background expansion, with all simulations sharing the same best-fit WMAP 9-yr cosmological parameters: $h = 0.7$, $\Omega_m = 0.2793$, $\Omega_b = 0.0463$ and $\Omega_\Lambda = 0.7207$. Therefore, the model is tested against two additional cosmologies with distinctly different background expansions. I consider cosmologies with higher and lower matter densities, Ω_m . Specifically, cosmologies with $\Omega_m = 0.2$, $\Omega_\Lambda = 0.8$, $h = 0.79$ and $\Omega_m = 0.4$, $\Omega_\Lambda = 0.6$, $h = 0.61$ are studied. Here I have chosen Ω_m and then varied h to keep the same distance to the surface of last scattering (which is well-determined from the CMB), I have also enforced that the cosmologies are spatially flat. Additionally, these cosmologies are normalised to the same value of σ_8 , so that there are approximately the same abundance of haloes in the simulations. I have also kept the ratio of dark matter to baryons, i.e. Ω_c/Ω_b , fixed. The technical details of the simulations are the same as those studied throughout this chapter (e.g., a box size of $400h^{-1}\text{Mpc}$ with 1024^3 particles, see Section 4.2 for details).

There are multiple ways in which the different background expansions will affect the evolution and final density profiles of the DM haloes. The most obvious aspect is the redshift evolution of the density fluctuations, as described through the linear growth factor, which will be distinctly different for these cosmologies. This difference will in turn affect the evolution and growth of the internal properties of the DM haloes. However, a more subtle way that changing the background expansion affects both the model and the results is through the mass definition. In this work I have chosen to use a M_{200c} mass definition, meaning that the halo mass and radius are defined so that the mean density within R_{200c} is $200\rho_{\text{crit}}$. Therefore, changing the background expansion not only changes how density fluctuations grow but also the density used to define the mass of the halo, which in turn affects the associated Lagrangian radius and effective scale in the linear power spectrum that sets the peak height value. Testing against these

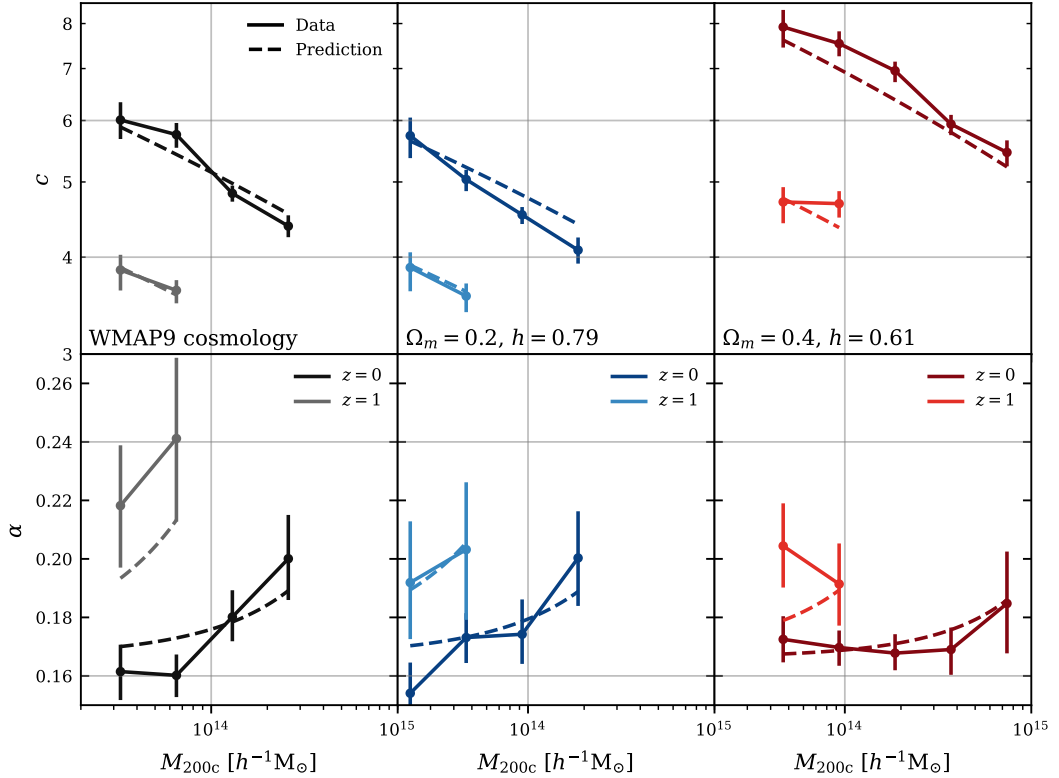


Figure 4.8: Resulting c - M_{200c} (top) and α - M_{200c} (bottom) relations for the WMAP 9-yr cosmology (left), $\Omega_m = 0.2$ (middle) and $\Omega_m = 0.2$ (right) cosmologies. For each cosmology the relations are shown at $z = 0$ and 1 (see legend). The solid lines with errors represent the data from the simulations while the dashed lines the predictions from the model. In general both c and α are accurately predicted by the model with any differences being within 5% (or approximately one sigma), demonstrating that the model generalises to cosmologies with different background expansions as well as changes to the linear power spectrum.

cosmologies will allow us to assess whether both these aspects, the change in growth of the density fluctuation and change in the mass definition, are accurately modelled for a general $H(z)$.

In Fig. 4.8 I present the results for these cosmologies, with the associated errors, alongside the predictions for c and α . Compared to the fiducial WMAP 9-yr cosmology, the $\Omega_m = 0.2$ cosmology matches very closely the mass and redshift evolution while the $\Omega_m = 0.4$ one exhibits a much clearer difference, particularly resulting in higher concentrations than the two other cosmologies. It can be seen that the model accurately predicts the mass and redshift evolution for these cosmologies. Most points are well within the errors, with any outlying point being of approximately only one

standard deviation away or within 5% of the observed value. It appears that the model and results of this chapter therefore do generalise to cosmologies with distinct background expansions. As can be seen in Fig. 4.8, the evolution of c and α as a function of mass and redshift for multiple cosmologies is rather complex. However, this complexity is naturally explained as a single dependence on ν_c and ν_α , as demonstrated by the accuracy of the model.

Although the changes studied in this work demonstrate significant differences to the underlying cosmology, both through the linear power spectrum and the background expansion, I have not tested it for even more extreme variations than presented here. The accuracy of the model may be reduced in these regimes, particularly for significantly larger or smaller peak height values than sampled by these simulations. For example, in a cosmology with a truncated power spectra (typically associated with warm dark matter), the c - M relation is not expected to be monotonic but instead exhibit a maximum concentration (e.g. Ludlow et al., 2016). For such a cosmology, ν_c would tend to a constant at small masses. Hence the model, with a single relation between c and ν_c , would not fully capture the expected turnover.

4.7 Summary and conclusions

The aim of this work has been to create a model that links the fluctuations in the initial linear power spectrum with the resulting density profile of DM haloes, modelling the dependence as a function of mass, redshift and cosmology. To fully describe the density profiles observed in cosmological simulations two parameters are required, halo concentration, c , and the shape parameter, α . I therefore aimed to create a model that consistently predicts both c and α in a consistent and physically-motivated framework. To this end, I have studied how c and α vary as a function of peak height, ν , a quantity previously shown to correlate strongly, though not perfectly, with both c and α and which is used in the Press-Schechter formalism (see Section 4.3 for definitions). I have explored free aspects of the formalism, focusing particularly on the window function, to determine if the relation between both c and α and peak height can be made to be

universal, i.e. are a single function for all cosmologies and redshifts. The results of this work can be summarised as follows:

(i) In this work I have used a subset of the cosmological simulations first presented in Brown et al. (2020) to study the cosmological dependence of the density profile of dark matter haloes, specifically using the ‘Planck pivot’ and ‘ $k_{\text{pivot}} = 1h \text{ Mpc}^{-1}$ ’ suites. For these simulations the slope and amplitude of the initial linear power spectrum has been systematically varied, resulting in haloes with a diverse range of formation and evolution histories. In Section 4.2 I present the details of the simulations and how the data has been processed to obtain robust and reliable estimates for c and α .

(ii) To explore a wide range of possible window functions I used a versatile functional form known as the smooth k -space window function (Eqn. (4.13); see also Leo et al. 2018), which is introduced and discussed in Section 4.5.1 (see Fig. 4.4). There are two free parameters associated with the smooth k -space window function: μ and β . μ determines the effective scale of the transition from unity to zero in the window function while β controls how quickly this transition occurs.

(iii) To quantify how close to universal the $c-\nu$ (or $\alpha-\nu$) relation is, I fitted a second order polynomial and evaluated the χ^2 error (quoting the reduced χ^2 value throughout) for the given relation, see Section 4.5.2. I studied how χ_r^2 varied as a function of μ and β (see Fig. 4.5 in Section 4.5.3). It was found that there are indeed choices of μ and β that result in universal $c-\nu$ and $\alpha-\nu$ relations with minimal values of $\chi_r^2 = 2.10$ and $\chi_r^2 = 1.83$ for c and α , respectively.

(iv) It was observed that there is a strong degeneracy between μ and β (again, see Fig. 4.7) with multiple values providing similarly optimal values of χ_r^2 . It was found that the dominant factor in setting the peak height is the scale where the window function is a maximum, when plotted as $k^2 W^2(kR)$. Therefore, to first order, the peak height is set by the amplitude of the linear power spectrum at the associated k -scale described by $\nu \propto R^3/P(\kappa/R)$. κ is where the window function (specifically $k^2 W^2(kR)$) is a maximum and depends on the given window function, see Sec-

tion 4.5.3 and Eqns.(4.16–4.17). For the smooth k -space window function κ depends on both μ and β , with contours of constant κ matching closely the observed degeneracy.

(v) The optimal window functions, and associated values of κ , are different for c and α . This strongly suggests that these two quantities are set by fluctuations on *different* physical scales in the linear power spectrum. The optimal values are $\kappa = 8.85$ and $\kappa = 2.0$ for c and α . For α the optimal window function (and value of κ) match very closely the standard spherical top hat (STH) window function, while for c the optimal values corresponds to smaller scales. In particular, this analysis indicates that the concentration of haloes is set by fluctuations on scales ≈ 4.5 times smaller than those that set α , or $\approx 1\%$ of the halo mass. As an example, for a WMAP-9 yr best-fit cosmology for a halo with mass $M_{200c} = 10^{13}h^{-1}M_{\odot}$, the concentration is set by fluctuations in the linear power spectrum at a scale of $k \approx 3.1 h\text{Mpc}^{-1}$, while the shape parameter is set by fluctuations at $k \approx 0.7 h\text{Mpc}^{-1}$.

(vi) As the relations between peak height and the density parameters can be made to be approximately universal, a simple model where c and α depend only on peak height, with the appropriate choice of window function, is able to be developed. Specifically, I introduced a generalised spherical top hat window function (Eqn. (4.19)) with the optimal parameters $\log \mu_g = -0.67$ and $\log \mu_g = -0.01$ for c and α respectively, see Section 4.5.4. The values for c and α can then be predicted by empirical relations, given in Eqn. (4.20) & (4.21). The smooth k -space window function also produces similarly accurate relations, the only disadvantage being that it requires two free parameters which are strongly degenerate.

(vii) In Section 4.6 I tested the reliability and accuracy of the model. When determining the optimal window function all cosmologies used shared the same background expansion histories, but with systemically varied initial linear power spectra. As such, I chose to test the predictions of the model against two cosmologies with a higher and lower matter density, resulting in distinctly different evolutions of the Hubble parameter $H(z)$. It was found that the model closely matches the observed c - M_{200c} and α - M_{200c} relations, with an accuracy typically better than 10%.

It is common to attribute the concentration of a halo to its formation time, with this interpretation offering an explanation for both the average halo mass dependence as well as scatter in concentration of individual haloes (e.g. Navarro et al., 1997; Wechsler et al., 2006; Ludlow et al., 2014). Initially, this view may seem at odds with the results presented in this work (as I do not discuss formation time), but the two pictures are not incompatible. In the model, the density of collapsed DM haloes are directly attributed to properties of the underlying cosmology (i.e., $P(k)$), quantitatively described through the peak height variables ν_c and ν_α . The halo formation time, on the other hand, can be viewed as a mediator between changes to the cosmology and the resulting response of the density profiles of DM haloes. Indeed, it seems likely that the idea of the halo concentration being set by fluctuation on a particular scale in the linear power spectrum is roughly equivalent to it being set by the formation time of the halo. One limitation of the model, as it is presented here, is that it only described the average density profiles at a fixed mass. There is expected to be scatter at fixed mass, something that can be explained by an equivalent scatter in formation time. However, formation time is not a fundamental quantity but rather depends on the given cosmology. As such, any prediction for the density profiles (using halo formation time) will require some theoretical framework to predict halo formation time (such as extended Press-Schechter theory), with its own potential systematics and limitations.

Interestingly, multiple studies that link concentration with halo formation time (for example Navarro et al., 1997; Ludlow et al., 2016) independently identify the same mass scale in their accretion history, specifically $\approx 1\%$ of their current mass, as being important (see the papers for the detailed definitions of formation time). Similarly, I find that the concentration of haloes is set by the effective spatial scale that is (traditionally) associated with $\approx 1\%$ of the halo mass. In my view, it seems unlikely to be a coincidence that both these models pick out similar mass scales as being in some sense ‘special’, though the physical significance of this finding remains to be elucidated.

To accurately predict the density profile of DM haloes both c and α are required. The model can therefore be used to improve the predictive power of many other cosmological tools and probes; by incorporating it into predictions from the halo model

(e.g. Smith et al., 2003; Mead et al., 2015) to improving the fit to stacked weak lensing maps (e.g. Linden von der et al., 2014; Hoekstra et al., 2015; McClintock et al., 2019). Having a model that accounts for changes in α is particularly important for galaxy cluster mass scales. At these masses α has the strongest mass dependence as well as deviating significantly from a value that closely resembles an NFW profile, i.e. the prediction is that $\alpha > 0.18$ at cluster masses.

One interesting application would be to use the concentration, or shape parameter, mass relations inferred from observations along with the predictions of ours (or similar) models to constrain the underlying cosmological parameters. Although baryonic changes are expected to play a non-negligible role in setting the total (DM and baryons) density and masses of haloes, these effects are much smaller on the DM component. Therefore, these issues can be mitigated by fitting to the DM *only* component in galaxies/clusters and comparing the inferred mass profiles from a DM only simulation, as discussed, e.g., in Debackere et al. (2021). Fitting for both halo concentration alongside cluster abundances is a promising way to help further constrain the cosmology of our Universe, as well as identifying potential systematics (as both should infer the same cosmological parameters).

This work demonstrates the link between the linear power spectra and the extremely non-linear formation and evolution of the internal density profiles of DM haloes. I have demonstrated that there is a clear universality that exists in the density of haloes in cosmologies dominated by collisionless DM, offering deeper insights into the origin of the structure of our own Universe. This universality leads to robust predictions for the density of DM haloes for a wide range of cosmologies that can be in turn used to further constrain the underlying cosmology of our own Universe.

Finally, I present a publicly available `Python` module to calculate the predictions of the model for c and α called `CASPER` (Concentration And Shape Parameter Estimation Routine). All relevant information about installation and usage can be found at <https://github.com/Shawn-T-Brown/CASPER>.

Chapter 5

ARTEMIS Dark

In this final chapter I present ongoing work. As such, the results presented here are not complete and there is key analysis that still needs to be done. However, this chapter still provides a good skeleton of what the final paper would, hopefully, look like and discusses some of the key questions we hope to answer.

In this chapter I explore the joint effects of warm dark matter (WDM) and baryonic processes on the satellite populations of Milky Way mass systems. The baryonic processes focus on studying stellar feedback and the assumed reionisation redshift. This is done in the context of full hydrodynamical zoom-in simulations from the ARTEMIS sample, using the EAGLE galaxy formation code. To efficiently and exhaustively explore how the properties of the satellite populations depend on the stellar feedback, epoch of reionisation and WDM mass (a total of 6 free parameters) an emulator is built using Gaussian processes. I will primarily focus on studying the observed stellar masses of these populations where it is found that there is a strong degeneracy between the WDM mass and the best fit stellar feedback parameters. This degeneracy highlights the need to jointly vary the feedback implementation when using cosmological simulations to try and constrain cosmological extensions such as WDM. Using a fixed feedback implementation and not effectively marginalising over the associated parameters will result in biased inferences for the constraints on such cosmological extensions.

5.1 Introduction

Numerical simulations of the formation and evolution of galaxies are an indispensable tool in interpreting and understanding observational data, with many such models now able to reproduce a wide range of observational properties (e.g. Schaye et al., 2015; Sawala et al., 2016; Hopkins et al., 2018; Nelson et al., 2019).

One particularly useful aspect of galaxy formation simulations is their ability to consistently model the complex non-linear effects of both baryonic processes and possible extensions to Λ CDM on the formation and evolution of galaxies. As such, these simulations offer the possibility of inferring the presence of non standard models such as self interacting dark matter, warm dark matter (WDM) or a running of the scalar spectral index (e.g. Stafford et al., 2020a).

One key limitation of modern galaxy formation models, that significantly limits their predictive power, is the heuristic implementation of feedback mechanisms often used. Many important physical processes happen below the resolution limit of most simulations, as such it is common to implement an effective feedback process through so-called ‘subgrid’ physics. These algorithms introduce a number of free numerical parameters associated with them. This freedom within the subgrid routines then allows, and requires, galaxy formation codes to be calibrated to reproduce chosen observables.

Typically, the approach when considering the effects of a given cosmological extension in a hydrodynamic galaxy formation simulation is to take an existing feedback model, and associated parameters, and vary the given extension(s), sampling multiple strengths (e.g. Lovell et al., 2017; Robertson et al., 2019b). This approach allows for the joint effects of cosmological extension to be modelled alongside, plausible, baryonic processes. However, the associated feedback parameters are not predetermined and, as mentioned previously, require calibration. Almost exclusively this calibration will have been performed assuming a Λ CDM cosmology. If it is expected that the cosmological extension being studied will affect the statistics originally used for calibration then that choice of feedback parameters may no longer be valid.

As such, what is needed is a joint exploration of both the cosmological extensions alongside the subgrid parameters. This would allow for any degeneracies between the two to be identified as well as uncertainties in the feedback prescription to be quantified. This is the focus of the chapter. Here I explore this in the context of the ARTEMIS simulations with a WDM cosmology. The ARTEMIS suite (Font et al., 2020) is a set of zoom-in high resolution simulations of Milky Way mass objects, using a (re)calibrated version of the EAGLE model (Schaye et al., 2015; Crain et al., 2015).

In Section 5.2 I cover the key details of the simulations. In Section 5.3 I discuss the baryonic (subgrid) parameters that we focus on, as well as how an emulator is built to predict various simulation statistics for a wide range of WDM masses and baryonic parameters. In Section 5.4 I use the emulator to study how the stellar masses of the host and satellite populations depend on both WDM, stellar feedback and the reionisation redshift. Finally, in Section 5.5 I summarise the results of this chapter and highlight future work.

5.2 Simulation details

In this section I highlight the key technical details of the simulations presented. Discussing how the systems to be resimulated were originally identified, how the zoom-in initial conditions are generated for the different WDM cosmologies and the key aspects of the EAGLE galaxy formation code.

5.2.1 Initial conditions

The simulations presented here are based on the ARTEMIS suite of high resolution zoom in simulations of Milky Way mass systems. The systems to be resimulated at a higher resolution were identified from an initial collisionless periodic volume with a box length of $25 h^{-1} M_{\odot}$ using 256^3 particles. From this a volume limited sample of DM haloes in the mass range $8 \times 10^{11} < M_{200c}/M_{\odot} < 2 \times 10^{12}$ were identified

as Milky Way mass systems. To minimise computational expense we focus on the smallest of the haloes in the sample (denoted as G42 in the original paper).

All simulations presented in this chapter share the same base Λ CDM parameters. These are the best fit WMAP9 cosmological parameters: $\Omega_m = 0.2793$, $\Omega_b = 0.2793$, $h = 0.70$, $\sigma_8 = 0.8211$, $n_s = 0.972$. CAMB (Lewis et al., 2000) is used to predict the linear power spectra, used to generate the initial conditions.

The zoom-in initial conditions are then generated using MUSIC (Hahn, Abel, 2011). Using the MUSIC terminology the base periodic volume uses a resolution level of 8 (256^3 particles), with the zoom region having resolution level of 11 (equivalent to 2048^3 particles). This corresponds to DM particle mass of $1.17 \times 10^5 h^{-1} M_\odot$ and an initial baryonic particles mass of $2.23 \times 10^4 h^{-1} M_\odot$. The zoom region was identified to contain all particles with $2R_{200c}$ of the $z = 0$ system in the initial, collisionless volume. The initial conditions are generated at $z = 127$ and use separate transfer functions for DM and gas particles.

The effects of WDM on the linear power spectrum can be written as

$$P_{\text{WDM}}(k) = T_{\text{WDM}}^2(k) P_{\text{CDM}}(k). \quad (5.1)$$

Where the functional form for T_{WDM}^2 proposed by Bode et al. (2001) is used,

$$T_{\text{WDM}}(k) = [1 + (\alpha k)^{2\nu}]^{-5/\nu}. \quad (5.2)$$

The values for α and ν use the best fit relations proposed by Viel et al. (2005) (assuming the WDM is composed of thermal relics). Here $\nu = 1.12$ and α is related to the DM mass, m_{DM} by

$$\frac{\alpha}{\text{Mpc } h^{-1}} = 0.039 \left(\frac{m_{\text{DM}}}{1 \text{keV}} \right)^{-1.11} \left(\frac{\Omega_m}{0.25} \right)^{0.11} \left(\frac{h}{0.7} \right)^{1.22}. \quad (5.3)$$

The CAMB transfer function is then modified by the above relations to generate the WDM initial conditions, again using MUSIC.

5.2.2 Baryonic and subgrid physics

The simulations presented in this chapter use the same prescription for baryonic processes as the EAGLE simulations. These are based on the Gadget-3 code (Springel, 2005), using a tree-PM method to solve for gravity and modelling hydrodynamics through a smooth-particle hydrodynamics scheme. The EAGLE model contains prescriptions for important processes that cannot be directly resolved, including metal-dependent radiative cooling in the presence of a photo-ionising UV background (Wiersma et al., 2009a), star formation (Schaye, Dalla Vecchia, 2008), stellar evolution and chemodynamics (Wiersma et al., 2009b), black hole formation and growth through mergers and gas accretion (Springel et al., 2005a), along with stellar feedback (Dalla Vecchia, Schaye, 2012) and feedback from AGN (Booth, Schaye, 2009). We refer the reader to the original EAGLE paper the above references for more details.

For the mass scales of interest here (Milky Way and below) AGN is ineffective at regulating star formation. Stellar feedback plays the most important role, with the assumed reionisation redshift being important at the smallest mass scales. As such, I focus on these two baryonic processes throughout this chapter. The details of how stellar feedback is implemented, along with the associated subgrid parameters, is outlined in the next section.

5.3 The Emulator

As mentioned previously, one of the key goals in this chapter is to simultaneously vary both the (subgrid) feedback parameters along with a cosmological extension, in this work that is WDM. However, this becomes a difficult problem due to the high dimensionality (here we will be exploring a 6 dimensional space) combined with the high computational expense of the simulations. One solution to this problem is to build an emulator that can quickly, and accurately, predict chosen statistics from a finite set of known realisations. This approach is currently becoming routine in many parts of cosmology and is used here to jointly explore cosmology and galaxy formation. In this

section I will firstly outline which parameters are chosen to vary, and how these are sampled. Then I will discuss how the emulator is built using a Gaussian process and which statistics are currently emulated.

5.3.1 Parameter choices

In this work I am primarily focused on studying the properties of the satellite populations of Milky way like systems. This is, therefore, within the dwarf regime. These mass scales are of particular interest as these are the objects most affected by changes to the assumed WDM mass. The corresponding baryonic parameters that are of interest are those that significantly affect these mass scales. This is primarily the stellar feedback, and at the smallest masses the reionisation redshift, with AGN feedback being inefficient at these scales. As such we aim to simultaneously vary the WDM mass, reionisation redshift and the stellar feedback parameters within the eagle model.

Due to the finite resolution of the simulations the feedback energy from supernova is distributed over too much mass. This results in a smaller temperature increase, corresponding to a too short radiative cooling time. This results in the effectiveness of stellar feedback to be interpreted in overdense environments. To compensate for this over cooling problem the EAGLE model (originally developed in Dalla Vecchia, Schaye (2012)) uses a stellar efficiency parameter that allows for the amount of energy coupled to the gas to vary as a function of environment, as detailed shortly. This relation cannot be predicted from first principle, and due to its numerical origin was used to calibrate the EAGLE model. Due to these freedoms the stellar feedback is a key focus in this chapter.

In the EAGLE model stellar feedback is implemented using a feedback efficiency parameter, based on the birth density of star particles. The functional form of this relation is

$$f(n_{\text{H,birth}}) = f_{\text{min}} + \frac{f_{\text{max}} - f_{\text{min}}}{1 + \left(\frac{n_{\text{H,birth}}}{n_{\text{H,0}}}\right)^{-\alpha}}. \quad (5.4)$$

Fig 5.1 shows the relation between feedback efficiency and stellar particle birth density,

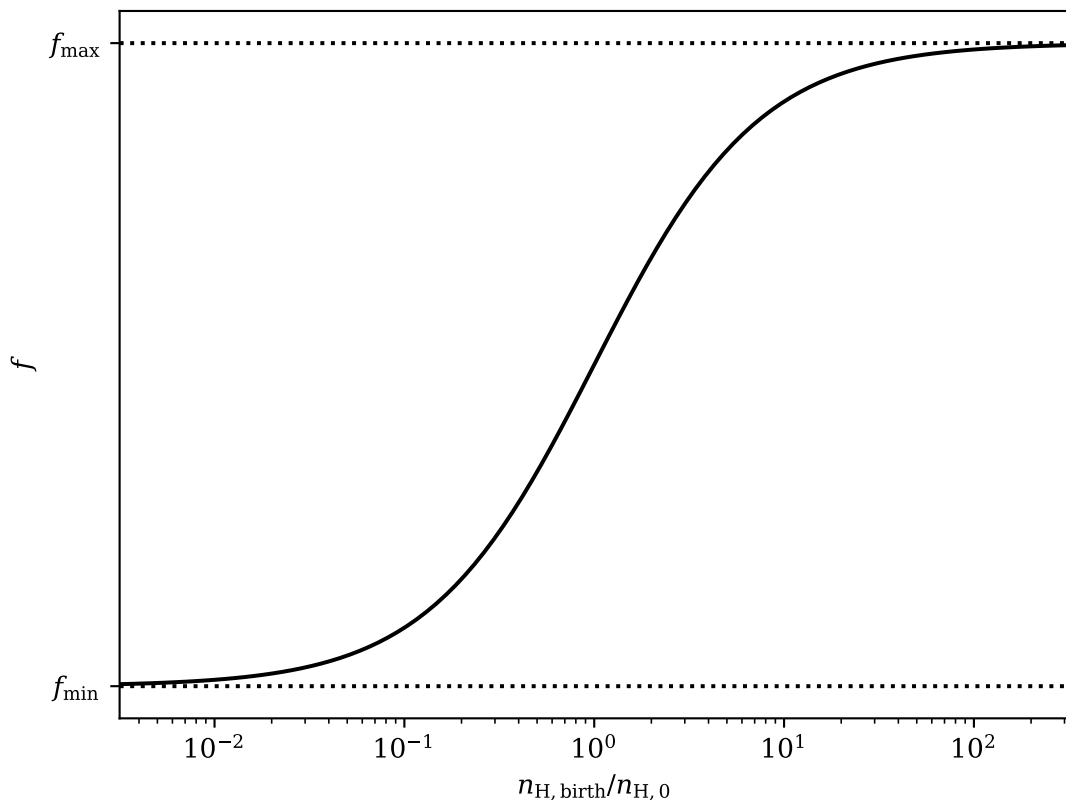


Figure 5.1: Example plot for the relation between the feedback efficiency and stellar birth density. This is the relation used in the `EAGLE` model to control the total effectiveness of stellar feedback in the simulations, see Eqn. (5.4). Here there are 4 free parameters. f_{min} and f_{max} control the minimum and maximum efficiencies, respectively, with $n_{\text{H},0}$ controlling the density at which the transition from low to high efficiencies occurs. α , not shown in the plot, controls how quickly the transition occurs with higher values of α corresponding to relation more closely following a step function.

Table 5.1: Table of the 6 parameters that are jointly varied for the simulations. This includes the WDM mass, m_{DM} , the reionisation redshift, z_{reion} , and four parameters associated with stellar feedback, f_{min} , f_{max} , $n_{\text{H},0}$ and α , see Eqn. (5.4). The fiducial values used in the ARTEMIS simulations are shown in the middle column. The final column shows the emulation range for these parameters.

Parameter	Fiducial value	Emulation range
m_{DM} [keV]	∞	[0.5, ∞]
z_{reion}	11.5	[5.5, 11.5]
f_{min}	0.3	[0.15, 0.4]
f_{max}	3.0	[1.5, 4.0]
$\log n_{\text{H},0}$ [cm^{-3}]	1.70	[0.0, 2.5]
α	1.0	[0.5, 4.0]

$n_{\text{H,birth}}$, with the main free parameters highlighted. As can be seen there are 4 free parameters in this relation that control the efficiency of the stellar feedback: f_{min} , f_{max} , $n_{\text{H},0}$ and α .¹ In general the behaviour of this relation is a step like function with low efficiencies of f_{min} at $n_{\text{H,birth}} \rightarrow 0$ and higher efficiencies of f_{max} as $n_{\text{H,birth}} \rightarrow \infty$. $n_{\text{H},0}$ controls at what scale this transition occurs, while α controls how quickly the transition occurs. It is then these parameters that were used to calibrate the stellar feedback in both the EAGLE and ARTEMIS simulations.

There are therefore 6 free parameters that need to be simultaneously varied; 4 stellar feedback parameters, the reionisation redshift and the WDM particle mass. The fiducial values used in the original ARTEMIS simulations are shown in Table 5.1.

To develop the emulator it is necessary to have a number of simulations that sample a combination of these 6 parameters. Ideally, this sampling should be relatively homogeneous. As such, an orthogonal Latin hypercube sampling is used, allowing for an even sampling of the 6-dimensional space. In this work 25 data points, corresponding to 25 different simulations, are used.

The range of the parameters sampled is shown in Table. 5.1. In general, the stellar feedback parameters are chosen to bracket the fiducial values but skewed to sample lower efficiencies (lower values for f_{min} and f_{max} , and larger values of $n_{\text{H},0}$). While, the reionisation redshift is chosen to, just, sample the fiducial value and cover

¹Note that the original eagle papers use a different symbol for α .

the currently preferred values ($z_{\text{re}} \sim 6$). Most of these ‘baryonic’ parameters are then linearly sampled, with $n_{\text{H},0}$ sampled logarithmically.

m_{DM} is not evenly sampled, as for the other parameters. This is primarily due to the issue that, ideally, the emulator should be able to sample a Λ CDM cosmology (effectively $m_{\text{DM}} = \infty$), but must be constructed to only sample a finite range. As such we use the following relation to sample the WDM mass,

$$m_{\text{DM}} = \begin{cases} (-45x + 49)/8 & \text{if } x > 0.2 \\ 1/x, & \text{if } x < 0.2. \end{cases} \quad (5.5)$$

Where x is assumed to be sampled from a uniform distribution between 0 and 1. From the above relation the range between $m_{\text{DM}} = \infty$ keV to $m_{\text{DM}} = 0.5$ keV can be sampled, corresponding to $x = 0$ and 1, respectively. The above equation has been constructed so that $m_{\text{DM}} = 5$ keV separates the different samplings; for $m_{\text{DM}} > 5$ the sampling is linear, while for $m_{\text{DM}} < 5$ the sampling is contracted by the $1/x$ relation. This mass scale is chosen as it, approximately, demarcates the regime where the effects of WDM become significant for the smallest resolved satellites in our simulations ($M_* \sim 10^6 M_{\odot}$).

The choices of parameters for the 25 simulations used to build the emulator are shown in Fig. 5.2 as a corner plot, showing all 2-dimensional projected combinations of parameters. As can be seen the use of an orthogonal Latin hypercube results in an even sampling of all parameters.

Alongside these 25 simulations there is an additional set used for testing the accuracy of the emulator. This includes 4 random choices of parameters, sampled within the range outlined above. As well as an additional 6 combinations of parameters chosen ‘by hand’ from an earlier stage of the project. This includes the fiducial Λ CDM cosmology with the same parameters used in the ARTEMIS suite of simulations.

All of these choices of parameters are then run for the smallest halo from the ARTEMIS sample, resulting in $25 + 4 + 6 = 35$ total simulations.

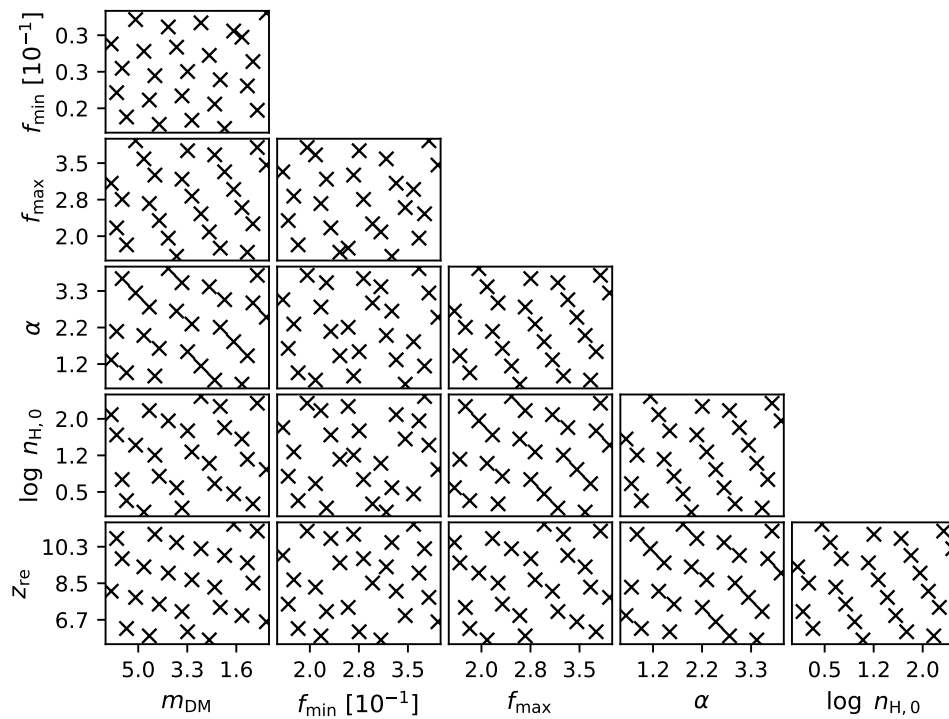


Figure 5.2: Corner plot showing the combination of the 6 parameters for the 25 simulations used to build the emulator. Here the sampling is done using an orthogonal Latin hypercube. This results in an even sampling of the space, as can be seen by all 2-dimensional projections shown.

5.3.2 Building the emulator

In this work a Gaussian process is used to build the emulator(s) that allows for fast predictions within the sampled parameter space. The emulator does not create a full realisation of a simulation, but instead aims to predict a set of statistics for a given combination of parameters. This is achieved by effectively interpolating between known realisations (referred to as nodes) in the 6-dimensional space. As such, the statistic(s) of interest must first be chosen. In this subsection I first describe the technical choices for the Gaussian process, before listing which statistics are focused on in this chapter as well as, where relevant, how the simulations are processed to infer the given statistic.

For the Gaussian process a combination of an anisotropic radial-basis function (RBF) and a white noise function are used for the kernel. The associated hyperparameters are then optimised to minimise the log-marginal-likelihood. The anisotropic RBF kernel allows for the dependence on the different parameters to be optimised. The white noise kernel allows for any noise in the data to be taken account, this is necessary as the results of galaxy formation simulations for a single object are somewhat stochastic in nature.² This version of the Gaussian process is used in all the emulators presented here, with the hyperparameters being separately optimised for each statistic.

The main statistics used are the stellar mass of the host and satellite galaxies. Specifically, the host stellar mass and cumulative satellite galaxy stellar mass function (GSMF) are emulated. The stellar mass of objects is taken to be the total stellar mass that is identified as being bound to each substructure from the SUBFIND algorithm. Additionally, only satellites within R_{200c} of the host are considered to remove the stochastic identification from the FOF algorithm. The cumulative satellite GSMF is calculated at 5 logarithmically spaced bins from $M_* = 10^6 - 10^8 h^{-1} M_\odot$. The training data from the Latin hypercube is presented in Fig. 5.3, with the fiducial Λ CDM cosmology shown for reference. As can be seen the sampling of these two statistics is somewhat biased, with respect to the fiducial Λ CDM realisation. Primarily, realisations with fewer satellites and a host with a lower stellar mass are sampled. The bias in

²Rerunning the simulation with the same feedback parameters, and same initial conditions, will not yield identical results. However, the mean of a large enough population will be unchanged.

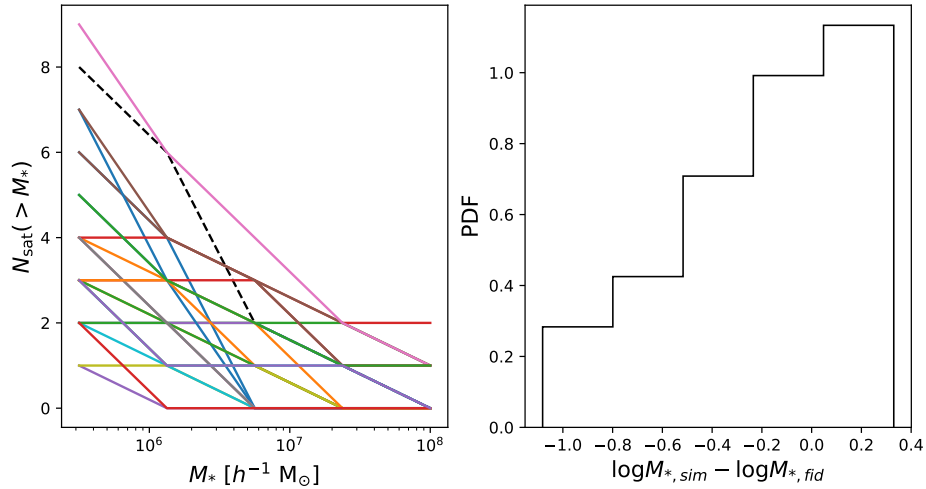


Figure 5.3: Resulting training data from the Latin hypercube sampling (see Fig 5.2). The left panel shows the cumulative satellite GSMF with different coloured lines corresponding to the different simulations, with the dashed black line showing the fiducial Λ CDM simulation for reference. The right panel shows the distribution of host stellar masses, quoted with respect to the fiducial Λ CDM simulation.

the number of satellites is primarily caused by the differences in WDM masses, which significantly reduces the satellite population. The bias in the host stellar mass appears to be caused by having off centred baryonic parameters, specifically chosen to sample less efficient feedback parameters to compensate for the effects of WDM.

In Fig. 5.4 I present the accuracy of the emulator for the test simulations, not used to train the Gaussian process. These include 4 random combinations of parameters and 6 combinations chosen ‘by hand’. As can be seen there are no significant systematic errors but non-negligible random deviations. The standard deviation of the difference from the emulator prediction to the simulation is used as the error on the emulator throughout this work.

5.4 Analysis

One of the main questions I will explore in this section is how closely the fiducial Λ CDM results can be reproduced for cosmologies with different assumed WDM masses when the baryonic parameters are allowed to vary. This is essentially asking if

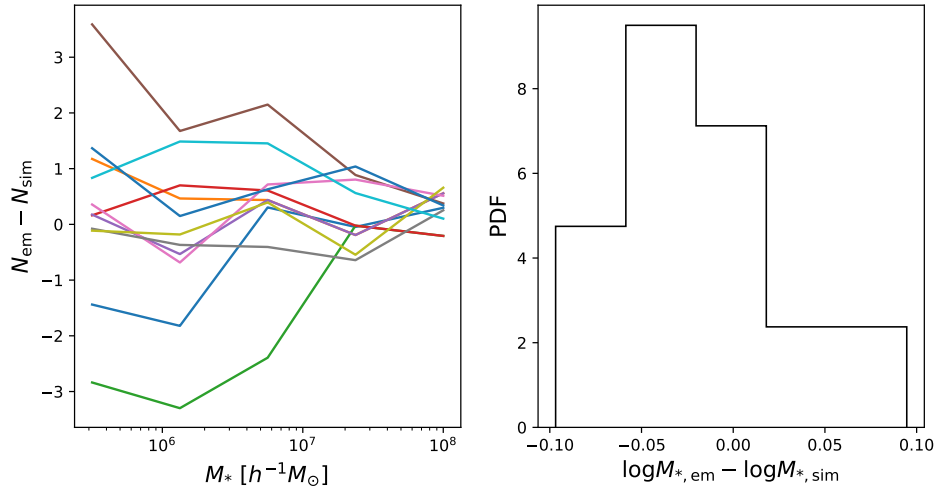


Figure 5.4: Accuracy of the emulator, tested against a range of simulations not in the training set. The left panel shows the difference in cumulative satellite GSMF from the emulator prediction to the simulation, with different coloured lines corresponding to different simulations. The right panel shows the distribution of differences in host stellar masses from the emulator prediction and the simulation results. The standard deviations from these plots are then treated as the error on the emulator.

the effects of WDM can be accounted for by recalibrating the simulations, and at what level are the effects of WDM and baryonic processes degenerate.

With these questions in mind, an effective way of exploring the 6-dimensional space effectively is to use Markov chain Monte Carlo (MCMC) sampling. The publicly available python package `emcee` (Foreman-Mackey et al., 2013) is used to perform all MCMC analysis in this chapter. A key part of any MCMC analysis is the definition of the likelihood function. In this work the log-likelihood will always take the following form, which assumes Gaussian errors.

$$\ln p(y|\theta) = -\frac{1}{2} \sum_n \left[\frac{(y_n - y_{em})^2}{\sigma_n^2} + \ln(2\pi\sigma_n^2) \right]. \quad (5.6)$$

Here, y denotes the given statistics considered, for this section it will either be the host stellar mass or cumulative GSMF, while θ represents a given choice of parameters (i.e. a given combination of WDM mass and baryonic parameters). y_{em} represents the prediction from the emulator, with σ_n the emulator’s error for the given statistic (see Section 5.3.2). y_n denotes the data to ‘fit’ to, which will be the fiducial Λ CDM

simulation, *not* the emulator prediction for that combination of parameters.

For the MCMC analysis the prior must also be specified. Throughout I will use a flat prior in the same range as the emulator.

By comparing the fiducial Λ CDM simulation, as described above, I am performing an ‘internal’ test for these simulations and the EAGLE model. This is clearly not the same as comparing the simulations to observational data. However, the fiducial Λ CDM simulations have been shown to closely match the satellite GSMF and, by construction, the host stellar mass of observed Milky Way massed objects. As such, this is a test of the predictive power of the simulations, comparing to a plausible host stellar mass and satellite GSMF.

5.4.1 Host stellar mass, fixed WDM mass

Initially, I present the MCMC analysis using just the host stellar mass, with a range of fixed WDM masses (specifically $m_{\text{DM}} = \infty, 5, 2.5$ and 1 keV). This is the statistic originally used for calibrating the ARTEMIS simulations. However, this calibration was achieved by only varying $n_{\text{H},0}$ from the original EAGLE calibration. The analysis in this subsection for the Λ CDM cosmology allows for an exploration of the freedoms within the original calibration when all parameters of the stellar feedback implementation are allowed to vary.

In Fig. 5.5 I present the posterior distributions for this analysis. The lower-left quadrant represents the corner plot showing all 2-dimensional projections, with the 1-sigma contour shown, and the 1-dimensional marginalised posterior for each parameter. The likelihood distribution is plotted in black in the top right, recall that this is a Gaussian distribution centred on the fiducial Λ CDM simulations host stellar mass with a standard deviation equal to the emulators accuracy (20%). The median host stellar mass from the MCMC chains. The different line colours represent different choices for the fixed WDM mass, see legend.

There are a number of key points that can be inferred from this plot, some more

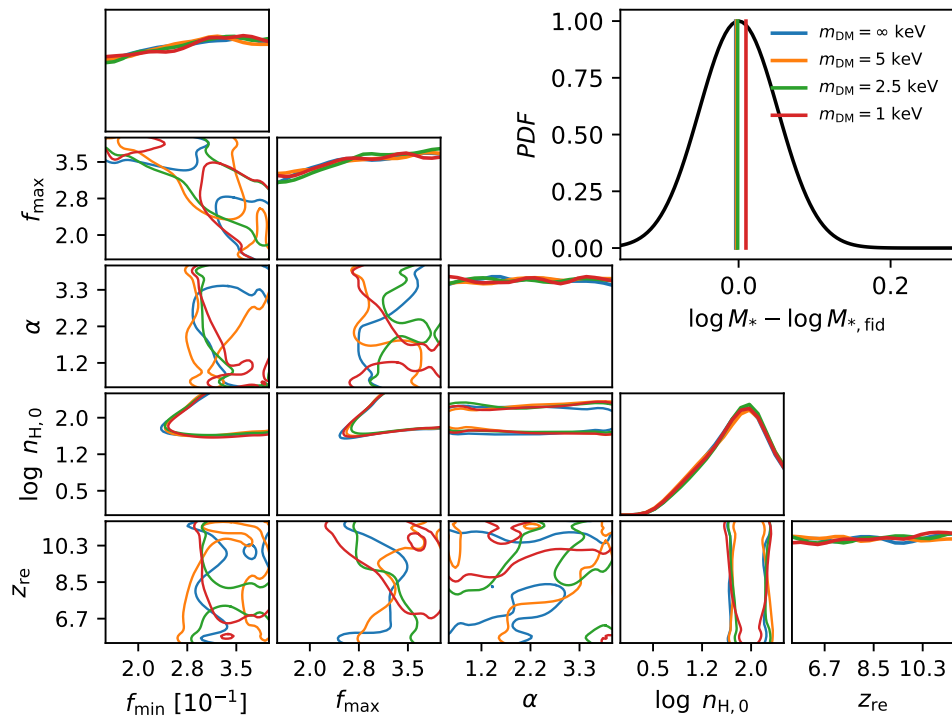


Figure 5.5: Posterior distribution from the MCMC analysis for the baryonic parameters, presented as a corner plot with the 2-dimensional projections showing the 1-sigma contours. Here the posterior is constrained by only the host stellar mass, see Section 5.4 for details. In the analysis the WDM mass is held fixed for a range of values, see legend. The top right panel shows the data being fit to (solid black Gaussian distribution), i.e. the host stellar mass, with the resulting median values from the MCMC chains shown as coloured lines.

intuitive than others. Initially, it is clear that the choice of WDM does not affect the results, this is most clearly seen from the 1-dimensional posteriors. This is expected as the range of WDM masses sampled here have a negligible effect on a $M_{200c} \sim 10^{12} h^{-1} M_{\odot}$ halo. Similarly, the results are insensitive to the reionisation redshift, as a system as large as the Milky Way is not sensitive to the effects of reionisation.

I now focus on the stellar parameters, $n_{H,0}$, f_{\min} , f_{\max} and α . As can be seen it appears that the host stellar mass is insensitive to the choice of α , a consistent theme throughout this work. However, there are clear preferences for the other three stellar feedback parameters. The host stellar mass is particularly sensitive to $n_{H,0}$, with a clearly defined maxima. This highlights why this parameter was used to calibrate the original ARTEMIS simulations. Unlike $n_{H,0}$ the f_{\min} and f_{\max} posterior do not have clear maxima, but do have preferred values. Generally, the largest values sampled are preferred. There is also a strong covariance between $n_{H,0}$ and f_{\min} and f_{\max} . Unfortunately, the full posterior for these parameters are not properly sampled, with all three parameters running into the edge of the emulation range.

5.4.2 Host stellar mass and satellite GSMF, fixed WDM mass

In this section I explore the posterior distribution when using both the host stellar mass, as was explored in the previous subsection, and the cumulative satellite GSMF. The results are presented in Fig. 5.6, with the structure of the plot the same as Fig. 5.5. Here the median resulting cumulative satellite GSMFs from the MCMC chains are shown with the fiducial Λ CDM simulation (black lines) and associated errors.

Before discussing the dependence of each parameter there are a few general trends that are important to discuss. Firstly, the posterior distribution now clearly depends on the assumed WDM mass. This highlights the need to jointly explore cosmological extensions alongside and the freedoms within the baryonic implementation, as is done in this work.

Focusing on the median GSMF for the Λ CDM cosmology highlights a key point

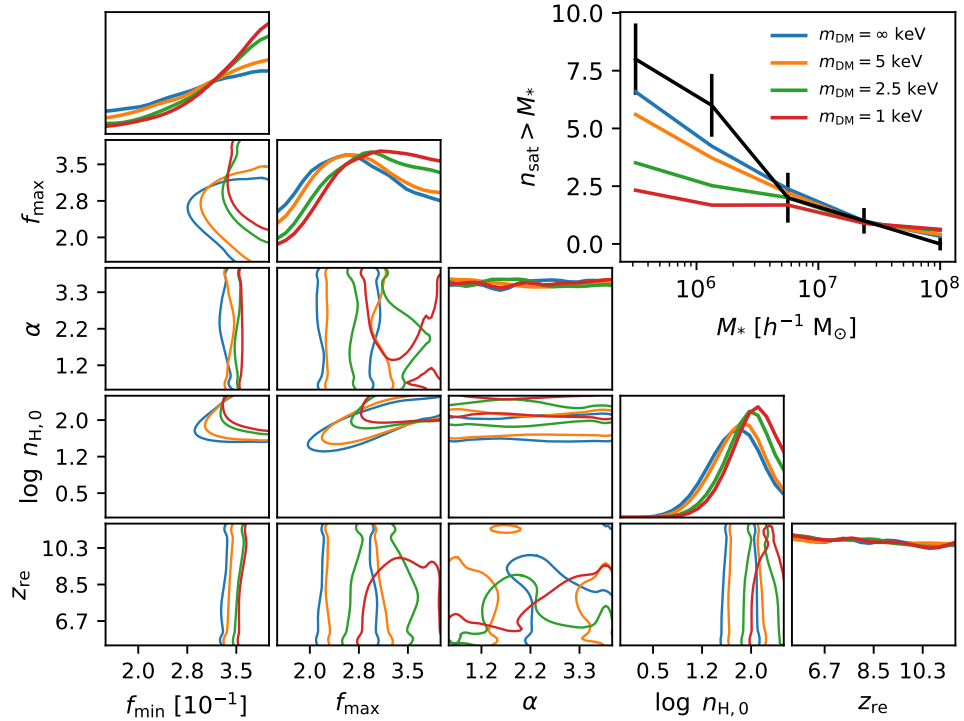


Figure 5.6: Same as Fig. 5.5, but fitting to both the host stellar mass and cumulative satellite GSMF. The top tight panel shows the data, with errors, being fit to (black lines) with the median relation from a random subsample of the MCMC chains (coloured lines).

that is relevant throughout this discussion. Here it is observed that the predictions from the emulator underestimate the GSMF at low masses. As the combination of parameters for the fiducial Λ CDM simulations are sampled by the emulator this indicates that there are some systematics within the emulator. However, the general behaviour for the different parameters should be unchanged, though the exact values and maxima may be somewhat biased.

As with the posterior from the fitting to only the host stellar mass it is observed that a subset of the baryonic parameters have little to no effect on the data. There is no indication that the GSMF is sensitive to the choice of α . Therefore I conclude that α is unimportant for setting the stellar mass of objects at all scales.

Similar to α it is observed that the results are insensitive to z_{re} . This is a surprising result, it is expected that the reionisation redshift should affect the number of

galaxies that form stars in the dwarf regime, which is sampled here. The current cause of this result is unclear, though there are a few possibilities. (i) The lack of a dependence on z_{re} is a general result, independent of these simulations and this analysis. This would be important, with significant impacts of our current understanding of the role of reionisation in galaxy evolution. (ii) This result is true for the EAGLE model, at this resolution, but not a general result for all galaxy formation models. This could either reflect the somewhat simple implementation of reionisation or possibly be due to the mass scales where reionisation plays an important role being at the resolution limit of these simulations. (iii) This result is primarily driven by some systematics in the emulator at small masses. Therefore, this result would be unique to the particular analysis presented here. The true origin of this result requires further analysis to determine which of these scenarios is happening. At the very least, these results do suggest that stellar feedback plays a more important role than reionisation in setting the GSMF at these scales.

Focusing initially on the Λ CDM results (blue lines) for $n_{\text{H},0}$, f_{min} and f_{max} it can be seen that introducing the GSMF puts tighter constraints on f_{min} and f_{max} . f_{min} still run into the edge of the emulators range, though the posterior now strongly disfavours lower values. f_{max} now has a clear maxima at $f_{\text{max}} \approx 2.5$, while $n_{\text{H},0}$ has a similar distribution as for fitting to just the host stellar mass. The covariance between f_{max} and $n_{\text{H},0}$ is also now more pronounced.

Arguably, the most interesting result here is the behaviour of the preferred values for $n_{\text{H},0}$, f_{min} and f_{max} for the different WDM masses. In general, stronger WDM cosmologies prefer larger values of $n_{\text{H},0}$, corresponding to weaker stellar feedback, while f_{min} and f_{max} prefer larger values, corresponding to stronger stellar feedback. This interplay between these parameters appears to be an attempt to fix the effectiveness of stellar feedback at high masses, i.e. to fix the stellar mass of the host and most massive satellites, while reducing the effective stellar feedback at low masses to boost their stellar mass and compensate for the reduced number of DM subhaloes. Although this behaviour is not unintuitive it would be difficult to predict without the results of this analysis, highlighting a key advantage of the approach presented here compared

to calibrating ‘by hand’.

The preferred baryonic parameters differ for the different WDM strengths. However, this is not able to completely compensate for the effects of WDM as can be seen by the sampled GSMFs. Here, all WDM cosmologies are below the data, as well as the sampled Λ CDM cosmologies (blue lines). This will be in part due to the emulation range being too narrow and not reliably marginalising over the baryonic parameters. As such it seems likely that some of the weaker WDM models, such as $m_{\text{WDM}} = 5$ keV, would be able to reproduce the fiducial Λ CDM result with a wider parameter space. However, it seems unlikely that the effects of stronger WDM models, such as $m_{\text{WDM}} = 1$ keV can be compensated for by changes to the stellar feedback.

5.4.3 Variable WDM

So far I have analysed the data using a fixed WDM masses to study the interplay between the baryonic implementation and the effects of WDM. However, this framework could also be used to put constraints on the WDM mass, marginalising over all other parameters. That is what is explored in this subsection. In Fig. 5.7 I present the posterior distributions when all parameters are allowed to be free, fitting to both the host stellar mass and cumulative satellite GSMF, as was done in the previous subsection. Here both the 1 and 2-sigma contours are shown.

It can be seen that this analysis allows for a strong constraint to be placed on the WDM mass, with an upper limit of $m_{\text{WDM}} = 8.4$ and 4.5 at the 1 and 2-sigma uncertainty. As the analysis strongly prefers a large WDM mass the posterior for the baryonic parameters closely resemble those from using a fixed Λ CDM cosmology (see Fig. 5.6, blue lines). The current prediction on the constraints for WDM is likely to be too strong. This is due to systematics in emulator, as even the predictions for the fiducial Λ CDM parameters are in mild tensions with the data, as well as the emulation range being too narrow to properly marginalise over the baryonic parameters. If these issues were not present, it is likely that the marginalised posterior for the WDM mass would be significantly weaker than quoted above. This analysis does demonstrate the

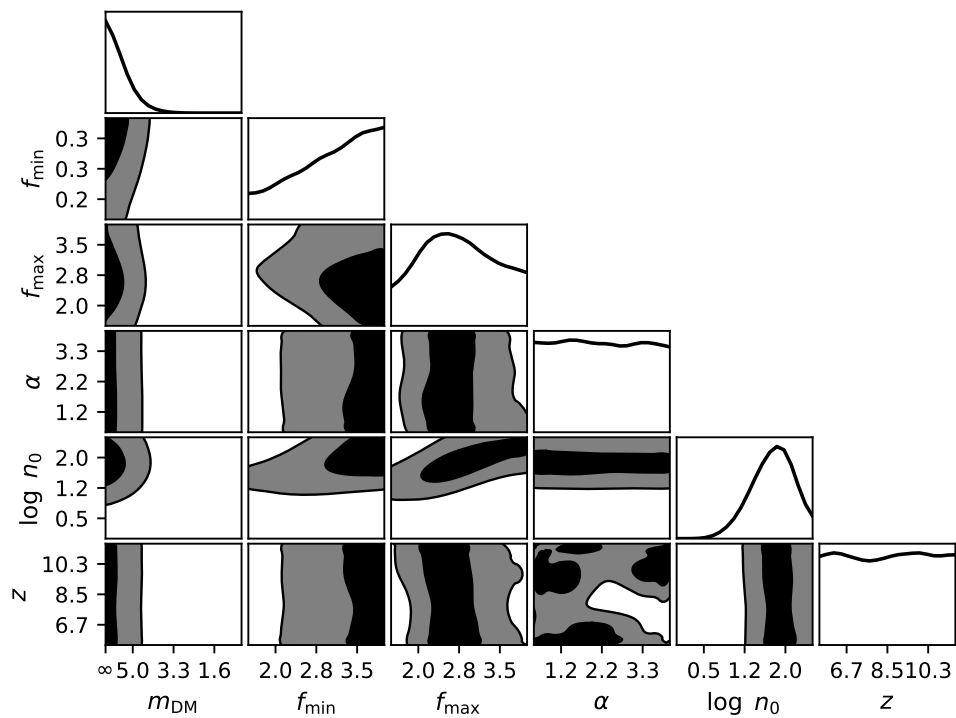


Figure 5.7: Same analysis as Fig. 5.6, fitting to both the host stellar mass and the GSMF. However, here the WDM mass was not held fixed but rather allowed to vary to test how well m_{DM} can be constrained. Here the corner plot now shows the 1 and 2-sigma contours. Note that the m_{DM} axis is scaled according to Eqn. (5.5), with a linear sampling for $m_{\text{DM}} < 5$ and a reciprocal scaling for $m_{\text{DM}} > 5$. As such, $m_{\text{DM}} = 0$ corresponds to the far left of the plotted axis.

way that meaningful constraints, that account for uncertainties in baryonic physics, can be placed on WDM and other cosmological extensions with similar effects.

5.5 Conclusions and future work

In this chapter I have explored the joint effects of WDM, stellar feedback and the reionisation redshift on the stellar masses of a Milky Way mass analogues and the satellite populations. To the best of my knowledge this is the first such study undertaken.

A fast and efficient exploration of the 6-dimensional (m_{WDM} , $n_{\text{H},0}$, f_{min} , f_{max} , α and z) parameter space is made possible by the use of emulation (Section 5.3.2). Here a Latin hypercube is used to sample the space with 25 simulations, from which a Gaussian process is trained to predict the statistics of interest. This reduces the computational expense by many orders of magnitude, with the simulations requiring $\sim 10^4$ cpu hours on a high performance supercomputer, while the emulator takes fractions of a second on a single cpu. This then allows for MCMC sampling to be used to explore the full parameter space.

One of the key things of interest in this work is identifying any degeneracies between the WDM mass and the baryonic parameters. Such degeneracies are indeed observed in Section 5.4.2 (see Fig 5.6). This result is particularly important as the majority of works looking at extensions to Λ CDM on these scales use a feedback model originally calibrated to a Λ CDM cosmology, and therefore do not take into account any uncertainty in the feedback implementation and, more importantly, any degeneracies between the feedback and the given cosmological extension. In this chapter I have demonstrated how these uncertainties and degeneracies can be accounted for to place reliable, marginalised constraints on various cosmological extensions. Here I have focused on WDM, though the general approach could be used for any extension to Λ CDM that has an effect at these scales.

There is still more analysis and work that needs to be done:

(i) The systematics in the emulator and the MCMC analysis running into the edge of the emulator's sampled range both need addressing. I expect both of these issues can be resolved by using a Latin hypercube with a wider range of parameters, where the necessary range can be estimated from the currently sampled posteriors (Fig. 5.6). Additionally, it would be useful to run the same analysis for a few additional haloes. The framework to do this is therefore already in place, and it is just the time necessary to rerun the simulations for the Latin hypercube.

(ii) In Section 5.4.2 it was found that the results are insensitive to the reionisation redshift, a surprising result. It is currently unclear if this is unique to this particular analysis, the EAGLE model or a general result. As such this requires further analysis. Running a Λ CDM simulation with the fiducial feedback parameters but with a significantly different reionisation redshift will help identify what is happening. Also an exploration of the star formation histories of the smallest haloes will help understand how the effects of reionisation propagate through to the stellar mass of dwarf haloes today.

(iii) Finally, it would be useful to consider how other statistics than stellar mass may help constrain cosmological extensions. As there is significant degeneracy between the stellar feedback and the WDM mass this suggests that this limits the ability to put strong constraints on m_{WDM} . As such, it would be useful to explore if additional statistics can break this degeneracy. Stellar feedback must be made less efficient at low masses to compensate for WDM, as such some promising statistics would be: the mass to light ratio as the DM mass of subhaloes is mostly insensitive to feedback. Additionally the metallicities and the quenched fractions should be promising statistics due to changes in the star formation histories of dwarf galaxies.

Chapter 6

Summary & Conclusions

In this section I review the research and results of this thesis. I will briefly summarise each research chapter in turn, highlighting some of the key results.

6.1 Connecting the structure of dark matter haloes to the primordial power spectrum

In Chapter 3 I study the link between the primordial power spectrum and the present day internal structure of DM haloes. This is achieved by systematically varying the amplitude and slope of the linear power spectrum, allowing for the two effects to be isolated. Interestingly, for cosmologies with significantly higher amplitudes than our Universe a number of assumed universal results break down. Specifically, it is observed that the density profiles of DM haloes deviate strongly from an NFW form, with observed outer slopes steeper than -3 . In general, there is no observed evidence for any limit to the steepness of the DM density profile; while these results conclusively demonstrate that there is not an outer asymptotic slope of -3 it seems unlikely that the general idea of an outer asymptotic slope is correct. The entropy profiles (or similarly PPSD profiles) are observed to obey a power law behaviour, however the slope is observed to exhibit a clear mass and cosmology dependence, not observed

before.

By isolating the effects of shape and amplitude changes to the linear power spectrum it is concluded that the density and velocity dispersion profiles are predominantly set by the amplitude of the linear power spectrum at an associated scale, with the slope, or shape, of the power spectrum having little to no effect.

6.2 Towards a universal model for the density profiles of dark matter haloes

In Chapter 4 I present a model to predict, for the first time, both halo concentration, c , and the shape parameter, α , for a general mass, redshift and cosmology.

Using the simulations introduced in Chapter 3 I explore the idea that halo concentration and shape parameters can be expressed as a single function of peak height, using a different window function than traditionally used. To explore a wide range of effective window functions the smooth k-space window function is used, with two free parameters, μ and β . The optimal window function is quantified through the χ^2 of the resulting c and α peak height relations. Here it is observed that there is a strong degeneracy between μ and β . The form of this degeneracy suggests that the important feature is getting the peak of the $k^2W^2(k)$ function at the correct scales. This in turn implies that it is the amplitude of the linear power spectrum at an associated scale that sets the concentration and shape parameter of DM haloes. Interestingly, this preferred scale is different for c and α , suggesting they are set by different scales in the primordial density field.

With the optimal window function constrained, accurate empirical fits to the resulting universal $c-\nu_c$ and $\alpha-\nu_\alpha$ relations are found. This then allows for a simple model to be created, where c and α can be predicted for a wide range of masses, redshifts and cosmologies from these empirical functions.

6.3 ARTEMIS Dark

In the final research chapter I present ongoing work studying the joint effects of warm dark matter and baryonic processes on Milky Way mass systems and their satellite populations. In this chapter I jointly vary the stellar feedback parameters alongside the epoch of reionisation and the assumed WDM mass, with the goal of exploring if WDM changes the preferred subgrid parameters from the fiducial calibration, as well as how the constraints on the WDM mass change when the baryonic parameters are effectively marginalised over.

A key challenge in undertaking such a study is the computational expense of the simulations. This is overcome by developing an emulator using Gaussian processes that can sample a combination of the emulator parameters extremely quickly. This allows for fast and exhaustive exploration of the available parameter space.

Currently, the analysis focuses on studying the stellar mass of these systems, primarily through MCMC sampling. Specifically studying the stellar mass of the host galaxy (the Milky Way analogue) and the satellite GSMF of the system. Here it is found that the key parameter in setting the host stellar mass is $n_{\text{H},0}$, the transition scale of the stellar feedback relation, with little to no constraint on the other baryonic parameters. It is also observed that the host stellar mass is unaffected by the sampled WDM masses (minimum mass of $m_{\text{DM}} = 0.5$ keV), as expected. When the MCMC analysis is constrained by both the host stellar mass and the satellite GSMF most of the baryonic parameters have clearly preferred values. Most importantly, the optimal values depend strongly on the assumed WDM mass, highlighting that a feedback model originally calibrated for a Λ CDM cosmology may not be appropriate for simulations studying cosmological extensions. Additionally, to be able to place reliable constraints on these cosmological extensions uncertainties in, and degeneracies with, the feedback implementation should be accounted for, as demonstrated in this chapter.

Appendix A

A.1 Density and velocity dispersion calculation methods

Typically throughout the literature radial density profiles are calculated using logarithmically spaced bins, essentially taking a histogram of the radial position of particles before normalising to convert to a mass density. Most often bins are taken as a set number, N_{bins} , spaced logarithmically from a minimum to a maximum fraction of R_{200c} , $r_{\text{min}}/R_{200c} < r/R_{200c} < r_{\text{max}}/R_{200c}$. Typical values are: $N_{\text{bins}} \sim 20 - 50$, $\log(r_{\text{min}}/R_{200c}) \sim -3 - -1$ and $r_{\text{max}}/R_{200c} \sim 0.7 - 1$ (or much higher if the work specifically focused past R_{200c}).

The standard approach described above is a particular form of a more general method to calculate the density (or similarly number/probability density) from a finite sample of data points. More generally a weight function can be used to estimate these quantities. There are two key free parameters associated with using a weight function, the ‘shape’ of the function used and its width. In the standard method the ‘shape’ is a top-hat function and the widths are chosen to be logarithmically spaced.

Associated with using a weight function are two types of error. The first being Poisson noise due to having a finite amount of data, this type of error is purely random. The second is systematic errors associated with the width of the kernel, essentially error due to trying to sample the density at a singular location by using data over

a range of radii. These two errors work in opposite ways, Poisson errors decrease with a larger kernel width while the systematics respond in the opposite manner. This suggests that for a particular problem there is an optimal kernel width to use.

Consider the following problem in one dimension. Given a set of particles (or simply data points) at positions x_i , where $i = 1, 2, 3 \dots N$, estimate the number density function, $n(x)$, that they have been sampled from. This is equivalent to trying to calculate the mass density as a function of radius for a halo, only with a different normalisation from 1D to 3D as well as a mass term. One way to estimate $n(x)$ is to use a weight function, as I will discuss here. To estimate $n(x)$ the following relation is used,

$$n_{\text{calc}}(x) = \sum W((x_i - x)/h). \quad (\text{A.1})$$

Here I have used the subscript $n_{\text{calc}}(x)$ to distinguish this as the estimate of the true $n(x)$. h is the ‘width’ of the weight function and is a free parameter of the method. $W(x)$ is a general weight function which is assumed to have the following properties: (i) the function is symmetric about $x = 0$, (ii) the function is zero in the range $|x - x_i|/h > 1$ and (iii) the weight function is normalised such that $\int_{-\infty}^{\infty} W(x)dx = 1$.

As discussed before, in general, $n(x) \neq n_{\text{calc}}(x)$ due to two main types of error. We can therefore write, with a summation ansatz, $n(x) = n_{\text{calc}} + n_{\text{Poisson}} + n_{\text{sys}}$. The first error term, n_{Poisson} , is the Poisson error and completely random. We expect this error to scale as $n_{\text{Poisson}} \propto \sqrt{N_{\text{Kern}}}$, the number of points contained within the kernel. The second term is the systematic error, and is the residual left when $N_{\text{Kern}} \rightarrow \infty$. The leading order dependence is as follows,

$$n(x) + n_{\text{sys}} = \int_{-\infty}^{\infty} n(x')W\left(\frac{x - x'}{h}\right)dx' = n(x) + \mathcal{O}(h^2n''(x)). \quad (\text{A.2})$$

The systematic error scales as $\mathcal{O}(n''(x)h^2)$.

We cannot put a strict form on the optimal $h(x)$ as this would involve *a priori* knowledge of $n''(x)$. We can, however, derive the scaling with the total number of data points N_{tot} , i.e. how h should behave in cases of different numerical resolution. If

we require that for all resolutions we wish to be in a regime where neither error term dominates the other then we require that $n_{\text{Poisson}}(N_{\text{tot}}) \propto n_{\text{sys}}(N_{\text{tot}})$.

To proceed we need to parameterise the general form with which we will vary the kernel width. There are a few possible options, including using a fixed number of particles in the kernel.¹ However, after trying a few different methods and comparing the results it appears the optimal option is choosing $h(x)$ such that it is equivalent to logarithmically spaced bins. The logarithmic spacing of bins can be calculated as the following,

$$\Delta = (\log_{10}(r_{\text{max}}) - \log_{10}(r_{\text{min}}))/N_{\text{bins}} \quad (\text{A.3})$$

and is related to the kernel width by

$$h(x) = (10^\Delta - 1)/(10^\Delta + 1)x = Ax. \quad (\text{A.4})$$

This highlights that the term ‘logarithmically spaced bins’ is equivalent to a kernel width that scales linearly with radius. To first order it is found that $n_{\text{Poisson}} = \sqrt{2n(x)h(x)}$ and $n_{\text{sys}} = n''(x)h^2(x)$. The kernel width should therefore scale with N_{tot} in the following way,

$$A = h_0 N_{\text{tot}}^{-1/3} \quad \text{or} \quad \Delta = \log\left(\frac{1 + h_0 N_{\text{tot}}^{-1/3}}{1 - h_0 N_{\text{tot}}^{-1/3}}\right) \approx \frac{h_0 N_{\text{tot}}^{-1/3}}{\ln 10}. \quad (\text{A.5})$$

The parameter, h_0 , depends in a complicated way on the particular weight function used and density function trying to be estimated. However, it is directly related to the ratio of systematic to random error, $n_{\text{Poisson}}/n_{\text{sys}}$, wished to be imposed. This derived behaviour with N_{tot} is consistent with the qualitative expectation; for a more highly sample function the kernel can be narrower to minimise systematics before counting error becomes dominant, and for more coarsely sampled profiles a wider kernel is required to have enough particles to reliably estimate $n(x)$.

An equivalent analysis can be applied to the velocity dispersion to find the equivalent scaling with N_{tot} . Although the systematic errors have a different N_{rmtot} depen-

¹Equivalent to how many smooth-particle hydrodynamics schemes estimate densities.

dence it is found that after imposing the condition that $n_{\text{Poisson}}(N_{\text{tot}}) \propto n_{\text{sys}}(N_{\text{tot}})$ that the same $N_{r_{\text{mtot}}}$ dependence is required. We therefore also use $A = h_0 N_{\text{tot}}^{-1/3}$ for calculating velocity dispersions.

A.1.1 Choosing appropriate parameters

We can relate the above discussion directly to calculating the density and velocity dispersion profiles of real haloes in a cosmological simulation. Working in scale-free dimensionless coordinates, with radii scales by R_{200c} , particle masses scales by M_{200c} and densities scaled by ρ_{200} then dark matter haloes are approximately self-similar. There is, however, a systematic dependence of the concentration parameter with mass that should be kept in mind. If, for the moment, we neglect this mass-concentration relation then what we would expect in such a self similar universe is the exact situation above were we want to estimate densities with a varying mass resolution (i.e. number of particles). For a density profile of finite mass $N_{\text{tot}} \propto N_{200}$, so we can directly use Eqn. (A.5) with N_{200} in place of N_{tot} . To be able to apply either method to a general N-body simulations we still need to find appropriate values of h_0 . I will find the optimal choice of h_0 empirically using a numerical approach.

I use a Monte-Carlo approach to study how well various values of h_0 recover the density and velocity dispersion profiles. For this I study Einasto density profiles at variable resolutions. I assume that haloes are statistically perfect Einasto profiles and generate random positions such that they match the equivalent probability density function. The number density (per unit volume) of such a profile can be written in the following way,

$$n(x) = B(\alpha, r_{-2}) N_{200} \exp(-2/\alpha((x/x_{-2})^\alpha - 1)). \quad (\text{A.6})$$

$x = r/R_{200c}$ (with x_{-2} assumed to be similarly normalised) and B is a normalisation factor, $B(\alpha, r_{-2}) = 1/(4\pi(x_{-2}/(2\alpha)^{1/\alpha})^3 \Gamma(3\alpha) \exp(2\alpha) \Gamma(3\alpha, 2/(\alpha x_{-2}^\alpha)))$. I then generate the probability density function by numerically solving for the cumulative

distribution function.

In this analysis I try to recreate the process that would be applied to haloes as accurately as possible. I calculate the density and velocity dispersion at 30 logarithmic spaced radii from $\log(r) = -2$ to 0 . The figure of merit used to define the errors is as follows,

$$\psi^2 = \sum_{N_{\text{bins}}} (\log(\rho_{\text{calc},i}) - \log(\rho))^2. \quad (\text{A.7})$$

I use this parameter to give an indication of the errors (both random and systematic) on the given profile. I also minimise this quantity to fit the calculated profiles. All profiles are only fit over the range where the sampled radii exceed the convergence radius (Ludlow et al., 2019b).

I also study how these quantities vary with different concentration parameters. I assume $\alpha = 0.16$ for all of the subsequent analysis. For each quantity I look at how errors vary with N_{200c} , concentration (assuming $\alpha = 0.16$) as well as the method employed. I also include a fiducial model where the standard method is used with 31 logarithmically spaced bins over the same range, with the key point being that it is a method whose width does not vary as a function of N_{200c} .

For each N_{200c} I average over 100 different random seeds to obtain typical values. As well as systematically varying x_{-2} (from $1/2$ to $1/50$).

In Fig. A.1 I present how ψ^2 (averaged over 100 different seeds) varies as a function of N_{200c} for a halo with $r_{-2} = 1/10$ and $\alpha = 0.18$. In general the wider the kernel (larger values of h_0) results in a smaller ψ^2 . The only exception to this is in the region $N_{200c} < 10^3$ which, for $h_0 = 10$, corresponds to the where $h > r$ so will end up with non-physical results. Looking at the fiducial model (black line) it appears that it is a middle ground to some of the other parameters, with errors at low N_{200c} larger than other models but performing better at high values. The fiducial model appears to be the optimal choice in regard to minimising ψ^2 at $N_{200c} = 10^6$, however for most simulations haloes of this size will only be a few and the errors for $h_0 = 10$ and 3.16 are still small.

I next focus on the averaged fitted parameters, x_{-2} and α , to make sure they can be reliably recovered. This part of the analysis should most definitely be considered as it was found that minimising ψ^2 does not necessarily minimise the error on the fit and can, if mismanaged, lead to significant systematic errors. I present the average of these fitted parameters in Fig. A.2. We can see that for the well resolved haloes, $N_{200c} > 10^3$, All choices of parameters other than $h_0 = 0.1$ results in minimal systematic on the fitted parameters with errors $\sim 1\%$.

Based on this analysis it appears that the best choice is $h_0 = 10$. However this analysis has been done on *mathematically perfect* haloes. For real haloes with substructure we want a kernel narrower than the optimal one found from this study. I therefore choose $h_0 = 500^{1/3}$. I also apply a resolution cut of $N_{200c} = 2000$ so that we are in the regime where $\psi^2 < 10^{-2}$ and the large scatter found in fitted parameters in the low resolution limit ($N_{200c} < 10^3$).

Although not presented here, the analysis was also applied to haloes with concentrations ranging from $c = 2$ to 50. The key results are the same and doesn't change the conclusion of the optimal value of h_0 . The only notable difference observed for differently concentrated haloes is that haloes with lower concentrations lead to larger errors both on the density profiles and the fits. This trend is fairly mild, but does rule out issues with calculating the densities for the extreme concentrations observed in this work. There were no observed differences in the reliability of finding the densities for variation in α .

All of the above analysis was applied to the velocity dispersions as well. To generate a velocity dispersion I numerically solve the Jeans equation, assuming isotropic velocities, to find the velocity dispersion as a function of radius for a given Einasto profile normalising it so that the maximum velocity dispersion is unity. The velocities are then assumed to be a Gaussian about zero with a standard deviation equal to the velocity dispersion. Although it didn't have to be the case it is found that $h_0 = 500^{1/3}$ is also optimal.

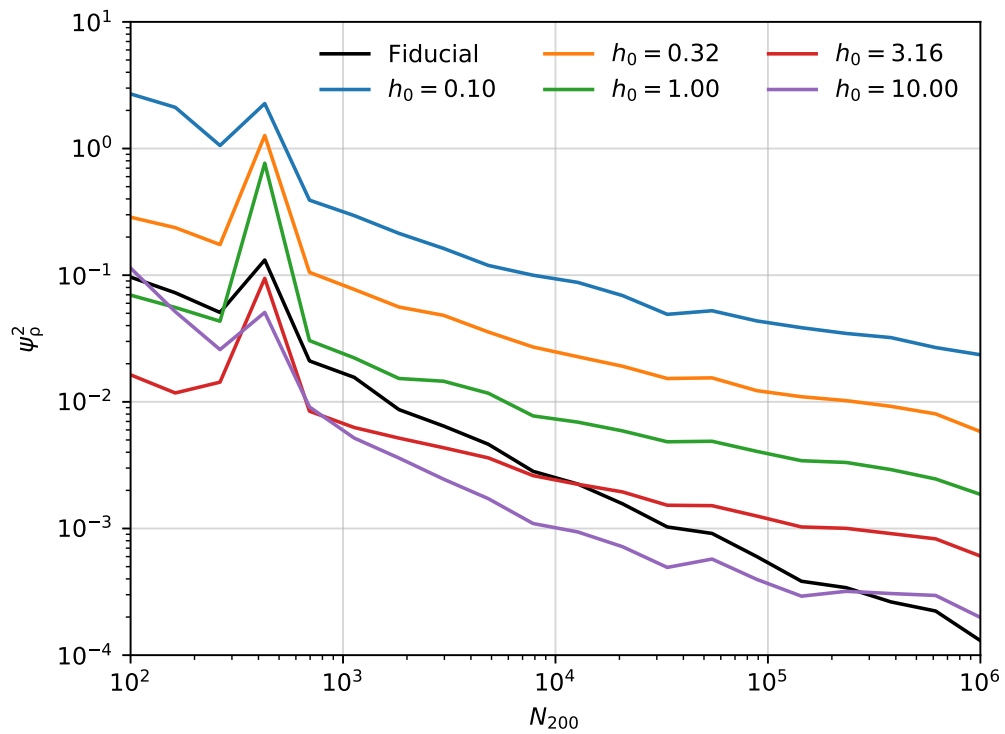


Figure A.1: Figure of merit for the calculated density profiles, see Eqn. A.7, as a function of resolution, N_{200c} . Each value is averaged over 100 different haloes. Each line represents a different choice of parameter, h_0 , see legend. Plotted in black on each plot is the standard method.

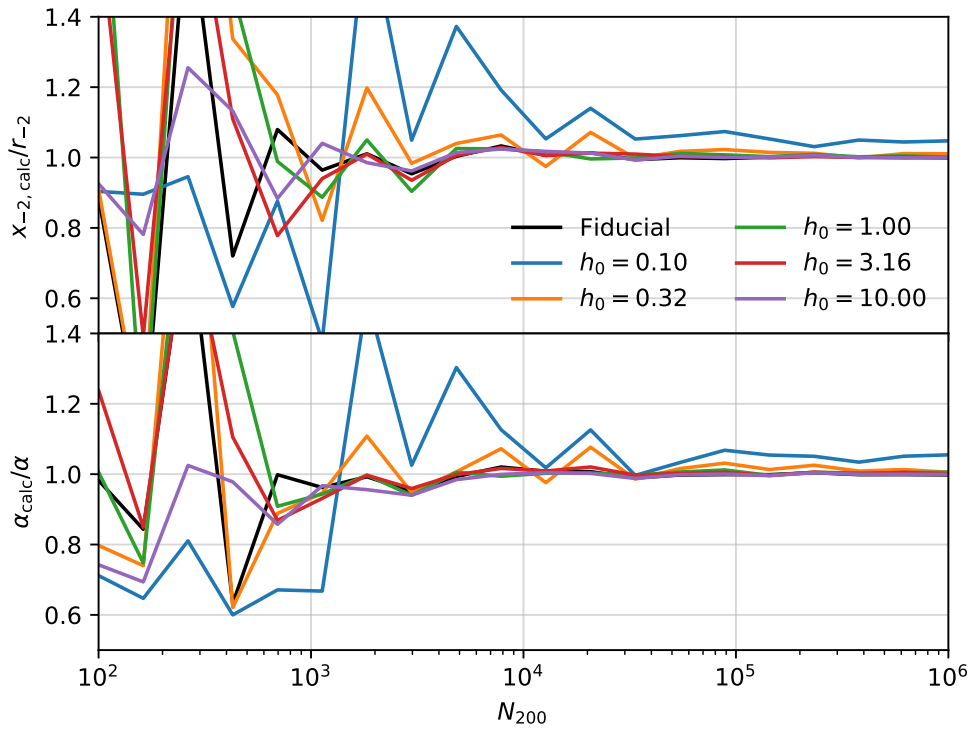


Figure A.2: Fitted Einasto parameters, x_{-2} (top panel) and α (bottom panel), as a function of resolution for the various sampled parameters, h_0 , see legend. The fitting is done to minimise ψ^2 and is fit over the range $r_{\text{conv}} < r < R_{200c}$, where r_{conv} is the convergence radius, and the values are averaged over 100 different haloes. In each panel the standard method is plotted in black for reference.

A.2 Resolution test and box size tests

In this work I have assumed that the density, entropy and velocity dispersion profiles are converged in the regime where $r > r_{\text{conv}}$. Where r_{conv} is the found using the relation in Ludlow et al. (2019b). In the work of Ludlow et al. (2019b) the condition for convergence was derived from a suite of simulations with cosmologies close to our own. As such the haloes studied were drastically different to some in this work, with orders of magnitude different concentrations. It is therefore possible that this condition for convergence does not hold in these more extreme cosmologies.

To check that this is not a factor in this work I have two different resolution simulations WMAP9 pivot with variable n_s suites with a box size of $100h^{-1}\text{Mpc}$. In this way I can make sure that both amplitude and shape changes to the initial power spectra are not a convergence issue. The two comparison suites of simulations are almost identical (same box size, same cosmologies, same initial redshift, etc) but use 512^3 and 256^3 particles, corresponding to particle masses of $4.62 \times 10^9 h^{-1} M_\odot$ and $5.78 \times 10^8 h^{-1} M_\odot$ respectively.² I have modified the scaling relations for the kernel width, Eqn. (3.7), to make the different resolution simulations equivalent and remove this as a factor in the comparison.

In Fig. A.3 I present the stacked density profiles for haloes between $10^{13}h^{-1} M_\odot$ and $10^{13.5}h^{-1} M_\odot$, hence directly comparable to Fig. 3.3, of the two different resolution suites of simulations. As with the rest of the paper different shades of red represent different values of n_s while here the two different line styles show the different resolutions, see legend. In the top panel is plotted the density, the middle panel the logarithmic slope and the bottom panel show the ratio of densities for the two different resolutions.

It can be seen in the ratio plots that all of the simulations studies here are indeed converged with $r > r_{\text{conv}}$. With maximum errors of $\sim 10\%$ and more typical errors of only a few percent. Although not shown here equivalent convergence trends are seen for the entropy and velocity dispersion profiles. In the regime $r > r_{\text{conv}}$ they are well

²The softening length has also been changes appropriately from $\epsilon = 4h^{-1} \text{Mpc}$ to $\epsilon = 2h^{-1} \text{Mpc}$.

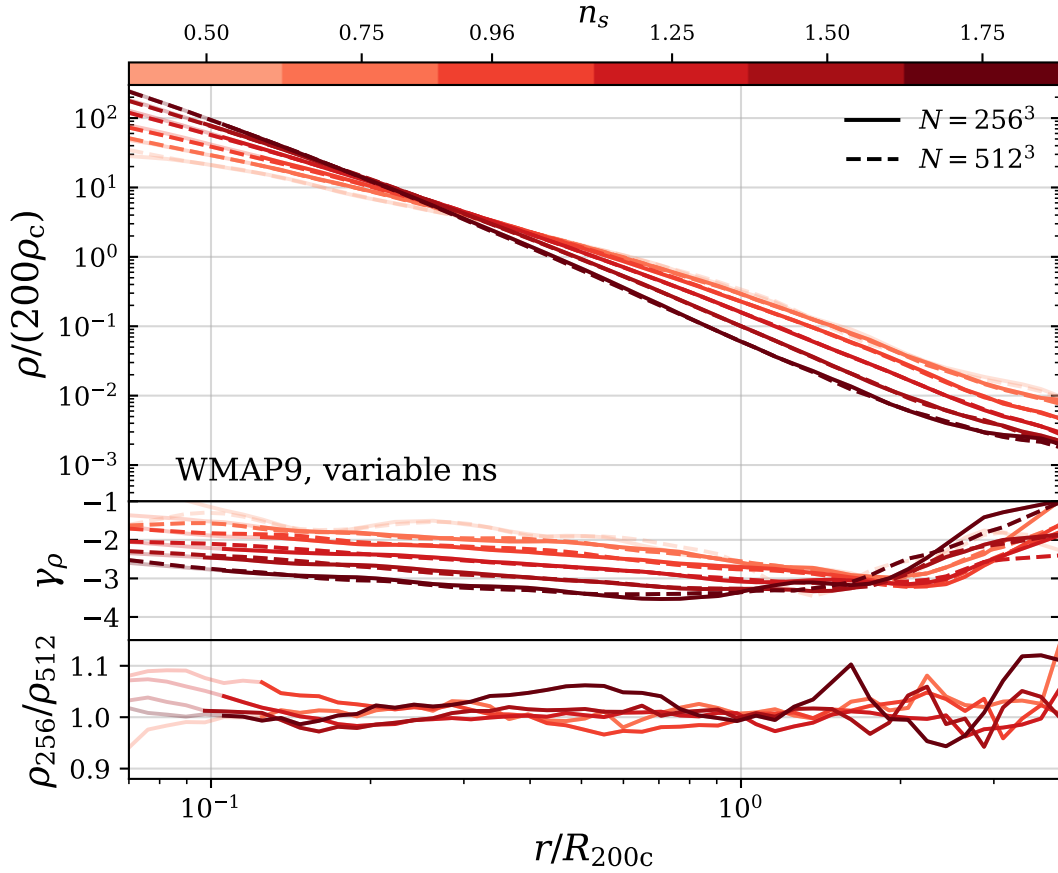


Figure A.3: Stacked density profiles for haloes in the mass range $M_{200,c} = 10^{13} - 10^{13.5} h^{-1} M_\odot$ for two different mass resolution simulations. Solid lines represent the simulation using 256^3 particles while dashed 512^3 . The different shades represent the different values of n_s used to generate the initial conditions. In the top panel is shown the density profiles, the middle panel shows the logarithmic slope while the bottom panel the density ratios for the two different resolutions. Transparent parts of the lines represent regions not meeting the condition for convergence, while opaque lines represent the opposite.

converged, again $< 10\%$.

Additionally I have checked that the finite box size is not an issue for the statistics studied in this work. This was done by simulating the most extreme cosmology in the suite with variable A_s , corresponding to $\sigma_8 = 8.103$ (see Table 3.1) at three different box sizes with consistent particle masses. The results of this test are shown in Fig. A.4, where it can be seen that the density profiles are converged to within a few percent for all box sizes studied here. Although not shown here I find similarly well converged results for the entropy and velocity dispersion/anisotropy profiles.

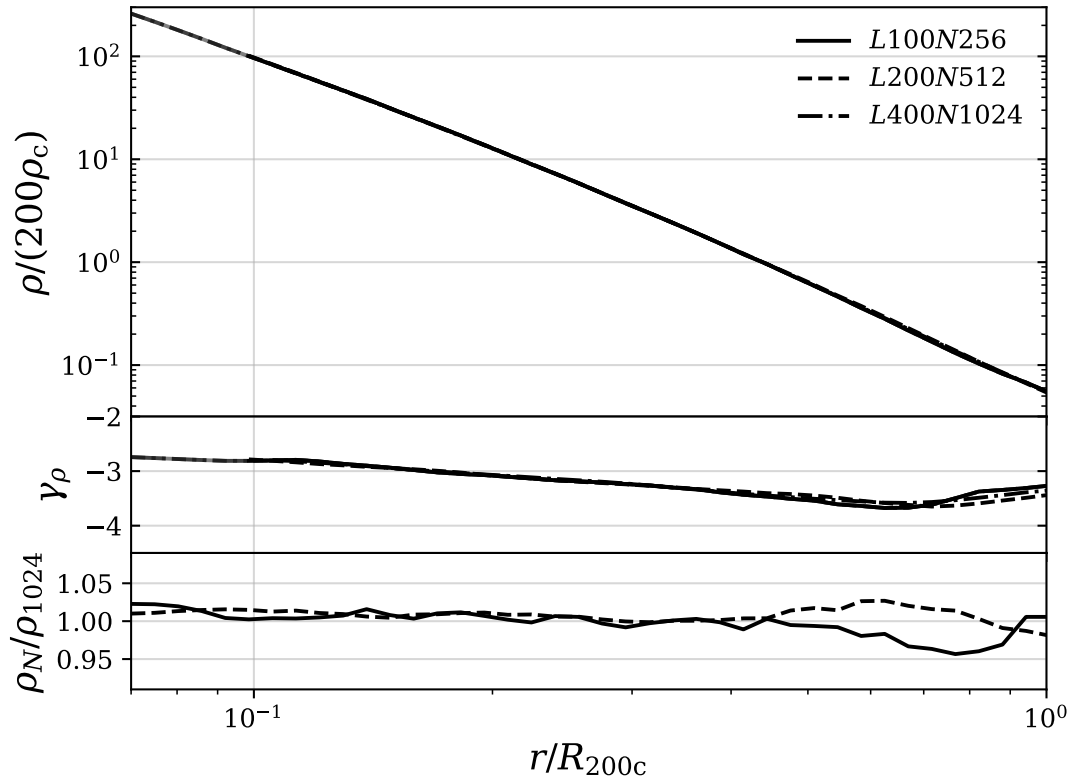


Figure A.4: Stacked density profiles for haloes in the mass range $M_{200,c} = 10^{13}\text{--}10^{13.5}h^{-1}M_{\odot}$ for the most extreme cosmology in the suite with variable A_s , corresponding to $\sigma_8 = 8.103$ (see Table 3.1), simulated at three different box sizes with fixed mass resolution. Solid lines represent the simulation using 256^3 particles and a box size of $100 h^{-1}\text{Mpc}$, dashed lines represent 512^3 particles with a box size of $200 h^{-1}\text{Mpc}$ and dot-dashed lines represent 1024^3 particles with a box size of $400 h^{-1}\text{Mpc}$. The top panel show the densities, the middle the logarithmic slope and the bottom panel the ratio with respect to the largest box.

Appendix B

B.1 Resolution and box size study

In this section I present the c -mass and α -mass relations as a function of varying box size and mass resolution for a few of the cosmologies presented in this paper. The following notation will be used to specify box size and number of particles used in the simulations: L<Boxsize>N<particle number>. For instance, L400N1024 denotes a simulation using a $400 h^{-1}M_{\odot}$ with 1024^3 particles, which is the box size and number of particles used throughout the main part of this work. Presented here are simulations with L200N512, L400N1024 and L200N1024. The details of the simulations and how they are analysed to determine values for c and α are identical to that described in Section 4.2 with the softening length changed appropriately for the higher-resolution L200N1024 simulation, with this simulation using $2 h^{-1}\text{Mpc}$ as opposed to the $4 h^{-1}\text{Mpc}$ used for the other two simulations. With these three simulations I can test both the effects of box size and mass resolution to make sure that neither systematically affect the results. The L400N1024 and L200N512 simulations have the same mass resolution with a different box size, while the L200N1024 and L200N512 simulations share the same box size but have different mass resolutions.

The c -mass and α -mass relations are presented in Fig. B.1 for the three different combination of box size and resolution for the standard WMAP 9-yr best fit and the Planck pivot with $n_s = 1.75$ cosmology. As can be seen, both c and α are well converged for all simulations for haloes resolved with an adequate number of particles. It

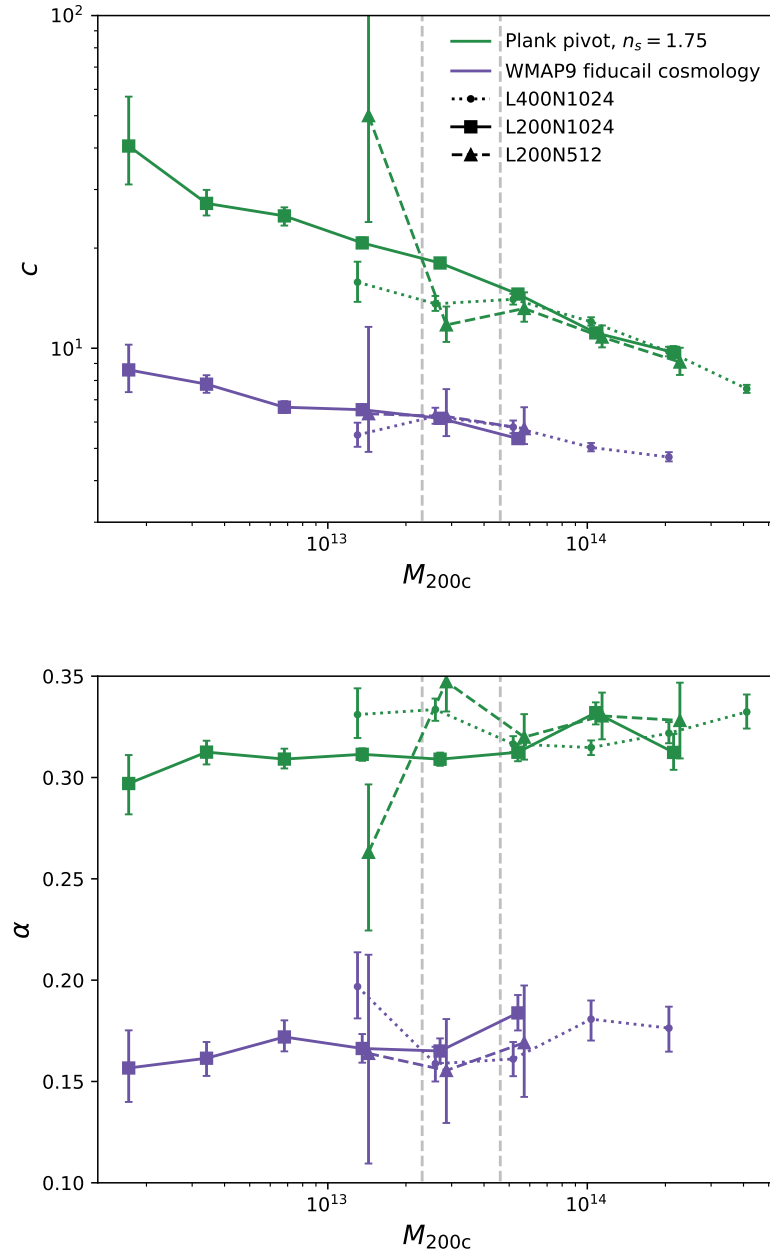


Figure B.1: The c -mass and α -mass relations for a variety of box sizes and resolutions to test the convergence and robustness of these results. Presented here are the $z = 0$ results for the fiducial best-fit WMAP y-yr cosmology (purple lines) and one that adopts a Planck pivot point and $n_s = 1.75$ (green lines), which is the most extreme cosmology studied in this work. The line styles represent the simulation box size and resolution (see legend). Data points have been artificially shifted horizontally for clarity: the L400N1024 data is at the true mass with the L200N1024 and L200N512 multiplied by an arbitrary constant of 1.05 and 1.05^2 , respectively. Additionally, the values of α for the Planck pivot cosmology have been increased by a constant of 0.15 with respect to their true value. The values of c have been unchanged due to the data naturally stratifying. The two vertical dashed lines represent haloes with 5,000 and 10,000 particles for the L400N1024 and L200N512 simulations.

is found that for the most extreme cosmology studied, i.e. the green lines presented here, at least 10,000 particles are needed to get sufficiently resolved values for c and α . Although not shown here, it is found that only 5,000 particles are required for all other cosmologies studied. I therefore use the associated mass cuts when analysing the simulations in this study.

As mentioned the analysis is identical for all simulations. A key part of the analysis is the radial range fit over, $r_{\text{conv}} < r < 0.7R_{200c}$, where r_{conv} is the convergence radius (see Eqn. (4.4)). r_{conv} primarily depends on the number of particles that the halo is resolved with, meaning that the higher resolution simulation (L200N1024) is fit over a wider effective range for the same mass halo. I do not find any systematic difference with mass resolution demonstrating that the c and α are robust to the radial range fit over, as long as an appropriately conservative convergence criterion is used to avoid fitting to the numerical core present. I also do not observe any degeneracy between c and α that is correlated with the radial range being fit over as found in other works (e.g. Udrescu et al., 2019). I attribute this primarily to fitting to stacked density profiles, resulting in smooth profiles without any discernible features from sub-structure.

Bibliography

Abbott T. M. C., Aguená M., Alarcon A., Allam S., Alves O., Amon A., Andrade-Oliveira F., Annis J., Avila S., Bacon D., Baxter E., Bechtol K., Becker M. R., Bernstein G. M., Bhargava S., Birrer S., Blazek J., Brandao-Souza A., Bridle S. L., Brooks D., Buckley-Geer E., Burke D. L., Camacho H., Campos A., Carnero Rosell A., Carrasco Kind M., Carretero J., Castander F. J., Cawthon R., Chang C., Chen A., Chen R., Choi A., Conselice C., Cordero J., Costanzi M., Croce M., da Costa L. N., da Silva Pereira M. E., Davis C., Davis T. M., De Vicente J., DeRose J., Desai S., Di Valentino E., Diehl H. T., Dietrich J. P., Dodelson S., Doel P., Doux C., Drlica-Wagner A., Eckert K., Eifler T. F., Elsner F., Elvin-Poole J., Everett S., Evrard A. E., Fang X., Farahi A., Fernandez E., Ferrero I., Ferté A., Fosalba P., Friedrich O., Frieman J., García-Bellido J., Gatti M., Gaztanaga E., Gerdes D. W., Giannantonio T., Giannini G., Gruen D., Gruendl R. A., Gschwend J., Gutierrez G., Harrison I., Hartley W. G., Herner K., Hinton S. R., Hollowood D. L., Honscheid K., Hoyle B., Huff E. M., Huterer D., Jain B., James D. J., Jarvis M., Jeffrey N., Jeltema T., Kovacs A., Krause E., Kron R., Kuehn K., Kuropatkin N., Lahav O., Leget P. F., Lemos P., Liddle A. R., Lidman C., Lima M., Lin H., MacCrann N., Maia M. A. G., Marshall J. L., Martini P., McCullough J., Melchior P., Mena-Fernández J., Menanteau F., Miquel R., Mohr J. J., Morgan R., Muir J., Myles J., Nadathur S., Navarro-Alsina A., Nichol R. C., Ogando R. L. C., Omori Y., Palmese A., Pandey S., Park Y., Paz-Chinchón F., Petravick D., Pieres A., Plazas Malagón A. A., Porredon A., Prat J., Raveri M., Rodriguez-Monroy M., Rollins R. P., Romer A. K., Roodman A., Rosenfeld R., Ross A. J., Rykoff E. S., Samuroff S., Sánchez C., Sanchez E., Sanchez J., Sanchez Cid D., Scarpine V., Schubnell M., Scolnic D., Secco L. F., Serrano S., Sevilla-Noarbe

- I., Sheldon E., Shin T., Smith M., Soares-Santos M., Suchyta E., Swanson M. E. C., Tabbutt M., Tarle G., Thomas D., To C., Troja A., Troxel M. A., Tucker D. L., Tutusaus I., Varga T. N., Walker A. R., Weaverdyck N., Wechsler R., Weller J., Yanny B., Yin B., Zhang Y., Zuntz J., DES Collaboration*. Dark Energy Survey Year 3 results: Cosmological constraints from galaxy clustering and weak lensing // *Phys. Rev. D*. I 2022. 105, 2. 023520.
- Adhikari Susmita, Dalal Neal, Chamberlain Robert T.* Splashback in accreting dark matter halos // *JCAP*. XI 2014. 2014, 11. 019.
- Angulo R. E., Springel V., White S. D. M., Jenkins A., Baugh C. M., Frenk C. S.* Scaling relations for galaxy clusters in the Millennium-XXL simulation // *MNRAS*. XI 2012. 426, 3. 2046–2062.
- Bardeen J. M., Bond J. R., Kaiser N., Szalay A. S.* The Statistics of Peaks of Gaussian Random Fields // *ApJ*. V 1986. 304. 15.
- Benitez-Llambay Alejandro.* py-sphviewer: Py-SPHViewer v1.0.0. VII 2015.
- Benson Andrew J., Ludlow Aaron, Cole Shaun.* Halo concentrations from extended Press-Schechter merger histories // *MNRAS*. VI 2019. 485, 4. 5010–5020.
- Bertschinger E.* Self-similar secondary infall and accretion in an Einstein-de Sitter universe // *ApJS*. V 1985. 58. 39–65.
- Bode Paul, Ostriker Jeremiah P., Turok Neil.* Halo Formation in Warm Dark Matter Models // *ApJ*. VII 2001. 556, 1. 93–107.
- Bond J. R., Cole S., Efstathiou G., Kaiser N.* Excursion Set Mass Functions for Hierarchical Gaussian Fluctuations // *ApJ*. X 1991. 379. 440.
- Booth C. M., Schaye Joop.* Cosmological simulations of the growth of supermassive black holes and feedback from active galactic nuclei: method and tests // *MNRAS*. IX 2009. 398, 1. 53–74.

- Boylan-Kolchin Michael, Bullock James S., Kaplinghat Manoj.* Too big to fail? The puzzling darkness of massive Milky Way subhaloes // MNRAS. VII 2011. 415, 1. L40–L44.
- Boylan-Kolchin Michael, Springel Volker, White Simon D. M., Jenkins Adrian, Lemson Gerard.* Resolving cosmic structure formation with the Millennium-II Simulation // MNRAS. IX 2009. 398, 3. 1150–1164.
- Brown Shaun T., McCarthy Ian G., Diemer Benedikt, Font Andreea S., Stafford Sam G., Pfeifer Simon.* Connecting the structure of dark matter haloes to the primordial power spectrum // MNRAS. VI 2020. 495, 4. 4994–5013.
- Brown Shaun T., McCarthy Ian G., Stafford Sam G., Font Andreea S.* Towards a universal model for the density profiles of dark matter haloes // MNRAS. II 2022. 509, 4. 5685–5701.
- Bryan Greg L., Norman Michael L.* Statistical Properties of X-Ray Clusters: Analytic and Numerical Comparisons // ApJ. III 1998. 495, 1. 80–99.
- Bullock J. S., Kolatt T. S., Sigad Y., Somerville R. S., Kravtsov A. V., Klypin A. A., Primack J. R., Dekel A.* Profiles of dark haloes: evolution, scatter and environment // Monthly Notices of the Royal Astronomical Society. Mar 2001a. 321, 3. 559–575.
- Bullock J. S., Kolatt T. S., Sigad Y., Somerville R. S., Kravtsov A. V., Klypin A. A., Primack J. R., Dekel A.* Profiles of dark haloes: evolution, scatter and environment // Monthly Notices of the Royal Astronomical Society. 03 2001b. 321, 3. 559–575.
- Cavagnolo Kenneth W., Donahue Megan, Voit G. Mark, Sun Ming.* Intracluster Medium Entropy Profiles for a Chandra Archival Sample of Galaxy Clusters // ApJS. May 2009. 182, 1. 12–32.
- Child Hillary L., Habib Salman, Heitmann Katrin, Frontiere Nicholas, Finkel Hal, Pope Adrian, Morozov Vitali.* Halo Profiles and the Concentration-Mass Relation for a Λ CDM Universe // ApJ. May 2018. 859, 1. 55.

- Clowe Douglas, Bradač Maruša, Gonzalez Anthony H., Markevitch Maxim, Randall Scott W., Jones Christine, Zaritsky Dennis.* A Direct Empirical Proof of the Existence of Dark Matter // *ApJ*. IX 2006. 648, 2. L109–L113.
- Corbelli Edvige, Salucci Paolo.* The extended rotation curve and the dark matter halo of M33 // *MNRAS*. I 2000. 311, 2. 441–447.
- Correa Camila A., Wyithe J. Stuart B., Schaye Joop, Duffy Alan R.* The accretion history of dark matter haloes - I. The physical origin of the universal function // *MNRAS*. VI 2015a. 450, 2. 1514–1520.
- Correa Camila A., Wyithe J. Stuart B., Schaye Joop, Duffy Alan R.* The accretion history of dark matter haloes - I. The physical origin of the universal function // *MNRAS*. Jun 2015b. 450, 2. 1514–1520.
- Correa Camila A., Wyithe J. Stuart B., Schaye Joop, Duffy Alan R.* The accretion history of dark matter haloes - II. The connections with the mass power spectrum and the density profile // *MNRAS*. Jun 2015c. 450, 2. 1521–1537.
- Correa Camila A, Wyithe J Stuart B, Schaye Joop, Duffy Alan R.* The accretion history of dark matter haloes–III. A physical model for the concentration–mass relation // *Monthly Notices of the Royal Astronomical Society*. 2015. 452, 2. 1217–1232.
- Crain Robert A., Schaye Joop, Bower Richard G., Furlong Michelle, Schaller Matthieu, Theuns Tom, Dalla Vecchia Claudio, Frenk Carlos S., McCarthy Ian G., Helly John C., Jenkins Adrian, Rosas-Guevara Yetli M., White Simon D. M., Trayford James W.* The EAGLE simulations of galaxy formation: calibration of subgrid physics and model variations // *MNRAS*. VI 2015. 450, 2. 1937–1961.
- Dalal Neal, Lithwick Yoram, Kuhlen Michael.* The Origin of Dark Matter Halo Profiles // *arXiv e-prints*. X 2010. arXiv:1010.2539.
- Dalla Vecchia Claudio, Schaye Joop.* Simulating galactic outflows with thermal supernova feedback // *MNRAS*. X 2012. 426, 1. 140–158.

- Davis M., Efstathiou G., Frenk C. S., White S. D. M.* The evolution of large-scale structure in a universe dominated by cold dark matter // *ApJ*. V 1985. 292. 371–394.
- Debackere Stijn N. B., Schaye Joop, Hoekstra Henk.* How baryons can significantly bias cluster count cosmology // *MNRAS*. VII 2021. 505, 1. 593–609.
- Dehnen Walter, McLaughlin Dean E.* Dynamical insight into dark matter haloes // *Monthly Notices of the Royal Astronomical Society*. 2005. 363, 4. 1057–1068.
- Diemer B., Kravtsov A. V.* Dependence of the Outer Density Profiles of Halos on Their Mass Accretion Rate // *ApJ*. VII 2014a. 789. 1.
- Diemer B., Kravtsov A. V.* Dependence of the Outer Density Profiles of Halos on Their Mass Accretion Rate // *ApJ*. VII 2014b. 789. 1.
- Diemer Benedikt.* COLOSSUS: A Python Toolkit for Cosmology, Large-scale Structure, and Dark Matter Halos // *The Astrophysical Journal Supplement Series*. Dec 2018. 239, 2. 35.
- Diemer Benedikt.* Universal at Last? The Splashback Mass Function of Dark Matter Halos // *The Astrophysical Journal*. Nov 2020. 903, 2. 87.
- Diemer Benedikt, Joyce Michael.* An Accurate Physical Model for Halo Concentrations // *The Astrophysical Journal*. Jan 2019. 871, 2. 168.
- Diemer Benedikt, Kravtsov Andrey V.* DEPENDENCE OF THE OUTER DENSITY PROFILES OF HALOS ON THEIR MASS ACCRETION RATE // *The Astrophysical Journal*. Jun 2014. 789, 1. 1.
- Diemer Benedikt, Kravtsov Andrey V.* A Universal Model for Halo Concentrations // *ApJ*. I 2015. 799, 1. 108.
- Diemer Benedikt, Kravtsov Andrey V.* A UNIVERSAL MODEL FOR HALO CONCENTRATIONS // *The Astrophysical Journal*. Jan 2015. 799, 1. 108.
- Duffy Alan R., Schaye Joop, Kay Scott T., Dalla Vecchia Claudio.* Dark matter halo concentrations in the Wilkinson Microwave Anisotropy Probe year 5 cosmology

- // Monthly Notices of the Royal Astronomical Society: Letters. 10 2008. 390, 1. L64–L68.
- Duffy Alan R., Schaye Joop, Kay Scott T., Dalla Vecchia Claudio.* Dark matter halo concentrations in the Wilkinson Microwave Anisotropy Probe year 5 cosmology // MNRAS. X 2008. 390, 1. L64–L68.
- Dutton Aaron A., Macciò Andrea V.* Cold dark matter haloes in the Planck era: evolution of structural parameters for Einasto and NFW profiles // Monthly Notices of the Royal Astronomical Society. May 2014. 441, 4. 3359–3374.
- Einasto J.* On the Construction of a Composite Model for the Galaxy and on the Determination of the System of Galactic Parameters // Trudy Astrofizicheskogo Instituta Alma-Ata. Jan 1965. 5. 87–100.
- Einasto Jaan.* On the Construction of a Composite Model for the Galaxy and on the Determination of the System of Galactic Parameters // Trudy Astrofizicheskogo Instituta Alma-Ata. 1965. 5. 87–100.
- Eke Vincent R., Navarro J. F., Steinmetz M.* The Power spectrum dependence of dark matter halo concentrations // Astrophys. J. 2001a. 554. 114–125.
- Eke Vincent R., Navarro Julio F., Steinmetz Matthias.* The Power Spectrum Dependence of Dark Matter Halo Concentrations // The Astrophysical Journal. Jun 2001b. 554, 1. 114–125.
- Faber S. M., Jackson R. E.* Velocity dispersions and mass-to-light ratios for elliptical galaxies. // ApJ. III 1976. 204. 668–683.
- Faltenbacher Andreas, Hoffman Yehuda, Gottlöber Stefan, Yepes Gustavo.* Entropy of gas and dark matter in galaxy clusters // Monthly Notices of the Royal Astronomical Society. 2007. 376, 3. 1327–1334.
- Fielder Catherine E., Mao Yao-Yuan, Zentner Andrew R., Newman Jeffrey A., Wu Hao-Yi, Wechsler Risa H.* Illuminating dark matter halo density profiles without subhaloes // MNRAS. XII 2020. 499, 2. 2426–2444.

- Fillmore J. A., Goldreich P.* Self-similar gravitational collapse in an expanding universe // *ApJ*. VI 1984. 281. 1–8.
- Flores Ricardo A., Primack Joel R.* Observational and Theoretical Constraints on Singular Dark Matter Halos // *ApJ*. V 1994. 427. L1.
- Font Andreea S., McCarthy Ian G., Belokurov Vasily, Brown Shaun T., Stafford Sam G.* Quenching of satellite galaxies of Milky Way analogues: reconciling theory and observations // *MNRAS*. III 2022. 511, 1. 1544–1556.
- Font Andreea S., McCarthy Ian G., Poole-Mckenzie Robert, Stafford Sam G., Brown Shaun T., Schaye Joop, Crain Robert A., Theuns Tom, Schaller Matthieu.* The ARTEMIS simulations: stellar haloes of Milky Way-mass galaxies // *MNRAS*. X 2020. 498, 2. 1765–1785.
- Foreman-Mackey Daniel, Hogg David W., Lang Dustin, Goodman Jonathan.* emcee: The MCMC Hammer // *PASP*. III 2013. 125, 925. 306.
- Frenk Carlos S., White Simon D. M., Davis Marc, Efstathiou George.* The Formation of Dark Halos in a Universe Dominated by Cold Dark Matter // *ApJ*. IV 1988. 327. 507.
- Gao Liang, Navarro Julio F., Cole Shaun, Frenk Carlos S., White Simon D. M., Springel Volker, Jenkins Adrian, Neto Angelo F.* The redshift dependence of the structure of massive Λ cold dark matter haloes // *MNRAS*. VI 2008a. 387, 2. 536–544.
- Gao Liang, Navarro Julio F., Cole Shaun, Frenk Carlos S., White Simon D. M., Springel Volker, Jenkins Adrian, Neto Angelo F.* The redshift dependence of the structure of massive Λ cold dark matter haloes // *MNRAS*. Jun 2008b. 387, 2. 536–544.
- Garrison-Kimmel Shea, Horiuchi Shunsaku, Abazajian Kevork N., Bullock James S., Kaplinghat Manoj.* Running with BICEP2: Implications for Small-Scale Problems in CDM // *Mon. Not. Roy. Astron. Soc.* 2014. 444, 1. 961–970.

- Gunn J. E., Gott J. R. III.* On the Infall of Matter Into Clusters of Galaxies and Some Effects on Their Evolution // *ApJ*. VIII 1972a. 176. 1.
- Gunn James E., Gott III J. Richard.* On the Infall of Matter Into Clusters of Galaxies and Some Effects on Their Evolution // *ApJ*. VIII 1972b. 176. 1.
- Hahn Oliver, Abel Tom.* Multi-scale initial conditions for cosmological simulations // *MNRAS*. VIII 2011. 415, 3. 2101–2121.
- Hansen Steen H., Moore Ben.* A universal density slope Velocity anisotropy relation for relaxed structures // *NA*. III 2006. 11, 5. 333–338.
- Hellwing Wojciech A., Frenk Carlos S., Cautun Marius, Bose Sownak, Helly John, Jenkins Adrian, Sawala Till, Cytowski Maciej.* The Copernicus Complexio: a high-resolution view of the small-scale Universe // *Monthly Notices of the Royal Astronomical Society*. Feb 2016. 457, 4. 3492–3509.
- Hernquist Lars.* An Analytical Model for Spherical Galaxies and Bulges // *ApJ*. VI 1990. 356. 359.
- Heymans Catherine, Tröster Tilman, Asgari Marika, Blake Chris, Hildebrandt Hendrik, Joachimi Benjamin, Kuijken Konrad, Lin Chieh-An, Sánchez Ariel G., van den Busch Jan Luca, Wright Angus H., Amon Alexandra, Bilicki Maciej, de Jong Jelte, Crocce Martin, Dvornik Andrej, Erben Thomas, Fortuna Maria Cristina, Getman Fedor, Giblin Benjamin, Glazebrook Karl, Hoekstra Henk, Joudaki Shahab, Kanawadi Arun, Köhlinger Fabian, Lidman Chris, Miller Lance, Napolitano Nicola R., Parkinson David, Schneider Peter, Shan HuanYuan, Valentijn Edwin A., Verdoes Kleijn Gijs, Wolf Christian.* KiDS-1000 Cosmology: Multi-probe weak gravitational lensing and spectroscopic galaxy clustering constraints // *A&A*. II 2021. 646. A140.
- Hill Alexander D., Crain Robert A., McCarthy Ian G., Brown Shaun T.* Intrinsic alignments of the extended radio continuum emission of galaxies in the EAGLE simulations // *MNRAS*. IV 2022. 511, 3. 3844–3862.

Hinshaw G., Larson D., Komatsu E., Spergel D. N., Bennett C. L., Dunkley J., Nolte M. R., Halpern M., Hill R. S., Odegard N., Page L., Smith K. M., Weiland J. L., Gold B., Jarosik N., Kogut A., Limon M., Meyer S. S., Tucker G. S., Wollack E., Wright E. L. Nine-year Wilkinson Microwave Anisotropy Probe (WMAP) Observations: Cosmological Parameter Results // *ApJS*. Oct 2013. 208, 2. 19.

Hoekstra Henk, Herbonnet Ricardo, Muzzin Adam, Babul Arif, Mahdavi Andi, Viola Massimo, Cacciato Marcello. The Canadian Cluster Comparison Project: detailed study of systematics and updated weak lensing masses // *MNRAS*. V 2015. 449, 1. 685–714.

Hoffman Yehuda, Romano-Diaz Emilio, Shlosman Isaac, Heller Clayton. Evolution of the Phase-Space Density in Dark Matter Halos // *The Astrophysical Journal*. dec 2007. 671, 2. 1108–1114.

Hopkins Philip F, Wetzel Andrew, Kereš Dušan, Faucher-Giguère Claude-André, Quataert Eliot, Boylan-Kolchin Michael, Murray Norman, Hayward Christopher C, Garrison-Kimmel Shea, Hummels Cameron, Feldmann Robert, Torrey Paul, Ma Xi-angcheng, Anglés-Alcázar Daniel, Su Kung-Yi, Orr Matthew, Schmitz Denise, Escala Ivanna, Sanderson Robyn, Grudić Michael Y, Hafen Zachary, Kim Ji-Hoon, Fitts Alex, Bullock James S, Wheeler Coral, Chan T K, Elbert Oliver D, Narayanan Desika. FIRE-2 simulations: physics versus numerics in galaxy formation // *Monthly Notices of the Royal Astronomical Society*. 06 2018. 480, 1. 800–863.

Hubble Edwin. A Relation between Distance and Radial Velocity among Extra-Galactic Nebulae // *Proceedings of the National Academy of Science*. III 1929. 15, 3. 168–173.

Huss A., Jain B., Steinmetz M. The formation and evolution of clusters of galaxies in different cosmogonies // *MNRAS*. X 1999. 308, 4. 1011–1031.

Jiang Fangzhou, Bosch Frank C. van den. Generating merger trees for dark matter haloes: a comparison of methods // *Monthly Notices of the Royal Astronomical Society*. 03 2014. 440, 1. 193–207.

- Klypin Anatoly, Kravtsov Andrey V., Valenzuela Octavio, Prada Francisco.* Where Are the Missing Galactic Satellites? // *ApJ*. IX 1999. 522, 1. 82–92.
- Knollmann Steffen R., Power Chris, Knebe Alexander.* Dark matter halo profiles in scale-free cosmologies // *Monthly Notices of the Royal Astronomical Society*. 2008. 385, 2. 545–552.
- Lacey Cedric, Cole Shaun.* Merger rates in hierarchical models of galaxy formation // *MNRAS*. VI 1993. 262, 3. 627–649.
- Lau Erwin T., Nagai Daisuke, Avestruz Camille, Nelson Kaylea, Vikhlinin Alexey.* Mass Accretion and its Effects on the Self-similarity of Gas Profiles in the Outskirts of Galaxy Clusters // *ApJ*. VI 2015. 806, 1. 68.
- Le Brun Amandine M. C., McCarthy Ian G., Schaye Joop, Ponman Trevor J.* Towards a realistic population of simulated galaxy groups and clusters // *Monthly Notices of the Royal Astronomical Society*. May 2014. 441, 2. 1270–1290.
- Leo Matteo, Baugh Carlton M., Li Baojiu, Pascoli Silvia.* A new smooth-k space filter approach to calculate halo abundances // *Journal of Cosmology and Astroparticle Physics*. Apr 2018. 2018, 04. 010–010.
- Lewis Antony, Challinor Anthony, Lasenby Anthony.* Efficient computation of CMB anisotropies in closed FRW models // *ApJ*. 2000. 538. 473–476.
- Linden Anja von der, Mantz Adam, Allen Steven W., Applegate Douglas E., Kelly Patrick L., Morris R. Glenn, Wright Adam, Allen Mark T., Burchat Patricia R., Burke David L., al. et.* Robust weak-lensing mass calibration of Planck galaxy clusters // *Monthly Notices of the Royal Astronomical Society*. Jul 2014. 443, 3. 1973–1978.
- Linder Eric V.* Exploring the Expansion History of the Universe // *Phys. Rev. Lett.* Mar 2003. 90. 091301.
- Lovell Mark R., Bose Sownak, Boyarsky Alexey, Crain Robert A., Frenk Carlos S., Hellwing Wojciech A., Ludlow Aaron D., Navarro Julio F., Ruchayskiy Oleg, Sawala Till, al. et.* Properties of Local Group galaxies in hydrodynamical simulations of sterile

neutrino dark matter cosmologies // *Monthly Notices of the Royal Astronomical Society*. Mar 2017. 468, 4. 4285–4298.

Lu Yu, Mo H. J., Katz Neal, Weinberg Martin D. On the origin of cold dark matter halo density profiles // *Monthly Notices of the Royal Astronomical Society*. 04 2006. 368, 4. 1931–1940.

Ludlow Aaron D., Angulo Raúl E. Einasto profiles and the dark matter power spectrum // *Monthly Notices of the Royal Astronomical Society: Letters*. feb 2017. 465, 1. L84–L88.

Ludlow Aaron D., Angulo Raúl E. Einasto profiles and the dark matter power spectrum // *MNRAS*. II 2017. 465, 1. L84–L88.

Ludlow Aaron D., Angulo Raúl E. Einasto profiles and the dark matter power spectrum // *Monthly Notices of the Royal Astronomical Society: Letters*. 10 2016. 465, 1. L84–L88.

Ludlow Aaron D., Bose Sownak, Angulo Raúl E., Wang Lan, Hellwing Wojciech A., Navarro Julio F., Cole Shaun, Frenk Carlos S. The mass-concentration-redshift relation of cold and warm dark matter haloes // *MNRAS*. Aug 2016. 460, 2. 1214–1232.

Ludlow Aaron D., Bose Sownak, Angulo Raúl E., Wang Lan, Hellwing Wojciech A., Navarro Julio F., Cole Shaun, Frenk Carlos S. The mass-concentration-redshift relation of cold and warm dark matter haloes // *Monthly Notices of the Royal Astronomical Society*. May 2016. 460, 2. 1214–1232.

Ludlow Aaron D., Navarro Julio F., Angulo Raúl E., Boylan-Kolchin Michael, Springel Volker, Frenk Carlos, White Simon D. M. The mass-concentration-redshift relation of cold dark matter haloes // *MNRAS*. Jun 2014. 441, 1. 378–388.

Ludlow Aaron D., Navarro Julio F., Angulo Raúl E., Boylan-Kolchin Michael, Springel Volker, Frenk Carlos, White Simon D. M. The mass-concentration-redshift relation of cold dark matter haloes // *Monthly Notices of the Royal Astronomical Society*. Apr 2014. 441, 1. 378–388.

Ludlow Aaron D., Navarro Julio F., Boylan-Kolchin Michael, Bett Philip E., Angulo Raúl E., Li Ming, White Simon D. M., Frenk Carlos, Springel Volker. The mass profile and accretion history of cold dark matter haloes // MNRAS. VI 2013. 432, 2. 1103–1113.

Ludlow Aaron D., Navarro Julio F., Boylan-Kolchin Michael, Bett Philip E., Angulo Raúl E., Li Ming, White Simon D. M., Frenk Carlos, Springel Volker. The mass profile and accretion history of cold dark matter haloes // Monthly Notices of the Royal Astronomical Society. 04 2013. 432, 2. 1103–1113.

Ludlow Aaron D., Navarro Julio F., Li Ming, Angulo Raul E., Boylan-Kolchin Michael, Bett Philip E. The dynamical state and mass-concentration relation of galaxy clusters // MNRAS. XII 2012. 427, 2. 1322–1328.

Ludlow Aaron D., Navarro Julio F., Springel Volker, Vogelsberger Mark, Wang Jie, White Simon D. M., Jenkins Adrian, Frenk Carlos S. Secondary infall and the pseudo-phase-space density profiles of cold dark matter haloes // MNRAS. VII 2010. 406, 1. 137–146.

Ludlow Aaron D., Navarro Julio F., White Simon D. M., Boylan-Kolchin Michael, Springel Volker, Jenkins Adrian, Frenk Carlos S. The density and pseudo-phase-space density profiles of cold dark matter haloes // MNRAS. Aug 2011. 415, 4. 3895–3902.

Ludlow Aaron D., Schaye Joop, Bower Richard. Numerical convergence of simulations of galaxy formation: the abundance and internal structure of cold dark matter haloes // MNRAS. Sep 2019a. 488, 3. 3663–3684.

Ludlow Aaron D., Schaye Joop, Bower Richard. Numerical convergence of simulations of galaxy formation: the abundance and internal structure of cold dark matter haloes // MNRAS. Sep 2019b. 488, 3. 3663–3684.

Lynden-Bell D. Statistical Mechanics of Violent Relaxation in Stellar Systems // Monthly Notices of the Royal Astronomical Society. 05 1967. 136, 1. 101–121.

- McCarthy I. G., Babul A., Bower R. G., Balogh M. L.* Towards a holistic view of the heating and cooling of the intracluster medium // *MNRAS*. May 2008. 386, 3. 1309–1331.
- McCarthy I. G., Schaye J., Bird S., Le Brun A. M. C.* The BAHAMAS project: calibrated hydrodynamical simulations for large-scale structure cosmology // *MNRAS*. III 2017. 465. 2936–2965.
- McClintock T., Varga T. N., Gruen D., Rozo E., Rykoff E. S., Shin T., Melchior P., DeRose J., Seitz S., Dietrich J. P., Sheldon E., Zhang Y., von der Linden A., Jeltema T., Mantz A. B., Romer A. K., Allen S., Becker M. R., Bermeo A., Bhargava S., Costanzi M., Everett S., Farahi A., Hamaus N., Hartley W. G., Hollowood D. L., Hoyle B., Israel H., Li P., MacCrann N., Morris G., Palmese A., Plazas A. A., Pollina G., Rau M. M., Simet M., Soares-Santos M., Troxel M. A., Vergara Cervantes C., Wechsler R. H., Zuntz J., Abbott T. M. C., Abdalla F. B., Allam S., Annis J., Avila S., Bridle S. L., Brooks D., Burke D. L., Carnero Rosell A., Carrasco Kind M., Carretero J., Castander F. J., Crocce M., Cunha C. E., D’Andrea C. B., da Costa L. N., Davis C., De Vicente J., Diehl H. T., Doel P., Drlica-Wagner A., Evrard A. E., Flaugher B., Fosalba P., Frieman J., García-Bellido J., Gaztanaga E., Gerdes D. W., Giannantonio T., Gruendl R. A., Gutierrez G., Honscheid K., James D. J., Kirk D., Krause E., Kuehn K., Lahav O., Li T. S., Lima M., March M., Marshall J. L., Menanteau F., Miquel R., Mohr J. J., Nord B., Ogando R. L. C., Roodman A., Sanchez E., Scarpine V., Schindler R., Sevilla-Noarbe I., Smith M., Smith R. C., Sobreira F., Suchyta E., Swanson M. E. C., Tarle G., Tucker D. L., Vikram V., Walker A. R., Weller J., DES Collaboration .* Dark Energy Survey Year 1 results: weak lensing mass calibration of redMaPPer galaxy clusters // *MNRAS*. I 2019. 482, 1. 1352–1378.
- Mead A. J., Peacock J. A., Heymans C., Joudaki S., Heavens A. F.* An accurate halo model for fitting non-linear cosmological power spectra and baryonic feedback models // *Monthly Notices of the Royal Astronomical Society*. Oct 2015. 454, 2. 1958–1975.

- Merritt David, Graham Alister W., Moore Ben, Diemand Jürg, Terzić Balša.* Empirical Models for Dark Matter Halos. I. Nonparametric Construction of Density Profiles and Comparison with Parametric Models // *AJ*. XII 2006. 132, 6. 2685–2700.
- Monaghan J. J., Lattanzio J. C.* A refined particle method for astrophysical problems // *A&A*. VIII 1985. 149. 135–143.
- Moore B., Quinn T., Governato F., Stadel J., Lake G.* Cold collapse and the core catastrophe // *Monthly Notices of the Royal Astronomical Society*. 12 1999. 310, 4. 1147–1152.
- Moore Ben.* Evidence against dissipation-less dark matter from observations of galaxy haloes // *Nature*. VIII 1994. 370, 6491. 629–631.
- Moore Ben, Ghigna Sebastiano, Governato Fabio, Lake George, Quinn Thomas, Stadel Joachim, Tozzi Paolo.* Dark Matter Substructure within Galactic Halos // *ApJl*. X 1999. 524, 1. L19–L22.
- More Surhud, Diemer Benedikt, Kravtsov Andrey V.* The Splashback Radius as a Physical Halo Boundary and the Growth of Halo Mass // *ApJ*. IX 2015. 810, 1. 36.
- Nadler Ethan O., Oh S. Peng, Ji Suoqing.* On the apparent power law in CDM halo pseudo-phase space density profiles // *MNRAS*. Sep 2017. 470, 1. 500–511.
- Natarajan Priyamvada, Chadayammuri Urmila, Jauzac Mathilde, Richard Johan, Kneib Jean-Paul, Ebeling Harald, Jiang Fangzhou, van den Bosch Frank, Limousin Marceau, Jullo Eric, Atek Hakim, Pillepich Annalisa, Popa Cristina, Marinacci Federico, Hernquist Lars, Meneghetti Massimo, Vogelsberger Mark.* Mapping substructure in the HST Frontier Fields cluster lenses and in cosmological simulations // *MNRAS*. VI 2017. 468, 2. 1962–1980.
- Navarro J. F., Frenk C. S., White S. D. M.* The Structure of Cold Dark Matter Halos // *ApJ*. V 1996a. 462. 563.

- Navarro J. F., Hayashi E., Power C., Jenkins A. R., Frenk C. S., White S. D. M., Springel V., Stadel J., Quinn T. R.* The inner structure of Λ CDM haloes - III. Universality and asymptotic slopes // MNRAS. IV 2004. 349, 3. 1039–1051.
- Navarro J. F., Ludlow A., Springel V., Wang J., Vogelsberger M., White S. D. M., Jenkins A., Frenk C. S., Helmi A.* The diversity and similarity of simulated cold dark matter haloes // MNRAS. II 2010a. 402. 21–34.
- Navarro Julio F., Frenk Carlos S., White Simon D. M.* The Structure of Cold Dark Matter Halos // ApJ. V 1996b. 462. 563.
- Navarro Julio F., Frenk Carlos S., White Simon D. M.* A Universal Density Profile from Hierarchical Clustering // ApJ. XII 1997. 490, 2. 493–508.
- Navarro Julio F., Frenk Carlos S., White Simon D. M.* A Universal Density Profile from Hierarchical Clustering // The Astrophysical Journal. Dec 1997. 490, 2. 493–508.
- Navarro Julio F., Ludlow Aaron, Springel Volker, Wang Jie, Vogelsberger Mark, White Simon D. M., Jenkins Adrian, Frenk Carlos S., Helmi Amina.* The diversity and similarity of simulated cold dark matter haloes // MNRAS. II 2010b. 402, 1. 21–34.
- Nelson Dylan, Springel Volker, Pillepich Annalisa, Rodriguez-Gomez Vicente, Torrey Paul, Genel Shy, Vogelsberger Mark, Pakmor Ruediger, Marinacci Federico, Weinberger Rainer, Kelley Luke, Lovell Mark, Diemer Benedikt, Hernquist Lars.* The IllustrisTNG simulations: public data release // Computational Astrophysics and Cosmology. May 2019. 6, 1. 2.
- Neto A. F., Gao L., Bett P., Cole S., Navarro J. F., Frenk C. S., White S. D. M., Springel V., Jenkins A.* The statistics of Λ CDM halo concentrations // MNRAS. XI 2007. 381. 1450–1462.
- Pfeifer Simon, McCarthy Ian G., Stafford Sam G., Brown Shaun T., Font Andreea S., Kwan Juliana, Salcido Jaime, Schaye Joop.* The BAHAMAS project: effects of dynamical dark energy on large-scale structure // MNRAS. X 2020. 498, 2. 1576–1592.

Planck Collaboration, Ade P. A. R., Aghanim N., Arnaud M., Ashdown M., Aumont J., Baccigalupi C., Banday A. J., Barreiro R. B., Bartlett J. G., Bartolo N., Battaner E., Battye R., Benabed K., Benoît A., Benoit-Lévy A., Bernard J. P., Bersanelli M., Bielewicz P., Bock J. J., Bonaldi A., Bonavera L., Bond J. R., Borrill J., Bouchet F. R., Boulanger F., Bucher M., Burigana C., Butler R. C., Calabrese E., Cardoso J. F., Catalano A., Challinor A., Chamballu A., Chary R. R., Chiang H. C., Chluba J., Christensen P. R., Church S., Clements D. L., Colombi S., Colombo L. P. L., Combet C., Coulais A., Crill B. P., Curto A., Cuttaia F., Danese L., Davies R. D., Davis R. J., de Bernardis P., de Rosa A., de Zotti G., Delabrouille J., Désert F. X., Di Valentino E., Dickinson C., Diego J. M., Dolag K., Dole H., Donzelli S., Doré O., Douspis M., Ducout A., Dunkley J., Dupac X., Efstathiou G., Elsner F., Enßlin T. A., Eriksen H. K., Farhang M., Fergusson J., Finelli F., Forni O., Frailis M., Fraisse A. A., Franceschi E., Frejsel A., Galeotta S., Galli S., Ganga K., Gauthier C., Gerbino M., Ghosh T., Giard M., Giraud-Héraud Y., Giusarma E., Gjerløw E., González-Nuevo J., Górski K. M., Gratton S., Gregorio A., Gruppuso A., Gudmundsson J. E., Hamann J., Hansen F. K., Hanson D., Harrison D. L., Helou G., Henrot-Versillé S., Hernández-Monteagudo C., Herranz D., Hildebrandt S. R., Hivon E., Hobson M., Holmes W. A., Hornstrup A., Hovest W., Huang Z., Huffenberger K. M., Hurier G., Jaffe A. H., Jaffe T. R., Jones W. C., Juvela M., Keihänen E., Keskitalo R., Kisner T. S., Kneissl R., Knoche J., Knox L., Kunz M., Kurki-Suonio H., Lagache G., Lähteenmäki A., Lamarre J. M., Lasenby A., Lattanzi M., Lawrence C. R., Leahy J. P., Leonardi R., Lesgourgues J., Levrier F., Lewis A., Liguori M., Lilje P. B., Linden-Vørnle M., López-Cañiego M., Lubin P. M., Macías-Pérez J. F., Maggio G., Maino D., Mandolesi N., Mangilli A., Marchini A., Maris M., Martin P. G., Martinelli M., Martínez-González E., Masi S., Matarrese S., McGehee P., Meinhold P. R., Melchiorri A., Melin J. B., Mendes L., Mennella A., Migliaccio M., Millea M., Mitra S., Miville-Deschênes M. A., Moneti A., Montier L., Morgante G., Mortlock D., Moss A., Munshi D., Murphy J. A., Naselsky P., Nati F., Natoli P., Netterfield C. B., Nørgaard-Nielsen H. U., Noviello F., Novikov D., Novikov I., Oxborrow C. A., Paci F., Pagano L., Pajot F., Paladini R., Paoletti D., Partridge B., Pasian F., Patanchon G., Pearson T. J., Perdereau O., Perotto L., Perrotta F., Pettorino V., Piacentini

F., Piat M., Pierpaoli E., Pietrobon D., Plaszczynski S., Pointecouteau E., Polenta G., Popa L., Pratt G. W., Prézeau G., Prunet S., Puget J. L., Rachen J. P., Reach W. T., Rebolo R., Reinecke M., Remazeilles M., Renault C., Renzi A., Ristorcelli I., Rocha G., Rosset C., Rossetti M., Roudier G., Rouillé d'Orfeuil B., Rowan-Robinson M., Rubiño-Martín J. A., Rusholme B., Said N., Salvatelli V., Salvati L., Sandri M., Santos D., Savelainen M., Savini G., Scott D., Seiffert M. D., Serra P., Shellard E. P. S., Spencer L. D., Spinelli M., Stolyarov V., Stompor R., Sudiwala R., Sunyaev R., Sutton D., Suur-Uski A. S., Sygnet J. F., Tauber J. A., Terenzi L., Toffolatti L., Tomasi M., Tristram M., Trombetti T., Tucci M., Tuovinen J., Türlér M., Umata G., Valenziano L., Valiviita J., Van Tent F., Vielva P., Villa F., Wade L. A., Wandelt B. D., Wehus I. K., White M., White S. D. M., Wilkinson A., Yvon D., Zacchei A., Zonca A. Planck 2015 results. XIII. Cosmological parameters // *A&A*. Sep 2016. 594. A13.

Planck Collaboration , Ade P. A. R., Aghanim N., Arnaud M., Ashdown M., Aumont J., Baccigalupi C., Banday A. J., Barreiro R. B., Bartlett J. G., Battaner E., Benabed K., Benoit-Lévy A., Bernard J. P., Bersanelli M., Bielewicz P., Bobin J., Bonaldi A., Bond J. R., Bouchet F. R., Burigana C., Cardoso J. F., Catalano A., Chamballu A., Chiang H. C., Christensen P. R., Clements D. L., Colombi S., Colombo L. P. L., Couchot F., Cuttaia F., Danese L., Davies R. D., Davis R. J., de Bernardis P., de Rosa A., de Zotti G., Delabrouille J., Dickinson C., Diego J. M., Dole H., Donzelli S., Doré O., Douspis M., Dupac X., Enßlin T. A., Eriksen H. K., Finelli F., Forni O., Frailis M., Franceschi E., Galeotta S., Galli S., Ganga K., Giard M., Giraud-Héraud Y., González-Nuevo J., Górski K. M., Gregorio A., Gruppuso A., Hansen F. K., Harrison D. L., Henrot-Versillé S., Hernández-Monteagudo C., Herranz D., Hildebrandt S. R., Hivon E., Hobson M., Holmes W. A., Hornstrup A., Hovest W., Huffenberger K. M., Jaffe A. H., Jaffe T. R., Jones W. C., Juvela M., Keihänen E., Keskitalo R., Kisner T. S., Kneissl R., Knoche J., Knox L., Kunz M., Kurki-Suonio H., Lagache G., Lähteenmäki A., Lamarre J. M., Lasenby A., Lawrence C. R., Leonardi R., Liddle A., Liguori M., Lilje P. B., Linden-Vørnle M., López-Cañiegos M., Lubin P. M., Macías-Pérez J. F., Maffei B., Maino D., Mandolese N., Maris M., Martin P. G., Martínez-González E., Masi S., Massardi M., Matarrese S., Mazzotta P.,

Melchiorri A., Mendes L., Mennella A., Migliaccio M., Mitra S., Miville-Deschênes M. A., Moneti A., Montier L., Morgante G., Munshi D., Murphy J. A., Naselsky P., Nati F., Natoli P., Noviello F., Novikov D., Novikov I., Oxborrow C. A., Pagano L., Pajot F., Paoletti D., Pasian F., Perdureau O., Perotto L., Perrotta F., Pettorino V., Piacentini F., Piat M., Pierpaoli E., Pietrobon D., Plaszczynski* S., Pointecouteau E., Polenta G., Popa L., Pratt G. W., Puget J. L., Rachen J. P., Rebolo R., Reinecke M., Remazeilles M., Renault C., Ricciardi S., Riller T., Ristorcelli I., Rocha G., Rosset C., Roudier G., Rouillé d'Orfeuil B., Rubiño-Martín J. A., Rusholme B., Sandri M., Savelainen M., Savini G., Spencer L. D., Spinelli M., Starck J. L., Sureau F., Sutton D., Suur-Uski A. S., Sygnet J. F., Tauber J. A., Terenzi L., Toffolatti L., Tomasi M., Tristram M., Tucci M., Umata G., Valenziano L., Valiviita J., Van Tent B., Vielva P., Villa F., Wade L. A., Wandelt B. D., White M., Yvon D., Zacchei A., Zonca A. Planck intermediate results. XVI. Profile likelihoods for cosmological parameters // *A&A*. Jun 2014. 566. A54.

Planck Collaboration , Aghanim N., Akrami Y., Ashdown M., Aumont J., Baccigalupi C., Ballardini M., Banday A. J., Barreiro R. B., Bartolo N., Basak S., Battye R., Benabed K., Bernard J. P., Bersanelli M., Bielewicz P., Bock J. J., Bond J. R., Borrill J., Bouchet F. R., Boulanger F., Bucher M., Burigana C., Butler R. C., Calabrese E., Cardoso J. F., Carron J., Challinor A., Chiang H. C., Chluba J., Colombo L. P. L., Combet C., Contreras D., Crill B. P., Cuttaia F., de Bernardis P., de Zotti G., Delabrouille J., Delouis J. M., Di Valentino E., Diego J. M., Doré O., Douspis M., Ducout A., Dupac X., Dusini S., Efstathiou G., Elsner F., Enßlin T. A., Eriksen H. K., Fantaye Y., Farhang M., Fergusson J., Fernandez-Cobos R., Finelli F., Forastieri F., Frailis M., Fraisse A. A., Franceschi E., Frolov A., Galeotta S., Galli S., Ganga K., Génova-Santos R. T., Gerbino M., Ghosh T., González-Nuevo J., Górski K. M., Gratton S., Gruppuso A., Gudmundsson J. E., Hamann J., Handley W., Hansen F. K., Herranz D., Hildebrandt S. R., Hivon E., Huang Z., Jaffe A. H., Jones W. C., Karakci A., Keihänen E., Keskitalo R., Kiiveri K., Kim J., Kisner T. S., Knox L., Krachmalnicoff N., Kunz M., Kurki-Suonio H., Lagache G., Lamarre J. M., Lasenby A., Lattanzi M., Lawrence C. R., Le Jeune M., Lemos P., Lesgourgues J., Levrier F., Lewis A.,

- Liguori M., Lilje P. B., Lilley M., Lindholm V., López-Caniego M., Lubin P. M., Ma Y. Z., Macías-Pérez J. F., Maggio G., Maino D., Mandolesi N., Mangilli A., Marcos-Caballero A., Maris M., Martin P. G., Martinelli M., Martínez-González E., Matarrese S., Mauri N., McEwen J. D., Meinhold P. R., Melchiorri A., Mennella A., Migliaccio M., Millea M., Mitra S., Miville-Deschênes M. A., Molinari D., Montier L., Morgante G., Moss A., Natoli P., Nørgaard-Nielsen H. U., Pagano L., Paoletti D., Partridge B., Patanchon G., Peiris H. V., Perrotta F., Pettorino V., Piacentini F., Polastri L., Polenta G., Puget J. L., Rachen J. P., Reinecke M., Remazeilles M., Renzi A., Rocha G., Rosset C., Roudier G., Rubiño-Martín J. A., Ruiz-Granados B., Salvati L., Sandri M., Savelainen M., Scott D., Shellard E. P. S., Sirignano C., Sirri G., Spencer L. D., Sunyaev R., Suur-Uski A. S., Tauber J. A., Tavagnacco D., Tenti M., Toffolatti L., Tomasi M., Trombetti T., Valenziano L., Valiviita J., Van Tent B., Vibert L., Vielva P., Villa F., Vittorio N., Wandelt B. D., Wehus I. K., White M., White S. D. M., Zacchei A., Zonca A. Planck 2018 results. VI. Cosmological parameters // *A&A*. IX 2020. 641. A6.
- Poole-McKenzie Robert, Font Andreea S., Boxer Billy, McCarthy Ian G., Burdin Sergey, Stafford Sam G., Brown Shaun T. Informing dark matter direct detection limits with the ARTEMIS simulations // *JCAP*. XI 2020. 2020, 11. 016.
- Power C., Navarro J. F., Jenkins A., Frenk C. S., White S. D. M., Springel V., Stadel J., Quinn T. The inner structure of Λ CDM haloes - I. A numerical convergence study // *MNRAS*. I 2003. 338, 1. 14–34.
- Prada Francisco, Klypin Anatoly A, Cuesta Antonio J, Betancort-Rijo Juan E, Primack Joel. Halo concentrations in the standard Λ cold dark matter cosmology // *Monthly Notices of the Royal Astronomical Society*. 2012. 423, 4. 3018–3030.
- Prada Francisco, Klypin Anatoly A., Cuesta Antonio J., Betancort-Rijo Juan E., Primack Joel. Halo concentrations in the standard Λ cold dark matter cosmology // *MNRAS*. VII 2012. 423, 4. 3018–3030.
- Press William H., Schechter Paul. Formation of Galaxies and Clusters of Galaxies by Self-Similar Gravitational Condensation // *ApJ*. II 1974. 187. 425–438.

Ratra Bharat, Peebles P. J. E. Cosmological consequences of a rolling homogeneous scalar field // *Phys. Rev. D.* Jun 1988. 37. 3406–3427.

Reed Darren, Governato Fabio, Verde Licia, Gardner Jeffrey, Quinn Thomas, Stadel Joachim, Merritt David, Lake George. Evolution of the density profiles of dark matter haloes // *Monthly Notices of the Royal Astronomical Society.* 02 2005. 357, 1. 82–96.

Riess Adam G., Filippenko Alexei V., Challis Peter, Clocchiatti Alejandro, Diercks Alan, Garnavich Peter M., Gilliland Ron L., Hogan Craig J., Jha Saurabh, Kirshner Robert P., Leibundgut B., Phillips M. M., Reiss David, Schmidt Brian P., Schommer Robert A., Smith R. Chris, Spyromilio J., Stubbs Christopher, Suntzeff Nicholas B., Tonry John. Observational Evidence from Supernovae for an Accelerating Universe and a Cosmological Constant // *AJ.* IX 1998. 116, 3. 1009–1038.

Riess Adam G., Filippenko Alexei V., Challis Peter, Clocchiatti Alejandro, Diercks Alan, Garnavich Peter M., Gilliland Ron L., Hogan Craig J., Jha Saurabh, Kirshner Robert P., al. et. Observational Evidence from Supernovae for an Accelerating Universe and a Cosmological Constant // *The Astronomical Journal.* Sep 1998. 116, 3. 1009–1038.

Riess Adam G., Yuan Wenlong, Macri Lucas M., Scolnic Dan, Brout Dillon, Casertano Stefano, Jones David O., Murakami Yukei, Breuval Louise, Brink Thomas G., Filippenko Alexei V., Hoffmann Samantha, Jha Saurabh W., Kenworthy W. D'arcy, Mackenty John, Stahl Benjamin E., Zheng Weikang. A Comprehensive Measurement of the Local Value of the Hubble Constant with 1 km/s/Mpc Uncertainty from the Hubble Space Telescope and the SH0ES Team // *arXiv e-prints.* XII 2021. arXiv:2112.04510.

Robertson Andrew, Harvey David, Massey Richard, Eke Vincent, McCarthy Ian G., Jauzac Mathilde, Li Baojiu, Schaye Joop. Observable tests of self-interacting dark matter in galaxy clusters: cosmological simulations with SIDM and baryons // *MNRAS.* IX 2019a. 488, 3. 3646–3662.

- Robertson Andrew, Harvey David, Massey Richard, Eke Vincent, McCarthy Ian G., Jauzac Mathilde, Li Baojiu, Schaye Joop.* Observable tests of self-interacting dark matter in galaxy clusters: cosmological simulations with SIDM and baryons // *MNRAS*. IX 2019b. 488, 3. 3646–3662.
- Sawala Till, Frenk Carlos S., Fattahi Azadeh, Navarro Julio F., Bower Richard G., Crain Robert A., Vecchia Claudio Dalla, Furlong Michelle, Helly John. C., Jenkins Adrian, al. et.* The APOSTLE simulations: solutions to the Local Group's cosmic puzzles // *Monthly Notices of the Royal Astronomical Society*. Feb 2016. 457, 2. 1931–1943.
- Schaye Joop, Crain Robert A., Bower Richard G., Furlong Michelle, Schaller Matthieu, Theuns Tom, Dalla Vecchia Claudio, Frenk Carlos S., McCarthy I. G., Helly John C., Jenkins Adrian, Rosas-Guevara Y. M., White Simon D. M., Baes Maarten, Booth C. M., Camps Peter, Navarro Julio F., Qu Yan, Rahmati Alireza, Sawala Till, Thomas Peter A., Trayford James.* The EAGLE project: simulating the evolution and assembly of galaxies and their environments // *MNRAS*. Jan 2015. 446, 1. 521–554.
- Schaye Joop, Dalla Vecchia Claudio.* On the relation between the Schmidt and Kennicutt-Schmidt star formation laws and its implications for numerical simulations // *MNRAS*. I 2008. 383, 3. 1210–1222.
- Schmidt M.* The distribution of mass in M 31 // *Bull. Astron. Inst. Netherlands*. XI 1957. 14. 17.
- Smith R. E., Peacock J. A., Jenkins A., White S. D. M., Frenk C. S., Pearce F. R., Thomas P. A., Efstathiou G., Couchman H. M. P.* Stable clustering, the halo model and non-linear cosmological power spectra // *Monthly Notices of the Royal Astronomical Society*. Jun 2003. 341, 4. 1311–1332.
- Smoot G. F., Bennett C. L., Kogut A., Wright E. L., Aymon J., Boggess N. W., Cheng E. S., de Amici G., Gulkis S., Hauser M. G., Hinshaw G., Jackson P. D., Janssen M., Kaita E., Kelsall T., Keegstra P., Lineweaver C., Loewenstein K., Lubin P., Mather*

- J., Meyer S. S., Moseley S. H., Murdock T., Rokke L., Silverberg R. F., Tenorio L., Weiss R., Wilkinson D. T.* Structure in the COBE Differential Microwave Radiometer First-Year Maps // *ApJl.* IX 1992. 396. L1.
- Spergel D. N., Verde L., Peiris H. V., Komatsu E., Nolta M. R., Bennett C. L., Halpern M., Hinshaw G., Jarosik N., Kogut A., Limon M., Meyer S. S., Page L., Tucker G. S., Weiland J. L., Wollack E., Wright E. L.* First-Year Wilkinson Microwave Anisotropy Probe (WMAP) Observations: Determination of Cosmological Parameters // *ApJS.* Sep 2003. 148, 1. 175–194.
- Springel Volker.* The cosmological simulation code GADGET-2 // *MNRAS.* Dec 2005. 364, 4. 1105–1134.
- Springel Volker, Di Matteo Tiziana, Hernquist Lars.* Modelling feedback from stars and black holes in galaxy mergers // *MNRAS.* VIII 2005a. 361, 3. 776–794.
- Springel Volker, White Simon D. M., Jenkins Adrian, Frenk Carlos S., Yoshida Naoki, Gao Liang, Navarro Julio, Thacker Robert, Croton Darren, Helly John, Peacock John A., Cole Shaun, Thomas Peter, Couchman Hugh, Evrard August, Colberg Jörg, Pearce Frazer.* Simulations of the formation, evolution and clustering of galaxies and quasars // *Nature.* VI 2005b. 435, 7042. 629–636.
- Springel Volker, White Simon DM, Tormen Giuseppe, Kauffmann Guinevere.* Populating a cluster of galaxies—I. Results at $z=0$ // *Monthly Notices of the Royal Astronomical Society.* 2001. 328, 3. 726–750.
- Stafford Sam G., Brown Shaun T., McCarthy Ian G., Font Andreea S., Robertson Andrew, Poole-Mckenzie Robert.* Exploring extensions to the standard cosmological model and the impact of baryons on small scales. 2020a.
- Stafford Sam G, McCarthy Ian G, Crain Robert A, Salcido Jaime, Schaye Joop, Font Andreea S, Kwan Juliana, Pfeifer Simon.* The bahamas project: effects of a running scalar spectral index on large-scale structure // *Monthly Notices of the Royal Astronomical Society.* Jan 2020b. 493, 1. 676–697.

- Stafford Sam G., McCarthy Ian G., Kwan Juliana, Brown Shaun T., Font Andreea S., Robertson Andrew.* Testing extensions to Λ CDM on small scales with forthcoming cosmic shear surveys // MNRAS. XII 2021. 508, 2. 2537–2555.
- Syer D., White Simon D. M.* Dark halo mergers and the formation of a universal profile // Monthly Notices of the Royal Astronomical Society. 02 1998. 293, 4. 337–342.
- Taylor A. N., Dye S., Broadhurst T. J., Benítez N., van Kampen E.* Gravitational Lens Magnification and the Mass of Abell 1689 // ApJ. VII 1998. 501, 2. 539–553.
- Taylor James E., Navarro Julio F.* The Phase-Space Density Profiles of Cold Dark Matter Halos // ApJ. Dec 2001. 563, 2. 483–488.
- Tinker Jeremy, Kravtsov Andrey V., Klypin Anatoly, Abazajian Kevork, Warren Michael, Yepes Gustavo, Gottlöber Stefan, Holz Daniel E.* Toward a Halo Mass Function for Precision Cosmology: The Limits of Universality // ApJ. XII 2008. 688, 2. 709–728.
- Tinker Jeremy, Kravtsov Andrey V., Klypin Anatoly, Abazajian Kevork, Warren Michael, Yepes Gustavo, Gottlöber Stefan, Holz Daniel E.* Toward a Halo Mass Function for Precision Cosmology: The Limits of Universality // The Astrophysical Journal. Dec 2008. 688, 2. 709–728.
- Udrescu Silviu M., Dutton Aaron A., Macciò Andrea V., Buck Tobias.* A deeper look into the structure of Λ CDM haloes: correlations between halo parameters from Einasto fits // MNRAS. II 2019. 482, 4. 5259–5267.
- Viel Matteo, Lesgourgues Julien, Haehnelt Martin G., Matarrese Sabino, Riotto Antonio.* Constraining warm dark matter candidates including sterile neutrinos and light gravitinos with WMAP and the Lyman- α forest // Phys. Rev. D. III 2005. 71, 6. 063534.
- Vogelsberger Mark, Genel Shy, Springel Volker, Torrey Paul, Sijacki Debora, Xu Dandan, Snyder Greg, Nelson Dylan, Hernquist Lars.* Introducing the Illustris Project: simulating the coevolution of dark and visible matter in the Universe // MNRAS. Oct 2014a. 444, 2. 1518–1547.

- Vogelsberger Mark, Zavala Jesus, Simpson Christine, Jenkins Adrian.* Dwarf galaxies in CDM and SIDM with baryons: observational probes of the nature of dark matter // *MNRAS*. XI 2014b. 444, 4. 3684–3698.
- Voit G. Mark, Kay Scott T., Bryan Greg L.* The baseline intracluster entropy profile from gravitational structure formation // *MNRAS*. Dec 2005. 364, 3. 909–916.
- Wang Jie, Bose Sownak, Frenk Carlos S., Gao Liang, Jenkins Adrian, Springel Volker, White Simon D. M.* Universality in the structure of dark matter haloes over twenty orders of magnitude in halo mass. 2019.
- Wang Jie, White Simon D. M.* Are mergers responsible for universal halo properties? // *Monthly Notices of the Royal Astronomical Society*. 06 2009. 396, 2. 709–717.
- Wechsler Risa H., Bullock James S., Primack Joel R., Kravtsov Andrey V., Dekel Avishai.* Concentrations of Dark Halos from Their Assembly Histories // *The Astrophysical Journal*. mar 2002. 568, 1. 52–70.
- Wechsler Risa H., Zentner Andrew R., Bullock James S., Kravtsov Andrey V., Allgood Brandon.* The Dependence of Halo Clustering on Halo Formation History, Concentration, and Occupation // *The Astrophysical Journal*. Nov 2006. 652, 1. 71–84.
- White S. D. M., Efstathiou G., Frenk C. S.* The amplitude of mass fluctuations in the universe // *MNRAS*. VI 1993. 262, 4. 1023–1028.
- Wiersma Robert P. C., Schaye Joop, Smith Britton D.* The effect of photoionization on the cooling rates of enriched, astrophysical plasmas // *MNRAS*. II 2009a. 393, 1. 99–107.
- Wiersma Robert P. C., Schaye Joop, Theuns Tom, Dalla Vecchia Claudio, Tornatore Luca.* Chemical enrichment in cosmological, smoothed particle hydrodynamics simulations // *MNRAS*. X 2009b. 399, 2. 574–600.
- Zel'dovich Ya. B.* Gravitational instability: An approximate theory for large density perturbations. // *A&A*. III 1970. 5. 84–89.

Zhao D. H., Jing Y. P., Mo H. J., Börner G. Mass and Redshift Dependence of Dark Halo Structure // *ApJ*. XI 2003. 597, 1. L9–L12.

Zhao D. H., Jing Y. P., Mo H. J., Börner G. Accurate Universal Models for the Mass Accretion Histories and Concentrations of Dark Matter Halos // *ApJ*. XII 2009. 707, 1. 354–369.

Zwicky F. Die Rotverschiebung von extragalaktischen Nebeln // *Helvetica Physica Acta*. I 1933. 6. 110–127.

van Daalen Marcel P., Schaye Joop. The contributions of matter inside and outside of haloes to the matter power spectrum // *MNRAS*. Sep 2015. 452, 3. 2247–2257.